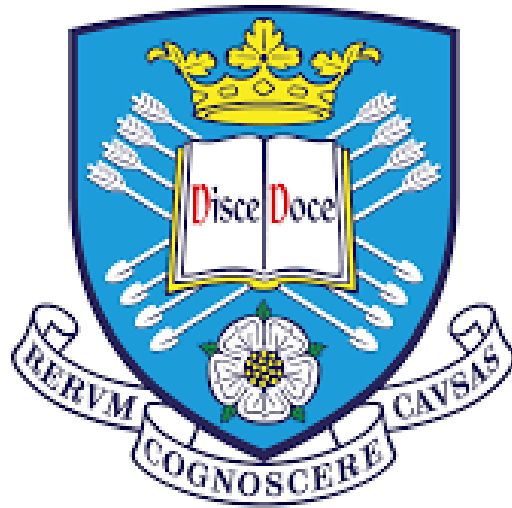


Energy Efficiency of Ultra-Dense Small Cell Radio Access Networks for 5G and Beyond



Hao Fu

A thesis presented for the degree of
Doctor of Philosophy

**Department of Electronic and Electrical
Engineering**

The University of Sheffield

July 2022

Abstract

Small cell base station (BS) densification in the radio access network (RAN) is an effective solution to improve the RAN capacity. However, small cell BS densification by adding more non-zero energy-consuming BSs increases energy consumption, compromising energy efficiency, which can be mitigated by adopting sleep mode. A comprehensive evaluation framework is applied in this research to analyse the capacity, energy consumption, and energy efficiency performance of the ultra-dense small cell RANs as a complete energy efficiency assessment, which is lacking in the literature. The impact of advanced techniques millimetre wave (mmWave), antenna array beamforming, and integrated access and backhaul (IAB) on RAN energy efficiency are also investigated. MATLAB-based simulation results show that the ultra-dense small cell RANs, where the number of BSs greatly exceeds the number of active user equipment (UEs), can only be energy efficient if all the empty cells without UE association are turned off completely. Energy efficiency enhancement comes from capacity improvement and energy consumption constraint. Specifically, the ultra-dense small cell RANs can achieve maximum performance improvement of 7.56-fold and 2.35-fold regarding capacity, 3780.11-fold and 32.38-fold regarding energy consumption using the current power model, and 28591.53-fold and 75.97-fold regarding energy efficiency in homogeneous and heterogeneous infrastructures, respectively, comparing the cases with and without the sleep mode. In addition, mmWave and IAB trade energy consumption and energy efficiency for capacity improvement and backhaul cost reduction. With mmWave and IAB, dense small cell RAN can achieve a maximum of 2.55-fold and 1.70-fold for capacity improvement, 2.46-fold and 2.89-fold for energy consumption reduction using the current power model, and 6.27-fold and 8.34-fold energy efficiency enhancement for UE densities of 900 and 300 UEs/km², respectively, comparing the cases with and without the sleep mode.

Acknowledgements

First, I'd like to thank my supervisor Professor Timothy O'Farrell for his constant guidance and support throughout my PhD study. He is not only an academic mentor but also a personal role model.

My gratitude also goes to my parents back in China. Without their understanding and support, none of this would have been possible.

I'd also like to thank my husband and my little boy for being such wonderful companions all the time and supporting me no matter what.

Contents

1	Introduction	19
1.1	General Background	19
1.2	Research Motivation	22
1.3	Research Aim and Objections	22
1.4	Research Contributions	24
1.5	Overview of Thesis Structure	27
1.6	List of Publication	29
2	Literature Review	30
2.1	Introduction	30
2.2	Energy Efficiency Evaluation Metric	31
2.2.1	Absolute Energy Efficiency Metrics	31
2.2.2	Relative Energy Efficiency Metrics	32
2.2.3	Energy Efficiency Evaluation Framework	35
2.3	Energy Efficiency of Ultra-Dense Small Cell RANs	36
2.3.1	Small Cells in the Homogeneous RAN Infrastructure	36
2.3.2	Small Cells in the Heterogeneous RAN Infrastructure	38
2.4	Energy Efficiency of Sleep Mode	40
2.4.1	Sleep Mode Cell Selection Methods	40
2.4.2	Sleep Mode Depths	42
2.5	Energy Efficiency of Millimetre Wave	43
2.6	Integrated Access and Backhaul	47

2.7	Summary	49
3	Energy Efficiency Evaluation Framework	51
3.1	Introduction	51
3.2	Ratio-Based Figures of Merit	52
3.2.1	Definitions of Figures of Merit	53
3.2.2	Derivatives of Figures of Merit	54
3.3	Power Model	56
3.3.1	Major Energy Consuming Components	56
3.3.2	Site Power Consumption Model	60
3.3.3	Power Model Case Studies	61
3.4	Summary	64
4	The Energy Efficiency of Ultra-Dense Homogeneous Small Cell RANs	66
4.1	Introduction	66
4.2	Homogeneous RAN System Model	68
4.2.1	Homogeneous RAN Layout	68
4.2.2	UE Received Power and Channel Model	69
4.2.3	UE Throughput and RAN Area Throughput	74
4.2.4	Scheduling Protocol and Jain’s Fairness Index	75
4.2.5	Homogeneous RAN Simulation Flowchart	77
4.3	Macro-RAN Densification	77
4.4	Small Cell RAN Densification	83
4.5	Pico-RAN Densification	90
4.5.1	Pilot Power Level from Empty Picocells	91
4.5.2	Sleep Mode Depths of Empty Picocells	96
4.5.3	Traffic Intensities in Pico-RAN Densification	101
4.5.4	Scheduling Protocol in Pico-RAN Densification	107
4.6	Case Study: Pico-RAN densification in the Internet of Things	112
4.6.1	IoT System Model and Evaluation Metric	114
4.6.2	Simulation Results for Different UE Distributions	116

4.6.3	Simulation Results for Different UE Counts	121
4.7	Summary	123
5	The Energy Efficiency of Ultra-Dense Heterogeneous RANs	126
5.1	Introduction	126
5.2	Heterogeneous RAN System Model	127
5.2.1	Heterogeneous RAN layout	128
5.2.2	UE Received Power and Channel Model	129
5.2.3	UE throughput and RAN Area Throughput	132
5.2.4	Heterogeneous RAN Power Consumption	133
5.2.5	Heterogeneous RAN Simulation Flowchart	133
5.3	Heterogeneous RAN Cell Peak Transmission Power Approach	135
5.4	Densification in Macrocell Layer of Heterogeneous RAN	140
5.4.1	Macrocell Densification without Sleep Mode	140
5.4.2	Macrocell Densification with the Sleep Mode	143
5.5	Densification in Picocell Layer of Heterogeneous RAN	146
5.5.1	Picocell Densification without Sleep Mode	147
5.5.2	Picocell Densification with the Sleep Mode	150
5.5.3	Picocell Densification Sensitivities	154
5.5.4	Picocell Densification with Schedulers	156
5.6	Summary	163
6	The Energy Efficiency of Dense Homogeneous RANs with Millimetre Wave and Integrated Access and Backhaul	166
6.1	Introduction	166
6.2	System Model	168
6.2.1	Homogeneous RAN Layout	168
6.2.2	UE Received Power and Channel Model	170
6.2.3	UE Throughput and RAN Area Throughput	174
6.2.4	Homogeneous RAN Simulation Flowchart Including Millimetre Wave and Integrated Access and Backhaul	175

6.2.5	Node Association	177
6.2.6	Backhaul Rate Constraint	183
6.2.7	Millimetre Wave Site Level Base Station Power Model	186
6.3	Small Cell RAN Densification using Millimetre Wave and Integrated Access and Backhaul	189
6.3.1	The Impact of Enabling Integrated Access and Backhaul	190
6.3.2	The Impact of Node Association Criteria	193
6.3.3	Resource Partitioning Methods	198
6.3.4	Node Backhaul Rate Constraints	201
6.3.5	Sleep Modes	205
6.4	Summary	209
7	Conclusions and Future Works	213
7.1	Conclusions	213
7.2	Future Works	216

List of Figures

3.1	Typical macro-BS site schematic, showing the major energy-consuming components for the power model derived from the Green Radio Project	57
3.2	Illustrated example of the working power level of a power amplifier	59
3.3	Power consumption percentage of radio-head (RH), overhead excluding backhaul (OH excl. BH), and backhaul (BH) within the total power consumption for different BS technologies	62
3.4	Site power consumption P_b versus normalised load activity factor α_c , comparing BS technologies, macro-BS site has $(n_a, n_c) = (1, 3)$, small cell BS site has $(n_a, n_c) = (1, 1)$, $B = \hat{B}$, $OBO = 8$ dB	63
3.5	Site power consumption P_b versus PA output backoff OBO , comparing BS technologies, macro-BS site has $(n_a, n_c) = (1, 3)$, small cell BS site has $(n_a, n_c) = (1, 1)$, $B = \hat{B}$, $\alpha_c = 1$	64
4.1	Examples of homogeneous RAN layout	68
4.2	3GPP antenna radiation pattern for a single macrocell, $\theta_{3dB} = 32$ degrees, $\phi_{3dB} = 70$ degrees, $A_m = 25$ dB, $\theta_{tilt} = 0$ degree, $SLA_v = 20$ dB	71
4.3	3GPP vertical antenna radiation pattern for a single microcell, $\theta_{3dB} = 40$ degrees, $SLA_v = 20$ dB, $\theta_{tilt} = 0$ degree	71
4.4	Probability of LoS transmission versus the 3D distance between BSs and UEs in units of metre, $Pr_{c,k}^{LoS}$, comparing different BS technologies	73
4.5	MATLAB-based simulation flowchart of homogeneous RAN	78
4.6	Macro-RAN Data Volume Gain against macrocell density, comparing different $\hat{P}_{tx,c}$ approaches	82

4.7	Macro-RAN Energy Consumption Gain against macrocell density, comparing different $\hat{P}_{tx,c}$ approaches	83
4.8	Macro-RAN Energy Efficiency Gain against macrocell density, comparing different $\hat{P}_{tx,c}$ approaches	84
4.9	RAN Data Volume Gain against cell density, comparing fixed and varied cell peak transmission power $\hat{P}_{tx,c}$ approaches and different BS technologies	87
4.10	RAN Energy Consumption Gain against cell density, comparing fixed and varied cell peak transmission power $\hat{P}_{tx,c}$ approaches and different BS technologies	88
4.11	RAN Energy Efficiency Gain against cell density, comparing fixed and varied cell peak transmission power $\hat{P}_{tx,c}$ approaches and different BS technologies	90
4.12	Pico-RAN Data Volume Gain against picocell density, comparing different pilot power levels in empty picocells: <i>Pilot10</i> has α_c of 10%, <i>Pilot5</i> has α_c of 5%, <i>Pilot1</i> has α_c of 1%, and <i>Pilot0</i> has α_c of 0%	93
4.13	Cumulative Distribution Function of UE SINR, comparing different pico-BS ISDs, with all empty cells have (a) <i>Pilot10</i> with α_c of 10% and (b) <i>Pilot0</i> with α_c of 0%	94
4.14	Pico-RAN Energy Consumption Gain against picocell density, comparing different pilot power levels in empty picocells: <i>Pilot10</i> has α_c of 10%, <i>Pilot5</i> has α_c of 5%, <i>Pilot1</i> has α_c of 1%, and <i>Pilot0</i> has α_c of 0%	95
4.15	Pico-RAN Energy Efficiency Gain against picocell density, comparing different pilot power levels in empty picocells: <i>Pilot10</i> has α_c of 10%, <i>Pilot5</i> has α_c of 5%, <i>Pilot1</i> has α_c of 1%, and <i>Pilot0</i> has α_c of 0%	96
4.16	Pico-RAN Data Volume Gain against picocell density, comparing different sleep mode depths in empty picocells: <i>Sleep0</i> has all three overhead components on, <i>Sleep1</i> turns off the the transceiver units, <i>Sleep2</i> turns off both the transceiver units and the baseband units, and <i>Sleep3</i> turns all the three overhead components off	98
4.17	Pico-RAN Energy Consumption Gain against picocell density, comparing different sleep mode depths in empty picocells: <i>Sleep0</i> has all three overhead components on, <i>Sleep1</i> turns off the the transceiver units, <i>Sleep2</i> turns off both the transceiver units and the baseband units, and <i>Sleep3</i> turns all the three overhead components off	99

4.18	Pico-RAN Energy Efficiency Gain against picocell density, comparing different sleep mode depths in empty picocells: <i>Sleep0</i> has all three overhead components on, <i>Sleep1</i> turns off the the transceiver units, <i>Sleep2</i> turns off both the transceiver units and the baseband units, and <i>Sleep3</i> turns all the three overhead components off	100
4.19	Pico-RAN Energy Consumption Gain against picocell density, comparing different backhaul power consumption P_{BH} in empty picocells, which turns off radio-head, transceiver and baseband units	102
4.20	Pico-RAN Energy Efficiency Gain against picocell density, comparing different backhaul power consumption P_{BH} in empty picocells, which turns off radio-head, transceiver and baseband units	103
4.21	Number of UEs per active picocell against picocell density, comparing different UE densities, empty cells are turned off completely	104
4.22	Pico-RAN Data Volume Gain against picocell density, comparing different UE densities, empty cells are turned off completely	105
4.23	Pico-RAN Energy Consumption Gain against picocell density, comparing different UE densities, empty cells are turned off completely	106
4.24	Pico-RAN Energy Efficiency Gain against picocell density, comparing different UE densities, empty cells are turned off completely	107
4.25	Pico-RAN Data Volume Gain against picocell density, comparing different schedulers, empty cells are turned off completely, 300 UEs/km ²	109
4.26	Pico-RAN Energy Consumption Gain against picocell density, comparing different schedulers, empty cells are turned off completely, 300 UEs/km ²	110
4.27	Pico-RAN Energy Efficiency Gain against picocell density, comparing different schedulers, empty cells are turned off completely, 300 UEs/km ²	110
4.28	Jain's fairness index of resource allocation, J_{RB} , against picocell density, comparing different schedulers, empty cells are turned off completely, 300 UEs/km ²	111
4.29	Jain's fairness index of UE throughput, J_S , against picocell density, comparing different schedulers, empty cells are turned off completely, 300 UEs/km ²	113
4.30	Cumulative distribution function versus ISD for various BS counts in IoT RAN . . .	117

4.31	RAN Volume Spectral Efficiency (VSE) versus picocell density for 100 UEs with different distributions, and sleep mode off (<i>Pilot10</i>), where empty cells have α_c of 10%, and sleep mode on (<i>Sleep0</i>), where empty cells have α_c of 0	118
4.32	RAN power consumption versus picocell density for 100 UEs with different UE distributions, and different empty cell status: <i>Pilot10</i> for sleep mode off, <i>Sleep0</i> for sleep mode on and OH on, <i>Sleep2</i> for sleep mode on and backhaul on, <i>Sleep3</i> for sleep mode on and OH off	119
4.33	RAN Energy Efficiency (EE) versus picocell density for 100 UEs with different UE distributions, and different empty cell status: <i>Pilot10</i> for sleep mode off, <i>Sleep0</i> for sleep mode on and OH on, <i>Sleep2</i> for sleep mode on and backhaul on, <i>Sleep3</i> for sleep mode on and OH off	120
4.34	RAN Volume Spectral Efficiency (VSE) versus picocell density for various UEs counts with clustered distribution, and sleep mode off (<i>Pilot10</i>), where empty cells have α_c of 10%, and sleep mode on (<i>Sleep0</i>), where empty cells have α_c of 0	122
4.35	RAN power consumption versus picocell density for different UE counts with clustered distribution, and different empty cell status: <i>Pilot10</i> for sleep mode off, <i>Sleep0</i> for sleep mode on and OH on, <i>Sleep2</i> for sleep mode on and backhaul on, <i>Sleep3</i> for sleep mode on and OH off	123
4.36	RAN Energy Efficiency (EE) versus picocell density for different UE counts with clustered distribution, and different empty cell status: <i>Pilot10</i> for sleep mode off, <i>Sleep0</i> for sleep mode on and OH on, <i>Sleep2</i> for sleep mode on and backhaul on, <i>Sleep3</i> for sleep mode on and OH off	124
5.1	Example of a heterogeneous RAN layout consisting of macrocell and small cell layers, 5 UE clusters with cluster radius of 40 m, minimum macro-BS and small cell BS separation is 75 m	128
5.2	Antenna radiation pattern for a sectored antenna, $\theta_{3dB} = 32$ degrees, $\phi_{3dB} = 70$ degrees, $A_m = 25$ dB, $\theta_{tilt} = 0$ degree, $SLA_v = 20$ dB	131
5.3	MATLAB based heterogeneous RAN simulator flowchart	134

5.4	Pico-UE count over total UE count against the HetNet densification, with macro-layer and pico-layer using (a) fixed and fixed $\hat{P}_{tx,c}$ approach, (b) fixed and varied $\hat{P}_{tx,c}$ approaches, (c) varied and fixed $\hat{P}_{tx,c}$ approaches, and (4) varied and varied $\hat{P}_{tx,c}$ approach, respectively	139
5.5	HetNet Data Volume Gain against macrocell density, comparing different picocell ISDs	141
5.6	HetNet Energy Consumption Gain against macrocell density, comparing different picocell ISDs	142
5.7	HetNet Energy Efficiency Gain against macrocell density, comparing different picocell ISDs	143
5.8	HetNet Data Volume Gain against macrocell density, comparing different picocell ISDs and sleep modes: <i>Site Sleep Mode</i> and <i>Cell Sleep Mode</i>	145
5.9	HetNet Energy Consumption Gain against macrocell density, comparing different picocell ISDs and sleep modes: <i>Site Sleep Mode</i> and <i>Cell Sleep Mode</i>	145
5.10	HetNet Energy Efficiency Gain against macrocell density, comparing different picocell ISDs and sleep modes: <i>Site Sleep Mode</i> and <i>Cell Sleep Mode</i>	146
5.11	HetNet Data Volume Gain against picocell density, comparing different macrocell ISDs	148
5.12	HetNet Energy Consumption Gain against picocell density, comparing different macrocell ISDs	149
5.13	HetNet Energy Efficiency Gain against picocell density, comparing different macrocell ISDs	150
5.14	HetNet Data Volume Gain against picocell density, comparing different macrocell ISDs and sleep modes: <i>Site Sleep Mode</i> and <i>Cell Sleep Mode</i>	151
5.15	HetNet Energy Consumption Gain against picocell density, comparing different macrocell ISDs and sleep modes: <i>Site Sleep Mode</i> and <i>Cell Sleep Mode</i>	153
5.16	HetNet Energy Efficiency Gain against picocell density, comparing different macrocell ISDs and sleep modes: <i>Site Sleep Mode</i> and <i>Cell Sleep Mode</i>	153
5.17	HetNet Energy Consumption Gain against picocell density, comparing different backhaul power consumption, P_{BH} , in empty picocells using <i>Site Sleep Mode</i> , macrocell ISD 300 m	155

5.18	HetNet Energy Efficiency Gain against picocell density, comparing different backhaul power consumption, P_{BH} , in empty picocells using <i>Site Sleep Mode</i> , macro-ISD 300 m	157
5.19	HetNet Energy Consumption Gain against picocell density, comparing different backhaul power consumption, P_{BH} , in empty picocells using <i>Cell Sleep Mode</i> , macro-ISD 300 m	158
5.20	HetNet Energy Efficiency Gain against picocell density, comparing different backhaul power consumption, P_{BH} , in empty picocells using <i>Cell Sleep Mode</i> , macro-ISD 300 m	159
5.21	HetNet Data Volume Gain against picocell density, comparing different schedulers and sleep modes: <i>Site Sleep Mode</i> and <i>Cell Sleep Mode</i> , macro-ISD 300 m	161
5.22	HetNet Energy Consumption Gain against picocell density, comparing different schedulers and sleep modes: <i>Site Sleep Mode</i> and <i>Cell Sleep Mode</i> , macro-ISD 300 m	161
5.23	HetNet Energy Efficiency Gain against picocell density, comparing different schedulers and sleep modes: <i>Site Sleep Mode</i> and <i>Cell Sleep Mode</i> , macro-ISD 300 m	162
5.24	HetNet average cell fairness, or UE throughput fairness, against picocell density, comparing different schedulers, macro-ISD 300 m, <i>Site Sleep Mode</i> on	164
6.1	Example of a Homogeneous small cell RAN layout with 19 BS sites and 57 cells, 19 or 3 donor sites out of the total 19 donor sites	169
6.2	3GPP rectangular panel antenna array schematic	171
6.3	3GPP small cell antenna array 3D radiation pattern, $G_{BS,c}$, maximum gain 32.08 dBi, boresight at (0,0) degrees, 128 antenna elements, cross-polarization, generated using MATLAB built-in objects and 3GPP suggested parameters	172
6.4	3GPP UE antenna array 3D radiation pattern, $G_{UE,k}$, maximum gain 17.04 dBi, boresight at (0,0) degrees, 8 antenna elements, cross-polarization, generated using MATLAB built-in objects and 3GPP suggested parameters	172
6.5	MATLAB-based simulation flowchart of homogeneous RAN using IAB	176
6.6	Flowchart of UE association	178
6.7	Example of donor-node association in IAB	179

6.8	Pico-RAN Data Volume Gain on mmWave against picocell density, with or without IAB	192
6.9	Pico-RAN Energy Consumption Gain on mmWave against picocell density, with or without IAB	193
6.10	Pico-RAN Energy Efficiency Gain on mmWave against picocell density, with or without IAB	194
6.11	Cumulative Distribution Function of Hop number, comparing different node association criteria combinations and pico-BS ISDs	196
6.12	Cumulative Distribution Function of Normalised UE number associated with all the donor-node chain starting with the same donor, comparing different node association criteria combinations and pico-BS ISDs	197
6.13	Pico-RAN Data Volume Gain on mmWave and IAB enabled against picocell density, with different node association criteria	198
6.14	Pico-RAN Energy Consumption Gain on mmWave and IAB enabled against picocell density, with different node association criteria	199
6.15	Pico-RAN Energy Efficiency Gain on mmWave and IAB enabled against picocell density, with different node association criteria	199
6.16	Pico-RAN Data Volume Gain on mmWave and IAB enabled, against picocell density, comparing fixed and load based resource partitioning methods	200
6.17	Pico-RAN Energy Consumption Gain on mmWave and IAB enabled, against picocell density, comparing fixed and load based resource partitioning methods	201
6.18	Pico-RAN Energy Efficiency Gain on mmWave and IAB enabled, against picocell density, comparing fixed and load based resource partitioning methods	202
6.19	Pico-RAN Data Volume Gain on mmWave and IAB enabled against picocell density, comparing different backhaul rate constraints on node UEs: dynamic S_{BH} sets constraints based on backhaul channel conditions, fixed S_{BH} sets fixed constraints, and no S_{BH} does not set constraint	203

6.20 Pico-RAN Energy Consumption Gain on mmWave and IAB enabled against pico-cell density, comparing different backhaul rate constraints on node UEs: dynamic S_{BH} sets constraints based on bakchaul channel conditions, fixed S_{BH} sets fixed constraints, and no S_{BH} does not set constraint 204

6.21 Pico-RAN Energy Efficiency Gain on mmWave and IAB enabled against picocell density, comparing different backhaul rate constraints on node UEs: dynamic S_{BH} sets constraints based on bakchaul channel conditions, fixed S_{BH} sets fixed constraints, and no S_{BH} does not set constraint 204

6.22 Pico-RAN Data Volume Gain on mmWave and IAB enabled against picocell density, with or without sleep mode, *Sleep1* only turns off pilot transmission in empty cells, *Sleep2 (Site Sleep Mode)* also turns empty sites off completely, *Sleep3 (Cell Sleep Mode)* turns empty cells off completely, UE densities of (a) 900UEs/km² (b) 300UEs/km² 207

6.23 Pico-RAN Energy Consumption Gain on mmWave and IAB enabled against picocell density, with or without sleep mode, *Sleep1* only turns off pilot transmission in empty cells, *Sleep2 (Site Sleep Mode)* also turns empty sites off completely, *Sleep3 (Cell Sleep Mode)* turns empty cells off completely, UE densities of (a) 900UEs/km² (b) 300UEs/km² 208

6.24 Pico-RAN Energy Efficiency Gain on mmWave and IAB enabled against picocell density, with or without sleep mode, *Sleep1* only turns off pilot transmission in empty cells, *Sleep2 (Site Sleep Mode)* also turns empty sites off completely, *Sleep3 (Cell Sleep Mode)* turns empty cells off completely, UE densities of (a) 900UEs/km² (b) 300UEs/km² 210

List of Tables

3.1	Power model parameters	61
4.1	Macro-RAN densification simulation parameters	80
4.2	Varied macrocell peak transmission power with RAN densification	81
4.3	Small cell RAN densification simulation parameters	85
4.4	Varied small cell peak transmission power with RAN densification	86
4.5	Cell normalised activity factors for different pilot power levels in cells	92
4.6	Sleep mode depths for empty picocells with α_c of 0%	97
4.7	Percentage power of an active picocell in IoT RAN	116
5.1	HetNet densification simulation parameters	136
5.2	Reduced cell peak transmission power against densification	137
6.1	Small cell types with integrated access and backhaul	183
6.2	Power parameters for pico-BS site	187
6.3	Small cell RAN densification simulation parameters using millimetre wave and integrated access and backhaul	191

List of Abbreviations

AC	Access Link
AI	Artificial Intelligence
ASE	Area Spectral Efficiency
BH	Backhaul
BB	Baseband
BS	Base Station
BTU	British Thermal Unit
CSI	Channel State Information
COOL	Cooling Unit
CDF	Cumulative Distribution Function
DVG	Data Volume Gain
D2D	Device-to-Device Communication
DL	Downlink
EARTH	Energy Aware Radio and Network Technology
ECG	Energy Consumption Gain
ECR	Energy Consumption Ratio
EE	Energy Efficiency
EEG	Energy Efficiency Gain
EER	Energy Efficiency Ratio
eICIC	Enhanced Inter-Cell Interference Coordination
5G	Fifth Generation
4G	Fourth Generation

HPBW	Half Power Bandwidth
HetNet	Heterogeneous RAN
HPPP	Homogeneous Poisson Point Process
iid	Independent and Identical Distribution
ICT	Information and Communication Technology
IAB	Integrated Access and Backhaul
IoT	Internet of Things
ISD	Inter-Site Distance
LoS	Line-of-Sight
LTE	Long Term Evolution
MBS	Macrocell Base Station
MUE	Macrocell User Equipment
MS	Main Power Supply
MSINR	Maximum Signal-to-Interference-plus-Noise-Ratio
mmWave	Millimetre Wave
MPF	Multi-Path Fading
MIMO	Multiple-Input Multiple-Output
NLoS	Non-Line-of-Sight
NOMA	Non-Orthogonal Multiple Access
OFDM	Orthogonal Frequency Division Multiple Access
OBO	Output Back-off
OH	OverHead
PL	Path Loss
PI	Performance Indicator
PUE	Picocell User Equipment
PPP	Poisson Point Process
PA	Power Amplifier
PS	Power Supply
PF	Proportional Fair

RAN	Radio Access Network
RF	Radio Frequency
RH	Radio-Head
RE	Range Expansion
RB	Resource Block
RR	Round Robin
SAT	Saturation
SF	Shadow Fading
SINR	Signal-to-Interference-plus-Noise-Ratio
SISO	Single-Input Single-Output
6G	Sixth Generation
SBS	Small Cell Base Station
SDM	Spacial Division Multiplexing
SE	Spectral Efficiency
3GPP	Third Generation Partnership Project
3D	Three Dimensional
TDM	Time Division Multiplexing
TRX	Transceiver
TTI	Transmission Time Interval
2D	Two Dimensional
UAV	Unmanned Aerial Vehicle
UE	User Equipment
VUE	Virtual User Equipment
VSE	Volume Spectral Efficiency

Chapter 1

Introduction

1.1 General Background

The fifth and sixth generations of mobile radio networks must support the continual growth in data demand arising from new mobile applications and use cases [1]–[5]. In [6] the authors predict an annual increase in data demand by 30% up to 2024. Other works in [7], [8] estimate a traffic size of five zettabytes per month by 2030 with a rate of 100 gigabits per second. The authors of [9] also mentioned an estimation from Ericsson such that from the year 2020 to 2026, the data would increase by seven times. To accommodate the growth in demand, three technical approaches are generally pursued [10]; increase available spectrum [11], [12], spatial reuse [13] and the number of base stations (BSs) within a given geographic area [14], [15]. All three solutions incur penalties. For example, increasing spectrum requires higher carrier frequencies, which increases path loss, whereas more antennas and radios are needed to increase spatial diversity. In [10] and [16], the authors illustrate how increasing the BS density, also known as BS densification in the radio access network (RAN), can increase area capacity by over a thousandfold. BS densification leads to the BS number increase in the RAN, and the corresponding reduction in BS coverage area (also known as cell size) and inter-site distance (ISD) between BSs. Note that BS densification does not change individual BS hardware characteristics or infrastructure.

The densification is primarily applied to the conventional macrocell BSs whose coverage area is large with high transmission power level and directional antenna pattern with high maximum gain [17], [18]. However, the RAN densification level of using macrocell BSs is limited by the

scarce geographical availability [19] and high construction costs [16], [20] of macro-BS sites. In contrast, small cell BSs are easier to deploy [21] and cost considerably less [22]. The concept of small cells is in contrast to conventional macrocells. Small cells have low transmission power to cover small areas, are equipped with higher energy-efficient hardware, and are usually placed in busy areas with high traffic intensity [23]. Also, small cells may be installed using different types of BSs, such as microcells, picocells, femtocells or relays. The advantages of coverage extension and capacity enhancement have been extensively studied in [10] for the homogeneous small cell RAN infrastructure and [24] for the coexisting of macrocells and small cells as a heterogeneous RAN infrastructure.

The problems with RAN densification, using macrocell BSs or small cell BSs, are the increasing implementation and maintenance cost [25], [26] as well as the increasing energy consumption [27]–[29]. In [30], the authors mentioned that the energy consumption of an individual BS would increase four-time when evolving the technology from fourth-generation (4G) to fifth-generation (5G). In contrast, the increase factor becomes 12 in terms of total RAN energy consumption, given that the 5G RANs usually have a denser infrastructure. The energy consumption increase would, in turn, incur more carbon emissions like CO_2 [31] that would damage the environment. Specifically, the authors of [31] have predicted that, by 2040, the carbon emissions generated by Information and Communication Technology (ICT) equipment would occupy 14% of the year 2016 total amount across the world. The increase in energy consumption could be mitigated by replacing macrocell BSs with small cell BSs. However, highly densified small cells still consume a significant amount of energy [10], [32].

To reduce energy consumption, a lot of solutions have been proposed in terms of RAN infrastructure evolution like smart city [33]–[35], repetitive data transmission avoidance using caching and device-to-device (D2D) communication [36], [37], or hardware efficiency improvement [38]–[40]. Among these advanced technologies, putting empty cells into low-power sleep mode, sometimes called idle mode, is effective without changing the RAN architecture or hardware. The cells without user equipment (UE) association are called empty cells, which are more likely to exist in highly densified RANs. Sleep mode’s effectiveness in energy consumption reduction has been well developed in the literature [24], [41]–[43].

This concern for the increasing energy consumption, along with the demand for improving RAN

capacity, makes energy efficiency (EE) another key RAN performance indicator. EE is defined as the amount of data transferred in the communication system when consuming a unit amount of energy, with the units of bit per joule [44]. In other words, EE measures how effectively energy is consumed to transmit data. Generally, two categories of EE metrics are applied in the literature: the absolute measurement between two observation points and the relative measurement upon achieving a specific task [45]. In the literature, the absolute EE measurement is usually represented by the energy consumed during a pre-set observation period like the works in [46]–[48], which generally lacks the capacity performance evaluation. In contrast, the relative EE measurement includes both the EE itself and its derivatives [49]–[65], which usually lacks energy consumption evaluation. The lack of either capacity or energy consumption evaluation requires a more comprehensive evaluation tool for a complete RAN energy efficiency evaluation.

The small cell RAN densification using the 4G Long Term Evolution (LTE) technology on the sub-6 GHz frequency band could benefit the capacity and energy efficiency in only one degree [10]. A further benefit would require the aforementioned spectrum increase or spatial diversity increase. The popular approach to increase the spectrum is to move the transmission band beyond 24 GHz, usually referred to as the millimetre wave (mmWave) due to its wavelength scale [66], [67]. High frequency results in high path loss. This used to make the mmWave an ineffective solution for capacity improvement, despite the wide transmission channel bandwidth [68]. However, for dense small cell RANs where cell coverage is usually small, mmWave could be applied effectively. Additionally, the mmWave with high frequency and thus small wavelength make antennas of small size feasible [67]. This enables compacting more antennas into arrays with a high directivity using beamforming that would increase the spatial diversity to improve the capacity and energy efficiency further [69].

Along with the small cell RAN densification also comes the increasing cost and difficulty of implementing and maintaining wired backhaul links for each small cell BS individually [70], [71]. It is mentioned in [6], [72] that the cost of implementing a fibre backhaul link is approximately 0.1 million USD per unit kilometre. With the mmWave band providing wide channel bandwidth, an advanced technique to enable BSs to share the wireless channel between access and backhaul links is introduced in [70]. This technology is called the integrated access and backhaul (IAB), or self-backhauling, with the benefits of being cheap, easy to implement, and flexibility [73]. In

a RAN with IAB, some BSs have the conventional fibre backhaul while the remaining BSs use wireless backhaul served by the former. The BSs with wired backhaul links are called donors, while the BSs with wireless backhaul links are called nodes. The overall cost of backhaul will be reduced with the co-existence of donors and nodes in the RAN.

1.2 Research Motivation

Small cell RAN densification is an effective solution to cope with users' ever-increasing data demand. However, adding more BSs to densify the RAN also increases energy consumption. This compromises energy efficiency, especially at a high RAN densification level. Most literature has studied the performance of small cell RAN densification in terms of capacity, or sometimes coverage area, and energy efficiency and showed promising results. Nevertheless, without a specific indication of the energy consumption tendency against the increasing BS density, the study on energy efficiency using any proposed technologies, algorithms, or architectures is incomplete. In some works, the concept of being green equates to providing higher energy efficiency, regardless of energy consumption reduction or increase. However, in this work, the technique or RAN architecture that trades off energy consumption for capacity to improve energy efficiency is not considered green.

Therefore in this research, both the capacity and energy consumption of the small cell RAN densification are analysed in addition to the energy efficiency for a complete EE evaluation. The three performance factors are evaluated using a comprehensive energy efficiency evaluation framework. In addition, the RAN densification is taken to an extreme level to seek energy efficiency limitations. Furthermore, techniques like sleep mode, mmWave, and IAB are also explored to investigate their impact on small cell RAN densification and whether they could change the densification limitation.

1.3 Research Aim and Objections

The primary aim of this research is to find the fundamental limit on small cell BS densification in the RAN, accounting for capacity, energy consumption, and energy efficiency. The study was conducted in the context of homogeneous RAN and heterogeneous RAN, where the small cells co-exist with the conventional macrocells for the latter. In addition, the impact of BS technologies, sleep mode depths (in terms of both the traffic dependent and independent aspects), traffic intensities, resource

scheduler, RAN layout model, carrier frequency and channel bandwidth, and backhaul technologies on the energy efficiency of the small cell RAN densification were also investigated. The detailed objectives are listed as follows:

1. Explore the fundamental understanding of RAN densification by densifying the macrocell BSs. Specifically, having set up the system model, increase the number of identical conventional macrocell BSs with large coverage area, high transmission power, and triple sectorization within a RAN and observe the tendency of RAN capacity, energy consumption, and energy efficiency. The study of homogeneous macrocell densification provides a basic understanding of the effect on energy efficiency when adding more identical BSs to the RAN.
2. Explore the theoretic limitation on RAN densification by replacing the conventional macrocell BSs with small cell BSs in a homogeneous manner. Small cell BSs could densify to higher levels than their macrocell BS counterpart for their small size, installation flexibility, and low power consumption. With a similar system model but different parameters, the identical small cell BS number was increased to observe the corresponding tendency of RAN capacity, energy consumption, and energy efficiency. Based on the observed results, the transmission power level and power consumption level of cells with no user association were gradually reduced to observe the impact on the three performance factors. Then the variations of traffic intensity, resource scheduler, and the BS and UE distribution model were explored to test the observations of small cell RAN densification. To an extreme level, the study of homogeneous small cell densification provides a fundamental understanding and theoretical guideline for energy efficient small cell RAN design.
3. Explore the limitation on RAN densification by overlaying small cell BSs with the conventional macrocells in a heterogeneous manner. Deploy small cell BSs in addition to the traditional macrocell BSs to target the clustered traffic. Using a similar system model but a different RAN layout from the homogeneous scenario, the RAN capacity, energy consumption, and energy efficiency are evaluated against the increasing BS densification in both the macrocell and small cell layers. Again, the sleep mode is applied to cells without UE association for potential performance improvement. The study of heterogeneous small cell densification, co-existing with macrocells, to an extreme level, provides the understanding of energy efficient

RAN densification in a more practical scenario.

4. Explore the understanding of RAN densification when moving the transmission band beyond the sub-6 GHz. The sub-6 GHz frequency band has already been well explored and developed, whereas the mmWave band has more opportunities in terms of RAN capacity and energy efficiency enhancement. Because of the wide bandwidth that comes with the mmWave, the large antenna array with a highly focused beam is feasible, and so is the resource sharing between access links to users and backhaul links to the core network, which is IAB. These would potentially benefit the capacity and energy efficiency more. Setting up the system model with different parameters and extra processes for IAB, the impact of the reduction in BS ISD on RAN capacity, energy consumption, and energy efficiency is explored. Specifically, node association criteria, resource partitioning methods, backhaul rate constraints, and sleep modes are analysed. The study of RAN densification in the context of mmWave and IAB moves this research further to fit in the more state-of-the-art concept and provides more insights into the energy efficiency of the densified small cell RANs.

1.4 Research Contributions

This research studies the energy efficiency of small cell RAN densification to an extreme level, with the advanced techniques of sleep mode, for interference and energy consumption reduction, mmWave, for capacity improvement, and IAB, for energy consumption and cost reduction. The specific contributions of this research are:

1. The exploration of energy efficiency of the small cell RAN densification in the homogeneous context for fundamental understanding. The densification level of small cells, particularly picocells in this work, was increased to a level where BSs are just one metre apart from each other in a hexagonal grid, equivalent to over one million small cells per square kilometre. The simulation results show that small cells perform better than their macrocell counterparts with the same cell densities in terms of capacity, energy consumption, and energy efficiency. However, boundless small cell BS densification, where the number of BS is significant, degrades capacity and energy efficiency due to increasing interference and energy consumption.

In contrast, the capacity improves monotonically with the increasing cell density until saturation if all the empty small cells in the RAN turn off their transmission using sleep mode. Additionally, the degraded RAN energy efficiency recovers when the energy consumption saturates with the increasing small cell density when all the empty small cells are turned off completely. These observations hold for different traffic intensities and BS models. Furthermore, the simple Round Robin (RR) scheduler is preferred for highly densified small cell RAN for its simplicity without performance degradation. Nevertheless, in the sub-6 GHz band, the small cell RAN densification with sleep mode should also be bounded but to a much higher level, beyond which adding more BSs become unnecessary when all the capacity, energy consumption, and energy efficiency saturate. These set guidelines when an ultra-dense and energy efficient small cell RAN is required.

2. Having obtained the fundamental understanding of the densification limitation of the homogeneous small cell RAN layout, the RAN infrastructure then evolved to be heterogeneous, where small cells work together with macrocells for capacity improvement. The BS densification in both macrocell and small cell layers was investigated. The densification in the small cell layer was carried out similarly to the extreme one-metre ISD case. The simulation results show that the capacity, energy consumption, and energy efficiency of the heterogeneous RAN (HetNet) densification perform similarly towards the homogeneous small cell RAN densification, with or without the sleep mode. The performance gap is caused by the co-existence with macrocells whose coverage area is bigger and whose power level is higher. With the increasing traffic offloading from macrocells to small cells, the highly densified HetNet would eventually migrate to a homogeneous small cell RAN, and macrocells only provide coverage. Therefore, the densification of HetNet would also be bounded where the capacity, energy consumption, and energy efficiency start to saturate. This also sets guidelines when the RAN designer wants an energy efficient HetNet without consuming more energy.
3. The impact of the mmWave and IAB on the capacity, energy consumption, and energy efficiency of the densified small cell RAN was explored. Moving the frequency band beyond 6 GHz increases the channel bandwidth and the feasibility of forming large arrays of antennas to increase spatial diversity. Based on Shannon's capacity formula, these two factors could also

improve the RAN capacity. Additionally, the wide bandwidth enables IAB which reduces the backhaul link implementation and maintenance cost. With the IAB enabled, different backhaul rate constraint approaches on node UEs, the resource partitioning methods, and sleep mode depths are compared for potential performance improvement. The simulation results show that mmWave significantly increases RAN capacity and energy consumption. This degrades the RAN energy efficiency compared with the LTE RANs. The IAB technology trades off the RAN capacity performance for the backhaul cost. The energy consumption could be reduced when sleep mode is enabled. The energy saving is sufficient to recover energy efficiency for 300 UEs/km² but insufficient for 900 UEs/km² under the current power model in the limited picocell density range. Changing the backhaul rate constraint approaches or resource partitioning methods has a negligible effect on energy efficiency.

4. The application of a comprehensive energy efficiency evaluation framework for the complete energy efficiency evaluation of small cell RAN densification. Specifically, the framework provides three ratio-based figures of merit to evaluate the RAN capacity, energy consumption, and energy efficiency against the increasing BS density. Based on the framework, the cause of the energy efficiency variation in terms of capacity and energy consumption could be more accurately identified. This could provide the RAN designer with a clear picture of any possible performance trade-offs regarding the improved RAN energy efficiency or the performance limiting factor that degrades the energy efficiency.
5. The modification of the Green Radio Project power model to accommodate more scenarios for power consumption calculation. The original power model from the Green Radio Project [74] can calculate the site power consumption of either a macrosite or a small cell site with corresponding parameters using the 4G LTE technologies. The first enhancement made in this work is the value of the power amplifier output back-off in the power model. Specifically, the output back-off changes with the peak transmission power so that no hardware replacement is required when reducing the latter with the increasing BS density. Secondly, when moving from the LTE sub-6 GHz frequency band to the mmWave band, the small cell site power consumption model is modified to fit more appropriately with the large antenna number and wide bandwidth.

The simulation results are obtained via a comprehensive MATLAB-based simulator, accommodating RAN densification for capacity, energy consumption, and energy efficiency evaluations. The simulator can generate BS and UE locations according to different distribution models, associating UEs with BSs or BSs with BSs if IAB is enabled, and allocating resources based on various scheduling metrics. Moreover, the simulator can also switch between BS technologies (macrocell BS or small cell BS), antenna patterns (directional, omni-directional, or isotropic), signal transmission frequency bands (sub-6 GHz or mmWave), traffic intensities (UE densities), sleep mode depths, wireless backhaul node association criteria, resource partitioning methods, and backhaul rate constraints if IAB is enabled. The developed simulator helps with the rigorous energy efficiency evaluation.

1.5 Overview of Thesis Structure

The rest of the thesis is outlined as follows:

1. Chapter 2 presents a detailed literature review regarding the energy efficiency metrics, the capacity-improving small cell densification, the energy-reducing sleep mode, the capacity-improving mmWave, and the cost-reducing IAB techniques.
2. Chapter 3 introduces the energy efficiency evaluation framework. Following the motivation of applying the framework, the three ratio-based figures of merit are presented: the Data Volume Gain for capacity evaluation, the Energy Consumption Gain for energy consumption evaluation, and the Energy Efficiency Gain for energy efficiency evaluation, based on a pre-set reference RAN. The definitions and derivatives of the figures of merit are included, along with the benefit of applying this framework for energy efficiency evaluation. Afterwards, the power model enhanced from the Green Radio Project is introduced, with the schematic component breakdowns, the power consumption quantification of different components, and the overall mathematical expressions for BS site power consumption. At the end of the chapter, a summary is drawn.
3. Chapter 4 presents the energy efficiency evaluation of ultra-dense homogeneous small cell RANs. The chapter first introduces the research motivation. Then a homogeneous system

model is presented, with the mathematical expressions for UE received power; channel loss, including the probability-weighted path loss and shadow fading, as well as the multipath fading; UE SINR; UE throughput; and the RAN throughput. Different resource scheduling metrics are also introduced with Jain's fairness indices for scheduling fairness evaluation. Then figures of merit results of the simulated homogeneous RAN densification are first presented in terms of different transmission power approaches. Then the small cell RAN densification is evaluated using the figures of merit regarding the small cell BS technologies, transmission power approaches, empty cell pilot power levels, empty cell sleep mode depths, power consumption of backhaul, traffic intensities, and scheduling protocol. The key finding is that the highly densified small cell RAN is energy efficient only when all the empty small cells are turned off completely.

4. Chapter 5 is about the energy efficiency evaluation of the ultra-dense heterogeneous RANs. The chapter first introduces the research motivation. Then the channel model, similar to the homogeneous case, is presented in terms of the RAN layout, UE throughput, and area RAN throughput calculations. Afterwards, the figure of merit results are used to analyse the energy efficiency of the HetNet when the densification occurs in the macrocell layer first and the small cell layer next. The results with and without sleep mode are evaluated, with a similar emphasis on the backhaul power consumption. The key finding is that when co-existing with macrocells, small cell densification still needs to turn off empty cells completely to make the RAN energy efficient.
5. Chapter 6 concerns the energy efficiency of densified small cell RANs with mmWave and IAB. Given the motivation of the research, a similar system model is presented. In addition, the node to donor backhaul association according to different criteria, resource partitioning methods based on fixed ratio or load, and the dynamic backhaul rate constraints on node UEs are also introduced. The impact of excluding and including the IAB technique on the small cell RAN energy efficiency is analysed first. Then the evaluation focus is moved to the node association criteria, the resource partitioning methods, the backhaul rate constraint, and the sleep mode depth. The key finding is that moving to mmWave increases RAN capacity and energy consumption significantly. The energy efficiency degrades within the densification level

range for high UE density but manages to recover for medium UE density. This is dominated by energy consumption.

6. Chapter 7 summarises all the significant observations on the energy efficiency of the small cell RAN densification using different infrastructures and technologies.

1.6 List of Publication

1. H. Fu and T. O’Farrell, “An energy efficiency evaluation framework for radio access networks,” in *2018 International Conference on Information and Communication Technology Convergence (ICTC)*, Jeju, Korea (South), 2018, pp. 577-580, doi: 10.1109/ICTC.2018.8539386.

This corresponds to Chapter 3 and Section 4.3.

2. H. Fu and T. O’Farrell, “The spectral and energy efficiency of ultra-dense IoT networks,” in *2022 IEEE 8th International Conference on Network Softwarization (NetSoft)*, Milan, Italy, 2022, pp. 55-60, doi: 10.1109/NetSoft54395.2022.9844097.

This corresponds to Section 4.6.

3. H. Fu and T. O’Farrell, “The volume spectral and energy efficiency of ultra-dense IoT networks with clustered users,” in *2022 20th International Symposium on Modeling and Optimization in Mobile, Ad hoc, and Wireless Networks (WiOpt)*, Torino, Italy, 2022, pp. 351-356, doi: 10.23919/WiOpt56218.2022.9930578.

This also corresponds to Section 4.6.

Chapter 2

Literature Review

2.1 Introduction

Capacity improvement has always been the priority when designing the advancing network to accommodate the continuously increasing data demand [1]. There are plenty of techniques and algorithms proposed and applied to increase the RAN capacity, among which the RAN densification by adding more BSs and reducing BS ISD is always the most straightforward solution [10].

However, RAN densification also increases the total energy consumption due to the increase in the BS number. This also increases the RAN implementation and maintenance cost and the carbon emissions [28], [31]. Therefore, in addition to the capacity, new RAN technique and architecture proposals also prioritise energy efficiency, defined as the amount of data transmitted when consuming one unit of energy [44].

The reduction of energy consumption could improve energy efficiency. The most popular solution is sleep mode, where cells without UE associations in the RAN are put into low power mode. This copes with the RAN densification effectively when the densification level is high and the number of empty cells is large [32].

The energy efficiency could also be improved by the capacity improvement driven by techniques other than the RAN densification. Having exploited the sub-6 GHz frequency band extensively for decades, the researchers and network operators are looking toward moving to a higher frequency band for unlicensed bands and broader channel bandwidth. Typically, frequencies higher than 24 GHz, also known as mmWave, attract the most attention. The mmWave band signal usually

has a much higher bandwidth than the sub-6 GHz counterpart and improves the RAN capacity [66]. Meanwhile, the high signal carrier frequency also makes the large-scale antenna array feasible due to the small wavelength [69]. The antenna array could generate a highly focused beam with significant gain using beamforming that would further benefit the RAN capacity. In addition, the wide channel bandwidth makes the wireless backhaul traffic integration, known as IAB, possible, which would reduce the implementation cost significantly [70].

The structure of the rest of this chapter is as follows. Section 2.2 presents the literature review on the energy efficiency metrics, expressing the need for a more comprehensive evaluation framework that provides a complete energy efficiency analysis. Section 2.3 concentrates on the energy efficiency of the small cell RAN densification in the literature, co-existing with macrocells or on their own for traffic serving. The works exploring the cell selection for sleep mode and different sleep mode depths are collected in section 2.4. Then the energy efficiency evaluation of mmWave in the literature is discussed in section 2.5, followed by the examples adopting IAB in section 2.6. Finally, section 2.7 gives the chapter conclusions.

2.2 Energy Efficiency Evaluation Metric

The RAN key performance indicator energy efficiency, or EE, is the amount of data in units of bit transmitted when consuming a unit of energy. The unit of EE is bit/J [44]. Many EE metrics are applied in the literature, including the definition of EE and its derivatives. These metrics could be divided into two categories: the absolute measurement observed between a starting and a finishing point and the relative measurement to achieve an event [75].

2.2.1 Absolute Energy Efficiency Metrics

Energy efficiency metrics falling into the absolute measurement category usually equate energy consumption reduction to energy efficiency improvement. In macrocell RANs, energy consumption is dominated by the traffic-dependent radio-head part. However, the traffic-independent overhead part dominates the densified small cell RAN energy consumption because the transmission power is usually low. So the works in [76]–[79] which only consider the radio-head energy consumption reduction in small cell RANs lack energy consumption evaluation accuracy. The following examples,

in contrast, considers both the radio-head and overhead for the energy consumption.

In [47], the authors minimise the per sub-carrier power consumption of a heterogeneous network with massive Multiple Input Multiple Output (MIMO) for energy efficiency improvement under UE throughput and power constraints. By varying the massive MIMO beamforming vectors for cell coordination, the simulation results show that per sub-carrier power consumption decreases against the increasing number of antennas at either macrocells or small cells for a fixed two bit/s/Hz UE throughput constraint. The per sub-carrier power consumption increases with the rising UE throughput constraint. This indicates a trade-off between the UE throughput and per sub-carrier power consumption, both of which impact energy efficiency. However, this is not mentioned in the paper. In other words, the energy consumption, which is the product of power consumption and observation time, is insufficient to evaluate the energy efficiency.

In [38], the authors interpret the concept of “green” for green networks as energy reduction. Therefore, they collectively present a list of energy efficiency metrics, some of which essentially measure the energy consumption of places such as the data centre and the network. The data centre energy consumption metrics are Power Usage Efficiency and Data Centre Efficiency, both accounting for the power input to the centre and the power consumed by all the hardware in the centre. The network-related metrics, called the Performance Indicator (PI), depend on the network coverage area or total UE number in addition to the site power consumption. However, the exclusion of capacity-related performance in the evaluation does not fit into the definition of energy efficiency. In other words, the energy consumption only contributes to incomplete energy efficiency evaluation.

2.2.2 Relative Energy Efficiency Metrics

Energy Efficiency metrics falling into the relative measurement category usually use the definition of EE or its derivatives as the metric. Unlike the absolute measurement category, the EE metrics in this category account for both the capacity and energy consumption performance simultaneously. Similarly, as the first EE metric category, the works in [80], [81] only consider the traffic-dependent energy consumption for the energy consumption, making inaccurate energy efficiency evaluation. In contrast, the following works consider both the radio-head and overhead parts regarding energy consumption when calculating EE.

In [82], the authors use power control to maximise the EE of individual small cell or D2D device included in the 5G HetNet. Specifically, BSs and D2D devices under power control have their transmission power varied individually by online learning for energy efficiency maximisation with Signal-to-interference-plus-ratio (SINR) and maximum transmission power constraints. The simulation results show that the proposed power control method achieves the highest RAN energy efficiency and the highest RAN spectral efficiency (SE) against the increasing small cell numbers, SINR constraints, and maximum transmission power constraints, compared with other power control methods. However, there is no indication of the RAN energy consumption, which is likely to increase with the increasing number of small cells. In other words, the energy efficiency improvement driven by the proposed power control method might also increase energy consumption. Only the EE and the SE analysis cannot provide a complete energy efficiency evaluation.

The work in [83] adjusts the small cell transmission power and bandwidth allocation simultaneously to maximise the HetNet RAN EE under constraints of macrocell UE SINR and the maximum small cell transmission power. All the small cell BSs are assumed to share the same bandwidth in the orthogonal manner, so no inter-cell interference is incurred. The optimal transmission power and bandwidth allocations for small cells are found using an iterative method. The simulation results show that the proposed resource management method could achieve the highest RAN EE and SE performance compared with other resource management methods where the transmission power or/and bandwidth allocation is fixed. The proposal improves the RAN EE and SE against the increasing maximum small cell transmission power constraint until saturation. However, the RAN EE first increases but then decreases against the growing number of antennas at the small cell BSs. This is due to the energy consumption increase caused by employing more antennas, which is not shown in the paper. Therefore, without the energy consumption analysis, the EE metric, with or without SE, cannot provide a complete energy efficiency evaluation.

In the context of HetNet with IAB, the authors of [84] propose a method to find the optimal beamforming vector for the macrocell BS (MBS) and transmission power for small cell BSs to maximise the RAN EE. The simulation results show that with sleep mode turning some small cells off, the proposed method achieves the highest RAN EE compared to other methods against the increasing maximum small cell transmission power constraint. Moreover, the RAN EE achieved by the proposal is also shown to decrease with the rising UE throughput constraint and the number

of small cells. This is due to the increasing energy consumption. Again, the EE metric alone is insufficient to provide this information for a complete energy efficiency evaluation.

Previous examples treat the small cell or sub-carrier equally when calculating the individual EE. In contrast, other literature uses weighted individual EE to meet various data demands. For example, three metrics are adopted in [85]: the weighted sum of per sub-carrier per BS rate, the total RAN EE, and the weighted sum of per sub-carrier per BS EE, where the various weights represent different demands and priorities. These metrics are used to find the optimum coordinated beamforming vectors under the maximum power constraint to maximise the capacity and energy efficiency for the BSs in the RAN with MIMO and orthogonal frequency division multiple access (OFDM). The simulation results show that the proposed beamforming approach could achieve optimal weighted sum per sub-carrier per BS rate, RAN EE and weighted sum of per sub-carrier per BS EE against the increasing power constraint and weights compared with other approaches. However, the lack of energy consumption analysis makes the evaluation incomplete. A similar weighted sum per BS EE is also used in the author's earlier work in [86] with another exponentially weighted product per sub-carrier per BS EE. The latter metric is believed to vary the EE of each sub-carrier by allocating more balanced transmission power levels compared with the weighted sum EE or RAN total EE. With the simultaneous coordination of UE scheduling, the simulation results show that the weighted EE metrics can provide more flexibility for designing a RAN than the original EE metric regarding resource management. However, the proposal's impact on energy consumption has not been discussed to provide a complete energy efficiency evaluation.

Moreover, the inverse of EE, called the Energy Consumption Ratio (ECR) with the units of J/bit [87], is also an applied energy efficiency metric in the literature that falls into the relative measurement category [88], [89]. The ECR is used in [90] to analyse the energy efficiency of a 5G small cell network on mmWave frequency bands in the indoor environment. Each small cell equips with a single omni-directional antenna or a linear eight-element antenna array to compare capacity and energy efficiency performance. The simulation results show that the single antenna approach could achieve higher capacity and energy efficiency than the multi-antenna approach with fully digital beamforming. The energy efficiency improvement comes from the energy consumption reduction despite capacity degradation. However, the ECR metric alone could not indicate this trade-off between capacity and energy consumption. This raises an evaluation ambiguity.

Besides the techniques included in this research, EE is also a popular metric to evaluate the energy efficiency of the architectures and techniques in the other wireless communication fields. The works in [91]–[93] apply the EE metric to evaluate the energy efficiency improvement of the power and spectrum allocations using the non-orthogonal multiple access (NOMA) techniques. Moreover, the EE metric is applied to measure the HetNet energy efficiency using the caching technique in [94] regarding various spectrum allocations. The authors of [95] assess the energy efficiency improvement of the cell-free massive MIMO using perfect channel estimation and power control, and the EE metric does the assessment. In addition, the network function virtualisation is discussed in [96] where the EE metric is used to evaluate the energy efficiency improvement brought by the joint resource allocation regarding power, spectrum, and antenna numbers. In [97], the solar energy harvesting powered small cells are put into and out of sleep mode dynamically according to the traffic demand. The EE is shown to improve because of the energy reduction. Furthermore, the EE metric is also used to evaluate the energy efficiency of visible light communication in [98] in terms of power and spectrum allocations. The simulation results show energy efficiency improvement due to capacity enhancement. Finally, the work in [99] sets the energy efficiency investigation scene in the cognitive radio with spectrum access strategies. The simulation results show improved energy efficiency and reduced computational complexity of the proposed spectrum access strategy with a compromised capacity performance compared with the capacity prioritised spectrum access strategy. These examples help with the statement that the EE metric alone cannot provide a complete energy efficiency evaluation, which also requires capacity and energy consumption evaluations.

2.2.3 Energy Efficiency Evaluation Framework

The absolute EE metrics only measure the energy consumption to represent energy efficiency performance without capacity evaluation. The works using these metrics might have reduced energy consumption and improved energy efficiency. Meanwhile, the capacity might be compromised. This raises the energy efficiency evaluation ambiguity. On the other hand, the relative EE metrics use the definition of EE or its derivatives to measure the energy efficiency performance. The corresponding examples always show promising improvement in energy efficiency. However, the capacity compromise or energy consumption increase is also incurred. This again raises the energy efficiency

evaluation ambiguity. The researchers and network designers would prefer the energy efficiency improvement with the capacity enhancement but without the energy consumption increase. In other words, capacity, energy consumption, and energy efficiency are necessary performance indicators for a complete energy efficiency evaluation, which cannot be measured by EE alone.

Therefore, in this research, the energy efficiency is evaluated using a comprehensive framework containing three figures of merit for the required assessments. Specifically, the Data Volume Gain, the Energy Consumption Gain, and the Energy Efficiency Gain are used for the capacity, energy consumption, and energy efficiency evaluations, respectively. Together, the energy efficiency evaluation is complete without any ambiguity. The network designers and operators would have a clear insight of the energy efficiency performance and make compromises if any performance trade-off exists. The evaluation framework will be introduced in detail in Chapter 3 and will be applied to analyse the energy efficiency of ultra-dense small cells or HetNet in the chapters after that.

2.3 Energy Efficiency of Ultra-Dense Small Cell RANs

The macrocell RAN densification reaches its limit to improve the capacity cost-effectively and energy-efficiently. The small cells, with a different BS infrastructure than the macrocell counterpart, emerge as an effective solution for their low cost in implementation, maintenance, and energy consumption aspects. Popular examples of small cells include microcells, picocells, femtocells, and relays [23]. Small cells have attracted attention and have been well developed in the literature. On the one hand, small cells could replace the macrocells for coverage and service provision. This is the homogeneous small cell RAN scenario. On the other hand, small cells could overlay the macrocells for coverage extension and capacity improvement. This is the heterogeneous small cell RAN scenario.

2.3.1 Small Cells in the Homogeneous RAN Infrastructure

The performance of ultra-dense homogeneous small cell RANs, where the BS number is much larger than the UE number, is studied extensively in the literature [53], [100]. The survey in [21] collectively provides this definition and characteristics of ultra-dense small cell RANs along with performance metrics, modelling methods, and other advanced techniques enabled by the small

cell RAN densification. Moreover, the authors in [43] increase the homogeneous Point Poisson Process (HPPP) modelled small cell density from 0.1 to 1000000 small cells per square kilometre to investigate its impact on the coverage probability and area spectral efficiency (ASE), with sleep mode enabled to switch off transmissions from empty cells. Other variations include the height difference between UEs and BSs, UE densities in the RAN, and the multipath fading models. The simulation results show that the small cell densification by increasing the cell density improves the coverage probability and ASE, which aligns with the mathematical analysis. Additionally, the ASE improves with the reduction in the height difference, especially for high small cell densities, when the UE density is fixed at 300 UEs/km². Meanwhile, the ASE first improves and then decreases with the increasing UE density from 300 to 2000 UEs/km² when the height difference is fixed at 8.5 m. This work provides the densification limitation on the capacity performance of small cell networks. However, it lacks the sensitivity analysis of the transmission power levels from the empty cells. In addition, an 8.5 m difference between UEs and BSs for the BS density as high as 1000000 BSs/km² (approximately 1 m between BSs) seems high when analysing the ASE caused by different UE densities. The authors' previous work in [10] has also included the energy efficiency improvement with the increasing densification level only if all the empty cells consume zero energy. Nevertheless, the analysis of RAN energy consumption caused by densification is not included in either work.

In [101], the authors propose a simultaneous power allocation and UE scheduling approach to maximise the average energy efficiency of each small cell in the ultra-dense small cell RAN. The BS ISD ranges from 6.5 m down to 3.5m. The simulation results show that the small cell energy efficiency decreases with the reducing BS ISD while the outage probability improves against the reducing ISD. In addition, the proposed approach outperforms the baseline approach, which maximises the EE under UE quality of service requirements regarding energy efficiency improvement and outage reduction. There is no analysis of energy consumption, though. At the end of [101], the authors mention an intention of involving sleep mode in future work, which is considered in this research. Also investigating resource management, the work in [53] proposes a joint power and spectrum allocation approach to maximise the energy efficiency of the ultra-dense RAN consisting of indoor small cells. Sleep mode is included to reduce energy consumption, and a BS clustering algorithm is used to reduce transmission power levels from interfering cells. The simulation results

show that the proposed resource allocation approach significantly improves the RAN throughput and energy efficiency.

Other advanced techniques are also investigated in ultra-dense small cell RANs. A network caching strategy and the computation offloading strategy are proposed in [102], depending on small cell density and UE mobility, to avoid the popular data being repetitively requested during rush hours and reduce the energy consumption on the UE side, respectively. In [103], the authors investigate the resource management in fog computing to meet the UE demands while minimising the energy consumption and computational complexity. The BSs attached to unmanned aerial vehicles (UAVs) are introduced in [104] to improve the RAN capacity and energy efficiency of the ultra-dense small cell RANs on the ground level.

2.3.2 Small Cells in the Heterogeneous RAN Infrastructure

Ultra-dense small cells can also work alongside the macrocells for performance improvement [105]–[111]. In [112], the authors analyse the coverage probability, UE throughput, and the energy efficiency of ultra-dense HetNet in terms of different UE association methods and transmission power approaches. Cell densification happens in macrocell and small cell layers. UEs associated with cells depend on instantaneously received power accounting for the multipath fading effect or the average received power without the multipath fading. Each BS could fix or reduce its transmission power level against the densification level. The simulation results validate the mathematical analysis and show that the instantaneous approach outperforms the average approach in terms of coverage probability for low to medium cell densities in the HetNet. Reducing the transmission power against the cell density improves the coverage probability and RAN EE compared to the fixed approach but compromises the UE throughput. The impact of sleep mode on ASE improvement for HetNet densification is included in the author’s later work in [41] considering range expansion (RE) and enhanced inter-cell interference coordination (eICIC). Again, the analysis of energy consumption against cell density is not included.

The authors in [113] concentrate on the interference to balance the trade-off between energy efficiency and spectral efficiency of an ultra-dense HetNet consisting of multiple macrocells and small cells. The authors form a RAN EE maximisation problem with SE constraints for both UEs and RAN and find the optimal UE SE to solve the problem. The simulation results show that

the proposed EE maximisation strategy improves the RAN energy efficiency while preserving the spectral efficiency compared with the scenario without the proposal. Also concentrating on the EE and SE trade-off, the work in [114] uses the product of exponentially weighted small cell SE and EE as a new performance metric to evaluate the proposed cooperative offloading scheme of an LTE-Advanced HetNet. The weights for SE and EE are complementary and can be adjusted according to different priorities of SE or EE. The simulation results show that the proposed cooperative offloading scheme achieves higher joint EE and SE performance than a conventional offloading scheme. In contrast, the impact of BS densities on the ultra-dense HetNet energy efficiency is investigated in [115]. The BSs in each layer of the HetNet is distributed following independent PPP models with different densities. The simulation results validate the mathematical analysis of the RAN EE and show that for a given UE density, different ratios between macrocell density and small cell density lead to different EE performance. There is always an optimal ratio that maximises the RAN EE. In addition, increasing the BS number in the macrocell or picocell layer increases the RAN energy consumption and degrades the RAN EE.

The energy efficiency of ultra-dense RANs using techniques not included in this research is also studied in the literature. In [116], the authors forecast the traffic variations, based on which the sleep mode is enabled in the 5G cloud-RAN to improve energy efficiency and reduce energy consumption. The energy harvesting is investigated in [117] where each small cell in the ultra-dense HetNet can be powered by the conventional electricity source (off-grid mode) or the harvested energy from renewable resources, macrocells, or the small cells in the off-grid mode. The simulation results show a trade-off between RAN EE and the outage probability, which the introduced energy harvesting technique could optimise.

To investigate the energy efficiency of the small cell RAN to extreme densification level of 1 m ISD between BSs, this research conducts experiments on ultra-dense small cell RANs in homogeneous and heterogeneous scenarios with reasonable UE-BS height difference. The capacity, energy consumption, and energy efficiency are analysed using the figures of merit included in the evaluation framework to provide a complete energy efficiency evaluation. In addition, different experiments are conducted to fill the research gap and investigate the energy efficiency sensitivity in terms of transmission power levels from empty cells and empty small cell power consumption levels. Details will be found in Chapters 4 to 5 on the LTE sub-6 GHz frequency band and Chapter 6 on the 5G

mmWave band.

2.4 Energy Efficiency of Sleep Mode

The total energy consumption increases significantly with the increasing number of BSs in the ultra-dense small cell RANs. Various solutions are proposed, among which the sleep mode, or sometimes idle mode, is proven to be effective in energy saving without the need to alter the RAN architecture or BS hardware [77]. Sleep mode is especially effective for dense RAN infrastructures where the number of BSs is far more than the number of UEs. Specifically, cells with few or no UE association could be put into a sleep mode where the pilot transmission level and overhead power consumption can be reduced. The studies of sleep mode can be categorised into three groups: cell selection, sleep mode depth, and cell re-activation. Cell selection determines which cells to be put into sleep mode and sleep mode depth determines the energy-saving scale by turning part or all the hardware off. In contrast, the process of slept cell re-activation is complicated regarding the network re-synchronization, re-activation starting time, and the probability of re-activation failure. This is beyond the scope of this research, so it will not be discussed here or in the following chapters.

2.4.1 Sleep Mode Cell Selection Methods

Cell selection for sleep mode is broadly discussed in the literature [118], [119]. In [120], the authors propose a method to improve the HetNet energy efficiency by considering UE association and small cell selection for sleep mode simultaneously under UE throughput constraints. The macrocells are distributed uniformly and overlaid by small cells. The RAN EE maximisation problem is solved using a three-layer algorithm that finds the optimal set of active cells and UE-BS associations. The simulation results show that the proposed algorithm converges and improves the HetNet energy efficiency with the increasing small cell number. A similar sleep mode cell selection method can also be found in [121].

A different cell selection method is introduced in [122]. Specifically, small cells in the LTE HetNet are selected to enter the sleep mode to minimise the sum of per small cell power consumption and load condition. The load condition captures the UE packet arrival rate, mean packet size, and the achieved data rate. The simulation results show that the proposed sleep mode cell selection

method reduces RAN energy consumption and improves energy efficiency under various traffic conditions compared to the case without the sleep mode.

In contrast, the authors of [123] set upper and lower UE number thresholds to guide the HetNet small cell sleep mode. When the small cell detects the UE number within its coverage being lower than the lower threshold, it enters into sleep mode and switches to active mode only if the UE number is above the upper threshold. The threshold set helps balance the RAN energy consumption reduction and the sleep/activation states switching frequency increase. UEs are mobile in this work. When all the small cells are treated equally and assigned with the same UE number thresholds, the universal optimal threshold set is found using the exhaustive search algorithm. In contrast, small cells can be given different threshold sets according to small cell locations and traffic conditions. The optimal threshold sets for energy consumption minimisation are found using the reinforcement learning algorithm and the heuristic algorithm. The simulation results show that small cells assigned with different sleep mode threshold sets consume less energy and thus achieve higher energy efficiency.

The cells selected to enter sleep mode are determined by the relative distance between small cells and macrocells in [124] to reduce energy consumption and improve the energy efficiency of the HetNet. Specifically, small cells within a certain distance away from macrocells enter sleep mode, and so do some of the small cells located at the edge of macrocells when surrounding small cells adopt range expansion to extend their coverage. The eICIC technique guarantees cell edge UE throughput. The simulation results show that the RAN energy consumption reduces with the increasing small cell range expansion bias. The proposed sleep mode method with RE and eICIC is shown to significantly reduce energy consumption more than the methods where only small cells within a specific range within the macrocell coverage sleep or small cells sleep randomly.

In [125], the authors put small cells in the LTE OFDM RAN into sleep mode to limit interference, improve resource utilisation, and improve RAN capacity without compromising the UE outage probability. The cell selection depends on the number of UEs receiving higher-than-a-threshold interference from each cell, the number of UEs associated with each cell but receiving higher-than-a-threshold interference from the neighbouring cells, the total number of UEs associated with each cell, the sum of the signal power received by all the associated UEs in each cell from that cell, and the sum of the interference received by all the UEs in each cell from all the other

cells. The small cells are selected one by one to enter sleep mode until the resultant total occupied resource block (RB) number is smaller than the previous value when the last selected small cell is active. The simulation results show that the proposed sleep mode method improves capacity by 34% via interference mitigation and enhances energy efficiency by 15.6% via energy consumption reduction. The proposed cell selection for sleep mode is also shown to perform towards the exhaustive cell selection method with low computational complexity. These hold for both homogeneous small cell RAN and HetNet infrastructures. However, the algorithm for cell selection is too complicated compared with the case where un-associated cells are chosen to sleep. The energy efficiency improvement is limited for such computational overhead. Instead, cells without UE association are selected to be put into sleep mode in this work for a fundamental understanding of the impact of sleep mode on energy efficiency.

2.4.2 Sleep Mode Depths

There is also literature concentrating on the sleep mode depths for energy consumption reduction and energy efficiency improvement. Different sleep mode depths are discussed in [42] for their impact on the energy efficiency of the ultra-dense small cell RANs. Different sleep mode depths mean turning different amounts of hardware off and leading to different cell power consumption levels. In [42], four sleep modes with increasing sleep depths and decreasing cell power consumption are considered. The simulation results show that the RAN energy efficiency first increases and then decreases against the increasing small cell density from 1 to 10000 cells/km² for different sleep mode depths. Only when the deepest sleep mode, where the empty cell only consumes 1% power of an active cell, is enabled does the energy efficiency improve monotonically with the increasing small cell density. This research has extended the densification level beyond 1000000 cells/km² and found that the monotonic energy efficiency improvement happens only when all the empty cells are turned off completely and consume zero energy.

The small cell sleep mode is discussed in [126] controlled by small cells, the core network, or UEs. When the sleep mode is governed by the small cells in the HetNet, each small cell has extra hardware capable of detecting power variations in the surrounding area for the appearance of potential UEs in the sleep mode. Once the detected power level exceeds a pre-defined threshold, the small cells will be activated to check whether the possible association could be granted. A 39.2% upper bound

on the per small cell power saving is reported using the presented power model. When the core network controls the sleep mode, small cells are in the sleep mode by default and are activated by the message from the core network through the backhaul link. The message sending is triggered if the core network detects the existence of small cells that UE could associate within the coverage area of a macrocell currently associated by the bespoke UE. The per small cell power consumption saving is up to 92%. In contrast, the UE-controlled sleep mode activates the slept small cells by sending messages from un-associated UEs. The per small cell power saving is similar to the small cell controlled case at 39.2%. Overall, the simulation results show that increasing the small cell number in HetNet increases the total energy consumption, which can be mitigated using the sleep modes mentioned earlier. However, the energy efficiency improvement is equated to energy consumption in this work, which is ambiguous without the capacity analysis.

A simple cell selection method is effective enough in this research where the sleep mode is adopted to constrain interference and reduce energy consumption. Specifically, the empty cells with zero UE association are put into sleep mode. The distance-dependent cell selection method mentioned above is realised by setting minimum separations between macrocells and picocells. The UE mobility is not considered in this research, so there is no need to consider cell re-activation. On the other hand, different sleep mode depths are analysed in this work regarding the pilot power levels from empty cells and the power consumption of an empty cell. This investigates the energy efficiency sensitivity from capacity and energy consumption variations in the ultra-dense small cell RANs. The application results of the sleep mode can be found in Chapters 4 to 6.

2.5 Energy Efficiency of Millimetre Wave

The LTE sub-6 GHz frequency band has been extensively exploited since the commercial launch. To further improve the network capacity, researchers have turned their attention to the under-explored frequency bands above 24 GHz, also called the mmWave band. UE data carried by mmWave could occupy significantly larger channel bandwidth than the sub-6 GHz counterparts. Based on Shannon's capacity formula, bandwidth expansion improves capacity and thus energy efficiency. On the other hand, the application of mmWave requires dense RAN infrastructure since high frequency leads to high path loss fading.

Signal transmitted using mmWave with high frequency and short wavelength has different characteristics from the conventional sub-6 GHz frequency bands. This has been surveyed broadly in the literature. The authors of [68] mention that the signal transmitted along the Line of Sight (LoS) path, which is the direct path between transmitter and receiver, differs significantly from the Non-LoS (NLoS) path. This is due to the high sensitivity of mmWave signals to blockage effect and alike and thus requires channel models different from the sub-6 GHz counterparts. In addition, mmWave makes large-scale antenna arrays feasible. Different transceiver architectures are also needed to process the signal in wide channel bandwidth and large antenna element numbers to balance the energy consumption, hardware constraints, and performance. This work provides ample understanding of the continuously developing mmWave technique and sets guidelines for modelling the mmWave RAN analytically or via simulations. More detail on the mmWave characteristics and modelling different from the sub-6 GHz counterpart could be found in [127]. In contrast, the mmWave is surveyed closely with massive MIMO and ultra-dense RAN infrastructure in [128]. The authors thoroughly introduce the evolution from sub-6 GHz frequency band usage to the mmWave band exploration, and from the Single-Input Single-Output (SISO) communication to MIMO to massive MIMO communication. The mmWave, massive MIMO, and ultra-dense RAN infrastructure are shown in the paper as performance enablers of each other. Similarly, the high sensitivity to the blockage effect and rain and atmospheric absorption is also mentioned, along with a detailed channel model introduction. This survey provides informative knowledge of mmWave massive MIMO.

The energy efficiency improvement brought by mmWave is developed in the literature. The work in [129] derives a mathematical analysis of the SINR coverage probability in the HetNet, and the study is later extended to rate coverage probability and RAN EE. The pure mmWave HetNet and the co-existence of sub-6 GHz and mmWave in HetNet are considered. The BS antenna pattern is approximated using sectors where the antenna gain is a constant maximum value within a narrow beam. In contrast, the antenna gain is a constant minimum value if the angles are outside the beam. Perfect alignment is also assumed between the typical UE and its serving BS. The simulation results validate the mathematical analysis and show that increasing the maximum antenna gain increases the RAN SINR coverage. In addition, increasing the value of bias assigned to small cells for offloading improves the small cell SINR coverage but compromises the RAN SINR

coverage. The RAN EE improves with the increasing bias value and decreases for a given small cell density, resulting in an optimal bias value that could maximise the RAN EE. These observations hold for both HetNet settings. The antenna pattern approximation could provide an optimistic performance evaluation with suppressed sidelobes that could cause interference. Instead, more practical antenna patterns are adopted in this research for BSs and UEs.

Millimetre wave is also applied in the literature together with techniques that are not included in this research. These techniques are worth exploring as future works. In [130], the authors propose a radio frequency (RF) chain selection scheme to balance the trade-off between SE and EE of a mmWave system with a massive MIMO technique. The signal is precoded in the transmitter using a hybrid analogue and digital architecture where RF chains connect the baseband unit with antenna elements. Compared with the exhaustive and random search algorithms, the proposed heuristic search algorithm selects a subset of RF chains for connection, reducing the computation overhead to maximise the system energy efficiency. The simulation results show that the energy efficiency improves and then decreases with the increasing number of selected RF chains. The proposed search algorithm trades off SE with a reasonable amount for computational complexity reduction. Turning away from the hardware, the authors of [131] focus on the user association and power allocation for a 5G mmWave ultra-dense HetNet using energy harvesting. The authors formulate a RAN EE maximisation problem depending on the transmission power level of each small cell and the UE association conditions constrained by the already associated load in each cell. Compared with a conventional maximum SINR association policy, the simulation results show that the proposed algorithm balances the load between macrocells and small cells and significantly improves energy efficiency with a slight UE throughput compromise.

The Green Radio Project and the Energy Aware Radio and Network Technology (EARTH) Project provide power models applied widely in the literature [132]–[134] for sub-6 GHz LTE and LTE-Advanced (LTE-A) technologies. The authors of [135] present the operational BS power consumption as:

$$P_{op} = \alpha \times L \times P_{RF\ max} + \rho \times P_{RF\ max} + \theta \times L + \lambda \quad (2.1)$$

where the constants α , ρ , θ , and λ are the weights of BS power-consuming components like power supply, antennas, power amplifiers, backhaul, and so on; L is the normalised load activity factor,

and $P_{RF\ max}$ is the peak BS transmission power. This power model accounts for a BS's traffic-dependent and static power consumption. Different parameters are applied to evaluate the power consumed by an LTE macro-SB or small cell BS under various traffic load conditions. The power model used in this research is enhanced from this formula and will be introduced in Chapter 3. In contrast, the EARTH Project in [136] introduces the power consumption of a fully-loaded BS as:

$$P_{in} = \begin{cases} N_{TRX} \times (P_0 + \Delta_p \times P_{out}) & 0 < P_{out} \leq P_{max} \\ N_{TRX} \times P_{sleep} & P_{out} = 0 \end{cases} \quad (2.2)$$

where N_{TRX} is the total number of transceiver (TRX) units in a BS, Δ_p represents the traffic dependent power consumption slope, P_{out} is the RF power output, P_{max} is the maximum RF output, P_{sleep} is the power consumed by the each TRX unit in sleep mode, and

$$P_0 = N_{TRX} \times \frac{\frac{P_{max} \times 1\%}{\eta_{PA} \times (1 - \sigma_{feed})} + P_{RF} + P_{BB}}{(1 - \sigma_{DC}) \times (1 - \sigma_{MS}) \times (1 - \sigma_{cool})} \quad (2.3)$$

is the static power consumption of a TRX unit, relating to the power consumption of power amplifier (PA), feeder (feed), RF units (RF), baseband units (BB), direct-current to direct-current power supply (DC), main power supply (MS), and cooling systems (cool). Different parameters can be substituted into Eq. (2.2) to calculate the BS power consumption of various types. Different load conditions are realised using different P_{out}/P_{max} .

However, the power models proposed for the sub-6 GHz BSs are difficult to cope with the wide channel bandwidth directly and the large antenna numbers that come with the mmWave. Therefore, the quantification of mmWave BS power consumption has attracted much attention. Different mmWave cell power consumption models are proposed in works [137]–[145] considering different parameters for similar sets of hardware components included in a mmWave BS. In contrast to these specific scenario-derived models, the works in [146] and [147] propose a similar scaling approach that allows the application of the sub-6 GHz power model into the mmWave case with the change of power-consuming parameters for different hardware components. Specifically, based on the data collections and comparisons, they state that the power consumed by the baseband and transceiver units scales linearly with the increased channel bandwidth and the number of antennas.

This avoids the necessity to derive a new mmWave dedicated power model. The parameters for other power-consuming components also need to update to reflect this advanced technique. This is the approach adopted in this research.

Note the power consumption in this research is always operational and corresponds to the power consumed due to the functioning of all the BS sites, being either active or empty, in the RAN. The embedded power consumption, on the other hand, is the power consumed to produce the elements such as BS site components. While the embedded power consumption is an important factor when it comes to the overall RAN design, it is out of the scope of this research and thus not included in the analysis.

In this research, the 28 GHz frequency with a 400 MHz bandwidth is selected when investigating the impact of mmWave on the energy efficiency of dense small cell RAN in Chapter 6. The fundamental fully digital signal processing architecture is adopted where each antenna element is connected to the baseband unit via an individual dedicated RF chain. Further work could evolve to a hybrid architecture for energy consumption reduction. In addition, IAB is also enabled by mmWave, whose literature review is in the next section, and detailed performance analysis is in Chapter 6.

2.6 Integrated Access and Backhaul

The IAB technique allows access and wireless backhaul links to share the same over-the-air transmission bandwidth for data transmission. The access links transmit data between BSs and UEs, while the backhaul link transmits data between BSs and the core network. Using the IAB technique would reduce the high cost of wired backhaul implementation and maintenance [70]. However, the IAB is not widely applied to the sub-6 GHz scenario due to the limited channel bandwidth. In contrast, the wide bandwidth that comes with the mmWave band frequencies makes IAB feasible. In a RAN with IAB enabled, some BSs, denoted as donors, are connected to the core network using the conventional wired fibre backhaul. The rest of the BSs, denoted as nodes, use wireless backhaul connections sharing the same resource with access links. If the single hop is allowed, all nodes are connected to donors directly. In contrast, if multi-hop is allowed, nodes can connect to donors directly or indirectly via other nodes. The nodes relaying backhaul transmissions to other nodes

are parent nodes, while the nodes only receiving backhaul on the downlink are children nodes.

The literature studying IAB is already well developed. However, most of them only concentrate on the capacity improvement brought by the IAB. For example, works in [148]–[151] investigate the general UE rate or SE performance led by IAB. In addition to the capacity performance, the authors of [152] propose an interference management algorithm to maximise the RAN cost efficiency, defined as the ratio between the transport capacity and the summation of energy cost and implementation cost. In contrast, different resource allocation strategies are discussed in [153]–[159] for mmWave RANs capacity improvement. Despite the capacity improvement, there is no analysis of the energy consumption or energy efficiency of the IAB RANs.

The studies investigating the energy efficiency of IAB RAN are limited. The works in [160]–[162] investigate the energy efficiency of IAB RAN on the sub-6 GHz frequency band. The authors of [160] propose a resource allocation approach regarding the sub-carrier and transmission power allocations in a HetNet to maximise the small cell energy efficiency. The single macrocell in the HetNet is the donor and provides wireless backhaul to small cells without serving any UEs. The simulation results show that the proposed resource allocation scheme achieves higher per small cell energy efficiency with lower small cell transmission power than the rate-maximization approach. Similarly, the work in [161] also considers a full-duplex HetNet consisting of one macrocell as a donor, which provides wireless backhaul to small cells but does not serve UEs. The authors adjust the beamforming vectors for both the access and backhaul links to maximise the RAN EE. The backhaul rate caps the UE throughput achieved in the access link. The simulation results show that the proposed approach outperforms the single antenna case regarding energy efficiency and sum rate. Concentrating on the imperfect channel state information (CSI), the work in [162] considers a HetNet where macrocell is a donor and serves UEs. A joint user association and power allocation algorithm are proposed to maximise the summation of UE logarithmic EE under maximum transmission power and backhaul rate constraints. Logarithmic EE over linear EE to preserve fairness among UEs. The simulation results validate the mathematical analysis and show that the proposed algorithm achieves higher energy efficiency and more traffic offloading from macrocells to small cells than the conventional max SINR algorithm. Nevertheless, operating in the sub-6 GHz with limited channel bandwidth would limit the performance of the IAB.

In contrast, the work in [163] considers a HetNet consisting of a donor macrocell, which serves

UEs and provides wireless backhaul on mmWave band, and full-duplex node small cells, which receive wireless backhaul on mmWave band but serves UEs on sub-6 GHz. The frequency orthogonality mitigates inter-layer interference. A sub-channel and power allocation approach is proposed to minimise the HetNet EE. The Macrocell is equipped with massive MIMO, which employs fully digital and hybrid signal processing architecture. The simulation results show that the proposed approach could improve energy efficiency while compromising the throughput compared with the scenario without the proposal. In addition, compared with the hybrid architecture, the fully digital architecture is shown to achieve the highest throughput at the cost of degrading energy efficiency because of higher energy consumption.

This research analyses the IAB with the wide-bandwidth mmWave for better performance. Instead of applying the IAB to a HetNet infrastructure, a homogeneous small cell RAN is chosen to gain a fundamental understanding of the impact of IAB on dense small cell RAN. In HetNets, the macrocells are usually the donors with fibre backhaul links connecting with the core network. In contrast, in a homogeneous RAN, the node small cells have to associate with the pre-selected donors for wireless backhaul connection. The capacity, energy consumption, and energy efficiency will be analysed. Details can be found in Chapter 6.

2.7 Summary

In addition to capacity, energy efficiency has become another key performance indicator for RAN performance evaluation. EE measures the joint performance of capacity and energy consumption. However, the applications of EE metrics in the literature lead to energy efficiency evaluation ambiguity. Specifically, the metrics in the absolute EE metric category usually equate to energy efficiency improvement over energy consumption reduction, which overlooks capacity performance. In contrast, the metrics in the relative EE metric category usually investigate capacity and energy efficiency without considering energy consumption. Metrics in either category provide complete energy efficiency evaluation. Therefore, this research applies a comprehensive energy efficiency evaluation framework that provides a complete energy efficiency performance assessment regarding capacity, energy consumption, and energy efficiency. The evaluation framework is presented in Chapter 3.

The study of ultra-dense small cell RANs is well developed in the literature. However, most works concentrate on the capacity and energy efficiency improvement brought by the dense RAN infrastructure while overlooking the potentially increasing energy consumption. Despite the enhanced RAN capacity energy efficiency, consuming more energy is not preferred by the RAN designers and operators. This research investigates the energy efficiency of ultra-dense RAN in homogeneous and heterogeneous infrastructures in Chapters 4 and 5, respectively. The EE performance is analyzed using the evaluation framework in all three aspects to identify the RAN design solution that is energy efficient and green.

Sleep mode is a popular energy reduction solution applied in the literature. While most studies show energy consumption reduction and/or energy efficiency enhancement due to sleep mode, there lacks a sensitivity study regarding the relationship between EE performance and BS densities. In this research, with the sleep mode, the energy efficiency sensitivity to the empty cell transmission power and power consumption levels are investigated to seek the RAN densification to over 1000000 cells/km² in the RAN regarding energy efficiency. The performance of sleep mode is analyzed in Chapters 4 to 6.

Though there exists literature that studies the energy efficiency performance of RANs using IAB, most of them are applied in the sub-6 GHz frequency band instead of the mmWave band. On the other hand, the studies of IAB using mmWave in the literature always concentrate on capacity performance. In other words, the study of capacity, energy consumption, and energy efficiency performance of dense small cell RANs with mmWave and IAB is lacking in the literature. In the final part of this research (Chapter 6), the impact of wide channel bandwidth, high antenna array gain, and enabling IAB on the energy efficiency of the dense small cell RAN are investigated.

Chapter 3

Energy Efficiency Evaluation Framework

3.1 Introduction

Traditionally, the priority is given to the RAN capacity and coverage when designing a new architecture or implementing a new technology [164]. With RAN densification enhancing the capacity [10], [16], on the other hand, the increasing number of BSs incurs a significant amount of energy consumption [28], [165]. Therefore, the design guidance nowadays has made energy efficiency another critical factor in addition to the capacity and coverage [164], [166].

Technologies and RAN architectures in communication have been advancing fast in recent years. Effective evaluation metrics are thus required for reliable energy efficiency performance analysis and comparisons. EE is defined as the amount of data transmitted in bits when consuming a unit amount of energy in J and has the units of bit/J [44]. It is a widely applied metric to evaluate the energy efficiency performance of a RAN [10] and simultaneously captures the capacity and energy consumption. But using the metric EE alone also has its disadvantage, as it does not indicate the individual capacity or energy consumption performance. Most literature has concentrated on improving capacity or energy efficiency brought by RAN densification or other technologies. However, they fail to capture the increasing energy consumption that might eventually compromise energy efficiency [49], [82]. Therefore, the complete evaluation of energy efficiency should include

not only the combined effect of capacity and energy consumption, which is the EE itself, but the separate effect of capacity and energy consumption as well. This is what the energy evaluation framework introduced in this chapter does.

In this chapter, an energy efficiency evaluation framework is presented [167] to evaluate the energy efficiency of different RAN densification scenarios. The evaluation framework includes three ratio-based figures of merit that assess the capacity, energy consumption, and energy efficiency, respectively: the Data Volume Gain (DVG), the Energy Consumption Gain (ECG), and the Energy Efficiency Gain (EEG). Though using actual values for capacity, energy consumption, and energy efficiency is more straightforward, adopting ratio-based figures of merit here emphasises the performance comparison. Using the ratio based on a common reference scenario avoids a constant benchmark referring when it comes to performance improvement or degradation. Moreover, the focus of the result analysis will be on the tendency instead of the actual number. The presented evaluation framework provides a complete RAN energy efficiency analysis. A power model derived from [74] is also introduced for the energy consumption calculation, which could accommodate different BS technologies and is scalable with traffic conditions.

The rest of this chapter is structured as follows. Section 3.2 introduces the three ratio-based figures of merit included in the evaluation framework regarding their definitions, advantages, derivatives, and applications. In addition, Section 3.3 introduces the power model with an emphasis on typical BS schematics, major energy-consuming components and their power consumption, and the overall BS site power consumption. Finally, Section 3.4 presents the chapter summary.

3.2 Ratio-Based Figures of Merit

This section introduces the three ratio-based figures of merit included in the energy efficiency evaluation framework: the Data Volume Gain (DVG), the Energy Consumption Gain (ECG), and the Energy Efficiency Gain (EEG) [18], [167]. Specifically, this section introduces the figures of merit definitions, the advantages of applying this framework for energy efficiency evaluation, the derivatives of the figures of merit, and the applications.

3.2.1 Definitions of Figures of Merit

The Data Volume Gain (DVG) compares the capacity performance of a RAN with new architecture or technology with a pre-defined reference RAN. The capacity performance is measured using the amount of data transmitted in the RAN for a certain time, either in the test field or via simulation. The definition of DVG is:

$$DVG = \frac{M_{RAN,test}}{M_{RAN,ref}} \quad (3.1)$$

where the subscripts *test* and *ref* are for RAN under test and reference, respectively; $M_{RAN,x}$, $x = test, ref$, is the amount of data in units of bit transmitted in a certain observation time period T in RAN case x .

The Energy Consumption Gain (ECG) compares the energy consumption of the same test RAN with the same reference RAN. The RAN energy consumption is calculated using the power model presented later in Section 3.3. ECG is defined as:

$$ECG = \frac{E_{RAN,ref}}{E_{RAN,test}} \quad (3.2)$$

where $E_{RAN,x}$, $x = test, ref$, is the RAN energy consumption for RAN case x with the units J for the same observation time period T as for the data transmission in Eq. (3.1).

The Energy Efficiency Gain (EEG) compares the RAN energy efficiency, whose mathematical expression is

$$EE_{RAN} = \frac{M_{RAN}}{E_{RAN}} \quad (3.3)$$

with the units of bit/J, between test and reference cases. EEG is defined as:

$$EEG = \frac{EE_{RAN,test}}{EE_{RAN,ref}} \quad (3.4)$$

and is the product of DVG and ECG:

$$EEG = \frac{M_{RAN,test}/E_{RAN,test}}{M_{RAN,ref}/E_{RAN,ref}} = \frac{M_{RAN,test} \times E_{RAN,ref}}{M_{RAN,ref} \times E_{RAN,test}} = DVG \times ECG \quad (3.5)$$

In addition to the definition, the mathematical expression indicates that EEG evaluates the com-

bined effect of capacity and energy consumption.

The advantages of using this evaluation framework are three-fold. First, this evaluation framework can evaluate not only the capacity and energy efficiency performance but also the energy consumption. This guarantees that the contribution of capacity and energy consumption could be explicitly identified for an energy efficiency variation. Only the RAN architectures or technologies that increase DVG and EEG without an increasing ECG can be considered green and energy efficient. Moreover, the arrangement of numerator and denominator, i.e., the corresponding subscripts for test or reference scenario, in each figure of merit guarantees that a larger-than-unity ratio always means better performance. Specifically, a larger-than-unity DVG means that test RAN could transmit more data than the reference case for the same given period; a larger-than-unity ECG implies that the test RAN consumes less energy than the reference, and the larger-than-unity EEG means that test RAN is more energy efficient. Finally, either the amount of data transmitted in units of bit in RAN or the energy consumption in units of J could be measured or calculated directly from the field test or simulation, after which the three figures of merit could be calculated [74].

3.2.2 Derivatives of Figures of Merit

By definition, the amount of data M_{RAN} transmitted in the RAN downlink is related to the RAN throughput S_{RAN} in units of bit/s and a single UE's throughput S_{UE} in units of bit/s as:

$$M_{RAN} = \sum_{t=0}^T S_{RAN} = \sum_{t=1}^T \sum_{k=1}^K S_{UE,k} \quad (3.6)$$

where k is an arbitrary active UE index and K is the total number of active UEs in the RAN during the observation period T . The total energy consumption of a RAN E_{RAN} is calculated as:

$$E_{RAN} = T \times P_{RAN} = T \times \sum_{b=1}^B P_b \quad (3.7)$$

where P_{RAN} is the RAN power consumption in watts, b is an arbitrary BS site index, B is the total number of BS sites in the RAN, and P_b is the site power consumption of the BS b , which can be calculated using the power model presented later in Section 3.3.

If both the numerator and denominator of the EE definition in Eq. (3.3) are divided by the

observation time period T , the expression of EE becomes:

$$EE_{RAN} = \frac{S_{RAN}}{P_{RAN}}. \quad (3.8)$$

EE_{RAN} can also be calculated as the ratio between the area RAN throughput and the area RAN power consumption, assuming a common RAN area. Cancelling the RAN area parameter in both area RAN throughput and area RAN power consumption leads to the same EE_{RAN} expression as in Eq. (3.8).

Similarly, for DVG and ECG, if both the numerator and denominator are divided by the observation period T , the expression becomes:

$$DVG = \frac{S_{RAN,test}}{S_{RAN,ref}} \quad (3.9)$$

and

$$ECG = \frac{P_{RAN,ref}}{P_{RAN,test}} \quad (3.10)$$

respectively. The throughput S_{RAN} is easier to measure in the field test or calculated in the simulation than M_{RAN} ; and the power consumption P_{RAN} can be calculated directly using the power model that will be presented in Section 3.3. Also, EEG could be expressed in a similar way as:

$$EEG = \frac{S_{RAN,test}/P_{RAN,test}}{S_{RAN,ref}/P_{RAN,ref}} = DVG \times ECG. \quad (3.11)$$

Furthermore, due to BS and UE distribution models, the RAN area A_{RAN} might differ between the test RAN and reference RAN. It is then more accurate to use the area RAN throughput in units of bit/s/km² and the area RAN power consumption in units of W/km². With the expression of EEG keeping the same, the DVG and ECG become:

$$DVG = \frac{S_{RAN,test}/A_{RAN,test}}{S_{RAN,ref}/A_{RAN,ref}} \quad (3.12)$$

and

$$ECG = \frac{P_{RAN,ref}/A_{RAN,ref}}{P_{RAN,test}/A_{RAN,test}} \quad (3.13)$$

respectively.

These figures of merit will then be applied to evaluate the performance of densification of homogeneous RAN and heterogeneous RAN in the following chapters. For DVG, the RAN throughput and RAN area are obtained directly from the RAN densification simulation. For ECG, the RAN power consumption is calculated using the power model presented in Section 3.3 with the number of BSs set in the simulation. The EEG results can be calculated using the product of DVG and EEG. In addition to the RAN densification simulations in this work, this evaluation framework could also be applied to evaluate the performance of other RAN architectures and technologies, test fields or simulations. The evaluation results would be consistent and complete regarding the energy efficiency performance that could be used as a RAN design guideline.

3.3 Power Model

This section presents the power model derived and enhanced from the Green Radio project [74], [167]. A typical macro-BS schematic will be introduced first, along with the identified major energy-consuming components. Then the power consumption breakdowns are presented in detail for each major energy-consuming component. An overall site power consumption equation will then be expressed, along with a discussion of the advantages of this power model. At the end of this section, this power model will be applied to different case studies to investigate the properties.

3.3.1 Major Energy Consuming Components

Fig. 3.1 shows a block diagram of the simplified macro-BS site schematic containing major energy-consuming components for the power model [74]. Typically, each BS site has its backhaul, power supply, cooling units, and radio frequency (RF) units, which are shared between all antenna links in each cell. The RF units could be further divided into baseband, transceiver, power amplifier (PA), and feeder cable that links to the antenna. Each antenna link in each cell has a complete set of RF units. Based on the dependence on the traffic conditions in the BS site, these components could be divided into two categories: the traffic-dependent part called the radio-head (RH), and the traffic-independent part called the overhead (OH). The RH components include the power amplifier and the feeder cables that link the antenna, whose energy consumption could be scaled

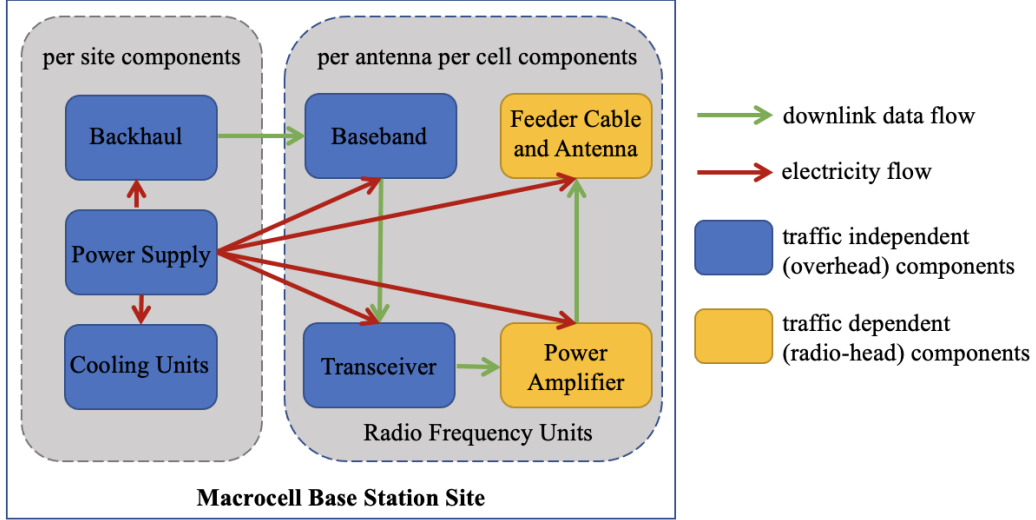


Figure 3.1: Typical macro-BS site schematic, showing the major energy-consuming components for the power model derived from the Green Radio Project

by traffic conditions. In contrast, the OH components include the backhaul, power supply, cooling units, baseband, and transceiver, whose energy consumption is related to traffic but modelled as traffic independent in this model. This research focuses only on the conventional RAN architecture, while advanced architectures like cloud-RAN are left for potential future works. The cloud-RAN adopts different infrastructures such as a centralised baseband unit connecting to BSs via fronthaul links [65], requiring different power models and parameters. This will impact the corresponding energy efficiency performance. Further discussions about individual component functions and power consumption calculations related to Fig. 3.1 are as follows.

Based on the analysis above about Fig. 3.1, the total site power consumption of macro-BS b can be mathematically expressed as:

$$P_b = P_{RF} + P_{COOL} + P_{PS} + P_{BH} \quad (3.14)$$

where the subscript RF , $COOL$, PS , and BH refer to the power consumption of RF units, cooling units, power supply, and backhaul, respectively [74]. In addition, the power consumption of the RF units can be further expressed as:

$$P_{RF} = n_a \times n_c \times (P_{BB} + P_{TRX} + P_{PA}) \quad (3.15)$$

where n_a is the number of antennas in each BS cell; n_c is the number of cells in each BS site; and the subscripts BB , TRX , and PA refer to power consumption of baseband units, transceiver units, and power amplifiers, respectively [74].

The transceiver units process the RF signal that will be forwarded to the antenna for transmission to users or received by the antenna from users [74]. The baseband units connect to the transceiver units responsible for the baseband processing of the signal, radio resource management, and site control functions [167]. The dependence of the transceiver and baseband's power consumption on traffic conditions is relatively small such that their power consumption is modelled as constants [167]. Based on the ratio between actual bandwidth usage B and total available bandwidth \hat{B} , the power consumption of the baseband P_{BB} and the transceiver P_{TRX} per antenna per cell are similarly represented as:

$$P_{BB} = \frac{B}{\hat{B}} \hat{P}_{BB} \quad (3.16)$$

and

$$P_{TRX} = \frac{B}{\hat{B}} \hat{P}_{TRX} \quad (3.17)$$

where \hat{P}_{BB} and \hat{P}_{TRX} are the peak power consumption of the baseband units and transceiver units, respectively, if occupying the total available channel bandwidth \hat{B} [74].

Furthermore, the power consumption of the power amplifier units P_{PA} , with the feeder cable efficiency η_{CL} embedded, is:

$$P_{PA} = \frac{P_{tx,c}/n_a}{\eta_{PA} \times \eta_{CL}} \quad (3.18)$$

where $P_{tx,c}$ is the total transmission power from the cell c belonging to the bespoke BS site b , and η_{PA} is the actual working efficiency of the PA [74]. The relationship between the PA efficiency η_{PA} and the transmission power $P_{tx,c}$ is dependent on both the PA's physical characteristics and the traffic condition [167], [168]:

$$\eta_{PA} = \hat{\eta}_{PA} \sqrt{\frac{P_{tx,c}}{P_{SAT}}} \quad (3.19)$$

where $\hat{\eta}_{PA}$ is the peak power amplifier efficiency, and P_{SAT} is the operational saturation output power of the power amplifier, which is calculated as:

$$P_{SAT} = OBO \times \hat{P}_{tx,c} \quad (3.20)$$

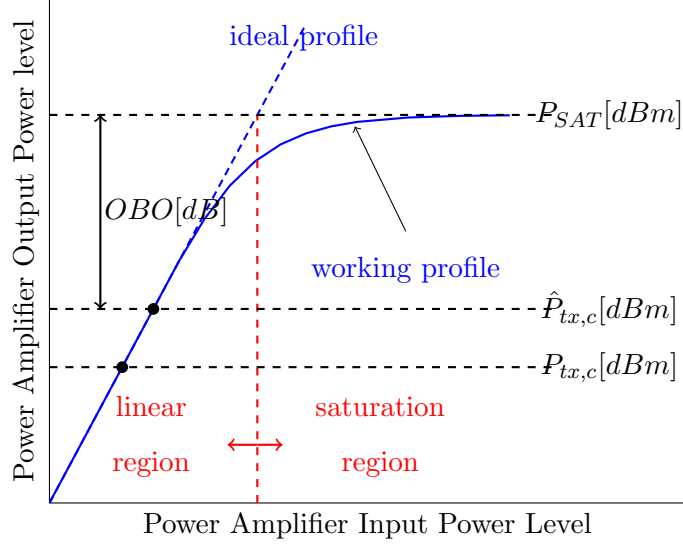


Figure 3.2: Illustrated example of the working power level of a power amplifier

where OBO is the output back-off of the power amplifier and $\hat{P}_{tx,c}$ is the peak transmission power of any BS cell c [167], [168]. The actual transmission power level $P_{tx,c}$ of the cell c is thus determined by a normalised load activity factor α_c as:

$$P_{tx,c} = \alpha_c \times \hat{P}_{tx,c} \quad (3.21)$$

[167], [168]. Fig.3.2 illustrates a visual example of a power amplifier power level relationship stated above where all the parameters are on a decibel scale. The x-axis is the PA input power level, and the y-axis is the output power level. Ideally, the PA would operate in the linear region. In contrast, the PA working profile is first linear in the linear region and then saturates in the saturation region [169]. Given the tradeoff between the linear operation and PA efficiency, the PA works at an output power level that is lower than the saturation power level, which are $\hat{P}_{tx,c}$ and P_{SAT} in this work, respectively. The actual output power $P_{tx,c}$ is not higher than the peak transmission power according to the normalised load activity factor α_c .

As drawn from the mains socket, the power consumption of the power supply is modelled as an efficiency that is denoted as η_{PS} [74]. The typical value for η_{PS} is 85 percent to 90 percent [167], [170].

In addition, the cooling system is necessary to keep all the components in the macro-BS site working at a suitable temperature. However, for small cell BSs, the cooling process is always done

by natural ventilation, so the cooling system becomes unnecessary [171]. In the adopted model, the power consumed by the macro-BS cooling system is quantified as:

$$P_{COOL} = \frac{3.4121}{EER} \left(P_{RF} - \frac{n_c \times P_{tx,c}}{\eta_{CL}} \right) \quad (3.22)$$

where EER stands for Energy Efficiency Ratio and has a fixed value of 11, assuming a 25 °C room temperature [167]; and the constant 3.4121 is for conversion to the British Thermal Units (BTU) per hour [74]. The expression in Eq. (3.22) shows that the power consumption of cooling system is also related to the RF power consumption.

Backhaul is a critical component in BSs that connects the BS site with the core network for data inquiries [172]. It could either be wired or wireless. However, an accurate power consumption model is difficult to quantify. Thus, in this work, a constant value of 10 W is chosen to represent a dedicated fibre backhaul power consumption P_{BH} between the mobile core network and a BS [74] unless stated otherwise. The comparatively small dependence on the traffic condition is also omitted here [74].

3.3.2 Site Power Consumption Model

Substituting the power consumption of each major component discussed above gives the total macro-BS site (MBS) power consumption:

$$P_b^{MBS} = \frac{n_c \times \hat{P}_{tx,c}}{\eta_{CL}} \left[\left(\frac{3.4121}{EER} + 1 \right) \frac{\sqrt{\alpha_c \times OBO}}{\eta_{PS} \times \hat{\eta}_{PA}} - \frac{3.4121}{EER} \alpha_c \right] + \left(\frac{3.4121}{EER} + 1 \right) \frac{n_a \times n_c}{\eta_{PS}} \times \frac{B}{\hat{B}} (\hat{P}_{BB} + \hat{P}_{TRX}) + P_{BH} \quad (3.23)$$

Removing the power consumption of the cooling system, the power consumption of a small cell BS site (SBS) can be derived as:

$$P_b^{SBS} = \frac{n_c \times \hat{P}_{tx,c} \times \sqrt{\alpha_c \times OBO}}{\eta_{CL} \times \eta_{PS} \times \hat{\eta}_{PA}} + \frac{n_a \times n_c}{\eta_{PS}} \times \frac{B}{\hat{B}} (\hat{P}_{BB} + \hat{P}_{TRX}) + P_{BH} \quad (3.24)$$

For P_b^y , $y = MBS, SBS$, the parts containing α_b are the traffic dependent RH part, and the rest is traffic independent OH part.

Cell Type	Macro-BS site	Micro-BS site	Pico-BS site
n_a, n_c	1, 3	1, 1	1,1
\hat{P}_{BB} [W]	30	27	3
\hat{P}_{TRX} [W]	13	6.5	1
η_{CL} (%)	50	79	100
$\hat{\eta}_{PA}$ (%)	70	77	93
OBO [dB]	8		
$\hat{P}_{tx,c}$ [W]	40	6.3	0.13
η_{PS} (%)	85		
EER	11		
P_{BH} [W]	10		
$P_b(\alpha_c = 1)$ [W]	1462.97	80.04	15.12

Table 3.1: Power model parameters

This power model can accommodate different BS technologies by specifying the power consumption parameters and various RAN architectures by varying the number of sectors and antenna links. Moreover, it is scalable with traffic conditions represented by the normalised load activity factor α_c . Thus in the same RAN, BS sites with different loads can have different power consumption.

3.3.3 Power Model Case Studies

Table 3.1 lists the parameters required by the power model for different BS technologies that will be considered in this work: the MBS and SBS, including micro-BS sites and pico-BS sites [74]. Note that η_{CL} for macro-BS sites, micro-BS sites, and pico-BS sites listed are equivalent to cable loss at 3 dB, 1 dB, and 0 dB, respectively. The parameters show that small cells, either microcells or picocells, have a lower power level than conventional macrocells.

Substituting the parameters in Table 3.1 into Eq. (3.23) and (3.24) gives the power consumption of a macro-BS site or small cell site, respectively. The percentage of the traffic-dependent RH power consumption and traffic-independent OH power consumption within a total BS site power consumption is shown in Fig 3.3 with an emphasis on the backhaul. Macro-BS site is assumed to have three cells and one antenna per cell, while the small cell site is assumed to have a single cell and one antenna per cell. The bandwidth occupation B is assumed to equal the total available bandwidth \hat{B} . The figure shows that the power consumption of a macro-site is heavily RH dominated at 85.72% when the normalised load activity factor α is 1. The contribution of the assumed

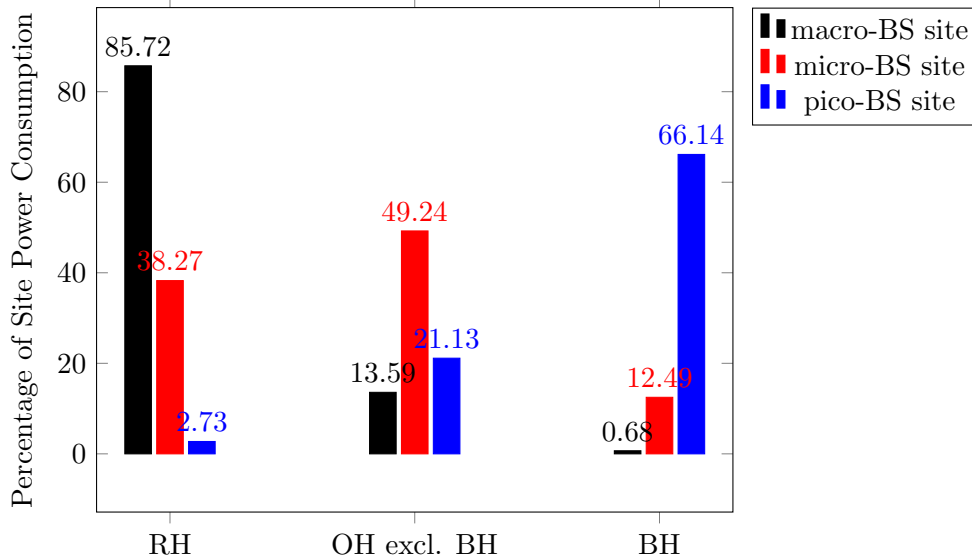


Figure 3.3: Power consumption percentage of radio-head (RH), overhead excluding backhaul (OH excl. BH), and backhaul (BH) within the total power consumption for different BS technologies

fibre backhaul to the total macro-BS site power consumption is negligible at 0.68%. This situation changes when switching from a macro-BS site to a small cell site. It is shown in the figure that the RH power consumption of a micro-BS site is less than 50%, while the pico-BS site has only 2.73% of the total power consumption due to RH. This indicates that compared with a macro-BS site, the power consumption of a small cell site with unity α has shifted from traffic dominated to overhead-dominated. Regarding the OH power consumption, on the other hand, the micro-BS site is more dominated by the cooling systems and power supply, while the pico-BS site is more dominated by the backhaul. Note that a 10 W backhaul power consumption is assumed for the pico-BS at this stage. Various power consumption levels for backhaul are studied in Section 4.5 to investigate the impact on RAN energy consumption and energy efficiency. The dependence on OH power consumption raises power-saving opportunities that will be discussed in detail in the following chapters.

Fig. 3.4 shows the power consumption P_b of an arbitrary BS site b in units of watt with the normalised load activity factor α_c as a variable for traffic condition variations, comparing different BS technologies. Macro-BS site is assumed to have three cells and one antenna per cell, while the small cell site is assumed to have a single cell and one antenna per cell. The bandwidth occupation B is assumed to equal the total available bandwidth \hat{B} . The site power consumption of all three

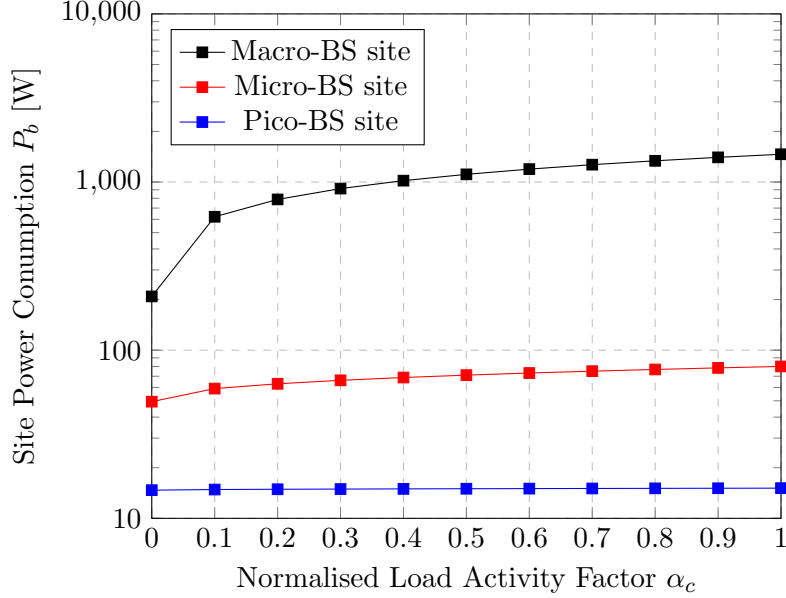


Figure 3.4: Site power consumption P_b versus normalised load activity factor α_c , comparing BS technologies, macro-BS site has $(n_a, n_c) = (1, 3)$, small cell BS site has $(n_a, n_c) = (1, 1)$, $B = \hat{B}$, $OBO = 8$ dB

BS technologies increases with α_c but at different rates. For the macro-BS site, P_b increases with α_c with the highest rate. This is in line with the fact that P_b^{MBS} is heavily RH-dominated. In contrast, micro-BS sites have their power consumption increase with α_c at a much lower rate, while the increasing rate for pico-BS site power consumption is negligible. In other words, small cell site power consumption is OH-dominated. The figure also shows that a macro-BS site with three cells consumes much more energy than a small cell site with a single cell. Specifically, when α_c is 0, which means no traffic in any cells in the BS site, the power consumption of a macro-BS site, a micro-BS site, and a pico-BS site are 208.84 W, 49.41 W, and 14.71 W, respectively. When α_c increases to 1, the power consumption of a macro-BS site, a micro-BS site, and a pico-BS site are 1462.97 W, 80.04 W, and 15.12 W, respectively.

Similarly, Fig. 3.5 shows the power consumption of an arbitrary BS b in units of watt with the power amplifier output back-off OBO as a variable for PA technology variations, comparing different BS technologies. Macro-BS site is assumed to have three sectors and one antenna per sector, while small cell sites have a single sector and one antenna per sector. The bandwidth occupation B is assumed to equal the total available bandwidth \hat{B} . The tendencies are similar as in Fig. 3.4 since OBO is also a traffic-dependent factor in the site power consumption. Both P_b^{MA}

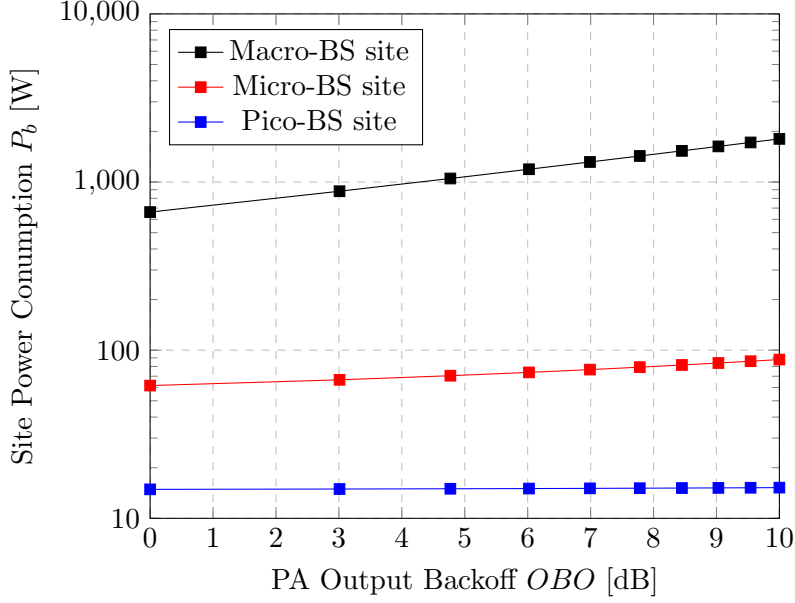


Figure 3.5: Site power consumption P_b versus PA output backoff OBO , comparing BS technologies, macro-BS site has $(n_a, n_c) = (1, 3)$, small cell BS site has $(n_a, n_c) = (1, 1)$, $B = \hat{B}$, $\alpha_c = 1$

and P_b^{SC} increase with OBO , but the former has a much greater increasing rate. OBO being 0 dB means that $P_{SAT} = \hat{P}_{tx,c}$, which is unrealistic due to the transmission signal distortion. In addition to α_c being 1, the PA is ideally working at its peak efficiency and thus has the lowest site power consumption of 662.88 W, 61.60 W, and 14.87 W for a fully loaded macro-BS site, a micro-BS site, and a pico-BS site, respectively. An increasing OBO trades off PA efficiency η_{PA} for linear operation and increases the site power consumption. When OBO is 10 dB, the power consumption of a macro-BS site, a micro-BS site, and a pico-BS site are 1805.60 W, 87.94 W, and 15.23 W, respectively.

3.4 Summary

This chapter has first introduced an energy efficiency evaluation framework consisting of three ratio-based figures of merit: the Data Volume Gain (DVG), the Energy Consumption Gain (ECG), and the Energy Efficiency Gain (EEG). DVG compares the capacity performance of a test RAN architecture or technology with a reference case, while ECG compares the energy consumption and EEG compares the energy efficiency. This evaluation framework provides a complete analysis of RAN energy efficiency with separate and joint investigations of capacity and energy consumption.

Moreover, all the three figures of merit are designed to show performance enhancement by having the corresponding ratio larger than unity. Additionally, the DVG could be calculated either through field test measurement or simulation, and the ECG could be computed using the power model also presented in this chapter. Then their product is the EEG. The power model shown is derived and enhanced from the Green Radio Project, which can accommodate different BS technologies and RAN architectures and scale with traffic conditions. Case studies of this power model show that the conventional macro-BS site power consumption is mainly traffic dependent. In contrast, traffic-independent components dominate the power consumption of the small cell BS sites. The energy efficiency evaluation framework and the power model will be applied to the following chapters to investigate the energy efficiency of RAN densifications. Specifically, Chapter 4 will analyse the energy efficiency of the ultra-dense homogeneous small cell RANs, comparing different transmission power and power consumption levels, UE densities, resource managing schedulers, and BS distribution models.

Chapter 4

The Energy Efficiency of Ultra-Dense Homogeneous Small Cell RANs

4.1 Introduction

The communication devices requiring data are ubiquitous nowadays. With the type of data needed shifting from low rate text to high rate video and alike, the communication network is expected to provide higher capacity [173]. Among various technologies seeking to increase the capacity, RAN densification has proved to be the most effective [10]. RAN densification increases the spatial reuse factor by adding more BSs into a given geographic area with reduced ISD.

RAN densification is primarily applied to the traditional macrocell RANs, abbreviated to macro-RANs. Macro-BSs have large coverage areas and high peak transmission power levels that provide reasonable services to some extent. However, macro-RAN densification has reached its limit regarding the geographic location constraints for the large dimension, and implementation cost of such sites [19]. The low-power small cell BSs have emerged to solve the problems with their smaller size and the more flexible and cheaper implementations [21], [22]. Moreover, the small cell BSs already have lower energy consumption that is expected to be more energy efficient than the macro-BS counterpart [173].

Nevertheless, a small cell RAN with high BS density for capacity improvement would still consume a considerable amount of energy, which inevitably degrades the energy efficiency [28].

Practically for highly densified RANs, the number of BSs may exceed the number of active UEs. This results in empty BSs that do not serve active UEs but consume energy. Putting these empty cells into low-power sleep mode would reduce the energy consumption and hence improve the energy efficiency [25]. The adoption of sleep mode would be especially effective for the ultra-dense RAN, where there are a lot of empty cells. Therefore, the combination of RAN densification with sleep mode should benefit the RAN energy efficiency [10].

This chapter analyses the energy efficiency of homogeneous RANs using the previously introduced energy efficiency evaluation framework and the power model. The macro-RAN densification will first be analysed as a performance benchmark, followed by micro-RAN and pico-RAN densification. Simulation results show that homogeneous RAN densification, regardless of BS technologies, could only benefit RAN capacity and energy efficiency to some extent. Further densification will degrade the capacity and energy efficiency unless the sleep mode is introduced to reduce energy consumption. The RAN densification is only energy efficient if all the empty cells are completely shut down. The analysis of homogeneous RAN densification provides a fundamental understanding of the network densification limit by uniformly distributing small cell BSs in an ultra-dense fashion within a given area.

The rest of the chapter is structured as follows. Section 4.2 introduces the system model for a homogeneous RAN. Section 4.3 presents the simulation results and energy efficiency analysis of homogeneous macro-RAN densification as a benchmark, with an emphasis on the peak transmission power. Moreover, homogeneous small cell RAN densification simulation results are presented in Section 4.4 for both micro-RANs and pico-RANs. The focus is then switched to pico-RAN densification in Section 4.5, emphasising peak transmission power, pilot power level from empty cells, sleep mode for empty cells, RAN traffic intensities, and scheduling protocols. Section 4.6 presents a special case study of the energy efficiency of RAN densification in the context of the Internet of Things (IoT) using a three-dimensional (3D) Homogeneous Point Poisson Process (HPPP) model. Finally, Section 4.7 presents the chapter summary.

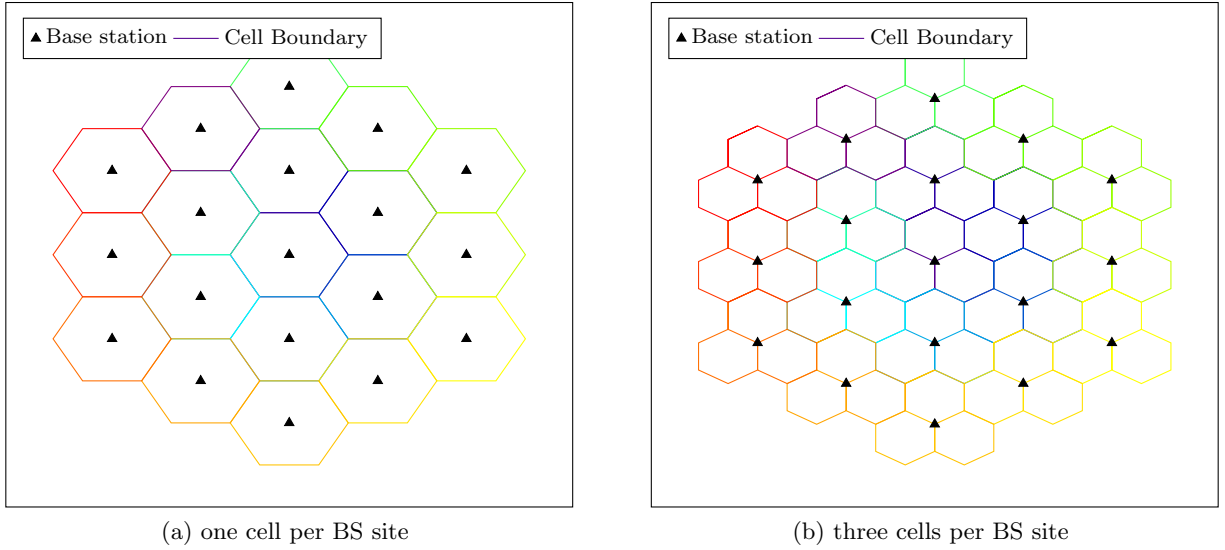


Figure 4.1: Examples of homogeneous RAN layout

4.2 Homogeneous RAN System Model

This section introduces the system model for homogeneous RANs on the downlink (DL). Specifically, the mathematical expressions for UE received power, channel loss, UE SINR, and UE throughput are presented according to different resource scheduling metrics.

4.2.1 Homogeneous RAN Layout

This chapter considers the LTE homogeneous RAN on the DL with an average UE rate cap at 100 Mbit/s [174]. Homogeneous RANs contains N_B identical BSs that can be denoted as set $\mathcal{B} = \{1, 2, \dots, b, \dots, N_B\}$. BSs are assumed to be uniformly and hexagonally distributed in the RAN area. Fig. 4.1a and Fig. 4.1b show examples of homogeneous RAN layouts with 19 BSs having a single or triple cell each, respectively. For Fig. 4.1a, the black triangles represent BSs located at the centre of each hexagonal coverage area, whose boundary colours vary from BS to BS. Similarly, in Fig. 4.1b, the black triangle represents BSs located at the joint centre of 3 cells, whose boundary colours vary from BS to BS. In this chapter, each macro-BS is assumed to have triple cells like in Fig. 4.1b; while a small cell BS is assumed to have a single cell like in Fig. 4.1a. In other words, a macro-BS site has three macrocells, while a small cell site has one small cell. The N_C cells in the homogeneous RAN are denoted as set $\mathcal{C} = \{1, 2, \dots, c, \dots, N_C\}$. Note that for small cell RANs, set \mathcal{B} and set \mathcal{C} are the same.

The wrap-around algorithm avoids the edge effect of the limited RAN area. Specifically, assume six virtual RANs are surrounding the RAN under investigation with identical layouts. The relative two-dimensional (2D) distance between a UE and a BS is the minimum distance between the UE location in the investigated RAN and the BS locations in all seven RANs. The 2D distance does not account for the height difference. The calculations of relative angles, 3D distance including the height difference, and the distance-dependent fading coefficients depend on this 2D distance.

All the active and outdoor UEs in demand for data transmission are assumed to follow a uniform random distribution within the RAN area. Specifically, independent uniform random x-coordinates and y-coordinates are generated for candidate UE locations, while only those within the RAN area are selected for the UEs. The UE set is denoted as $\mathcal{K} = \{1, 2, \dots, k, \dots, K\}$. Each UE is assumed to have an isotropic antenna. The full buffer traffic model is assumed so that active UEs are always in demand of data on the DL. The UE association is according to the strongest received signal power, equivalent to the minimum channel loss excluding the antenna gain.

4.2.2 UE Received Power and Channel Model

For an outdoor active UE k at an arbitrary location, it receives both signal power from its serving cell c and other interfering cells $c' \in \mathcal{C} \setminus \{c\}$, assuming universal frequency reuse. Note that $c' \in \mathcal{C} \setminus \{c\}$ means cell c' belongs to the intersection of set \mathcal{C} and the set only containing c . The per RB per Transmission Time Interval (TTI) received power in dBm for UE k from cell c is:

$$P_{rx,c,k}(n, t) [\text{dBm}] = P_{tx,c,k}(n) [\text{dBm}] + G_{BS,c,k} [\text{dBi}] + G_{UE,c,k} [\text{dBi}] - L_{c,k}(n, t) [\text{dB}] \quad (4.1)$$

where n is the RB index in a TTI; $t = 1, \dots, T$ is the TTI index; $P_{tx,c,k}(n)$ is the transmission power in dBm from cell c on RB n independent of time; $G_{BS,c,k}$ and $G_{UE,c,k}$ are the antenna gains from cell c and UE k , respectively; and $L_{c,k}(n, t)$ is the channel loss for RB n in TTI t . Without considering any power control approaches, the total cell transmission power $P_{tx,c}$ is assumed to be equal between all the RBs in each TTI. Mathematically:

$$P_{tx,c,k}(n) = \frac{P_{tx,c}}{N_{RB}} \quad (4.2)$$

where N_{RB} is the total number of RBs per TTI for a given LTE bandwidth.

The Third Generation Partnership Project (3GPP) suggests the antenna pattern for a single macrocell in an MBS from [175] as:

$$G_{BS,c,k}^{MBS} [\text{dB}] = G_{BS,max}^{MBS} [\text{dBi}] - \min \left[- \left(G_{V,c,k}^{MA}(\theta_{c,k}) [\text{dB}] + G_{H,c,k}^{MA}(\phi_{c,k}) [\text{dB}] \right), A_m \right] \quad (4.3)$$

where

$$G_{V,c,k}^{MBS}(\theta_{c,k}) [\text{dB}] = - \min \left[12 \left(\frac{\theta_{c,k} - \theta_{tilt}}{\theta_{3dB}} \right)^2, SLA_v \right] \quad (4.4)$$

and

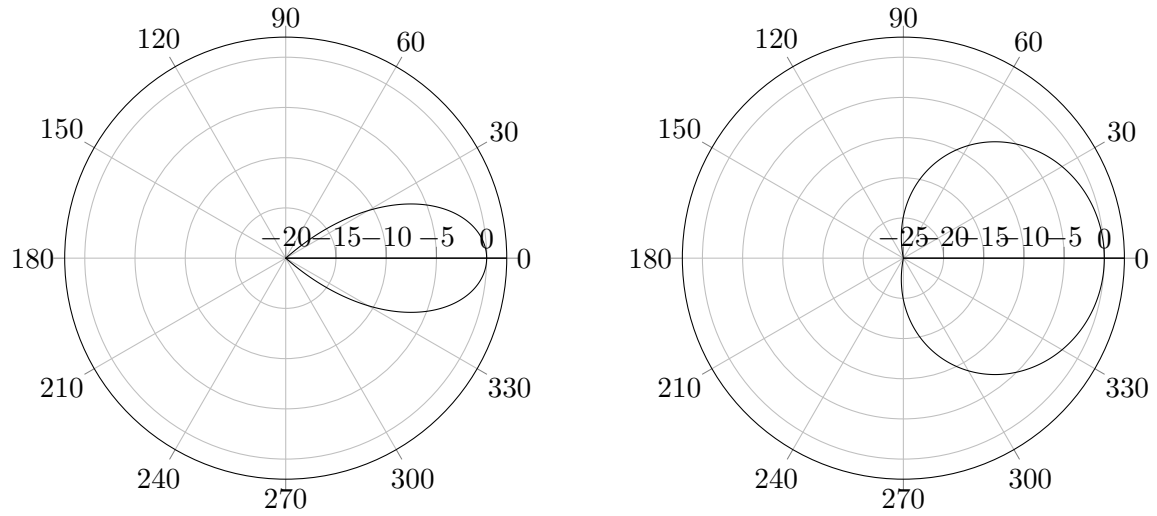
$$G_{H,c,k}^{MBS}(\phi_{c,k}) [\text{dB}] = - \min \left[12 \left(\frac{\phi_{c,k}}{\phi_{3dB}} \right)^2, A_m \right] \quad (4.5)$$

are the vertical and horizontal antenna patterns, respectively; $G_{BS,max}^{MBS}$ is the maximum antenna gain in the boresight direction in units of dBi; θ_{3dB} and ϕ_{3dB} are the vertical and horizontal half power beamwidth (HPBW), respectively, in units of degree; $\theta_{c,k}$ and $\phi_{c,k}$ are the relative vertical and horizontal angles, ranging from zero to 360 degrees, of the UE k 's location with respect to cell c 's location; A_m is the absolute value of the antenna front-to-back attenuation; θ_{tilt} is the antenna down-tilt in units of degree; and SLA_v is absolute value of the antenna sidelobe attenuation. The minus sign at the beginning of Eq. (4.4) and (4.5) indicates they are in fact antenna attenuation in the corresponding directions. The cell antennas are down-tilted so that their upper HPBW is targeting at cell edge for the best in-cell capacity performance. Fig. 4.2 shows the vertical and horizontal antenna radiation patterns for $\theta_{3dB} = 32$ degrees [176], $\phi_{3dB} = 70$ degrees [175], $A_m = 25$ dB, $\theta_{tilt} = 0$ degree, $SLA_v = 20$ dB.

In contrast, the antenna pattern for a microcell in an SBS is assumed to be omni-directional in the horizontal plane, whose expression is simplified as:

$$G_{BS,c,k}^{SBS} [\text{dB}] = G_{SC,max}^{SBS} [\text{dBi}] - \min \left[12 \left(\frac{\theta_{c,k} - \theta_{tilt}}{\theta_{3dB}} \right)^2, SLA_v \right] [\text{dB}]. \quad (4.6)$$

The horizontal antenna pattern for a microcell has 0 dB for all 360 degrees. An example vertical antenna radiation pattern is shown in Fig. 4.3 with $\theta_{3dB} = 40$ degrees [177], $SLA_v = 20$ dB, $\theta_{tilt} = 0$ degree.



(a) Vertical Antenna Radiation Pattern, G_V^{MBS}

(b) Horizontal Antenna Radiation Pattern, G_H^{MBS}

Figure 4.2: 3GPP antenna radiation pattern for a single macrocell, $\theta_{3dB} = 32$ degrees, $\phi_{3dB} = 70$ degrees, $A_m = 25$ dB, $\theta_{tilt} = 0$ degree, $SLA_v = 20$ dB

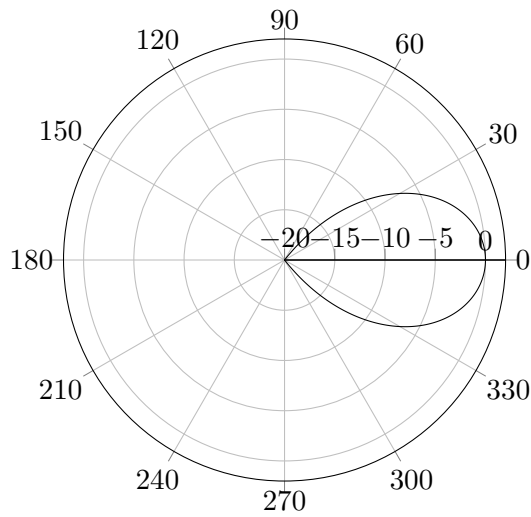


Figure 4.3: 3GPP vertical antenna radiation pattern for a single microcell, $\theta_{3dB} = 40$ degrees, $SLA_v = 20$ dB, $\theta_{tilt} = 0$ degree

The antenna patterns for picocells in SBS are assumed to be isotropic, which is mathematically expressed as:

$$G_{BS,c,k}^{SBS} = 0 \text{ [dBi]} \quad (4.7)$$

Active UEs are assumed to have isotropic antennas, so that:

$$G_{UE,c,k} = 0 \text{ [dBi]} \quad (4.8)$$

Channel loss considered here is the combined effect of path loss fading (PL), shadow fading (SF), and multipath fading. The path loss and shadow fading are large-scale fading phenomena and depend on the locations of BSs and UEs, which changes every independent Monte Carlo run over T TTIs. In contrast, multipath fading is small-scale fading that changes every RB per TTI.

The path loss model is probability-weighted between LoS and NLoS scenarios, as suggested in [175], [178]. The general expression for the adopted path loss model between UE k and arbitrary cell c is:

$$L_{PL,c,k} = \begin{cases} \beta^{LoS} + \zeta^{LoS} \times \log_{10}(d_{c,k}) \text{ [dB]} & \text{if LoS} \\ \beta^{NLoS} + \zeta^{NLoS} \times \log_{10}(d_{c,k}) \text{ [dB]} & \text{if NLoS} \end{cases} \quad (4.9)$$

where β^z , $z = \text{LoS, NLoS}$, is a dimensionless path loss constant that is dependent on the communication environment and signal carrier frequency; ζ^z , $z = \text{LoS, NLoS}$, is the path loss exponent that is dependent on BS and UE heights in addition to the communication environment and signal carrier frequency; and $d_{c,k}$ is the 3D distance between UE k and the BS in cell c with units of metre including the height difference between the UE and BS. The LoS probabilities for different scenarios are also suggested in [175], [178] as:

$$Pr_{c,k}^{LoS} = \begin{cases} \min\left(\frac{18}{d_{c,k}}, 1\right) \times \left[1 - \exp\left(\frac{-d_{c,k}}{63}\right)\right] + \exp\left(\frac{-d_{c,k}}{63}\right) & \text{if macro-RAN} \\ \min\left(\frac{18}{d_{c,k}}, 1\right) \times \left[1 - \exp\left(\frac{-d_{c,k}}{36}\right)\right] + \exp\left(\frac{-d_{c,k}}{36}\right) & \text{if micro-RAN} \\ 0.5 - \min\left(0.5, 5 \times \exp\left(\frac{-156}{d_{c,k}}\right)\right) + \min\left(0.5, 5 \times \exp\left(\frac{d_{c,k}}{30}\right)\right) & \text{if pico-RAN} \end{cases} \quad (4.10)$$

where the parameters for the expression are collected from the field tests [179]. Fig. 4.4 shows the probability of LoS transmission versus the 3D distance between BSs and UEs in units of metre,

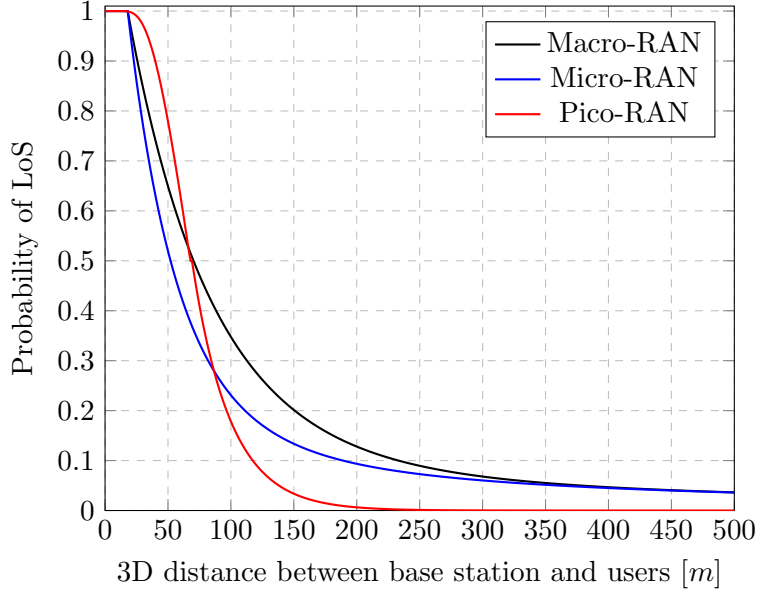


Figure 4.4: Probability of LoS transmission versus the 3D distance between BSs and UEs in units of metre, $Pr_{c,k}^{LoS}$, comparing different BS technologies

comparing different BS technologies. Generally, the larger the separation between BSs and UEs, the lower the probability of LoS transmission, regardless of BS technologies. This is due to the increasing probability of having objects in the transmission path interfering with LoS transmission with the increasing separation. The BS heights differ between different BS technologies, where the macro-BS is higher than the micro-BS, and the micro-BS is higher than the pico-BS. The specific parameters can be found in Table. 4.1 and 4.3 in the following sections. Thus the same 3D distance considering the height difference between BSs and UEs leads to different 2D distances. Specifically, at the same 3D distance, UE is closer to a macro-BS in the horizontal plane than a micro-BS; thus, the corresponding LoS probability is higher since signal reflection or diffraction is less likely to occur. In addition, microcells usually have wider HPBW than macrocells, leading to lower LoS probability. For short 3D distances smaller than 80 m, the signal transmitted in pico-RAN always has the highest LoS probability. Given the limited large-scale fading within this distance range, the received signal strength in the picocell is expected to be the strongest, leading to the highest capacity performance.

Without loss of generality, the shadow fading $L_{SF,c,k}$ between UE k and the BS in cell c is modelled as a normal distribution on a dB scale for simplicity, for which the mean and standard deviation are suggested in [175], [178] and listed in Tables 4.1 and 4.3 in the following sections

for different BS technologies. The shadow fading is calculated as the combined NLoS and LoS components weighted by the LoS probability. The Rayleigh multipath fading $L_{MPF,c,k}(n, t)$ for an arbitrary RB n in TTI t is modelled as an independent and identically distributed (iid) random variable [18]. Thus the per RB per TTI channel loss $L_{c,k}(n, t)$ on RB n is expanded as:

$$L_{c,k}(n, t) \text{ [dB]} = \left(L_{PL,c,k}^{LoS} \text{ [dB]} + L_{SF,c,k}^{LoS} \text{ [dB]} \right) \times Pr_{c,k}^{LoS} + \left(L_{PL,c,k}^{NLoS} \text{ [dB]} + L_{SF,c,k}^{NLoS} \text{ [dB]} \right) \times (1 - Pr_{c,k}^{LoS}) + L_{MPF,c,k}(n, t) \text{ [dB]} \quad (4.11)$$

4.2.3 UE Throughput and RAN Area Throughput

Using Shannon's formula, the UE throughput per RB per TTI is calculated as:

$$\tilde{S}_{UE,k}(n, t) = \frac{12 \times 14 \times \log_2 \left(1 + I_{c,k}(n, t) \times \gamma_{c,k}(n, t) \right)}{\delta_t} \quad (4.12)$$

where the constants 12 and 14 correspond to the 12 sub-carriers and 14 symbols in a single RB with a time spread $\delta_t = 1$ ms (1 TTI); $I_{c,k}(n, t)$ is an allocation indicator determined by the scheduling metric that equals one if the RB n in TTI t is allocated to UE k from cell c , and 0 otherwise; and $\gamma_{c,k}(n, t)$ is the per RB per TTI SINR experienced by UE k expressed as:

$$\gamma_{c,k}(n, t) = \frac{P_{rx,c,k}(n, t)}{\sum_{c' \in \mathcal{C} \setminus \{c\}} P_{rx,c',k}(n, t) + \sigma_n^2}. \quad (4.13)$$

In Eq. (4.13), $c' \in \mathcal{C} \setminus \{c\}$ means that c' belongs to the intersection of the total cell set \mathcal{C} and the sub-set only containing UE k 's serving cell c , $\sum_{c' \in \mathcal{C} \setminus \{c\}} P_{rx,c',k}(n, t)$ thus accounts the total interference received by UE k f, and σ_n is the standard deviation of the noise on the UE side in the DL, including the thermal noise at temperature of 25 °C and a 4 dB user noise figure [18], [74]. In this work, the intra-site interference for a tri-sectored BS site is considered, which means an arbitrary UE receives the interference from the other two cells belonging to the same BS site. However, this intra-site interference is mitigated due to the antenna radiation pattern.

For an observation period T , the UE average throughput S_{UE} is calculated as:

$$S_{UE,k} = \frac{1}{T} \sum_{t=1}^T \sum_{n=1}^{N_{RB}} \tilde{S}_{UE,k}(n, t) \quad (4.14)$$

Thus the RAN throughput could be calculated as:

$$S_{RAN} = \sum_{k=1}^K S_{UE,k} \quad (4.15)$$

For a homogeneous RAN with hexagonally distributed identical BSs, the RAN area A_{RAN} is calculated as:

$$A_{RAN} = A_c \times N_C \quad (4.16)$$

where the total number of cells N_C in RAN equals to the number of BSs N_B if each BS has a single cell or $3 \times N_B$ if each BS has 3 cells; and the hexagonal area of a cell A_c is calculated as:

$$A_c = \begin{cases} \frac{3\sqrt{3} \times R_1^2}{2} & \text{if } n_c = 1 \\ \frac{3\sqrt{3} \times R_3^2}{8} & \text{if } n_c = 3 \end{cases} \quad (4.17)$$

where $R_1 = ISD/\sqrt{3}$ is the cell radius of the BS with a single sector, and $R_3 = ISD/1.5$ is the cell radius of the BS with 3 sectors. Both Eq. (4.15) and (4.17) can then be used for DVG calculation as the RAN capacity performance.

4.2.4 Scheduling Protocol and Jain's Fairness Index

One of the common schedulers called Maximum SINR (MSINR) could be used to maximize the RAN throughput and average UE throughput [18]. Assume \mathcal{K}' is a subset of \mathcal{K} which contains all the N_K UEs associated with cell c . The MSINR metric for the allocation of RB n in TTI t is:

$$\max_{k \in \mathcal{K}'} \left\{ \tilde{S}_{UE,k}(n, t) \right\}. \quad (4.18)$$

In other words, each RB is allocated to the UE, which could achieve the highest throughput on that RB. The RB allocation determined by the MSINR scheduler could maximise the RAN and average UE throughput by exploiting the UE diversity. However, this metric always favours the UEs on good channels with small loss and allocate RBs to them. This compromises the fairness between UEs.

The Round Robin (RR) scheduler is designed to treat UEs in the same cell equally and allocates

RBs to UEs in turn [10], [18]. As a result, UEs on different channel conditions are allocated with the same number of RBs if the scheduling period is sufficiently long. However, this also leads to RAN throughput degradation for two reasons. First, UEs on good channels with high SINR only have limited RB allocation, so the resultant throughput is limited. In contrast, UEs on bad channels with low SINR cannot achieve high throughput despite the ample RB allocation.

To balance the trade-off between throughput and fairness, the Proportional Fair (PF) scheduler has been proposed [10], [18]. The PF metric for the allocation of RB n in TTI t is expressed as:

$$\max_{k \in \mathcal{K}'} \left\{ \frac{\tilde{S}_{UE,k}(n, t)}{S_{UE,k}^w(t-1)} \right\} \quad (4.19)$$

where $S_{UE,k}^w(t-1)$ is the weighted average throughput of UE k_c achieved over the previous $t-1$ TTIs, updated as:

$$S_{UE,k}^w(t) = \frac{(t_w - 1) \times S_{UE,k}^w(t-1) + \tilde{S}_{UE,k}(t)}{t_w} \quad (4.20)$$

where t_w is the time window to calculate the weighted throughput. The longer the t_w , the closer $S_{UE,k}^w(t-1)$ is to unity, thus the closer the PF performance to MSINR. In contrast, the shorter the t_w , the more closer $S_{UE,k}^w(t-1)$ is to $\tilde{S}_{UE,k}(t)$, and the closer the PF performance to RR. With a reasonable value for t_w , the PF scheduling metric considers both the previously obtained UE throughput and the potential instantaneous UE throughput that could achieve a comparatively higher RAN throughput than RR via user diversity, with a reduced bias between individual UE throughput that provides better fairness than MSINR. In the simulation, RR is first applied for 20 TTIs to ensure all the UEs have non-zero $S_{UE,k}^w(t-1)$ before switching to PF.

In addition to the achieved capacity or energy efficiency, fairness is another major performance indicator in comparing schedulers. This work considers two types of fairness when comparing different schedulers: the RB allocation fairness, and the UE throughput fairness, both of which are quantified using Jain's fairness index. The RB allocation fairness of cell c is calculated as:

$$J_{RB,c} = \frac{\left(\sum_{k \in \mathcal{K}'} \left(\sum_{t=1}^T \sum_{n=1}^{N_{RB}} I_{c,k}(n, t) \right) \right)^2}{N_K \times \sum_{k \in \mathcal{K}'} \left(\sum_{t=1}^T \sum_{n=1}^{N_{RB}} I_{c,k}(n, t) \right)^2}. \quad (4.21)$$

The input to the standard Jain's fairness index formula is the total number of RBs allocated to

each UE in T TTIs. $J_{RB,c}$ provides the fairness measurement of how the resource of cell c is divided between all the UEs associated with it. In contrast, the UE throughput fairness of the cell c is:

$$J_{S,c} = \frac{\left(\sum_{k \in \mathcal{K}'} S_{UE,k}\right)^2}{N_K \times \sum_{k \in \mathcal{K}'} S_{UE,k}^2}. \quad (4.22)$$

The input to Jain's fairness index formula is the UE average throughput. $J_{S,c}$ provides the fairness measurement of the UE throughput achieved based on the resource allocation. These two fairness measurements will be applied to compare the performance of different schedulers in later sections.

4.2.5 Homogeneous RAN Simulation Flowchart

Fig. 4.5 shows the overall MATLAB-based flowchart of the homogeneous RAN densification simulation process. The hexagonal BS distribution is fixed once the ISD is set. The uniform UE locations change randomly between each Monte Carlo run to provide enough degree of generalisation. One hundred such independent RAN snapshots are executed to represent the traffic dynamically. Only the path loss, shadow fading, and antenna gain are considered when associating UE to serving cells, assuming all the cells are active and transmit at peak power. This averaged channel loss avoids the potentially severe computation overhead generated if the UE association is based on instantaneous channel loss. In contrast, when calculating the instantaneous SINR, the multipath fading is added to both the signal power channel and interfering channel. Having run all the Monte Carlo runs, the simulation output includes the UE SINR, area RAN throughput used for Data Volume Gain calculation, the number of active cells out of the total cell count for power consumption calculation, and the Jain's fairness index for scheduling protocol comparison.

4.3 Macro-RAN Densification

The homogeneous Macro-RAN densification is the primary approach to improve the RAN capacity to meet the increasing user demand. So in this section, after setting up the simulation parameters, the energy efficiency of densified macro-RAN is analysed as a RAN densification performance benchmark using the three figures of merit included in the evaluation framework and the power model. The capacity results, measured by DVG, are obtained directly from simulations. The energy

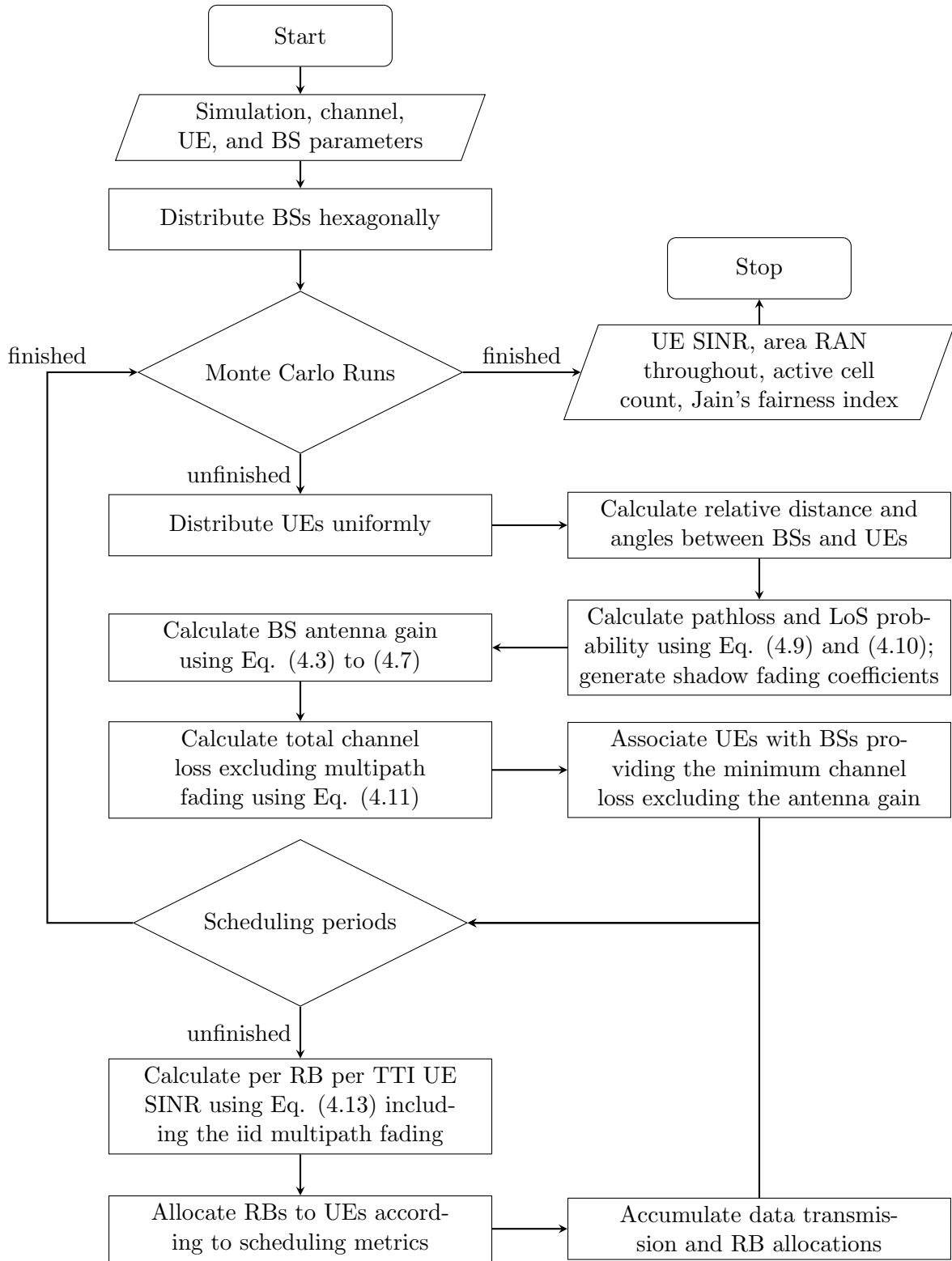


Figure 4.5: MATLAB-based simulation flowchart of homogeneous RAN

consumption results, measured by ECG, are calculated using the power model with the input of the number of cells from the simulation. The energy efficiency results, measured by EEG, are calculated using both the capacity and energy consumption results. In addition to the RAN densification, the peak transmission power of each cell is also analysed in terms of interference mitigation and energy consumption reduction.

The key simulation parameters for macro-RAN densification are listed in Table 4.1 [18], [175]. The macro-BS ISD ranges from 500 m down to 300 m for macro-RAN densification. All macro-BS sites have three cells with one antenna each, as shown in Fig. 4.1b, to increase the capacity via spacial reuse on top of BS densification. The equivalent macrocell density ranges from 13.86 macrocells per square kilometre to 38.49 macrocells per square kilometre. The carrier frequency is in the sub-6 GHz range with a bandwidth of 20 MHz that could offer 100 RBs per TTI. The occupied bandwidth B is assumed to equal the available channel bandwidth \hat{B} for capacity performance optimisation. When a cell c has UE associated, it is active and assumed to be fully loaded with α_c equaling to unity. In contrast, when no UE is associated with cell c , it is empty, and α_c equals 10% for just pilot broadcasting. The 10% level is derived from the daily traffic load variations in the figure from [167]. The macro-BS site antenna patterns are given by Eq. (4.3) to (4.5) and are shown in Fig. 4.2 in the previous section. RR is used as the primary scheduler for simple calculation and as the performance benchmark unless stated otherwise. When the scheduler is switched to PF, the observation time window t_w for the weighted average UE throughput calculation in Eq. (4.20) is set to 50 ms via simulations for better capacity performance closer to MSINR. The UE density is fixed at 300 per square kilometre [10]. The actual UE count K in RAN could then be calculated using the RAN area A_{RAN} and are all assumed to be active and outdoor. All UEs are assumed to be equipped with an isotropic antenna.

When reducing the ISD between macro-BSs, UEs are closer to their serving cells and the surrounding interfering cells. To reduce the interference without degrading the signal power quality, the peak transmission power per cell could reduce accordingly with the ISD reduction. The signal power quality is measured as the cell edge sensitivity, which is the received signal power level at the cell edge. Regarding the cell edge sensitivity of the 500 m ISD case as the reference, the varied cell peak transmission power for smaller ISDs is given in Table 4.2. Note that OBO also changes with $\hat{P}_{tx,c}$ for a fixed PA saturation power according to Eq. (3.20), which means reducing $\hat{P}_{tx,c}$

Parameter Name	Parameter Value
Site Count (N_B) / Cell Count (N_C)	19/57
Cell Count Per Site (n_c)	3
Antenna Count Per Cell (n_a)	1
BS/UE Height (h_{BS} / h_{UE}) [m]	15/1.5
UE Density per square kilometre	300
BS ISD [m]	300 - 500
Carrier Frequency [GHz]	2
Bandwidth [MHz]	20
RB Count Per TTI (N_{RB})	100
Peak Transmission Power Per Cell ($\tilde{P}_{tx,c}$) [dBm]	46.02
Maximum Antenna Gain ($G_{BS,max}^{MA}$) [dBi]	14
Vertical/Horizontal HPBW (θ_{3dB} / ϕ_{3dB}) [degree]	32/70
Antenna Front-to-Back Attenuation (A_m) [dB]	25
Antenna Sidelobe Attenuation (SLA_v) [dB]	20
Pathloss Dimensionless Constants (β^{LoS} / β^{NLoS}) [dB]	30.8/2.9
Pathloss Exponents (ζ^{LoS} / ζ^{NLoS})	24.2/42.8
Shadow Fading Mean (μ^{LoS} / μ^{NLoS}) [dB]	0/0
Shadow Fading Standard Deviation (σ^{LoS} / σ^{NLoS}) [dB]	8/8
Noise Variance per RB (σ_n^2) [dBm]	-117.38
Proportional Fair Observation Time Window (t_w) [ms]	50

Table 4.1: Macro-RAN densification simulation parameters

ISD [m]	500	450	400	350	300
$\hat{P}_{tx,c}$ [dBm]	46.02	43.95	41.61	38.92	35.78

Table 4.2: Varied macrocell peak transmission power with RAN densification

with RAN densification does not require a hardware replacement of PA.

The energy efficiency evaluation framework will then be applied to analyse the energy efficiency of macro-RAN densification. The reference RAN for figures of merit calculation is the macro-RAN with tri-sectorised BSs and 500 m ISD (13.86 macrocells/km²), 300 UEs/km², and RR scheduler. All macro-RANs considered in this section have a UE density of 300 UEs/km² and RR scheduler.

Fig. 4.6 shows the Data Volume Gain of the macro-RAN with macrocell density as a variable for both fixed and varied $\hat{P}_{tx,c}$ approaches. This figure compares the capacity performance of macro-RAN densification with the reference macro-RAN using DVG. The major observations are:

1. The almost overlapping DVG profiles in the figure indicate no capacity performance degradation when varying $\hat{P}_{tx,c}$ with the increasing macrocell densities. The reduction in UE signal power when reducing $\hat{P}_{tx,c}$ is counter-balanced by the interference limitation.
2. For both $\hat{P}_{tx,c}$ approaches, DVG increases linearly with the macrocell density. This is mainly due to the signal power strengthening by bringing UEs closer to their serving cells, which exceeds the NLoS interference increase. UEs are now in the noise-limited region where the increasing macrocell density improves RAN capacity continuously. Thus DVGs are always greater than unity.
3. When increasing the macrocell density from 13.86 to 38.49 macrocells per square kilometre, DVGs for the fixed and the varied $\hat{P}_{tx,c}$ approaches increase from 1 to 2.83 and 2.84, respectively. The slightly higher DVG for varied $\hat{P}_{tx,c}$ approach is caused by a slight capacity improvement due to interference limitation.
4. The more-than-3-times macrocell density increase results in less-than-3-times capacity improvement. This means that the existence of intra-site interference does degrade the capacity.

Overall, the macro-RAN densification in the noise-limited region improves the RAN capacity.

Fig. 4.7 shows the Energy Consumption Gain of the macro-RAN with macrocell density as

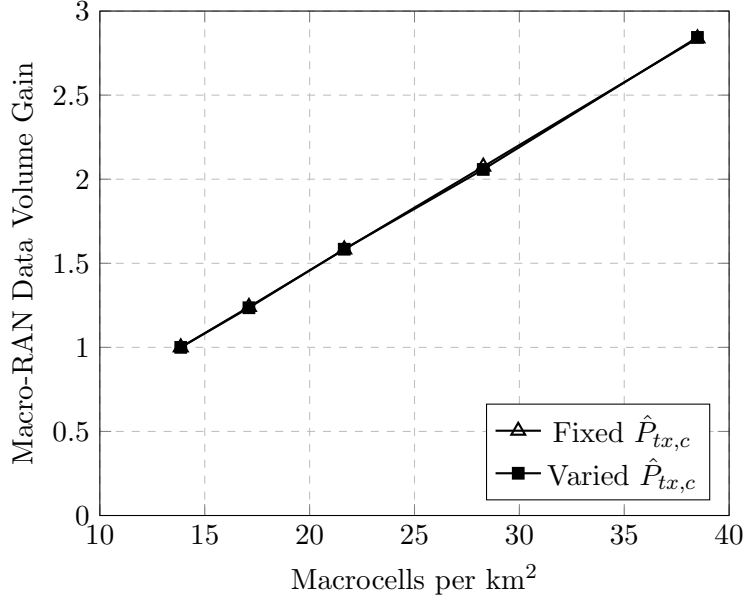


Figure 4.6: Macro-RAN Data Volume Gain against macrocell density, comparing different $\hat{P}_{tx,c}$ approaches

a variable for both fixed and varied $\hat{P}_{tx,c}$ approaches. ECG compares the energy consumption of densified macro-RAN with the reference macro-RAN. Adding more identical high-power macro-BSs into the same area increases the total energy consumption. Therefore, ECG reduces exponentially against the increasing macrocell density when $\hat{P}_{tx,c}$ is fixed. In contrast, the varied $\hat{P}_{tx,c}$ approach reduces $\hat{P}_{tx,c}$ with densification, which reduces energy consumption and improves ECG. However, the reduction in energy consumption is insufficient to stop the overall ECG reducing tendency. Therefore, regardless of $\hat{P}_{tx,c}$ approaches, the densified macro-RAN always consumes more energy than the reference macro-RAN and has ECG lower than unity. Specifically, when increasing the macrocell density from 13.86 to 38.49 macrocells per square kilometre, the ECGs for the fixed and the varied $\hat{P}_{tx,c}$ approaches reduce from 1 to 0.36 and 0.86, respectively.

Fig. 4.8 shows the Energy Efficiency Gain of the macro-RAN with macrocell density as a variable for both fixed and reduced cell peak transmission power $\hat{P}_{tx,c}$ approaches. This figure compares the energy efficiency performance of macro-RAN densification with the reference macro-RAN using EEG, which is the product of DVG and ECG. For the fixed $\hat{P}_{tx,c}$ approach, the EEG profile is fixed at unity against the increasing macrocell densities. This is due to the cancellation of the capacity improvement and energy consumption increase. However, when the varied $\hat{P}_{tx,c}$ approach

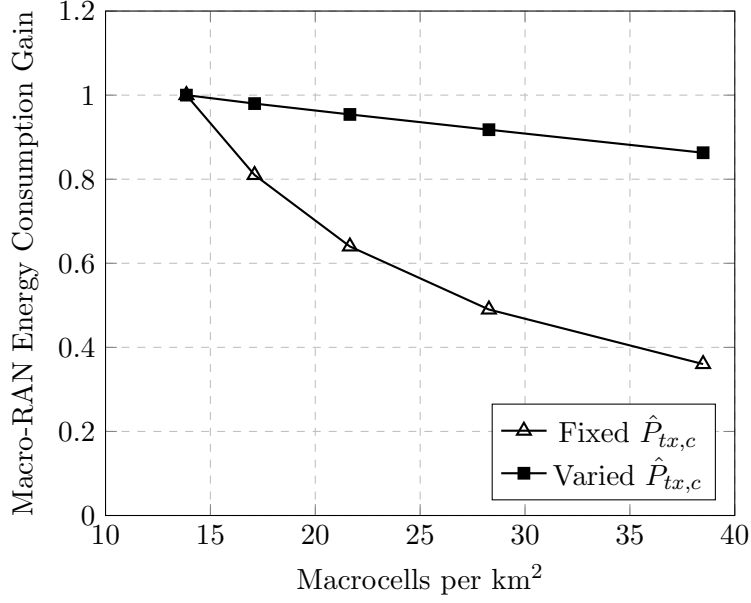


Figure 4.7: Macro-RAN Energy Consumption Gain against macrocell density, comparing different $\hat{P}_{tx,c}$ approaches

is used, the increase of RAN energy consumption is limited. The improving capacity dominates the energy efficiency performance, so the EEG increases with the increasing macrocell density. When increasing the macrocell density from 13.86 to 38.49 macrocells per square kilometre, EEG increases from 1 to 2.45. Nevertheless, the energy efficiency enhancement comes from capacity improvement only, and energy consumption still increases. This indicates that densified macro-RAN is energy efficient but is not green. Thus small cell RAN densification is then analysed in the next section to show its capability of reducing energy consumption and thus enhancing energy efficiency.

4.4 Small Cell RAN Densification

In addition to the limitation in macro-BS implementation cost, the previous section has shown that macro-RAN densification increases the RAN energy consumption. Therefore, homogeneous macro-RAN densification is not a green solution to the future network, even though it could improve RAN capacity and energy efficiency. So in this section, small cell BSs replace the macro-BS for their potential to reduce the RAN energy consumption. Specifically, this section presents the simulation results of the small cell RAN densification capacity, the simulation and calculation results of the RAN energy consumption, and the resultant energy efficiency. The energy efficiency evaluation

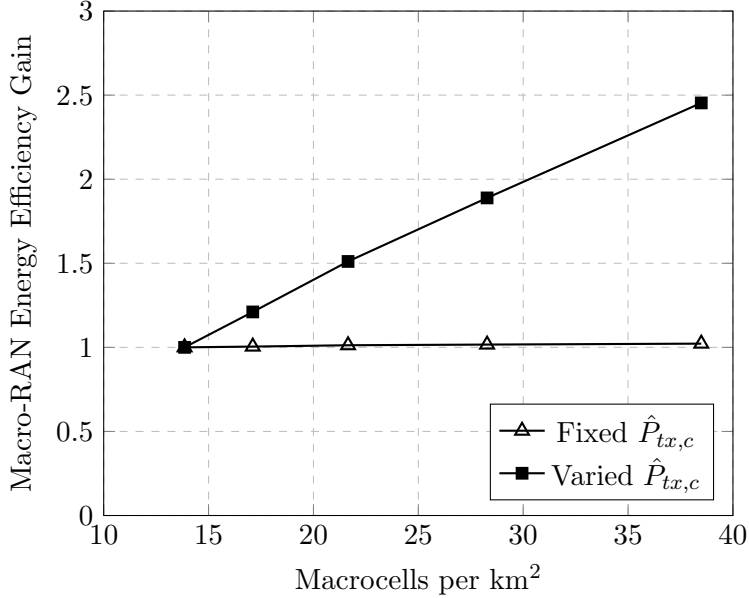


Figure 4.8: Macro-RAN Energy Efficiency Gain against macrocell density, comparing different $\hat{P}_{tx,c}$ approaches

framework evaluates the results with the same reference macro-RAN with three cells per site (500 m ISD or 13.86 macrocells/km²), 300 UEs/km², and RR scheduler.

The key simulation parameters for the homogeneous small cell RAN densification are listed in Table 4.3 [175], [178]. Both micro-RANs and pico-RANs are considered. The site count N_B and cell count N_C in small cell RANs with different BS ISDs might change to ensure an integer and not-too-small number of UEs in the RAN for the fixed 300 UEs/km² density. The micro-BS ISD range is from 500 m down to 100 m, overlapping ranges with considered macro-RANs for performance comparison. The smaller pico-BS ISD range is from 200 m down to 5 m, overlapping ranges with considered micro-RANs for performance comparison. Though micro-BS and pico-BS have a single cell and a single antenna per cell, the former is assumed to have an omni-directional antenna in the horizontal plane to boost capacity within a bigger coverage area. The latter is assumed to have an isotropic antenna for a smaller coverage area. The small cell RAN layout is shown in Fig. 4.1a and the vertical antenna radiation pattern of a micro-BS is demonstrated in Fig. 4.3. The equivalent small cell density range for micro-RAN is from 4.62 to 115.47 microcells per square kilometre, and the picocell density range is from 28.87 to 46188.02 picocells per square kilometre. Like macro-RAN, the signal carrier frequency is also 2 GHz with 20 MHz bandwidth,

Parameter Name	Micro-BS	Pico-BS
Cell Count Per Site (n_c)	1	
Antenna Count Per Cell (n_a)	1	
UE Density per square kilometre	300	
Carrier Frequency [GHz]	2	
Bandwidth [MHz]	20	
RB Count Per TTI (N_{RB})	100	
Shadow Fading Mean (μ^{LoS} / μ^{NLoS}) [dB]	0/0	
Noise Variance per RB [dBm] (σ_n^2)	-117.38	
Proportional Fair Observation Time Window (t_w) [ms]	50	
BS/UE Height (h_{BS} / h_{UE}) [m]	4.5/1.5	3/1.5
BS ISD [m]	100 - 500	5-200
Peak Transmission Power Per Cell ($\hat{P}_{tx,c}$) [dBm]	37.99	21.14
Maximum Antenna Gain ($G_{BS,max}^{SC}$) [dBi]	4	0
Vertical HPBW (θ_{3dB}) [degree]	40	-
Antenna Sidelobe Attenuation (SLA_v) [dB]	20	-
Pathloss Dimensionless Constants ($\beta^{LoS} / \beta^{NLoS}$) [dB]	(34.02, 4.02)/30.5	41.1/32.9
Pathloss Exponents ($\zeta^{LoS} / \zeta^{NLoS}$)	(22, 40)/36.7	20.9/37.5
Shadow Fading Standard Deviation ($\sigma^{LoS} / \sigma^{NLoS}$) [dB]	3/4	10/10

Table 4.3: Small cell RAN densification simulation parameters

providing 100 RBs per TTI. The occupied bandwidth B is assumed to equal the total available bandwidth \hat{B} for optimised capacity performance. All UEs are assumed to be active. Active small cells have unity α_c , while empty small cells have 10% for α_c for just pilot broadcasting. Note that the micro-BS LoS path loss model has two segments, differentiated at a distance of 46.7 m under current settings [178]. RR is the chosen scheduler for its simple computation.

Table 4.4 shows the reduced cell peak transmission power $\hat{P}_{tx,c}$ levels for micro-BSs and pico-BSs. The 500 m ISD micro-BS sets the reference cell edge sensitivity for micro-BSs with smaller ISDs, and the 200 m ISD pico-BS sets the reference for pico-BSs. Note that the cell peak transmission power is low when either micro-RAN or pico-RAN is highly densified. The low transmission power values seem unrealistic in the real-life scenario, but rather the calculation results regarding the cell edge sensitivities and extremely small ISDs for energy efficiency performance comparison.

Fig. 4.9 shows the Data Volume Gain of the small cell RAN with small cell density as a variable for both fixed and varied $\hat{P}_{tx,c}$ approaches. The DVGs for macro-RAN densification are also included for capacity performance comparison. The main observations are:

1. The difference in DVG profiles between different $\hat{P}_{tx,c}$ approaches is negligible regardless of

Micro-ISD [m]	500	400	350	300	250	200	150	100
$\hat{P}_{tx,c}$ [dBm]	37.99	34.24	31.94	29.18	25.69	20.93	13.80	2.56
Pico-ISD [m]	200	150	100	75	50	25	10	5
$\hat{P}_{tx,c}$ [dBm]	21.14	12.55	-1.35	-8.43	-14.33	-20.95	-29.01	-34.53

Table 4.4: Varied small cell peak transmission power with RAN densification

BS technologies or cell densities.

2. Micro-RAN DVG improves with the increasing microcell density. The UE signal strengthening dominates this. Compared with the macro-RAN counterpart with the same cell density, micro-RAN always has a higher DVG. Because macro-BSs are tri-sectorised and micro-BSs have single cells, the same cell density leads to different BS ISDs. Specifically, at the same cell density, micro-BSs have shorter ISD than their macro-BS counterparts, so microcell UEs are closer to the BSs in their serving cells and have improved throughput. When increasing the microcell density from 4.62 to around eight microcells per square kilometre, the micro-RAN has a lower capacity than the reference macro-RAN, and DVGs are less than unity. Similarly, microcell UEs are further away from the BSs in their serving cells than the reference macro-RAN, leading to lower capacity and DVG. Further microcell densification improves the DVG, reaching 11.30 when microcell density is 115.47 per square kilometre for both $\hat{P}_{tx,c}$ approaches.
3. Pico-RAN DVG improves with the increasing picocell density but starts to decrease at 461.88 picocells per square kilometre (pico-ISD 50 m). The increasing phase is dominated by the UE signal strengthening, while the decreasing phase is dominated by interference increase. When pico-ISD is smaller than 50 m, UEs are close to the BSs in both serving and interfering cells. The signal transmission is likely to be LoS dominated. UEs then shift from the noise-limited region to the interference-limited region. This degrades the RAN capacity and DVG. Furthermore, compared with the micro-RAN counterparts with the same small cell densities, pico-RANs have higher DVG because of interference limitations. Micro-BSs equipped with horizontally omni-directional antenna patterns with wide vertical HPBW would cause higher interference to UEs than pico-BSs equipped with an isotropic antenna. When picocell density increases from 28.87 to 46188.02 picocells per square kilometre, DVG is first improved from 3.80 and 3.81 to 22.06 and 20.97 for fixed and varied $\hat{P}_{tx,c}$ approaches, respectively; then

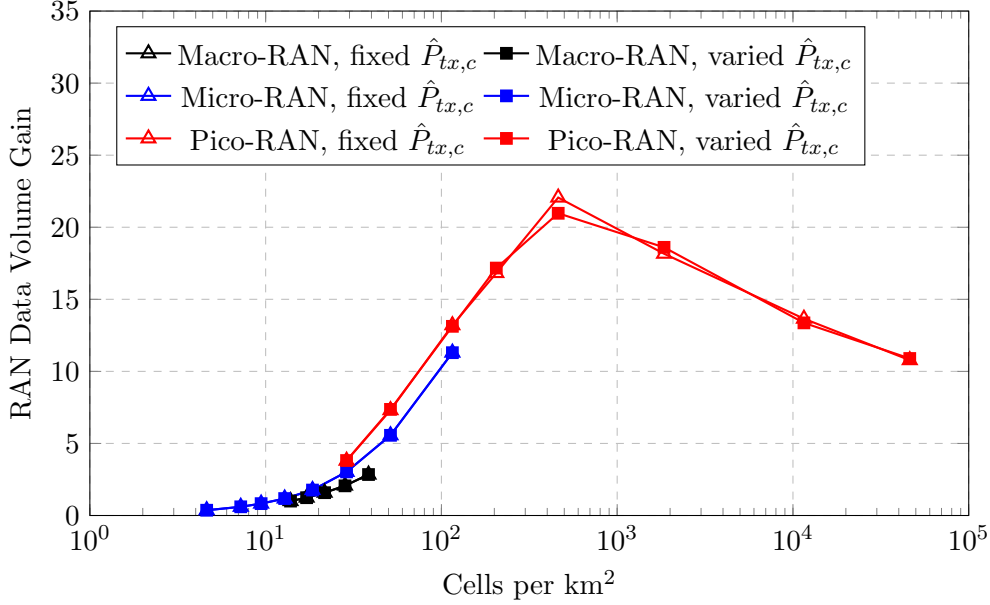


Figure 4.9: RAN Data Volume Gain against cell density, comparing fixed and varied cell peak transmission power $\hat{P}_{tx,c}$ approaches and different BS technologies

decreased to 10.78 and 10.89, respectively. The slightly higher DVG at 461.88 picocells per square kilometre using the fixed $\hat{P}_{tx,c}$ approach is due to higher transmission power. But this benefit of fixing $\hat{P}_{tx,c}$ vanishes when the interference increases further with densification.

In general, small cell RAN densification could significantly improve the RAN capacity compared to macro-RAN densification. Nevertheless, if no actions are taken, highly densified small cell RAN suffers from severe interference that eventually degrades the RAN capacity.

Fig. 4.10 shows the Energy Consumption Gain of the small cell RAN with small cell density as a variable for both fixed and varied $\hat{P}_{tx,c}$ approaches. Macro-RAN ECGs are also included for energy consumption comparison. The main observations are:

1. Adding more BSs into the RAN always consumes more energy. Therefore, RAN ECG decreases monotonically against the increasing cell density for all BS technologies. When densifying the RAN, this cannot be overcome by reducing $\hat{P}_{tx,c}$.
2. As shown in Fig. 3.3 and Table 3.1, changing the BS technology from macro-BS to micro-BS to pico-BS reduces the site power consumption, but also reduces the dependence of site power consumption on the radio-head part. Therefore, at the same cell density, macro-RAN consumes more energy than micro-RAN, and the latter consumes more energy than

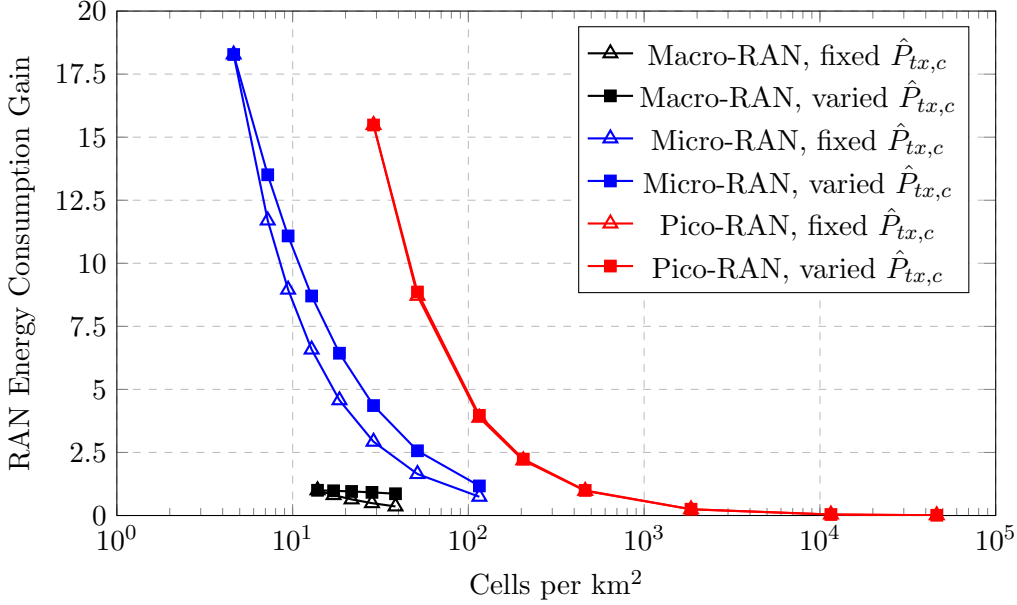


Figure 4.10: RAN Energy Consumption Gain against cell density, comparing fixed and varied cell peak transmission power $\hat{P}_{tx,c}$ approaches and different BS technologies

pico-RAN. However, energy consumption reduction caused by varying $\hat{P}_{tx,c}$ diminishes as micro-RAN replaces macro-RAN, and pico-RAN replaces micro-RAN.

3. When increasing the microcell density from 4.62 to 115.47 microcells per square kilometre, the micro-RAN ECG reduces from 18.28 for both $\hat{P}_{tx,c}$ approaches to 0.74 and 1.17 for fixed and varied $\hat{P}_{tx,c}$ approaches, respectively. Thus, within the considered micro-RAN ISD ranges, the varied $\hat{P}_{tx,c}$ approach always saves energy compared with the reference macro-RAN. However, the micro-ISD lower bound should be set to 100 m for the fixed $\hat{P}_{tx,c}$ approach if expecting the micro-RAN to consume no more energy than the reference macro-RAN.
4. Increasing the picocell density from 28.87 to 46188.02 picocells per square kilometre reduces the Pico-RAN ECG from 15.48 to 0.01 for both $\hat{P}_{tx,c}$ approaches. Compared to the reference macro-RAN, the pico-ISD lower bound should be set at 50 m for energy saving.

Therefore, energy-saving techniques are required to further densify the small cell RANs beyond the lower ISD bounds. Otherwise, small cell RAN densification, like the macro-RAN counterpart, consumes more energy.

Fig. 4.11 shows the Energy Efficiency Gain of the small cell RAN with small cell density as a variable for both fixed and varied $\hat{P}_{tx,c}$ approaches. Macro-RAN EEGs are also included for energy

efficiency performance comparison. The main observations are:

1. Given the similar capacity performance, the varied $\hat{P}_{tx,c}$ approach reduces energy consumption, thus improving energy efficiency for all BS technologies. However, the reduction in energy-saving effect by the varied $\hat{P}_{tx,c}$ approach when changing BS technologies also diminishes energy efficiency improvement. Specifically, for highly densified pico-RAN, the energy consumption is so significant that reducing $\hat{P}_{tx,c}$ has a negligible impact on energy consumption and energy efficiency.
2. For micro-RANs, the improvement in capacity exceeds the increase in energy consumption, improving energy efficiency with the increasing microcell density. This holds until there are 51.32 picocells per square kilometre (pico-ISD 150 m) in the RAN, after which the energy efficiency is dominated by the increasing energy consumption and starts to degrade. At the same cell density, micro-RAN is more energy efficient than the macro-RAN counterpart because of its higher capacity and lower energy consumption. When microcell density increases from 4.62 to 115.47 microcells per square kilometre, the micro-RAN EEG increases from 6.68 to 9.15 and 14.28, then decreases to 8.40 and 13.25 using fixed and varied $\hat{P}_{tx,c}$ approaches, respectively. Micro-RAN EEG is always higher than unity, indicating improved energy efficiency compared with the macro-RAN.
3. Similarly, pico-RAN EEGs first increase from 58.85 to 63.65 and 65.24 for fixed and varied $\hat{P}_{tx,c}$ approaches, respectively; then decrease to 0.11 for both $\hat{P}_{tx,c}$ approaches, respectively, when the picocell density increases from 28.87 to 46188.02 picocells per square kilometre. Energy efficiency improvement is dominated by improving capacity. In contrast, the energy efficiency degradation is caused by the increasing energy consumption and worsened by the capacity decrease due to the LoS interference increase. The performance turning point is 51.32 picocells per square kilometre (pico-ISD 150 m), which is lower than the DVG turning point. At the same cell density, pico-RAN with higher capacity and lower energy consumption achieves higher energy efficiency than the micro-RAN counterpart. Compared with the reference macro-RAN, pico-RAN is more energy efficient until the picocell density increases to around 11547.01 picocells per square kilometre (pico-ISD 10 m), where the significant RAN energy consumption starts to degrade the energy efficiency. Compared with the reference macro-

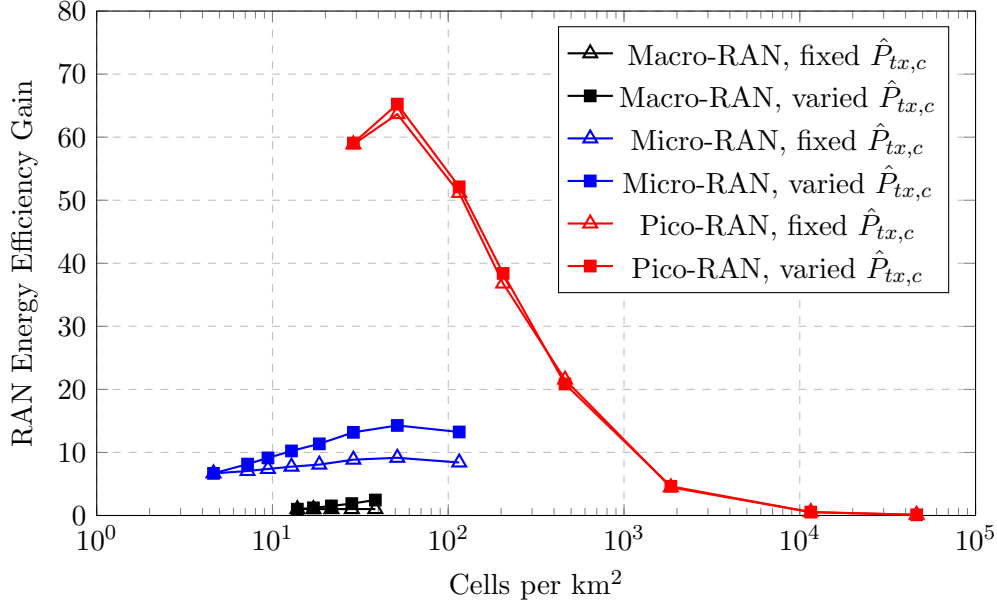


Figure 4.11: RAN Energy Efficiency Gain against cell density, comparing fixed and varied cell peak transmission power $\hat{P}_{tx,c}$ approaches and different BS technologies

RAN, this is the densification limitation for an energy efficient pico-RAN.

In general, densified small cell RAN is more energy efficient than the conventional macro-RAN due to both capacity improvement and energy consumption reduction. However, highly densified small cell RAN compromises energy efficiency because of capacity degradation and significant energy consumption. Techniques for interference mitigation and energy saving are thus required to recover the densified small cell RAN energy efficiency. This will be discussed in the next section.

4.5 Pico-RAN Densification

The previous section shows that small cell RAN densification cannot grow boundless, as the decreasing capacity and increasing energy consumption would eventually degrade the RAN energy efficiency. Thus in this section, the pico-RAN densification is analysed in more detail to evaluate possible solutions to keep the small cell RAN densification energy efficient. The choice of pico-RAN over the micro-RAN is because the former could be densified to an ultra-dense level with a reasonable antenna tilt. This enables the analysis of the energy efficiency performance of a homogeneous small cell RAN to an extreme densification level.

In this section, the fixed $\hat{P}_{tx,c}$ approach is adopted for a comparatively reasonable transmission

power level. The results in the previous section guarantee that the performance will not be affected much compared with the varied $\hat{P}_{tx,c}$ approach. In addition, the pico-BS ISD will be further reduced to 1 m in this section for the ultra-dense scenario, equivalent to 1154700.54 picocells per square kilometre. The other simulation and power model parameters are the same as in previous sections unless stated otherwise. The pilot power level from empty cells, sleep mode depths in empty cells, traffic intensities, and schedulers will be discussed in this section. Similarly, the capacity performance is obtained via simulation and evaluated by DVG; the energy consumption is calculated using both simulation results and the power model and assessed by ECG, and the energy efficiency is calculated using both the capacity and energy consumption and evaluated by EEG. The reference RAN is the tri-sectorized macro-RAN with 500 m ISD (13.86 macrocells/km²), 300 UEs/km², and an RR scheduler to keep the comparison consistent.

4.5.1 Pilot Power Level from Empty Picocells

Conventionally, empty cells without UE association in the RAN are still broadcast at a certain pilot level to support the appearance of potential UEs. The pilot level is reflected by the product of the cell normalised load activity factor α_c , which is set to 10% for previous simulation results, and the cell peak transmission power $\hat{P}_{tx,c}$. UEs in the highly densified pico-RAN suffer from severe interference. The major contribution to interference is the empty cell pilots. For a limited UE density, the higher the densification level, the more empty cells in the RAN, the higher the interference experienced by all the UEs, and the worse the achieved throughput. Reducing the pilot power level from empty cells seems like an effective solution for interference mitigation.

Table 4.5 shows the different cell normalised activity factors, α_c , for different pilot power levels from both active and empty picocells. The pilot power level in empty cells would be reduced gradually to zero for interference mitigation sensitivity analysis. How to detect the potential UE appearance without the pilot is not considered here. When a picocell is active with UE association, it is said to be at pilot level *Pilot100* with α_c being 100%. This applies to all the active picocells. When a picocell is empty without any UE association, it is said to be at pilot levels from *Pilot10* to *Pilot0* with α_c being reduced from 10% down to 0%. Specifically, *Pilot5* has α_c of 5%, and *Pilot1* has α_c of 1%.

Fig. 4.12 shows the Data Volume Gain of pico-RAN densification with the picocell density as

Cell State	Pilot Level	Cell Normalised Activity Factors, α_c , [%]
Active	<i>Pilot100</i>	100
Empty	<i>Pilot10</i>	10
	<i>Pilot5</i>	5
	<i>Pilot1</i>	1
	<i>Pilot0</i>	0

Table 4.5: Cell normalised activity factors for different pilot power levels in cells

the variable, comparing different pilot levels from empty pico-cells. Specifically, the pilot level from empty cells is reduced gradually to reduce the interference when *Pilot10* to *Pilot0* is applied. It is shown in the figure that reducing the pilot power level mitigates the interference experienced by UEs in RAN and improves the DVG, especially for picocell densities higher than 461.88 picocells/km² (pico-ISD 50 m) with a lot of empty cells. The lower the pilot broadcasted from empty picocells, the better the DVG results. However, only when the pilot transmission from empty cells is completely switched off (*Pilot0*) does the DVG increase monotonically with picocell density increasing. Otherwise, the total amount of interference comes from many empty cells, even with individual pilot transmission power at 1% of $\hat{P}_{tx,c}$, at high picocell densities is still severe and degrades capacity. This indicates that highly densified pico-RAN is highly sensitive to the power transmitted from empty cells. When picocell density is 1154700.54 picocells per square kilometre (pico-ISD of 1 m), *Pilot10* has a DVG of 6.04, while *Pilot5*, *Pilot1*, and *Pilot0* improves DVG to 10.02, 20.23, and 45.72, respectively. In summary, only when the empty cells switch off the pilot broadcasting completely does the RAN DVG and capacity increase with picocell densification monotonically.

The improvement of DVG when reducing the pilot power level from 10% to 0% of $\hat{P}_{tx,c}$ in empty picocells could also be demonstrated by the UE SINR Cumulative Distribution Function (CDF) shown in Fig. 4.13 between different pico-BS ISDs. The observations are:

1. When *Pilot10* is used, empty picocells transmit an interfering signal to all the UEs, which becomes stronger when ISD is smaller. Thus in Fig. 4.13a, the UE SINR CDF improves briefly before deteriorating with the reduction of ISD. The strengthened signal power partly compensates for the increasing interference for ISD ranging from 150 m down to 50 m. Thus the SINR degradation is limited. Further ISD reduction down to 4 m leads to the situation where the increasing interference dominates the UE SINR such that the SINR CDF degrades

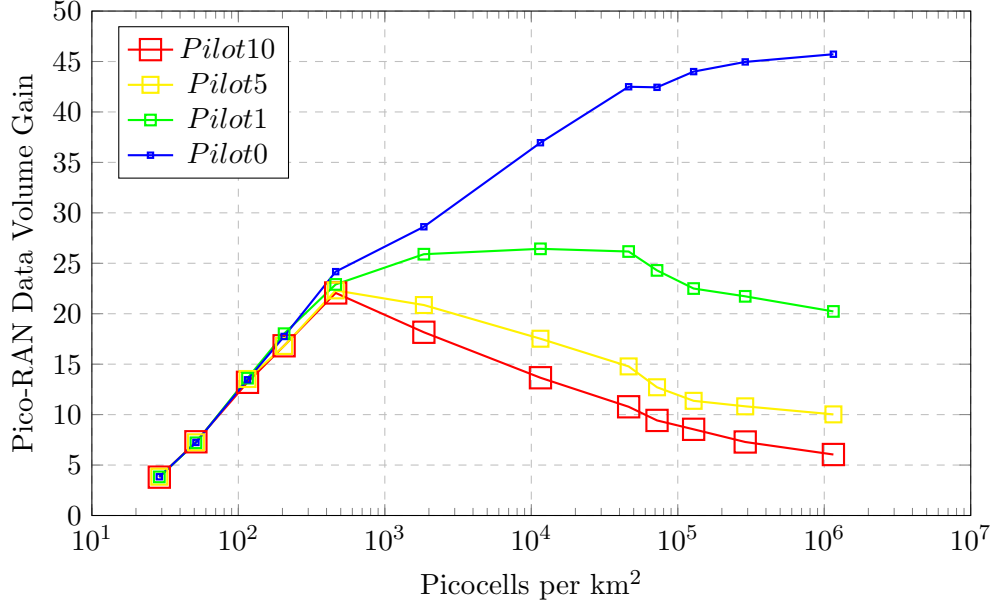


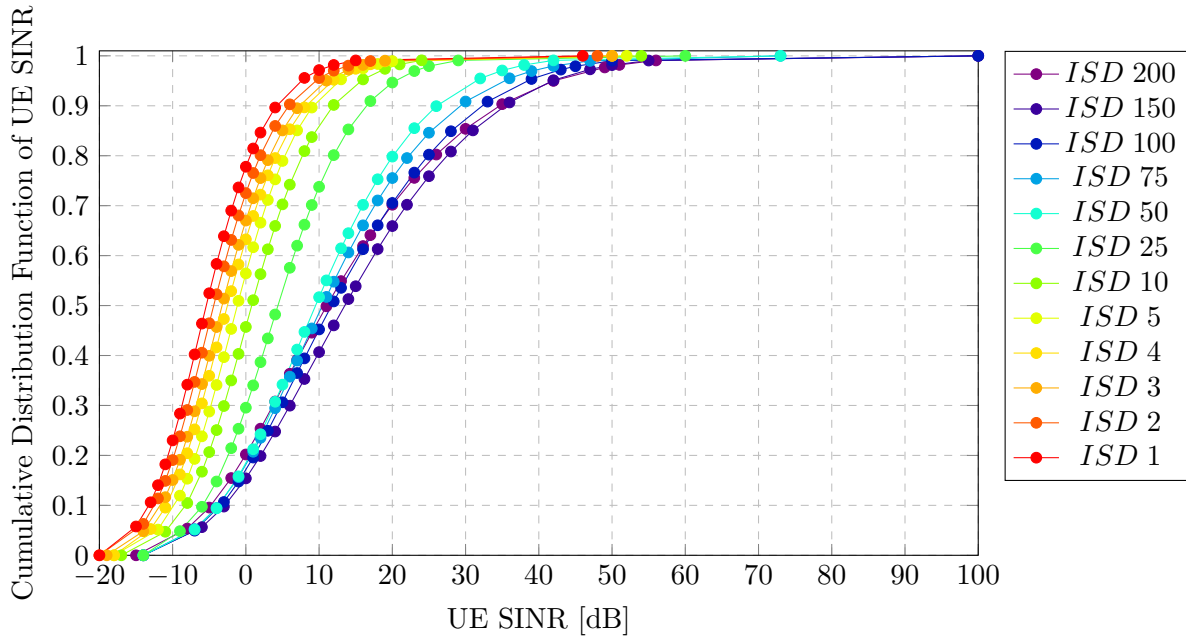
Figure 4.12: Pico-RAN Data Volume Gain against picocell density, comparing different pilot power levels in empty picocells: *Pilot10* has α_c of 10%, *Pilot5* has α_c of 5%, *Pilot1* has α_c of 1%, and *Pilot0* has α_c of 0%

quickly. When the ISD continues to reduce, the signal power strengthening re-takes the domination of SINR performance, reducing the rate of UE SINR degradation.

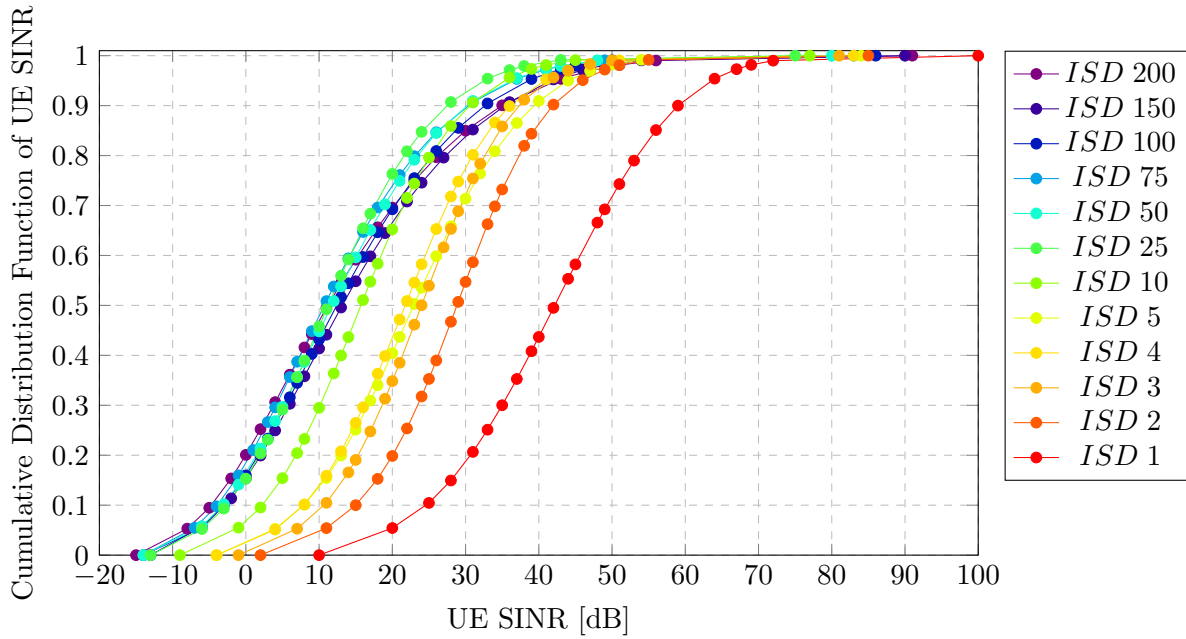
2. In contrast, Fig. 4.13b shows improving UE SINR with the reduction of ISD, especially for smaller ISD ranges. When all empty picocells do not transmit anything, they do not contribute to interference. Thus UEs only experience interference from active picocells, whose number first increases and then saturates against the increasing total number of picocells with densification. Therefore, for large ISD ranges from 200 m to 10 m, the signal power and interference increase could counterbalance each other. This leads to similar UE SINR CDFs. Further ISD reduction would strengthen signal power and limit interference power, resulting in improved UE SINR performance.

The observations from Fig. 4.13 are in line with the observations and conclusions from Fig. 4.12: switching the pilot transmission from empty picocells off when densifying the pico-RAN leads to monotonic capacity improvement.

Fig. 4.14 shows the Energy Consumption Gain of pico-RAN densification with the picocell density as the variable, comparing different pilot levels of empty pico-cells. This figure compares



(a) *Pilot10*



(b) *Pilot0*

Figure 4.13: Cumulative Distribution Function of UE SINR, comparing different pico-BS ISDs, with all empty cells have (a) *Pilot10* with α_c of 10% and (b) *Pilot0* with α_c of 0%

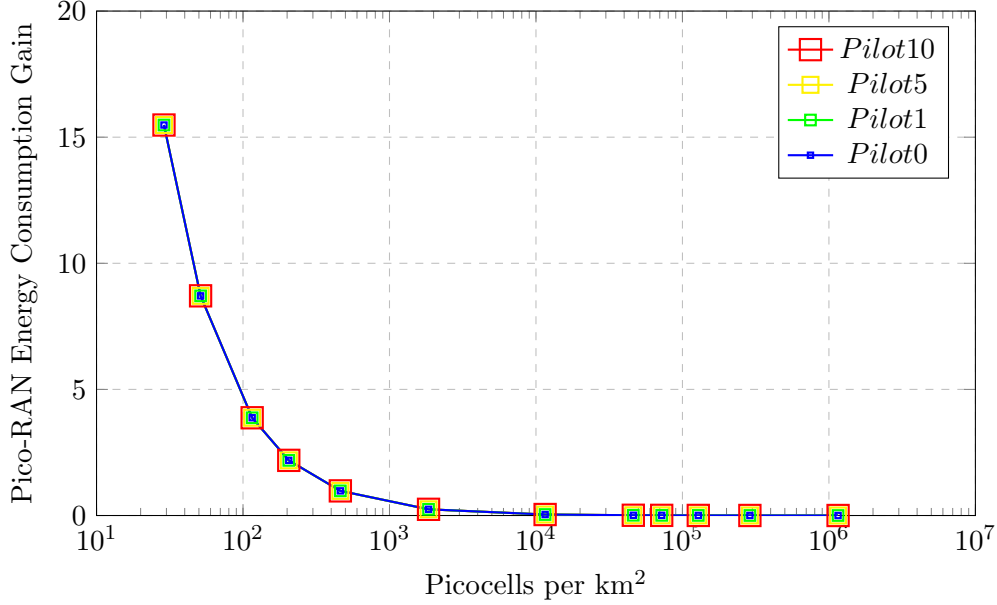


Figure 4.14: Pico-RAN Energy Consumption Gain against picocell density, comparing different pilot power levels in empty picocells: *Pilot10* has α_c of 10%, *Pilot5* has α_c of 5%, *Pilot1* has α_c of 1%, and *Pilot0* has α_c of 0%

the energy consumption of pico-RAN densification with the reference macro-RAN using ECG. The ECG profiles for different empty picocell pilot levels overlap and decrease against the increasing picocell density. This is because the pico-site power consumption is heavily overhead dominant. So the reduction in $\hat{P}_{tx,c}$ has a negligible impact on the total RAN energy consumption. Therefore, reducing the pilot power level from empty picocells when densifying the pico-RAN does not affect RAN energy consumption.

Fig. 4.15 illustrates the Energy Efficiency Gain of pico-RAN densification with the picocell density as the variable, comparing different pilot levels of empty pico-cells, for similar cases as in Fig. 4.12 and 4.14. This figure compares the energy efficiency of pico-RAN densification with the reference macro-RAN using EEG, which is the product of DVG and ECG. The EEG profiles of different empty picocell pilot power levels almost overlap with slight improvement from DVG. Interference limitation scales cause the difference. However, the overall first-increase-then-decrease tendency does not change when the pilot power level is reduced in empty picocells. Therefore, extra energy-saving techniques are required to improve the ECG and thus EEG, which will be discussed next.

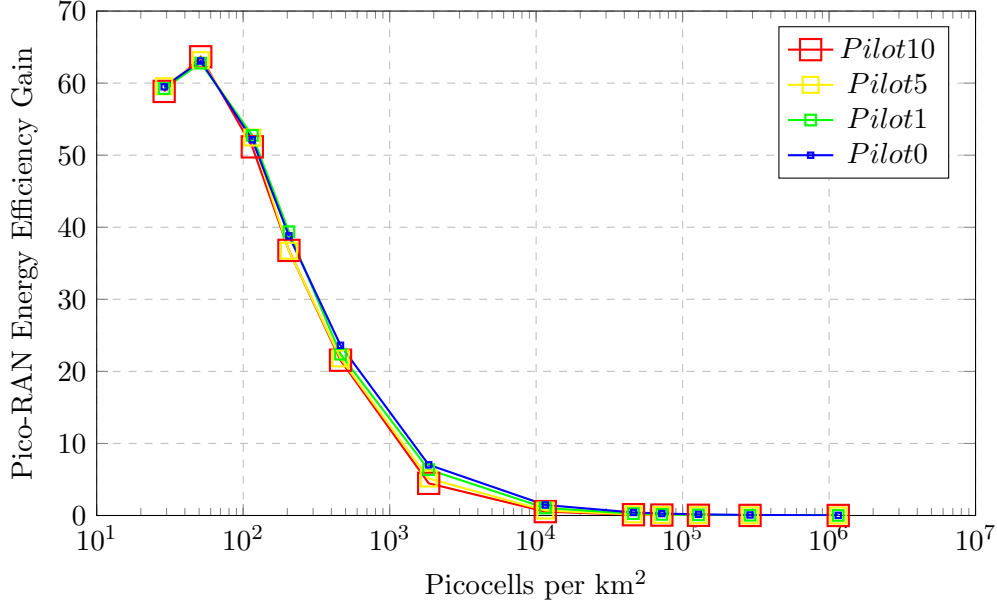


Figure 4.15: Pico-RAN Energy Efficiency Gain against picocell density, comparing different pilot power levels in empty picocells: *Pilot10* has α_c of 10%, *Pilot5* has α_c of 5%, *Pilot1* has α_c of 1%, and *Pilot0* has α_c of 0%

4.5.2 Sleep Mode Depths of Empty Picocells

As discussed previously, a highly densified pico-RAN has a lot of empty picocells for a limited UE density of 300 UEs per square kilometre. According to the current power model, this empty cell broadcast pilot causes interference and consumes similar energy as an active picocell. In the previous sub-section, it is shown that switching off the pilot from empty picocells completely when densifying the RAN constrains the interference, thus improving the capacity. However, this technique does not positively impact the total energy consumption of the heavily overhead-dominated picocells.

To reduce energy consumption and thus improve energy efficiency, sleep mode will be applied to empty picocells in this sub-section. Specifically, sleep mode could put empty cells into a low power consumption mode that reduces the total RAN energy consumption, especially for highly densified RANs. According to the power model, a pico-BS site's major energy-consuming units are the transceiver units, the baseband units, and the backhaul. So they will be turned off one by one in empty picocells for different sleep mode depths.

Table 4.6 lists the different sleep mode depths considered in this work when the major energy-consuming overhead units in empty cells are turned off one by one. Turning units off means their

Sleep Mode Depth, i	OH Components State			Empty Site Power Consumption, $P_b^{SBS,i}(\alpha_c = 0)$ [W]
	Transceiver	Baseband	Backhaul	
<i>Sleep0</i>	on	on	on	$\frac{n_a \times n_c}{\eta_{PS}} \times (\hat{P}_{BB} + \hat{P}_{TRX}) + P_{BH}$
<i>Sleep1</i>	off	on	on	$\frac{n_a \times n_c}{\eta_{PS}} \times \hat{P}_{BB} + P_{BH}$
<i>Sleep2</i>	off	off	on	P_{BH}
<i>Sleep3</i>	off	off	off	0

Table 4.6: Sleep mode depths for empty picocells with α_c of 0%

power consumption becomes 0 W. *Pilot0* is applied in this sub-section where empty cells have no pilot transmission ($\alpha_c = 0$), because it provides the best capacity performance. When sleep mode is off, denoted as *Sleep0*, all the transceiver units, baseband units, and backhaul are on. The empty picosite power consumption is calculated using $P_b^{SBS,Sleep0}(\alpha_c = 0)$ with parameters shown in Table. 3.1. Moreover, *Sleep1* turns the transceiver units off; *Sleep2* turns the baseband units off on top of *Sleep1*, and *Sleep3* turns all the three components off. The corresponding empty picosite power consumption are $P_b^{SBS,Sleep1}(\alpha_c = 0)$, $P_b^{SBS,Sleep2}(\alpha_c = 0)$, and $P_B^{SBS,Sleep3}(\alpha_c = 0)$, respectively, whose expressions are listed in the Table 4.6. From *Sleep0* to *Sleep3*, the sleep mode depth gets deeper, and the empty site power consumption decreases.

Fig. 4.16 shows the Data Volume Gain of pico-RAN with the picocell density as a variable, comparing different sleep mode depths for empty picocells. This figure compares the capacity with the reference macro-RAN using DVG. The DVG profiles for all four sleep mode depths overlap perfectly and increase monotonically with pico-RAN densification. This is because different sleep mode depths limit interference by the same scale using *Pilot0*.

Fig. 4.17 shows the Energy Consumption Gain in the logarithmic scale of pico-RAN with the picocell density as a variable, comparing different sleep mode depths for empty picocells. This figure compares the energy consumption with the reference macro-RAN using ECG. With the current power model and parameters, the power consumption of the radio-head part, transceiver units and baseband units are negligible compared with the backhaul power consumption. Therefore, compared with *Sleep0*, turning off the transceiver units (*Sleep1*) or turning the transceiver and baseband units off together (*Sleep2*) saves negligible energy. Their RAN ECG profiles overlap and decrease against the increasing picocell density. In contrast, *Sleep3* turns the empty picocells completely off, including the backhaul, and saves energy significantly when the densification level is

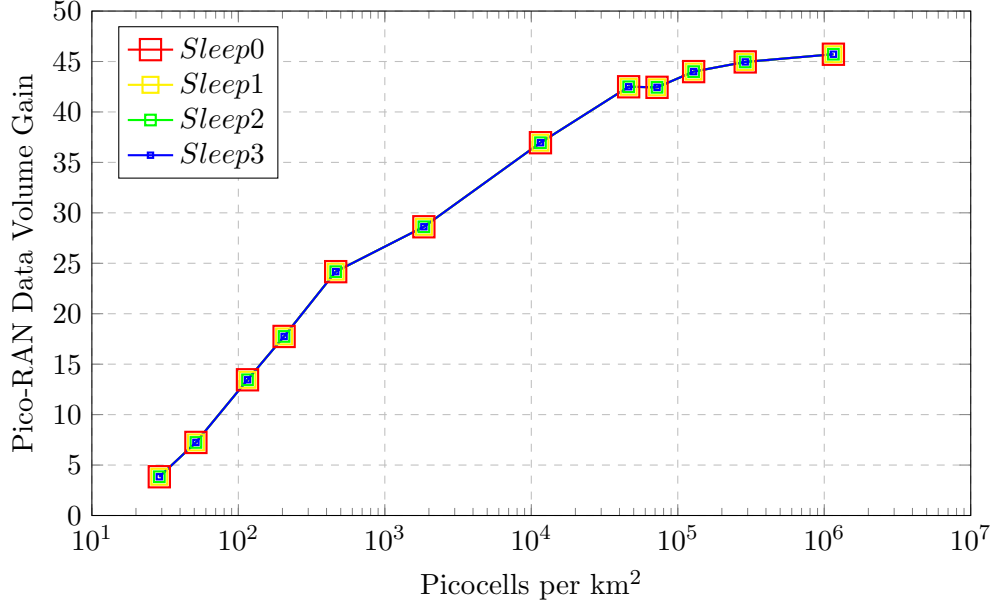


Figure 4.16: Pico-RAN Data Volume Gain against picocell density, comparing different sleep mode depths in empty picocells: *Sleep0* has all three overhead components on, *Sleep1* turns off the the transceiver units, *Sleep2* turns off both the transceiver units and the baseband units, and *Sleep3* turns all the three overhead components off

high using the current power model. Specifically, the ECG decreasing rate becomes negligible at a picocell density of 1847.52 picocells/km² (pico-ISD 25 m), and the ECG saturates at 1.49 compared with the reference macro-RAN. Therefore, sleep mode is an effective solution for reducing RAN energy consumption. Nevertheless, only by turning empty cells in the pico-RAN off completely using sleep mode depth *Sleep3* alongside the pico-RAN densification that the RAN energy consumption stops increasing.

Fig. 4.18 shows the Energy Efficiency Gain of pico-RAN with the picocell density as a variable, comparing different sleep mode depths for empty picocells under the same conditions as Fig. 4.16 and 4.17. This figure compares the energy efficiency with the reference macro-RAN using EEG. The main observations are:

1. For low picocell densities from 28.87 to 51.32 picocells per square kilometre (pico-ISD of 200 m and 150 m), the pico-RAN densification improves the energy efficiency, which is dominated by the increasing capacity. This holds for different sleep mode depths. The DVG profiles overlap due to a few empty cells in the RAN.
2. For picocell densities from 51.32 to 1847.52 picocells per square kilometre (pico-ISD of 150 m

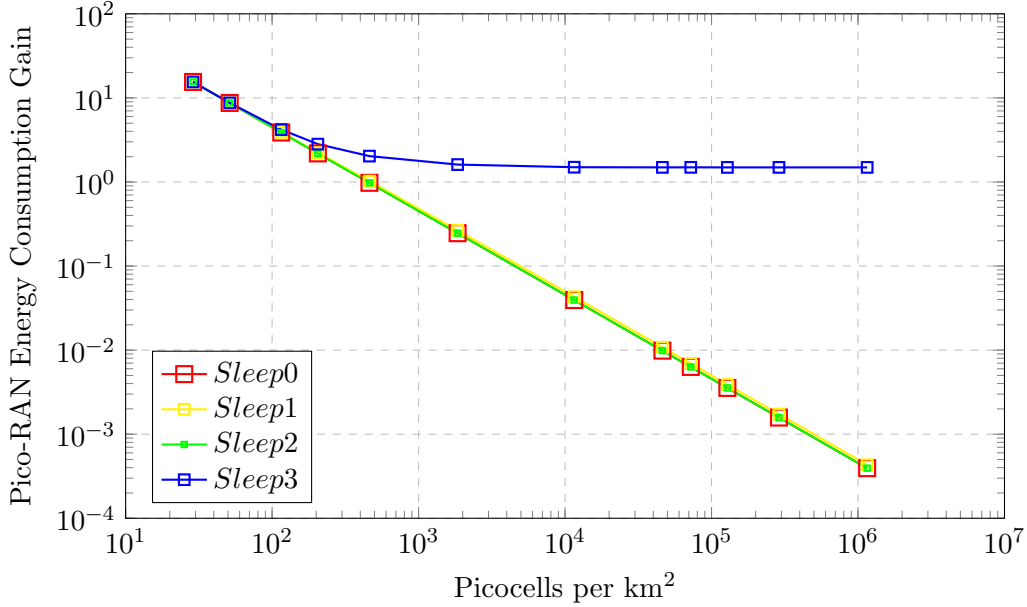


Figure 4.17: Pico-RAN Energy Consumption Gain against picocell density, comparing different sleep mode depths in empty picocells: *Sleep0* has all three overhead components on, *Sleep1* turns off the the transceiver units, *Sleep2* turns off both the transceiver units and the baseband units, and *Sleep3* turns all the three overhead components off

and 25 m), the pico-RAN energy efficiency decreases against the increasing picocell density, which is dominated by the increasing energy consumption for all sleep mode depths. With the number of empty cells increasing, deeper sleep mode depth saves more energy and improves energy consumption further. At 1847.52 picocells per square kilometre, pico-RAN with *Sleep0* has an EEG of 7.03. This EEG increases to 7.60, 9.72, and 46.08 by increasing the sleep mode depths from *Sleep1* to *Sleep3*, respectively.

3. For picocell densities larger than 1847.52 picocells per square kilometre, the pico-RAN densification using *Sleep0*, *Sleep1*, and *Sleep2* continues to degrade the energy efficiency, which is dominated by the increasing energy consumption. However, the energy efficiency using *Sleep3* starts to recover. This increase is due to the continuously growing capacity and the saturated energy consumption.

In summary, the energy efficiency of pico-RAN densification benefits from putting empty cells into sleep mode. Only when the empty picocells are turned off completely does the pico-RAN densification become energy efficient. The energy efficiency improvement comes from increasing capacity and constrained energy consumption.

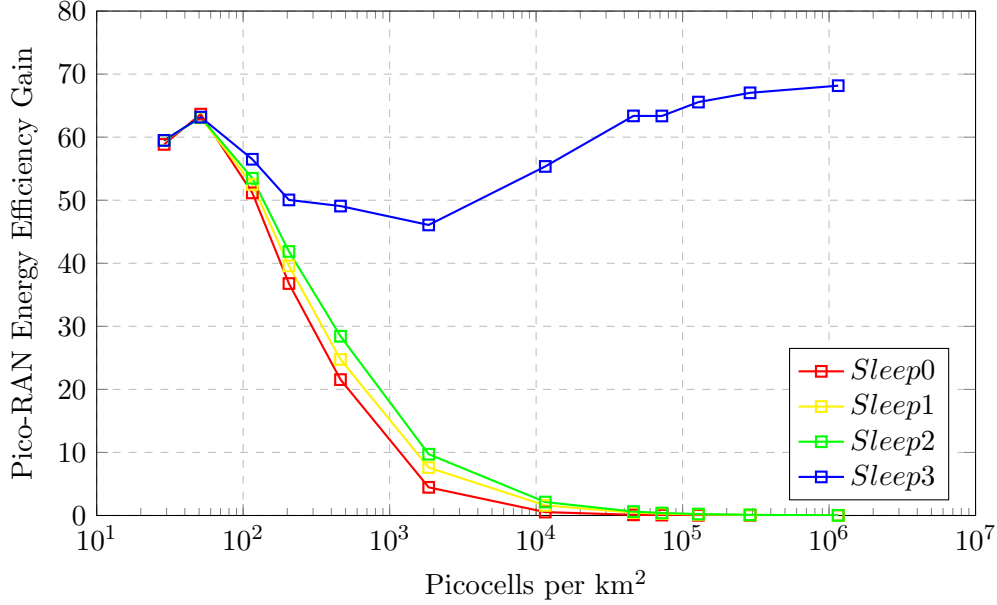


Figure 4.18: Pico-RAN Energy Efficiency Gain against picocell density, comparing different sleep mode depths in empty picocells: *Sleep0* has all three overhead components on, *Sleep1* turns off the the transceiver units, *Sleep2* turns off both the transceiver units and the baseband units, and *Sleep3* turns all the three overhead components off

The ECG and EEG gaps between *Sleep2* and *Sleep3* in Fig. 4.17 and Fig. 4.18, respectively, are caused by the on/off state change of the 10 W backhaul power consumption. To further analyse the impact of backhaul on energy consumption and energy efficiency, the backhaul power consumption will be gradually reduced from 10 W to 0 W in the following to fill the aforementioned performance gaps. The change in backhaul power consumption means a change in fibre backhaul efficiency or partially powering the backhaul with renewable energy. DVG results are not included since the difference in the backhaul power consumption does not affect the capacity performance.

Fig. 4.19 shows the Energy Consumption Gain of pico-RAN densification using picocell density as a variable, comparing the different values of backhaul power consumption, P_{BH} , when the pilot transmission, transceiver units, and baseband units are all off in empty cells. The figure shows that the gradual reductions of P_{BH} save energy accordingly to fill the ECG gap between P_{BH} being 10 W (*Sleep2*) and P_{BH} being 0 W (*Sleep3*). When P_{BH} is less than 0.01 W, the increase in energy consumption diminishes briefly up to 46188.02 picocells/km² (pico-ISD 5 m). However, further densification starts to increase the energy consumption gradually. For high picocell densities larger than 128300.06 picocells/km² (pico-ISD 3 m), most of the picocells being empty results in a

significant amount of energy consumption even if each empty picocell has a power level at 0.0001 W. Only when the empty cells are turned off completely (*Sleep3*), including the backhaul, does the energy consumption stop increasing and ECG saturate against the increasing picocell density.

Fig. 4.20 shows the Energy Efficiency Gain of pico-RAN densification using picocell density as a variable, comparing the different values of backhaul power consumption, P_{BH} , under the same conditions as for Fig. 4.19. When P_{BH} is less than 0.1 W, the RAN EEG recovers briefly from 1847.52 picocells/km² (pico-ISD 25 m). This is dominated by the brief stop of energy consumption increase. Lower P_{BH} improves RAN EEG further and keeps the increasing tendency till higher picocell density. However, when there are more than 128300.06 picocells/km² (pico-ISD 3 m) in the RAN and P_{BH} is non-zero, the continuous energy consumption increase degrades energy efficiency. RAN EEG starts to decrease against the increasing picocell density. Therefore, the energy efficiency of dense pico-RAN is highly energy consumption dominated. Using the current power model, energy efficiency is highly backhaul-dominated. Only when the empty picocells are turned off completely does the ultra-dense pico-RAN energy efficient. The following sub-section will test this conclusion under different traffic intensities.

4.5.3 Traffic Intensities in Pico-RAN Densification

300 UEs/km² represents a medium traffic intensity. This is used in previous results analysis to obtain the general dense small cell RAN performance regarding capacity, energy consumption, and energy efficiency. In this sub-section, the UE density range will be extended to represent low to high traffic intensities. Specifically, the UE densities range is from 100 UEs/km² as a low traffic intensity to 2000 UEs/km². High traffic intensity represents the Internet of Things (IoT) scenario [180]. Empty cells are turned completely off in this sub-section because this leads to the best performance regarding capacity, energy consumption, and energy efficiency.

Before presenting the figures of merit results for pico-RAN densification using different UE densities, Fig. 4.21 shows the number of UEs per active picocell against the picocell density for different UE densities. Pico-RAN densification adds more picocells to the RAN but keeps the UE density fixed. Therefore, the average number of UEs per active picocells decreases to saturation against the increasing picocell density. Higher UE densities activate more picocells, so the saturation happens at higher picocell densities. However, the average number of UE per

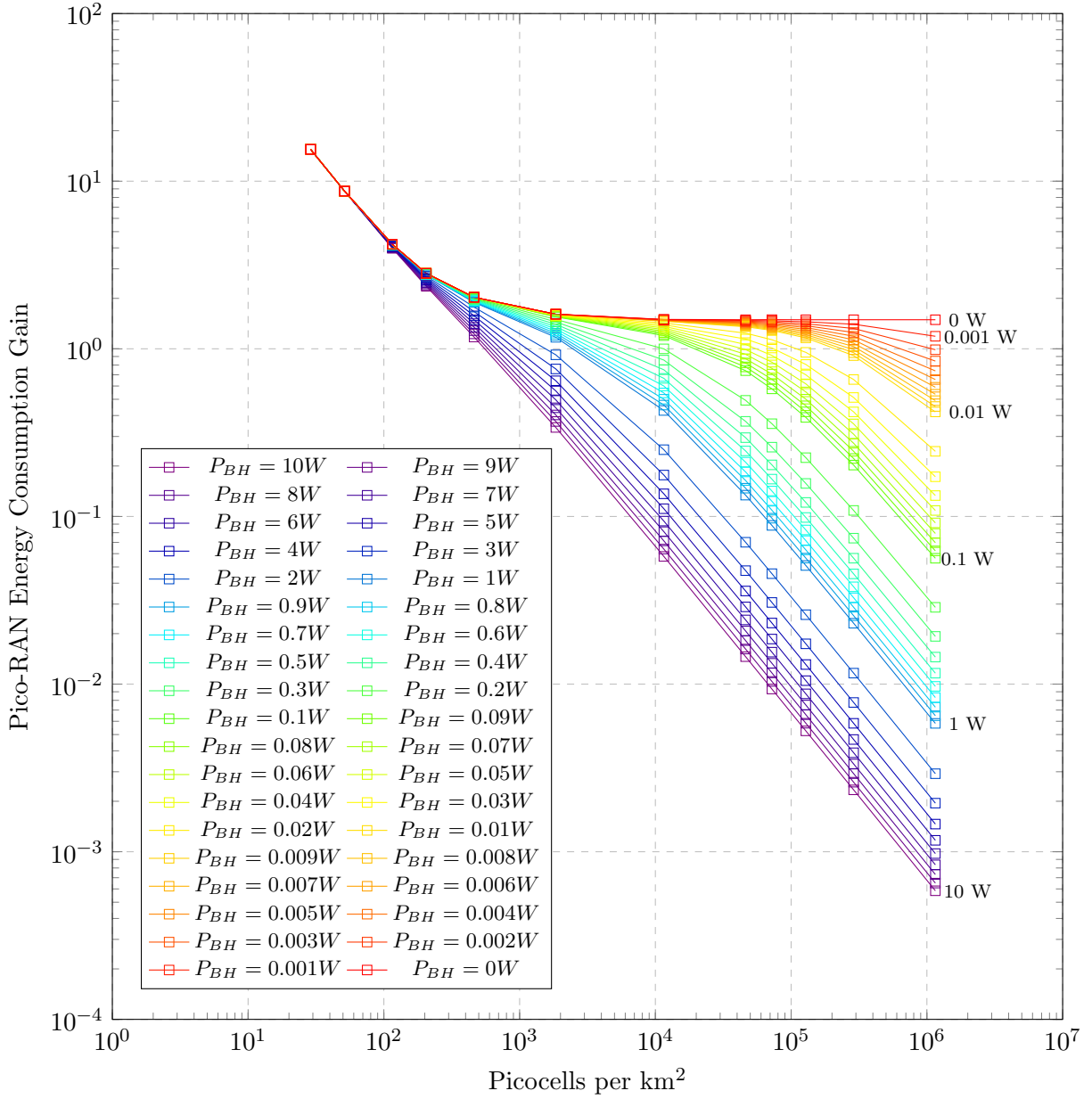


Figure 4.19: Pico-RAN Energy Consumption Gain against picocell density, comparing different backhaul power consumption P_{BH} in empty picocells, which turns off radio-head, transceiver and baseband units

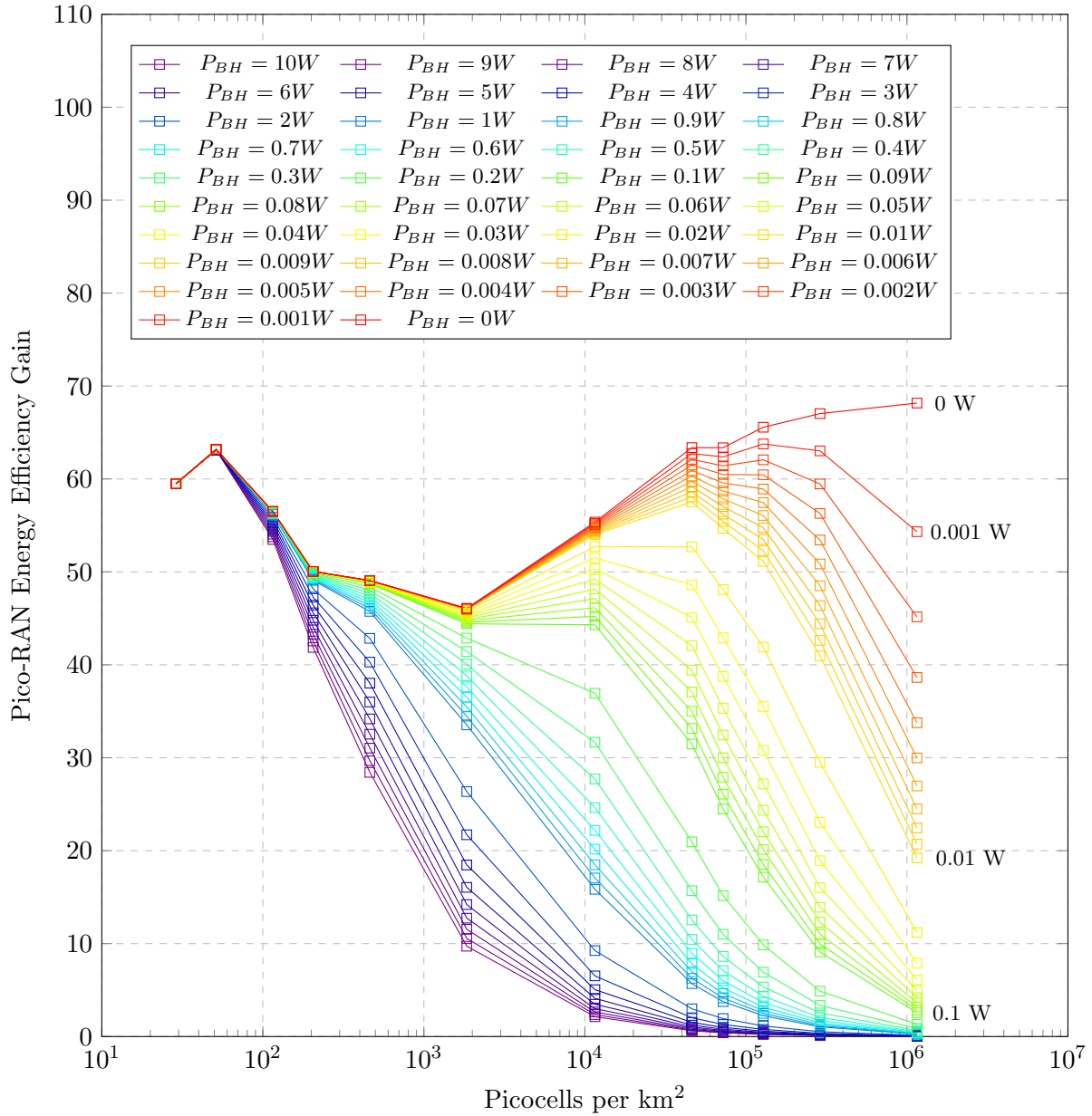


Figure 4.20: Pico-RAN Energy Efficiency Gain against picocell density, comparing different backhaul power consumption P_{BH} in empty picocells, which turns off radio-head, transceiver and base-band units

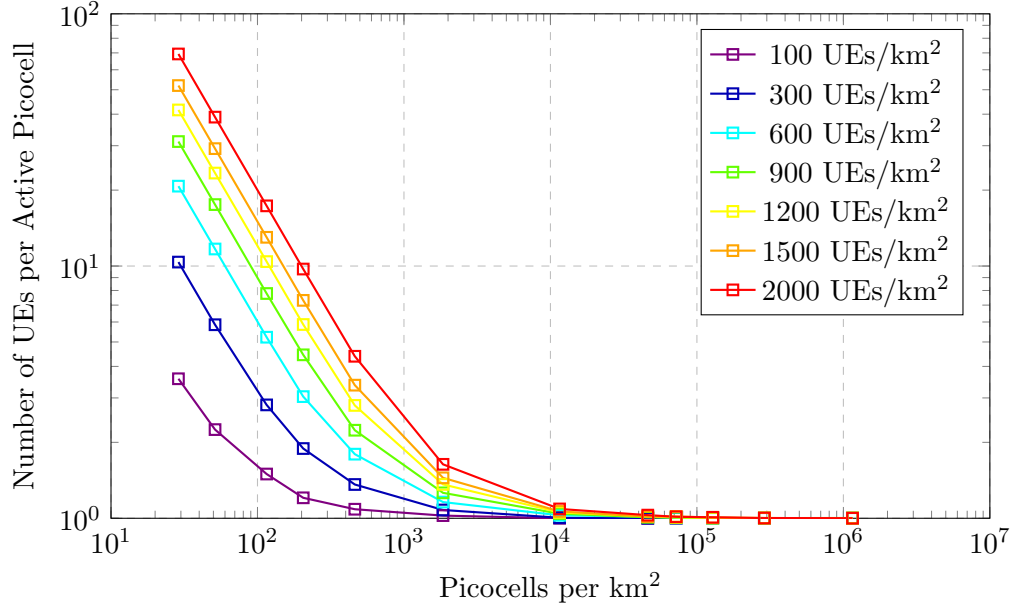


Figure 4.21: Number of UEs per active picocell against picocell density, comparing different UE densities, empty cells are turned off completely

active picocell saturation level is unity for all UE densities. This is a 1-UE-per-active-picocell state where each active cell only serves one UE. Further picocell densification only adds empty picocells, so the pico-RAN remains in the 1-UE-per-active-picocell state. Specifically, only 100 and 300 UEs/km² cases have reached the 1-UE-per-active-picocell state, while 600, 900, 1200, 1500, and 2000 UEs/km² almost reach the 1-UE-per-active-picocell state. This would impact the final condition of the DVG profiles shown in Fig. 4.22, which will be addressed as follows.

Fig. 4.22 shows the pico-RAN Data Volume Gain using the picocell density as a variable, comparing different UE densities. All the empty cells are turned off completely to limit interference. The figure shows that the RAN DVG increases with the increasing UE density. Higher UE density activates more picocells at high picocell densities, and thus more data is transmitted. This leads to higher RAN capacity and DVG. When the pico-RAN enters the 1-UE-per-active-picocell state, the newly added picocells, by further densification, remain off. These picocells do not contribute to interference or data accumulation. Therefore, the RAN capacity and DVG saturate against the increasing picocell density. This is observed for 100 and 300 UEs/km² cases which already reached the 1-UE-per-active-picocell state. The DVG of the 100 UEs/km² case saturates at low picocell density than the 300 UEs/km² case because the former needs less active picocells to serve the traffic.

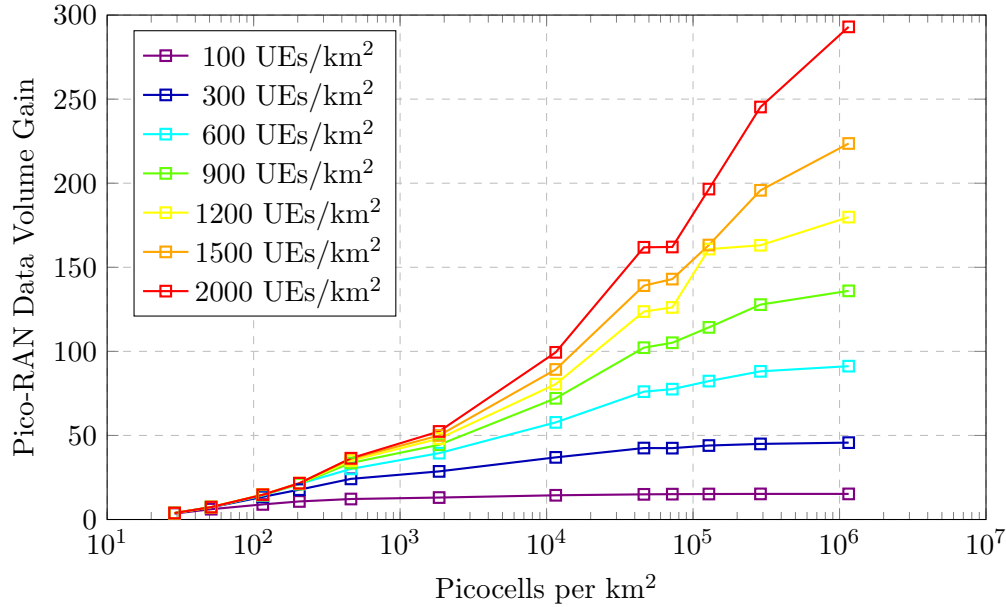


Figure 4.22: Pico-RAN Data Volume Gain against picocell density, comparing different UE densities, empty cells are turned off completely

In contrast, pico-RANs with higher UE densities have not reached the 1-UE-per-active-picocell state yet, so their DVGs still increase with the increasing picocell density with a diminishing manner at 1154700.54 picocells/km² (pico-ISD 1 m). Their DVG profiles are expected to saturate at higher picocell densities with higher saturation levels dependent on UE densities. In summary, with all the empty picocells turned off, pico-RAN densification improves the capacity until a saturation level, regardless of UE densities. The absolute DVG value and corresponding picocell density for the final DVG saturation against densification increase with UE density.

Fig. 4.23 shows the Energy Consumption Gain of pico-RAN densification with picocell density as the variable, comparing different UE densities under the same conditions as in Fig. 4.22. Higher UE densities activate more picocells and increase RAN energy consumption. Therefore, the RAN ECG decreases against the increasing UE density. However, when all the empty cells are turned off to save energy, the total energy consumption saturates after reaching a specific picocell density, and so does the RAN ECG. This is true for all UE densities. Though the pico-RAN with UE densities higher than 300 UEs/km² has yet reached the 1-UE-per-active-picocell state, they are close enough. When the picocell density increases, there is a negligible difference in the total number of active picocells in the RAN. The final ECG saturation levels are proportional to UE densities. Because

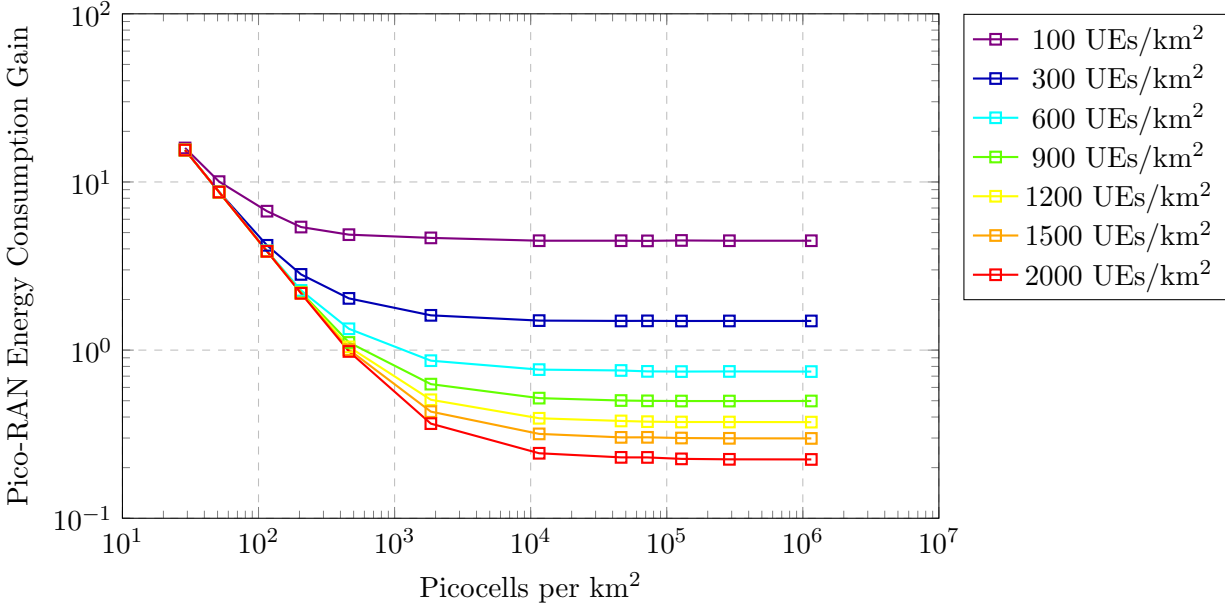


Figure 4.23: Pico-RAN Energy Consumption Gain against picocell density, comparing different UE densities, empty cells are turned off completely

of many active picocells, pico-RAN with higher densification levels and high UE densities might consume more energy than the reference macro-RAN. Specifically, for the 600 UEs/km² case, the RAN ECG reduces below unity at around 1000 picocells/km². Higher UE densities have lower ECG limiting picocell densities, which should be set as densification limits if an energy-saving pico-RAN over the reference macro-RAN is preferred for a specific UE density. In summary, turning empty picocells off completely when densifying the pico-RAN consumes more energy due to adding more BSs. The energy consumption level saturates since newly added picocells do not consume energy. Higher UE densities activate more picocells and have higher energy consumption saturation levels.

Fig. 4.24 shows the Energy Efficiency Gain of pico-RAN densification with picocell density as a variable, comparing different UE densities in the RAN under the same conditions as Fig. 4.22 and 4.23. The dominating role of RAN EEG is DVG briefly till 51.32 picocells/km² (pico-ISD 150 m) and ECG afterwards. Therefore, EEG increases, decreases and then recovers against the increasing picocell density for all UE densities. The decreasing phase is due to increased energy consumption, while the recovery phase is due to capacity improvement and energy consumption constraints. In addition, higher UE densities lead to lower ECG results and thus lower EEG results. However, the saturation tendencies observed in capacity and energy consumption lead to the saturation of energy

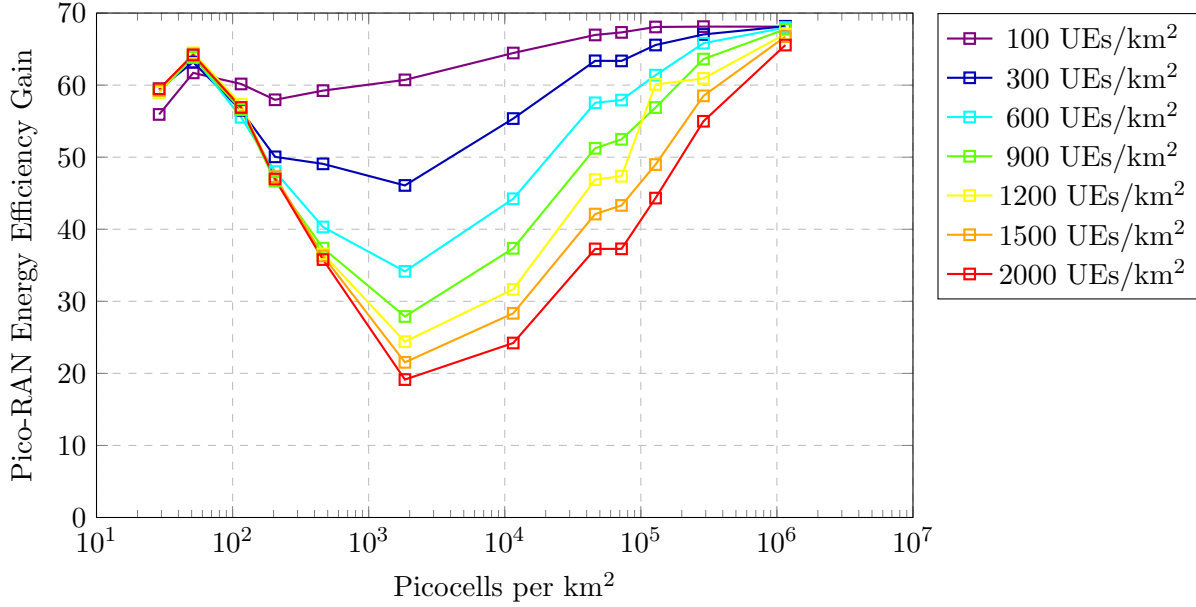


Figure 4.24: Pico-RAN Energy Efficiency Gain against picocell density, comparing different UE densities, empty cells are turned off completely

efficiency. The differences in capacity and energy consumption saturation levels cancel each other and result in a similar energy efficiency level at 67 when picocell density is 1154700.54 picocells/km² (pico-ISD 1 m). In summary, dense pico-RANs with empty picocells consuming nothing are always more energy efficient than the reference macro-RAN, regardless of UE densities. This is because of improving capacity and constrained energy consumption. Nevertheless, some pico-RANs with high traffic intensities trade capacity for energy consumption to improve energy efficiency. These pico-RANs should have bounded densification if more energy consumption is not wanted. To continue to explore the energy efficiency improvement, the scheduler of the pico-RAN densification is analysed next for capacity enhancement.

4.5.4 Scheduling Protocol in Pico-RAN Densification

Up to this point, the benchmark Round Robin (RR) scheduler has been used for resource allocation. This scheduling method is simple: every UE in the same cell is treated equally and receives the same amount of resources for every TTI. However, RR trades off computational simplicity for RAN capacity. Specifically, UEs on bad channels with significant channel loss would not benefit much from the fair share of the resource. On the other hand, UEs on good channels with low channel

loss would have performance constrained by insufficient resource allocation. In contrast, Maximum SINR (MSINR) and Proportional Fair (PF) could exploit UE diversity in cells to improve the RAN capacity with different trade-offs. The UE diversity is the total number of UEs in an active picocell that the BS can choose regarding RB allocations. MSINR trades off the fairness between UEs for capacity, while PF trades off the computation complexity shown in Eq. (4.19) and (4.20). In this sub-section, the figures of merit will be applied to analyse the performance of these three scheduling protocols, along with the extra fairness comparison using Jain’s fairness index based on Eq. (4.21) and (4.22). Empty cells are turned off completely for best performance regarding capacity, energy consumption, and energy efficiency. UE density is 300 UEs/km² for performance generalisation regarding traffic intensity.

Fig. 4.25 shows the Data Volume Gain of pico-RAN densification using picocells density as the variable, comparing different schedulers. As mentioned, the constant for the time window t_w in Eq. (4.20) is chosen as 50 for PF to perform more closely to MSINR, which is shown in the figure. For picocell density smaller than 11547.01 picocells² (pico-ISD 10 m), MSINR and PF result in higher DVG than the benchmark RR because of UE diversity exploitation. Intuitively, the UE diversity is expected to vanish when reaching 300 picocells/km² for a uniform 300 UEs/km² UE density, leading to overlapping DVGs for different schedulers afterwards. However, as shown in Fig. 4.21, this is not the case. A much higher picocell density (in this case, 11547.01 picocells²) is required for the RAN to reach the 1-UE-per-active-picocell state and completely lose the UE diversity. At 28.87 picocells/km² (pico-ISD 200 m), changing the scheduler from RR to MSINR and PF improves the DVG from 3.84 to 6.74 and 6.64, respectively, without any hardware or RAN infrastructure change. In contrast, within the range from 51.32 to 11547.01 picocells/km² (pico-ISD of 150 and 10 m), PF performs slightly better than MSINR. MSINR always chooses the UEs on the best channel to allocate RBs, leading to highly biased resource allocation and individual UE throughput. The RAN throughput, which is the summation of all UE throughput, thus suffers. At the same time, PF preserves resource allocation fairness to some extent, resulting in less biased UE throughput and higher RAN throughput than MSINR. Further densification enables UEs to associate with different picocells. There is no UE diversity in active cells. The DVG profiles for different scheduling protocols thus overlap. Therefore, for highly densified pico-RAN with no UE diversity, the choice of the simple RR is sufficient without any performance degradation.

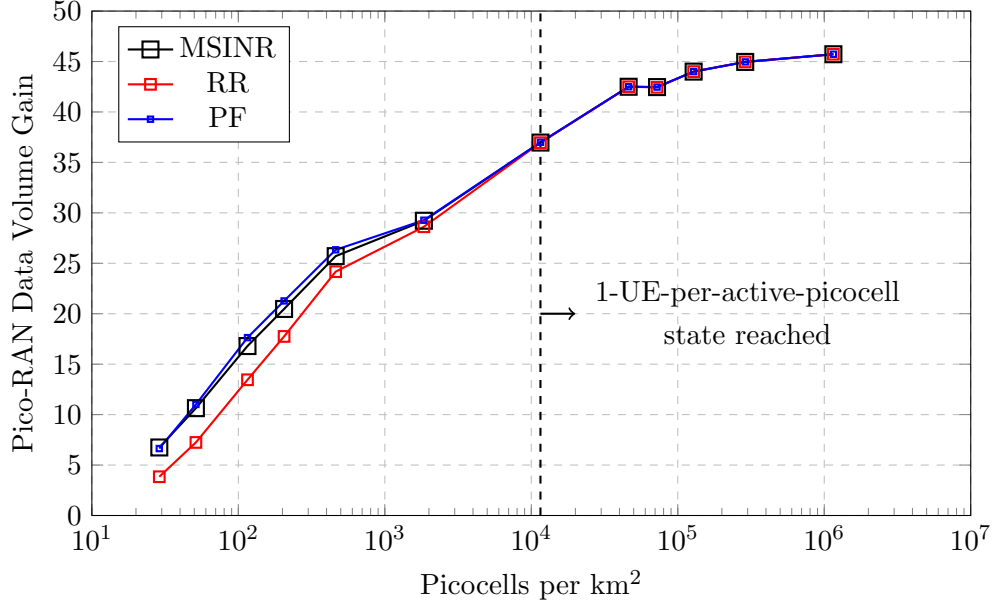


Figure 4.25: Pico-RAN Data Volume Gain against picocell density, comparing different schedulers, empty cells are turned off completely, 300 UEs/km²

Fig. 4.26 shows the Energy Consumption Gain of the pico-RAN densification with the picocell density as the variable, comparing different schedulers under the same conditions as Fig. 4.25. Since the scheduler and resource allocation metrics do not change the number of active picocells in the RAN, the RAN energy consumption does not change. So the ECG profiles for all scheduling protocols overlap and increase with the increasing picocell density.

Fig. 4.27 shows the Energy Efficiency Gain of the pico-RAN densification with the picocell density as the variable, comparing different schedulers. EEG is the product of DVG and ECG. Compared with the benchmark RR, the adoption of MSINR and PF improves the RAN EEG to 11547.01 picocells/km² (pico-ISD 10 m) due to improved DVG. Specifically, at 28.87 picocells/km² (pico-ISD 200 m), MSINR and PF could achieve an extra EEG of 44.91 and 43.26, respectively, compared with the 59.49 achieved by RR. With the decrease in UE diversity, further densification using MSINR and PF has diminishing energy efficiency improvement over RR. PF has slightly higher EEG than MSINR since the former has slightly higher DVG than the latter. Eventually, the schedulers have no impact on energy efficiency when capacity and energy consumption overlap.

To complete the evaluation of scheduler performance, Fig. 4.28 shows the Jain's fairness index of resource allocation J_{RB} with the picocell density as the variable, comparing schedulers. J_{RB}

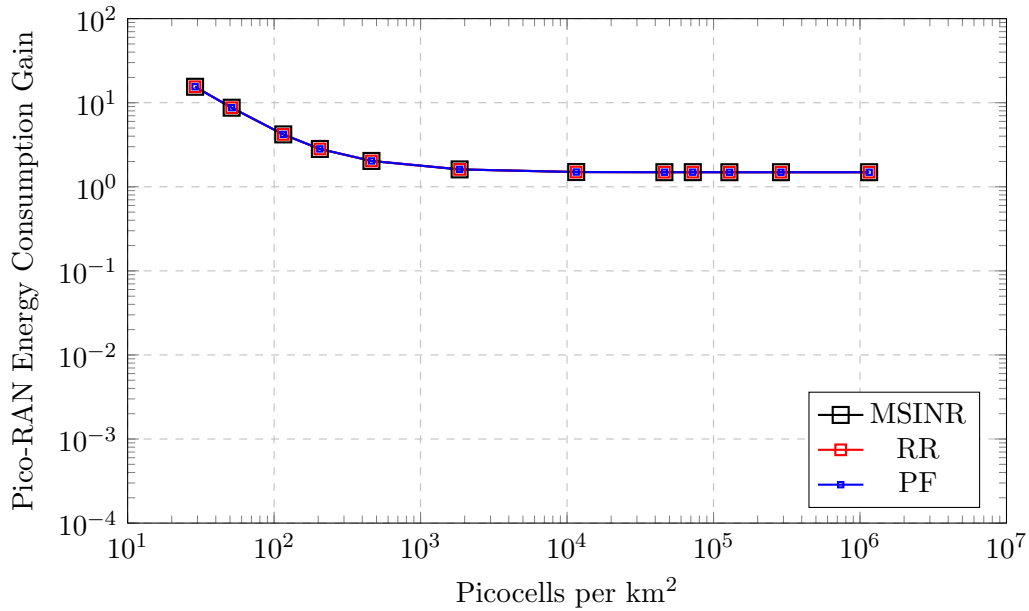


Figure 4.26: Pico-RAN Energy Consumption Gain against picocell density, comparing different schedulers, empty cells are turned off completely, 300 UEs/km²

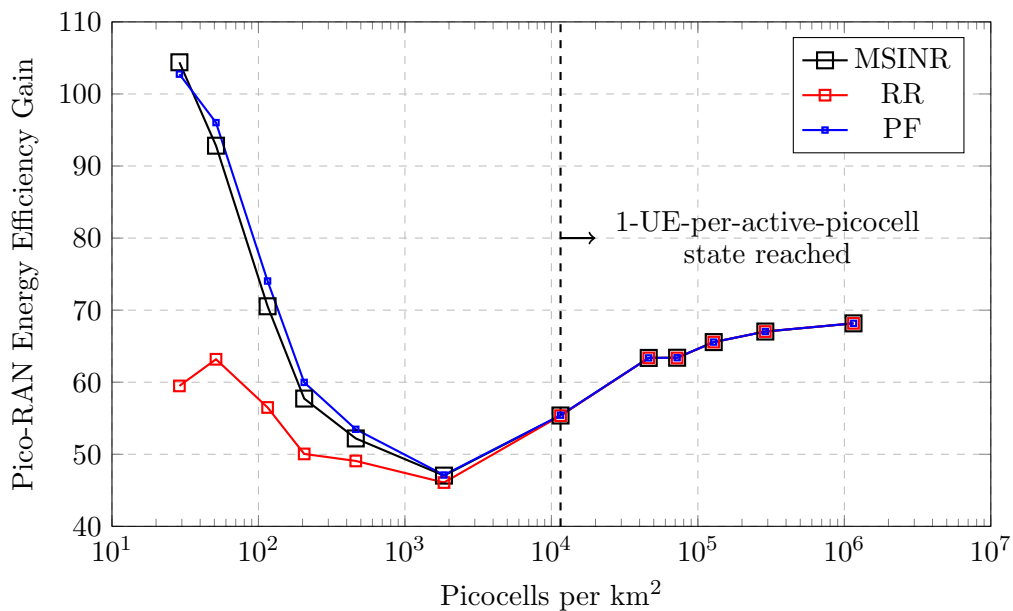


Figure 4.27: Pico-RAN Energy Efficiency Gain against picocell density, comparing different schedulers, empty cells are turned off completely, 300 UEs/km²

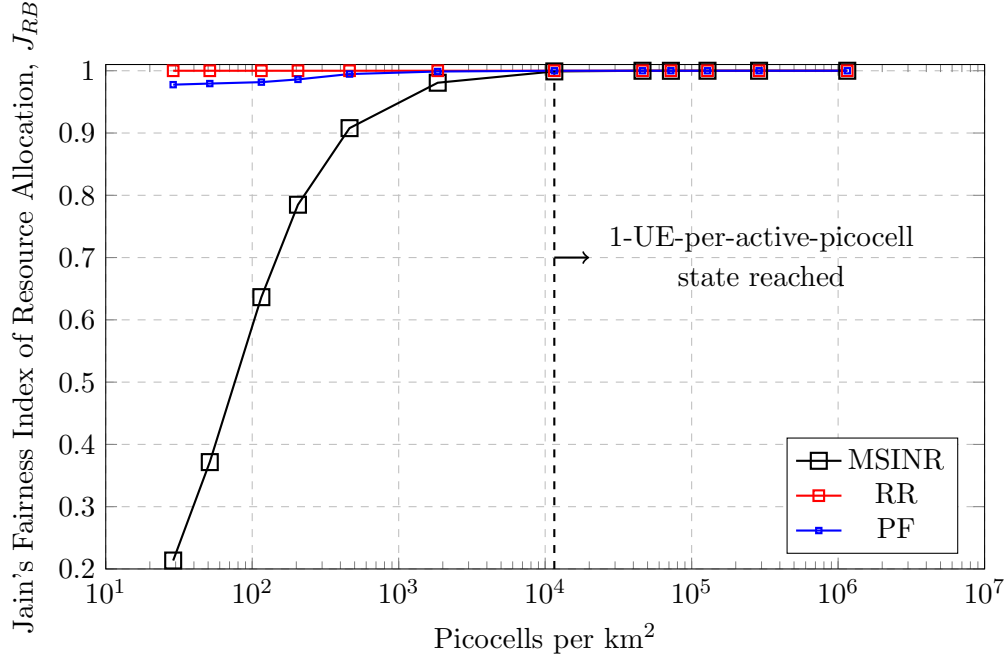


Figure 4.28: Jain’s fairness index of resource allocation, J_{RB} , against picocell density, comparing different schedulers, empty cells are turned off completely, 300 UEs/km²

uses the total number of RB each UE obtained as the input to Jain’s fairness index formula. By definition, the more diverse the input set, the lower the Jain’s fairness index. Specifically, the figure confirms that MSINR is a highly biased scheduler with the lowest J_{RB} value. With densification, the UE diversity decreases, and the bias mitigates, J_{RB} of MSINR thus increases. In contrast, all UEs could acquire the same amount of RB allocation regardless of channel conditions when RR is used. Therefore the J_{RB} of RR is flat of value one and independent of pico-RAN densification. Moreover, J_{RB} of PF is better than MSINR since the former also considers previous UE throughput but slightly worse than RR by considering channel conditions. Again, the difference in J_{RB} for different schedulers reduces with pico-RAN densification and completely disappears when there is no UE diversity after 11547.01 picocells/km² (pico-ISD 10 m).

Fig. 4.29 shows the Jain’s fairness index of achieved UE throughput, J_S , with the picocell density as the variable, comparing different schedulers. J_S uses UE average throughput as the input to Jain’s fairness index formula. Specifically,

1. J_S of MSINR is similar to J_{RB} , for the bias in RB allocation is directly translated to the achieved throughput. Specifically, UEs on good channels have higher SINR and more RB

allocation. Thus they achieve higher throughput. While UEs on bad channels have worse SINR and less RB allocation, thus they achieve lower throughput. The significant variation in RB allocations leads to variation in throughput. Similarly, this variation reduces with the UE diversity reduction caused by the pico-RAN densification. At 28.87 picocells/km² (pico-ISD 200 m), the J_S of MSINR is only 0.23.

2. The perfect resource allocation fairness of RR, on the other hand, is not translated directly to the UE throughput fairness. UEs scheduled by RR obtain the same amount of RBs. But they are on different channel conditions and thus have different SINR values. Therefore, the achieved average throughput varies and reduces J_S . However, this variation in individual throughput reduces with the decreasing UE diversity. At 28.87/km² (pico-ISD 200 m), the J_S of RR is 0.66.
3. PF has the best UE throughput fairness since the metric considers both the per RB throughput and the previously achieved throughput. The variation in UE throughput is thus the smallest among the three considered schedulers. At 28.87 picocells/km² (pico-ISD 200 m), the J_S of PF is 0.77.

Similar to J_{RB} , the difference between J_S of different scheduler diminishes from 11547.01/km² (pico-ISD 10 m).

In summary, changing the scheduler from RR to MSINR or PF could only benefit the RAN capacity and energy efficiency to some extent. This improvement is brought by user diversity at the expense of either fairness degradation (MSINR) or computation complexity increase (PF). However, for highly densified pico-RAN where UE diversity no longer exists, RR is the preferred scheduler for its simplicity without any performance degradation.

4.6 Case Study: Pico-RAN densification in the Internet of Things

5G IoT networks need to carry far more data than their 4G counterparts [3], [181]. Among all the other technologies, small cell densification could still be an effective solution for both capacity boost [10], [16] and energy efficiency improvement. However, densification alone only improves EE up to a point, beyond which excessive interference limits the RAN throughput, whereas deploying

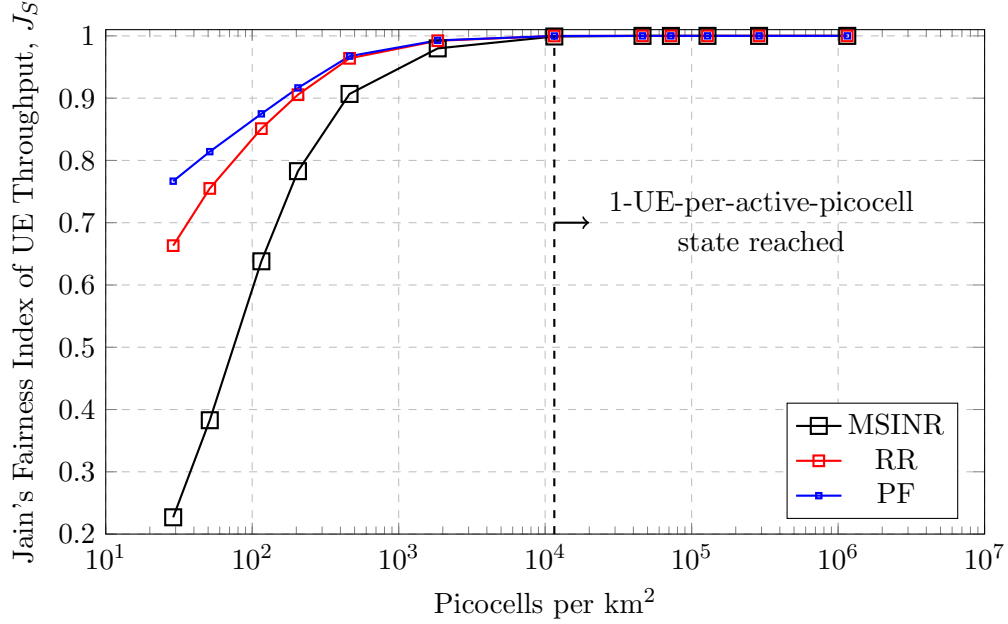


Figure 4.29: Jain’s fairness index of UE throughput, J_S , against picocell density, comparing different schedulers, empty cells are turned off completely, 300 UEs/km²

more always on BSs progressively increases the RAN energy consumption [10], [182]. To reduce the interference and energy consumption and thus improve the energy efficiency further, sleep mode is also adopted in addition to the RAN densification [24].

In IoT networks, the location of BSs is far more variable than conventional cellular mobile networks [180], [183]. For example, in Industry 4.0 use cases, IoT sensors and actuators distribution across robotic and machining fabric or plants frequently occurs in a three-dimensional manufacturing space. In particular, the heights of BSs may vary considerably [184]. The same is true for IoT devices or UEs, which are often deployed in large numbers throughout a given geographic volume [185]. For these reasons, this section uses a 3D HPPP model of the IoT network to contribute a new evaluation of the volume spectral efficiency (VSE) and EE of IoT ultra-dense RANs [32]. Note that the regular hexagon BS distribution, where all adjacent BSs are some fixed ISD away from each other so that the interference is easier to constrain, models an ideal RAN layout and provides an upper bound of the RAN performance. In contrast, the HPPP distribution allows BSs to be placed more randomly with various ISD between adjacent BSs, capturing more dynamics but might end up in extreme scenarios where BSs might be co-located. So the HPPP model provides the lower bound of the RAN performance.

4.6.1 IoT System Model and Evaluation Metric

This section still considers the DL of LTE homogeneous RAN comprising identical pico-BSs to support an IoT network. Unlike the regular hexagonal distribution used before, the pico-BSs in IoT RAN are distributed according to a 3D HPPP model with a density of λ_{BS} BSs per cubic kilometre. The pico-BS set is denoted as $\mathcal{B} = \{1, 2, \dots, b, \dots, B\}$, where each pico-BS is assumed to have a single isotropic antenna. So one BS per picocell, and the BS density is the same as picocell density here. A typical UE is placed at the centre of the observation space, which is also equipped with a single isotropic antenna. In addition, virtual UEs (VUEs) are distributed following another independent 3D HPPP model with VUE density λ_{VUE} UEs per cubic kilometre. VUEs realises BS activation. That is, where a VUE falls within the radio coverage of a BS, the pico-BS is regarded as being activated or turned on.

The received power of the typical UE, the channel model, and the throughput of the typical UE are the same as those specified by Eq. (4.1) to (4.13) in Section 4.2. However, the simulation results are unsuitable to be evaluated using the framework presented in Chapter 3. For the figures of merit from Chapter 3, BSs and UEs are assumed to be placed in a 2D plane with an additional fixed height difference, so the metrics are interpreted using area parameters. In contrast, in this section, BSs and UEs are placed in 3D space with various heights, and the metrics are expressed using volume parameters instead. Specifically, the capacity performance is evaluated using the RAN Volume Spectral Efficiency (VSE) with units of bit/s/Hz/m³; energy consumption is calculated using the same power model presented in Section 3.3 with slightly adjusted parameter values, and the energy efficiency performance is measured using the RAN Energy Efficiency with units of bit/J [32].

The RAN VSE is defined as:

$$VSE_{RAN} = \frac{S_{RAN}}{B \times V_{RAN}} \quad (4.23)$$

where S_{RAN} is the RAN throughput determined by the product of the total number of UEs N_{UE} (i.e. the number of VUEs plus the 1 typical-UE) and the throughput of the typical-UE in (4.12) with the allocation indicator being 1 for all the RBs:

$$S_{RAN} = N_{UE} \times S_{UE} \quad (4.24)$$

V_{RAN} is the RAN volume in units of cubic kilometre calculated as the product of the chosen cuboid space's length, width, and height. The mapping of the typical-UE throughput to the RAN throughput is based on the assumption that the UE occupies all of the BS resources, which provides an upper bound on S_{RAN} . For highly densified RAN scenarios, where the number of cells is significantly greater than the number of UEs, the 1-UE-per-active-cell assumption becomes accurate.

The RAN EE is defined as:

$$EE_{RAN} = \frac{M_{RAN}}{E_{RAN}} \quad (4.25)$$

based on the definition of EE in [44], where M_{RAN} is the total amount of data transmitted in the RAN with units of bit and is determined by the product of the total number of UEs and the amount of data sent to the typical-UE as given by:

$$\begin{aligned} M_{RAN} &= N_{UE} \times \sum_{t=1}^T M_{UE,t} \\ &= N_{UE} \times \sum_{t=1}^T \left(12 \times 14 \times \sum_{n=1}^{n_{RB}} \log_2(1 + \gamma_{b_0,n}) \right). \end{aligned} \quad (4.26)$$

The total RAN energy consumption E_{RAN} during a certain (simulation) time T is given by:

$$E_{RAN} = T \times P_{RAN} = T \times \sum_{b \in \mathcal{B}} P_b(\alpha_b) \quad (4.27)$$

where P_b is power consumption of a pico-BS site given in Eq. (3.24), α_b is the normalised load activity factor of the BS b , whose value is unity if the cell is active and 10% if the cell is empty unless stated otherwise. Comparing Eq. (4.12) with the allocation indicator being 1 for all the RBs, (4.24), and (4.26), M_{RAN} may be calculated as the product of the RAN throughput S_{RAN} and the total simulation time T . If both the numerator and denominator in (4.25) are divided by T , the RAN EE expression reduces to:

$$EE_{RAN} = \frac{S_{RAN}}{P_{RAN}}. \quad (4.28)$$

Like the RAN VSE metric, mapping the M_{UE} of the typical UE to M_{RAN} provides an upper bound

Components	Radio-head	Overhead excl. Backhaul	Backhaul
Percentage(%)	0.04	0.47	0.49

Table 4.7: Percentage power of an active picocell in IoT RAN

on the RAN throughput, which becomes accurate at high cell densities. Again, the UE density comprises the typical UE and VUEs.

4.6.2 Simulation Results for Different UE Distributions

This sub-section presents RAN VSE and RAN EE results under IoT RAN densification based on the 3D HPPP model [32]. BSs are uniformly randomly scattered in a $100m \times 100m \times 30m$ cuboid space whose volume is 0.00015 km^3 . The number of BSs in the cuboid space ranges from 2 to 1000, equivalent to $13000 \leq \lambda_{BS} \leq 6666667$ BSs per cubic kilometre. A total of 100 active UEs are placed in the same space comprising the typical UE placed at the cuboid centre and 99 virtual UEs. VUEs could be randomly scattered in the cuboid space with an independent 3D HPPP distribution with densities of 330000 virtual UEs per cubic kilometre for different total UE counts. In contrast, VUEs could be scattered in clusters. Specifically, one-third of these VUEs are randomly uniformly scattered in the cuboid space. At the same time, the remaining VUEs are randomly uniformly scattered in five spherical clusters with a 1.5 m radius (a typical room size). The height of each BS varies between 0 m to 30 m, either above or below the location of the typical UE by up to 15 m when 3D HPPP modelling is used. Compared with the conventional 2D model where BS heights are both fixed and equal, this height variation can capture more realistic BS spacial distributions in, for example, manufacturing, enterprise or urban hotspots. This approach also holds for the heights of the virtual UEs. For the pico-BS case, other system model parameters are listed in Table 4.3. The picocells in 3D IoT RAN fix their transmission power to 0.13 W, or 21.06 dBm, independent of the BS densification. Moreover, the power consumption of the backhaul for picocells in IoT RAN is assumed to be 5 W, while the remaining power model parameters are the same as listed in Table 3.1 for the pico-BS case. Table 4.7 lists the percentage power consumption of the traffic-independent overhead and traffic-dependent radio-head components in an active picocell in IoT RAN. The table shows that the cell power consumption is heavily overhead-dominated, and backhaul consumes the most power.

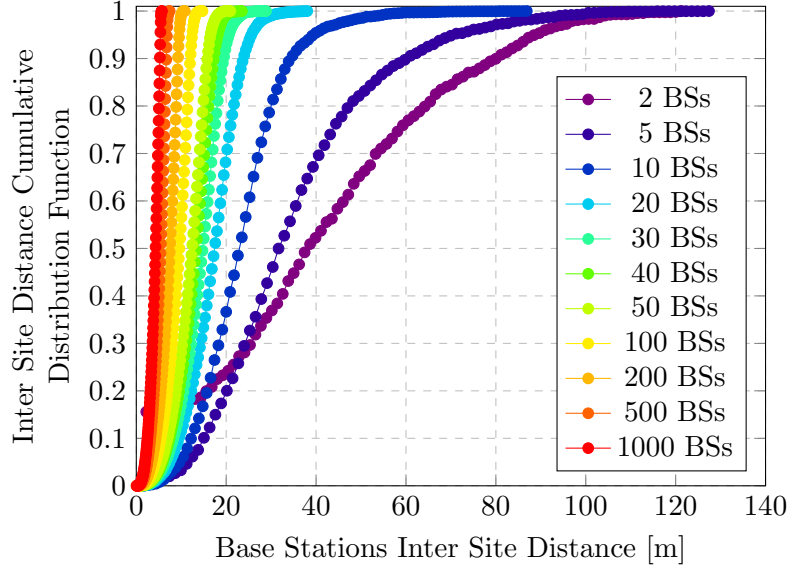


Figure 4.30: Cumulative distribution function versus ISD for various BS counts in IoT RAN

Fig. 4.30 plots the CDF of BS ISD with the number of BSs as a parameter. Densification adds more picocells into the same space, reducing the ISDs and the BS-UE separation. The results show that by increasing the number of BSs from 2 to 100 to 1000, the average ISD reduces from 38.66 m to 9.60 m to 4.29 m, respectively. For this ISD range, the BS-UE separations are smaller. Hence, the signal and interference power at the typical UE from all transmitting BSs are high. Thus the typical UE is interference limited with interference dominating the capacity performance. Note that when there are only 2 BSs in the RAN, the probability of ISD being close to zero is very low. Hence there is a big jump in the CDF profile.

Fig. 4.31 graphs the IoT RAN Volume Spectral Efficiency versus picocell density with both sleep mode status and UE distribution as varying parameters. There are 100 UEs in the RAN. The main observations are:

1. When sleep mode is off (*Pilot10*), the typical UE only briefly experiences the benefit of getting closer to its serving picocell, which increases the UE throughput and RAN VSE; then suffers from the high interference and degrades RAN VSE when picocell density continues to grow. This holds for both UE distributions, with the performance turning point being around 13653 picocells/km³ (4 BSs in the RAN). The RAN VSE decreases quickly at small picocell densities up to 65540 picocells/km³ (20 BSs in the RAN) when the distance between UEs

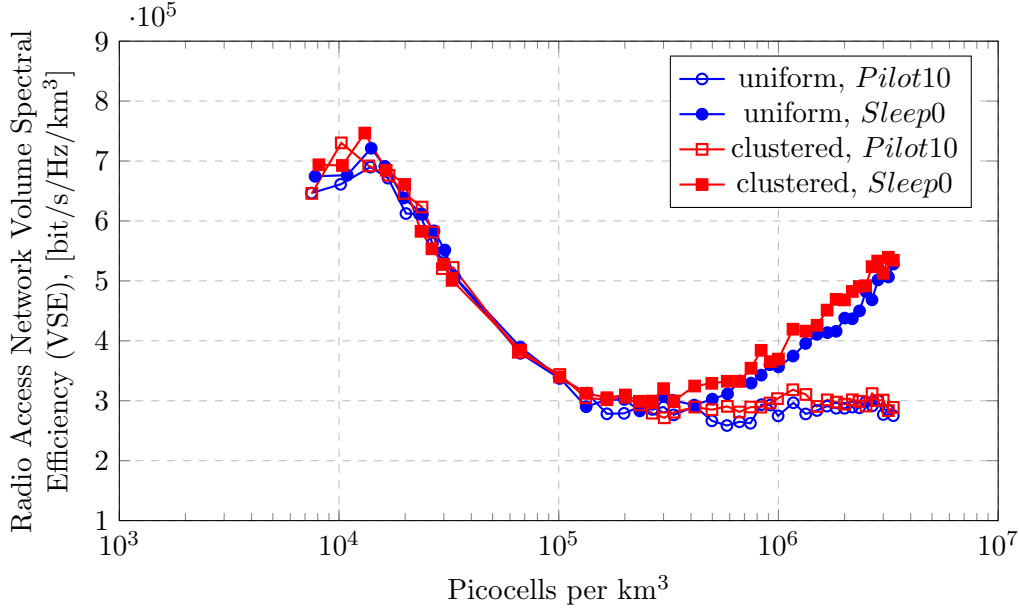


Figure 4.31: RAN Volume Spectral Efficiency (VSE) versus picocell density for 100 UEs with different distributions, and sleep mode off (*Pilot10*), where empty cells have α_c of 10%, and sleep mode on (*Sleep0*), where empty cells have α_c of 0

and BSs reduces quickly, which is reflected in Fig. 4.30. Further BS densification slows down the UE-BS separate decreasing rate. Thus the decrease in RAN VSE also slows down.

2. When sleep mode is on, *Sleep0* turns off the transmission from empty cells that constrain the interference, which is more effective for high BS densities. Therefore, the RAN VSE increases at 233000 and 335653 picocells/km³ (70 and 100 BSs in the RAN) for uniform and clustered UE distributions, respectively.
3. The uniform UE distribution achieves slightly lower RAN VSE than the clustered distribution, with and without the sleep mode. This is because UEs in clusters activate fewer BSs than the uniform UEs and thus have lower interference to compromise the throughput of the typical UE.

Fig. 4.32 graphs the IoT RAN power consumption versus picocell density with both sleep mode status and UE distribution as varying parameters for RAN UE count being 100. *Pilot10* represents the case without any sleep mode such that empty cells have a pilot transmission that is 10% of the peak transmission power level and all the overhead components (baseband, transceiver, and backhaul) on. In contrast, *Sleep0*, *Sleep2*, and *Sleep3*, defined in Table 4.6, represent different

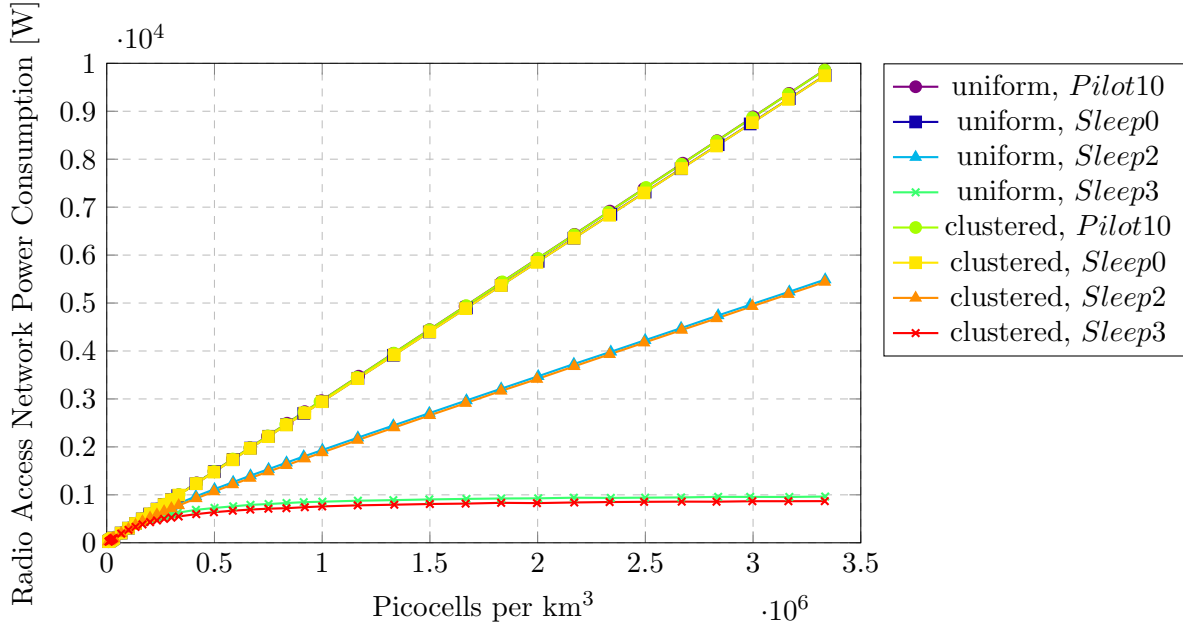


Figure 4.32: RAN power consumption versus picocell density for 100 UEs with different UE distributions, and different empty cell status: *Pilot10* for sleep mode off, *Sleep0* for sleep mode on and OH on, *Sleep2* for sleep mode on and backhaul on, *Sleep3* for sleep mode on and OH off

sleep mode depths where empty picocells turn off the transmission and turn off some or all overhead components. Specifically, *Sleep0* keeps all the overhead components in empty picocells on, *Sleep2* keeps only backhaul in empty picocells on, and *Sleep3* turns all the overhead components, including backhaul, in empty picocells off. The figure shows that the RAN power consumption increases with or without sleep mode with the increasing BS density for both UE distributions. Changing the status of empty picocells from *Pilot10* to *Sleep0*, where only transmission is off, reduces the RAN power consumption negligibly for both UE distributions since the power consumption of the picocell is heavily overhead dominated. In contrast, when empty picocells enter status *Sleep2* and only backhaul is on, the RAN power consumption is nearly half for both UE distributions. This energy reduction scale is determined by the percentage power consumption of the backhaul within a picocell. Furthermore, turning backhaul off and entering empty cells into *Sleep3* where empty cells are turned off completely reduces RAN power consumption. It only increases slightly after reaching 1000000 picocells/km³ (300 BSs in the RAN) for both UE distributions. In addition, when UEs are distributed in clusters that potentially activate fewer BSs, the RAN power consumption is slightly lower than the uniform distributed case.

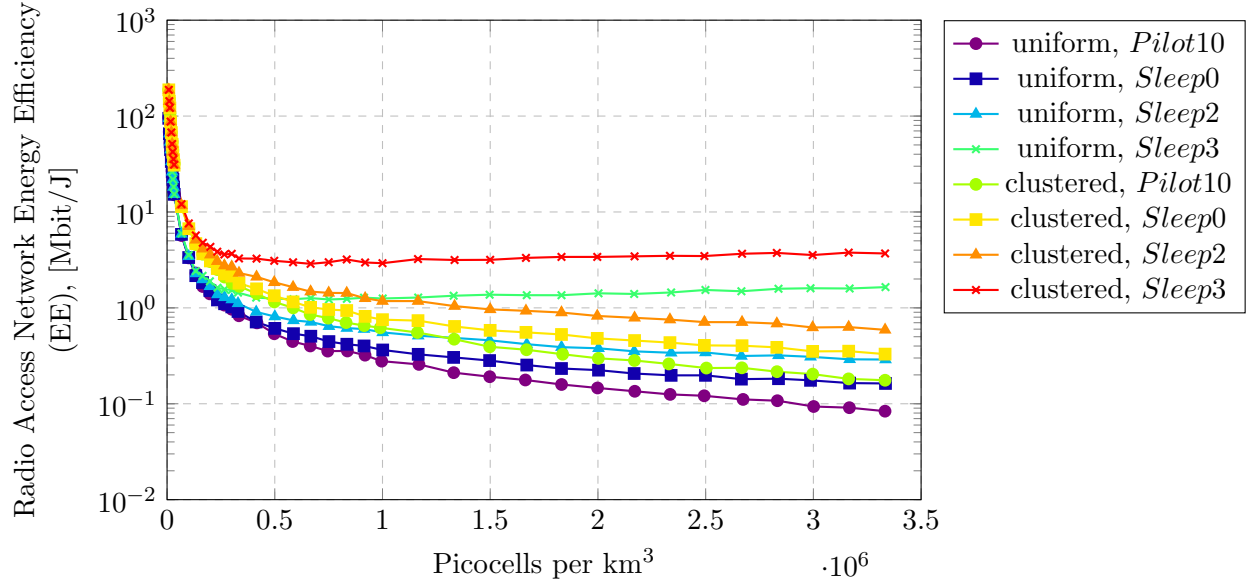


Figure 4.33: RAN Energy Efficiency (EE) versus picocell density for 100 UEs with different UE distributions, and different empty cell status: *Pilot10* for sleep mode off, *Sleep0* for sleep mode on and OH on, *Sleep2* for sleep mode on and backhaul on, *Sleep3* for sleep mode on and OH off

Fig. 4.33 graphs the IoT RAN Energy Efficiency versus picocell density with sleep mode status and UE distributions as parameters for 100 UEs in the RAN. RAN EE is the joint performance of both capacity and power consumption of the RAN densification, as stated in Eq. (4.28). Without the sleep mode (*Pilot0*), the increasing power consumption and decreasing capacity lead to decreasing energy efficiency, regardless of UE distributions. The clustered UE distribution activates fewer BSs than the uniform case, leading to higher capacity, lower energy consumption, and eventually higher energy efficiency. However, this does not change the decreasing EE tendency. Putting empty picocells into deeper sleep mode depth from *Sleep0* to *Sleep2* to *Sleep3* with the increasing picocell density reduces the power consumption and improves the capacity, so the RAN EE improves as well. Similarly, with the sleep mode turned on, the IoT RAN with clustered UE distribution has higher EE due to higher capacity and lower power consumption. The turning point is 1000000 picocells/km³ (300 BSs in the RAN) for both UE distributions, which is slightly higher than the second RAN VSE point for the energy consumption to be constrained.

4.6.3 Simulation Results for Different UE Counts

Based on previous sets of results, this sub-section will evaluate the energy efficiency of the IoT RAN densification with different traffic intensities. 100, 200, and 500 active UEs are placed in the same $100m \times 100m \times 30m$ cuboid space, comprising the typical UE placed at the cuboid centre and 99, 199, and 499 virtual-UEs with clustered distribution, respectively. The corresponding VUE densities are 330000, 663333, and 1663333 VUEs per cubic kilometre. The other simulation parameters are kept the same as in the previous sub-section.

Fig. 4.34 graphs the IoT RAN Volume Spectral Efficiency versus picocell density with both sleep mode status and clustered UE count as varying parameters. Overall, the change of UE density does not change the RAN VSE tendency against the increasing BS density: first increase due to signal strengthening; then decrease continuously due to interference increase without the sleep mode (*Pilot10*), or decrease then increase with sleep mode on (*Sleep0*) due to constrained interference. However, more UEs in the same space activate more BSs and accumulate more capacity. This results in higher interference experienced by the typical UE and higher RAN VSE. Additionally, more UEs activating more BSs means higher BS densities are required to end up with empty cells. Therefore, a higher UE count case has a higher turning point for sleep mode *Sleep0* to be effective with a smaller improvement in RAN VSE compared to the smaller UE count.

Fig. 4.35 graphs the IoT RAN power consumption versus picocell density with sleep mode status and UE count as parameters. For any UE count, the RAN power consumption behaves similarly as in Fig. 4.32. When sleep mode is off (*Pilot10*), all BSs consume power, so the RAN power consumption increases with the increasing picocell density. When sleep mode *Sleep0* is on and only the transmission in empty picocells is off, the reduction in RAN power consumption is negligible since the percentage power consumption of traffic-dependent radio-head is negligible. In other words, the power consumption difference is negligible between an active picocell, an empty picocell without sleep mode, or an empty picocell with sleep mode *Sleep0*. This reason has also led to the overlapping power consumption profiles for different UE counts with empty picocell status *Pilot10* and *Sleep0*. In contrast, when empty picocells enter sleep mode *Sleep2* and only backhaul is left on, the RAN power consumption reduces significantly with the increasing picocell density for all UE counts. Moreover, now that an empty picocell only consumes nearly half of the power

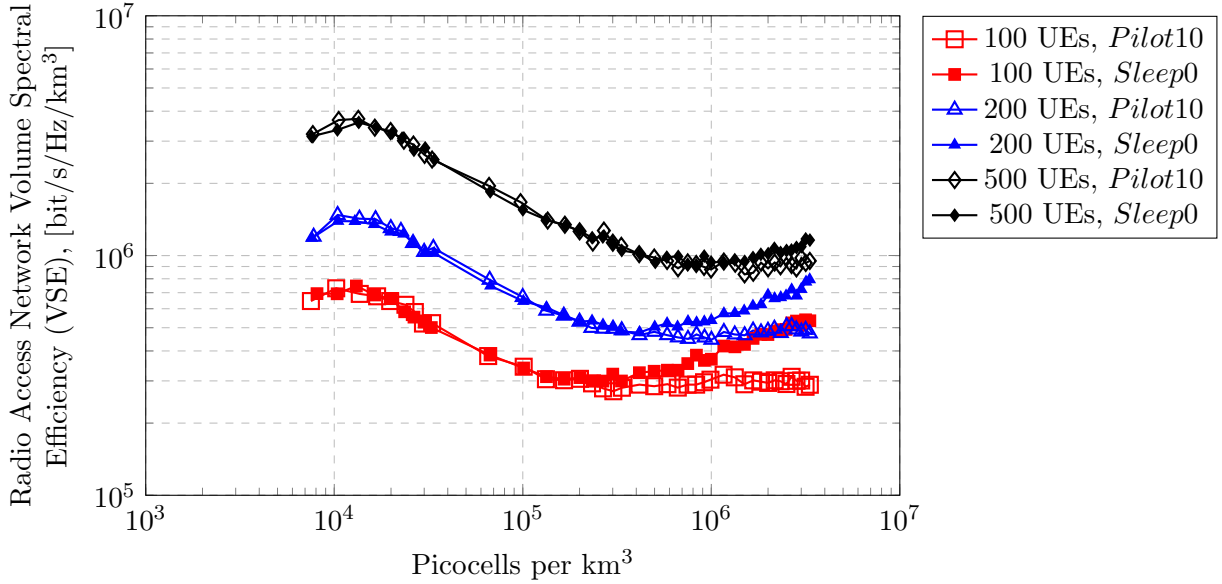


Figure 4.34: RAN Volume Spectral Efficiency (VSE) versus picocell density for various UEs counts with clustered distribution, and sleep mode off (*Pilot10*), where empty cells have α_c of 10%, and sleep mode on (*Sleep0*), where empty cells have α_c of 0

an active picocell consumes, a higher UE count activates more BSs leading to higher RAN energy consumption. A similar but more distinct comparison in RAN power consumption regarding UE counts could also be observed from the *Sleep3* profiles, whose absolute RAN power consumption is the lowest.

Fig. 4.36 graphs the IoT RAN Energy Efficiency versus picocell density with sleep mode status and UE count as parameters. The RAN EE with the same UE count behaves similarly against the increasing BS densification as in Fig. 4.33. Adding more UEs to the same space activates more BSs, thus consuming more power. This effect is the most prominent for *Sleep3*, where the power consumption of active and empty BS differs the most. The improvement in capacity shown in Fig. 4.34 by accumulating more data transmission for more UEs could only ameliorate this power consumption increase to some extent. As a result, the RAN EE improves diminishingly with the increasing UE count for empty cell status *Pilot10*, *Sleep0*, and *Sleep2*. In contrast, for *Sleep3*, the RAN EE improves with the increasing UE count for small BS densities up to 1000000 picocells/km³ (300 BSs in the RAN), then starts to decrease with the increasing UE count. This is the scenario where the limited improvement in the capacity accumulated by more UEs in the RAN, shown in Fig. 4.34, is insufficient to compensate for the extra power consumed by extra active picocells,

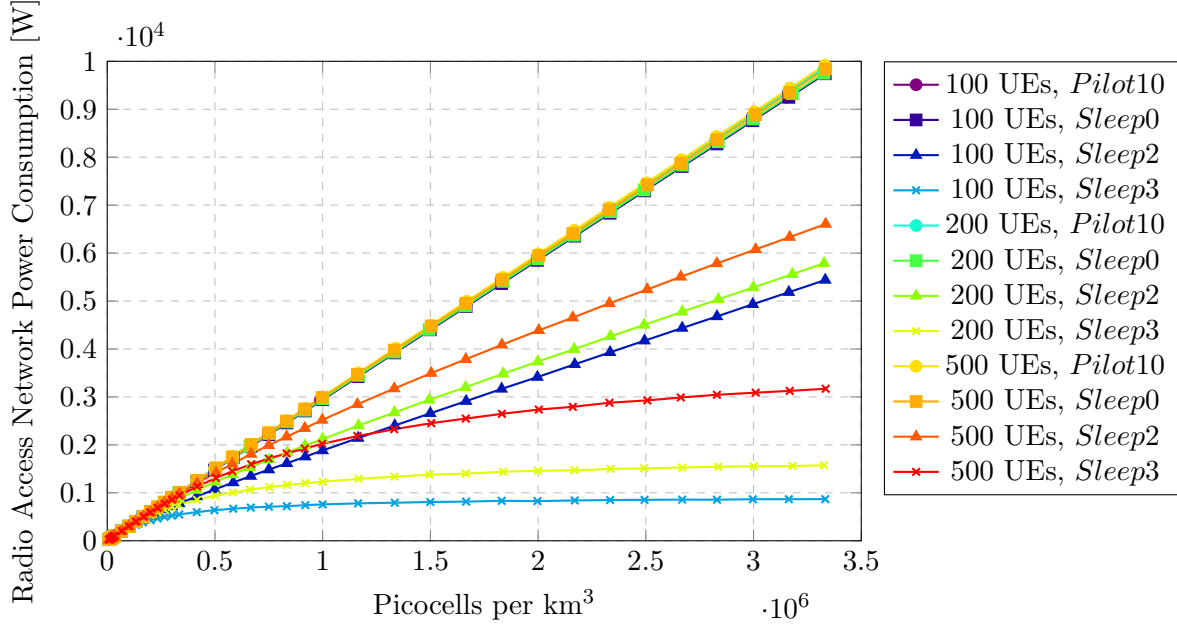


Figure 4.35: RAN power consumption versus picocell density for different UE counts with clustered distribution, and different empty cell status: *Pilot10* for sleep mode off, *Sleep0* for sleep mode on and OH on, *Sleep2* for sleep mode on and backhaul on, *Sleep3* for sleep mode on and OH off

which leads to RAN EE degradation.

To summarise the key observations in this section, the simulation results of the IoT RAN densification in a 3D space, where BSs and UEs follow independent HPPP distributions, have shown that without the sleep mode, both the RAN capacity and energy efficiency would degrade with the increasing densification level due to interference and power consumption, respectively. Only by completely turning off empty picocells the IoT RAN densification becomes energy efficient, resulting from improved capacity and constrained power consumption increase. This makes the power consumption, or energy consumption if including the observation period, the performance-limiting factor for the energy efficiency of the homogeneous small cell RAN densification. This observation holds for different UE distributions and different traffic intensities.

4.7 Summary

This chapter has analysed the capacity, energy consumption, and energy efficiency of homogeneous RAN densification using the three figures of merit: Data Volume Gain, Energy Consumption Gain, and Energy Efficiency Gain, from the previously presented evaluation framework. The performance

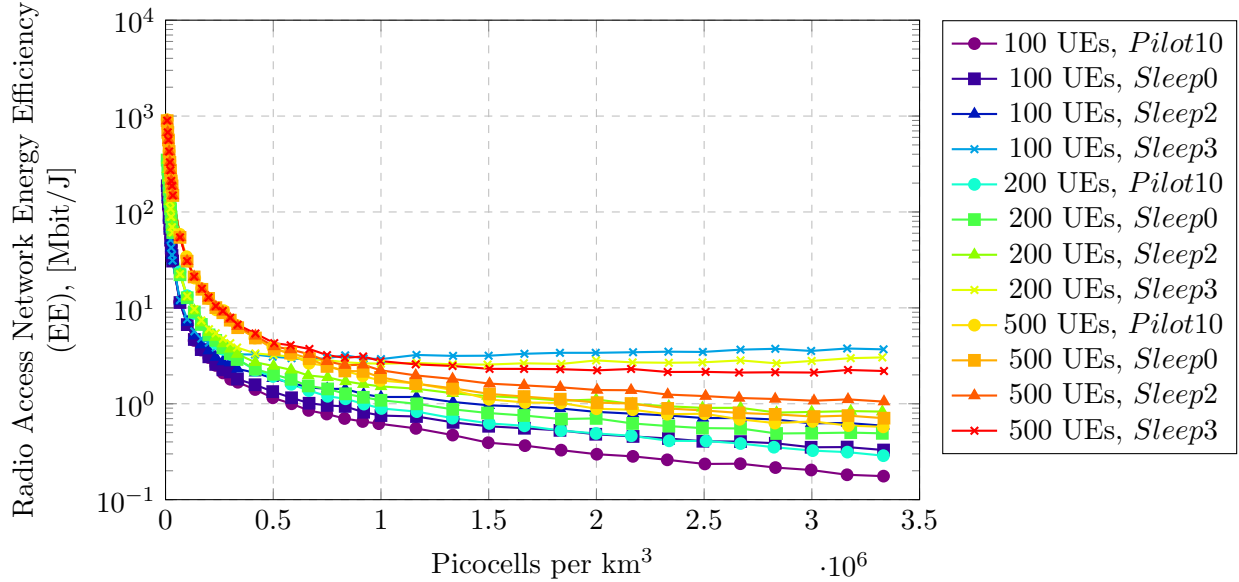


Figure 4.36: RAN Energy Efficiency (EE) versus picocell density for different UE counts with clustered distribution, and different empty cell status: *Pilot10* for sleep mode off, *Sleep0* for sleep mode on and OH on, *Sleep2* for sleep mode on and backhaul on, *Sleep3* for sleep mode on and OH off

is evaluated based on a common reference macro-RAN with ISD of 500 m, three cells per site, 300 UEs per square kilometre, RR as the scheduler, active cells have unity load activity factor, and empty cells have 10% as the normalised load activity factor.

Having presented the system model, the homogeneous macro-RAN densification is first evaluated as the performance benchmark. The macro-ISD is reduced from 500 m to 300 m. The figures of merit results show that the macro-RAN densification improves the energy efficiency when reducing the peak transmission power from all macrocells with densification. However, this energy efficiency improvement comes from capacity improvement only since the energy consumption increases.

Then the densification of both micro-RAN and pico-RAN are analysed similarly for energy-saving purposes. The results of figures of merit show that changing from macrocells to small cells saves energy but does not change the decreasing tendency. The unbounded densification of small cell RAN would eventually degrade the capacity alongside the consistently increasing energy consumption. Thus, the energy efficiency of small cell RAN densification increases and then decreases with a larger scale.

The evaluation then focuses on pico-RAN densification to closely analyse the densification limitation on capacity, energy consumption, and energy efficiency. The introductions of pilot level

reduction and sleep mode into empty picocells are shown to limit the interference and energy consumption of pico-RAN, respectively. Specifically for the interference constrain, only turning the pilot transmission completely off from empty cells does the pico-RAN capacity improve monotonically with densification. In addition, only when the empty cells are completely turned off, including the key limiting factor backhaul, does the energy consumption stop increasing with densification, leading to higher energy efficiency. This conclusion is also tested for different UE densities and holds. Finally, the scheduler is compared to seek capacity improvement without needing to change hardware or RAN infrastructure. The figures of merit show that changing the scheduler from the benchmark Round Robin to Maximum SINR would improve the capacity and energy efficiency to some extent at the expense of losing both the resource allocation fairness and UE throughput fairness. In contrast, changing the scheduler from Round Robin to Proportional Fair would also improve the capacity and energy efficiency similarly with slight resource allocation fairness degradation and UE throughput fairness improvement. Proportional Fair trades off the complexity of scheduling metrics for better capacity and fairness. However, highly densified pic-RAN has one UE per active picocell that no UE diversity could be exploited for capacity improvement. So the benchmark Round Robin is preferred for its simplicity without any performance degradation. Except for the scheduler, the above observations also hold when BSs and UEs are distributed in a 3D cuboid space and follow independent HPPP distributions.

In summary, without sleep mode, homogeneous small cell RAN densification should be limited. Otherwise, both the capacity and energy efficiency would degrade. Secondly, the homogeneous small cell RAN densification is energy efficient only if all the empty cells are turned completely off. The energy consumption is the limiting factor for the energy consumption of the homogeneous small cell RAN densification. Nevertheless, the densification of homogeneous small cell RAN with sleep mode on should also be limited but to a much higher density level where both the capacity and energy consumption are saturated unless more technologies are included to improve the capacity or reduce the energy consumption. This is the fundamental study of the small cells with extreme densification levels, which could be used as the design guideline for an energy efficient small cell RAN. In the next chapter, the picocells will overlay with the conventional macrocells, thus forming the heterogeneous RAN (HetNet) for a more practical RAN infrastructure. The energy efficiency of the HetNet densification is thoroughly studied similarly.

Chapter 5

The Energy Efficiency of Ultra-Dense Heterogeneous RANs

5.1 Introduction

The constant increase of the data demand has motivated the advancement of communication technologies for capacity enhancement [173]. At the same time, the increasing energy consumption brought by the technology advancing has made energy efficiency another key performance indicator of the RAN evaluation [28]. Among various technologies proposed and applied, the densification of the low-powered small cell BSs has proved effective with regard to both capacity and energy efficiency [21].

There are generally two RAN infrastructures that involve the small cells. The first is the homogeneous small cell RAN, where only the identical small cell BSs are deployed in a highly dense manner [43]. The investigation of the ultra-dense homogeneous small cell RANs provides a fundamental understanding of the limitation of RAN densification regarding capacity, energy consumption, and energy efficiency. Specifically, the empty small cells should be turned off completely to mitigate interference and save energy for energy efficiency improvement. In contrast, the other RAN infrastructure is heterogeneous, where the small cells overlay with the macrocells for coverage compensation [186] and capacity improvement [187]. The co-existence of macrocells and small cells forms a more practical infrastructure where small cells with small ISDs do not have to cover the

whole RAN area physically. With the homogeneous RAN energy efficiency having been analysed in the previous chapter, this chapter focuses on the energy efficiency analysis of the ultra-dense HetNet.

Nevertheless, the highly densified small cells still consume a significant amount of energy that would cause more carbon footprint [25], [31] and degrade the energy efficiency eventually [10]. To cope with this problem, putting empty cells with no UE associations into low-power sleep mode is expected to reduce energy consumption and thus maintain energy efficiency [25]. This is effective for ultra-dense scenarios where the number of cells exceeds the number of UEs. Different sleep mode depths reduce the empty small cell energy consumption by different scales, thus resulting in different RAN energy efficiency performances [10].

In this chapter, the energy efficiency of the ultra-dense HetNet will be analysed using the evaluation framework and power model introduced in Chapter 3. The densification will occur in both the macrocell and small cell layers. Simulation results will show that HetNet densification behaves similarly to the homogeneous small cell RAN but with different absolute values for capacity, energy consumption, and energy efficiency. The adoption of sleep mode reduces the RAN energy consumption and inter-cell interference, thus improving energy efficiency.

The rest of the chapter is structured as follows: Section 5.2 introduces the HetNet system model regarding the channel model, RAN throughput and RAN power consumption. Section 5.3 analyses the transmission power approach for both macrocells and small cells against densification. Sections 5.4 and 5.5 present the simulation results and figures of merit of macrocell layer densification and small cell layer densification, respectively. Section 5.6 draws the chapter summary.

5.2 Heterogeneous RAN System Model

This section introduces the system model for heterogeneous RANs. Specifically, the mathematical expressions for UE received power, channel loss, UE SINR, UE and RAN throughput, and HetNet RAN power consumption are presented.

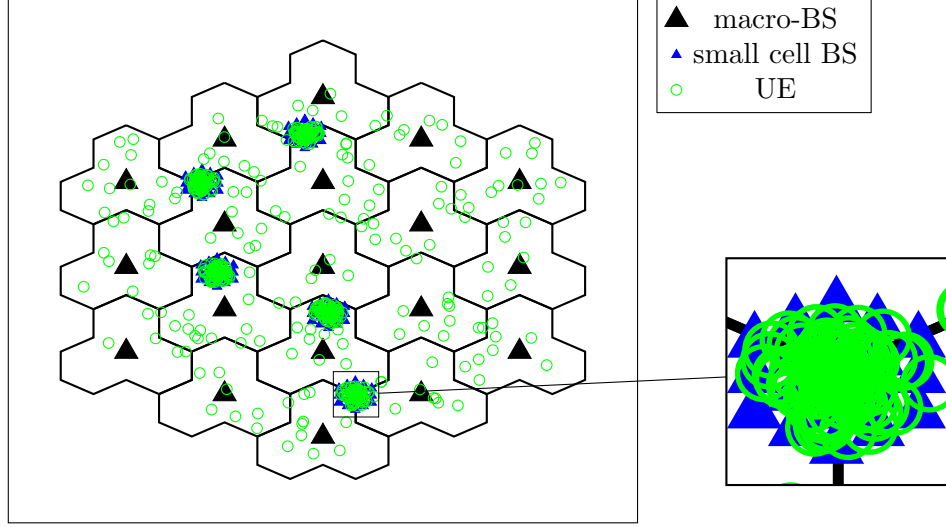


Figure 5.1: Example of a heterogeneous RAN layout consisting of macrocell and small cell layers, 5 UE clusters with cluster radius of 40 m, minimum macro-BS and small cell BS separation is 75 m

5.2.1 Heterogeneous RAN layout

This chapter considers the DL traffic of a LTE HetNet, consisting of macrocells and small cells. Fig. 5.1 shows an example HetNet layout. Macro-BSs (MBSs) have hexagonal distribution and are denoted as the set $\mathcal{B}^{MBS} = \{1, 2, \dots, b^{MBS}, \dots, N_B^{MBS}\}$. All macro-BSs are assumed to be tri-sectored, which means one macro-BS site has three macrocells. The macrocells are denoted as the set $\mathcal{C}^{MBS} = \{1, 2, \dots, c^{MBS}, \dots, N_C^{MBS}\}$. The macrocells provide the overall coverage and define the RAN area A_{HetNet} .

In contrast, the small cell layer has small cell BSs (SBSs) with hexagonal distribution within several clusters to target the clustered traffic. Fig. 5.1 shows five clusters, which have centres randomly distributed in the total RAN area. The small cell BSs and small cells are denoted as $\mathcal{B}^{SBS} = \{1, 2, \dots, b^{SBS}, \dots, N_B^{SBS}\}$ and $\mathcal{C}^{SBS} = \{1, 2, \dots, c^{SBS}, \dots, N_C^{SBS}\}$, respectively. All the small cell BSs are assumed to have a single cell, such that \mathcal{B}^{SBS} and \mathcal{C}^{SBS} are identical. Macrocells and small cells are assumed to share the same frequency bandwidth, so both inter-cell interference and inter-layer interference are considered. The total set of BSs and cells are denoted as $\mathcal{B} = \{1, 2, \dots, b, \dots, N_B\}$ and $\mathcal{C} = \{1, 2, \dots, c, \dots, N_C\}$, respectively, where $\mathcal{B} = \mathcal{B}^{MBS} \cup \mathcal{B}^{SBS}$, $\mathcal{C} = \mathcal{C}^{MBS} \cup \mathcal{C}^{SBS}$, $N_B = N_B^{MBS} + N_B^{SBS}$, and $N_C = N_C^{MBS} + N_C^{SBS}$.

All the UEs in HetNet are assumed to be outdoor and active with the clustered distribution.

Specifically, the total UEs are divided into two groups. In the first group, or the uniform group, UEs are allocated with uniform random x-coordinates and y-coordinates with the in-RAN guarantee. This is the same as described in Section 4.2. In the second group, or the clustering group, UEs are distributed in several clusters. The centre of each circular cluster with a fixed radius is distributed within the RAN. There is a global minimum separation set for the cluster centres so that the small cells distributed on top of each cluster do not overlap. UEs in the clustered group are then divided evenly for each cluster. Within a cluster, on the other hand, UEs have uniform random angles and distances away from the centre within the circular area. These UE clusters model the traffic in crowded places such as outdoor shopping fairs. Small cells are distributed specifically to cover the traffic in these UE clusters. All UEs are assumed to have a single isotropic antenna. The UE set is denoted as $\mathcal{K} = \{1, 2, \dots, k, \dots, K\}$. Each UE can associate with either a macrocell or a small cell, depending on the strongest received power. The full buffer traffic model is assumed so that all the UEs always demand data on the DL. The average UE rate cap is 100 *Mbps*.

5.2.2 UE Received Power and Channel Model

The signal from an arbitrary cell c to an arbitrary UE k would experience both the large-scale fading path loss and shadow fading as well as the small-scale multipath fading. However, the parameters for fading effects differ between MBSs and SBSs. The large-scale fading parameters depend on the locations of cells and UEs and vary every Monte Carlo run. The small-scale fading parameters vary on each RB and update every TTI $t = 1, \dots, T$. The per RB per TTI received power in dBm for UE k from a random cell c on RB n in TTI t is:

$$P_{rx,c,k}(n, t) [\text{dBm}] = P_{tx,c,k}(n) [\text{dBm}] + G_{BS,c,k} [\text{dBi}] + G_{UE,c,k} [\text{dBi}] - L_{c,k}(n, t) [\text{dB}] \quad (5.1)$$

where $P_{tx,c,k}(n)$ is the transmission power in dBm from cell c on an arbitrary RB n in TTI t ; $G_{BS,c,k}$ and $G_{UE,c,k}$ are the antenna gains from cell c and UE k , respectively; and $L_{c,k}(n, t)$ is the per RB per TTI channel loss. The per RB transmission power is linked to the total cell transmission power $P_{tx,c}$ as:

$$P_{tx,c,k}(n) = \frac{P_{tx,c}}{N_{RB}} \quad (5.2)$$

where N_{RB} is the total number of RBs included in a TTI for a given channel bandwidth. Note that macrocells and small cells in HetNet are assumed to share the same bandwidth so N_{RB} is the same from all cells.

Suggested from the 3GPP documents in [175], [178], the general 3D BS antenna pattern is:

$$G_{BS,c,k} [\text{dB}] = G_{BS,max} [\text{dBi}] - \min \left[- \left(G_{V,c,k}(\theta_{c,k}) [\text{dB}] + G_{H,c,k}(\phi_{c,k}) [\text{dB}] \right), A_m \right] \quad (5.3)$$

where

$$G_{V,c,k}(\theta_{c,k}) = \begin{cases} 0 [\text{dB}] & \text{if isotropic} \\ - \min \left[12 \left(\frac{\theta_{c,k} - \theta_{tilt}}{\theta_{3dB}} \right)^2, SLA_v \right] [\text{dB}] & \text{otherwise} \end{cases} \quad (5.4)$$

and

$$G_{H,c,k}^{MA}(\phi_{c,k}) = \begin{cases} - \min \left[12 \left(\frac{\phi_{c,k}}{\phi_{3dB}} \right)^2, A_m \right] [\text{dB}] & \text{if sectored} \\ 0 [\text{dB}] & \text{otherwise} \end{cases} \quad (5.5)$$

are the vertical and horizontal antenna patterns, respectively. Macrocells have tri-sectored antenna patterns, while small cells have isotropic antenna patterns. In Eq. (5.3) to (5.5), $G_{BS,max}$ is the maximum antenna gain in the bore-sight direction in units of dBi; θ_{3dB} and ϕ_{3dB} are the vertical and horizontal HPBW, respectively, in units of degree; $\theta_{c,k}$ and $\phi_{c,k}$ are the relative vertical and horizontal angles between cell c and UE k in units of degree; A_m and SLA_v are the absolute values of the dB scale antenna front-to-back attenuation and sidelobe attenuation, respectively; and θ_{tilt} is the antenna down-tilt in units of degree. The antennas from all cells are down-tilted so that their upper HPBW is targeted at the cell edge for the best in-cell capacity performance. Fig. 5.2 shows the example of a sectored antenna radiation pattern. In contrast, each UE has an isotropic antenna pattern:

$$G_{UE,c,k} = 0 [\text{dBi}] \quad (5.6)$$

Given the 3D distance between an arbitrary cell c to UE k being $d_{c,k}$, the path loss model is:

$$L_{PL,c,k}^z = \beta^z + \zeta^z \times \log_{10}(d_{c,k}) [\text{dB}], \quad z = \text{LoS or NLoS} \quad (5.7)$$

where the path loss constants β^z and ζ^z , $z = \text{LoS, NLoS}$, differ between BS technologies in different

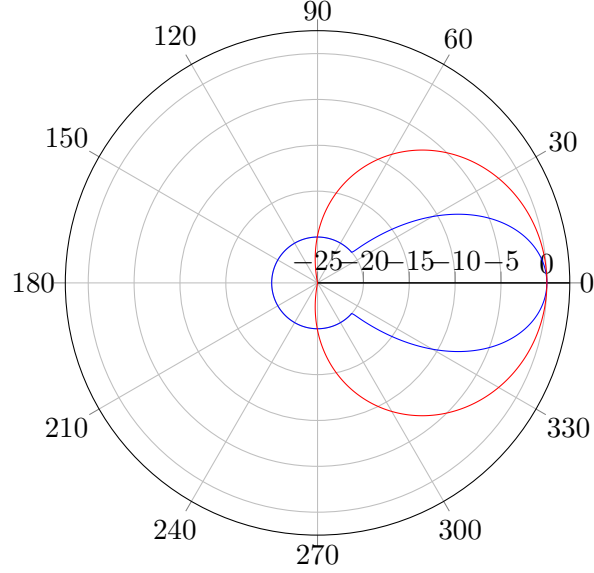


Figure 5.2: Antenna radiation pattern for a sectored antenna, $\theta_{3dB} = 32$ degrees, $\phi_{3dB} = 70$ degrees, $A_m = 25$ dB, $\theta_{tilt} = 0$ degree, $SLA_v = 20$ dB

layers. According to the potentially wide distance range considered, the overall path loss between an arbitrary BS and UE pair is LoS probability weighted using the LoS probabilities from [175], [178]:

$$prob_{c,k}^{LoS} = \begin{cases} \min\left(\frac{18}{d_{c,k}}, 1\right) \times \left[1 - \exp\left(\frac{-d_{c,k}}{63}\right)\right] + \exp\left(\frac{-d_{c,k}}{63}\right) & \text{if macrocell} \\ \min\left(\frac{18}{d_{c,k}}, 1\right) \times \left[1 - \exp\left(\frac{-d_{c,k}}{36}\right)\right] + \exp\left(\frac{-d_{c,k}}{36}\right) & \text{if microcell} \\ 0.5 - \min\left(0.5, 5 \times \exp\left(\frac{-156}{d_{c,k}}\right)\right) + \min\left(0.5, 5 \times \exp\left(\frac{d_{c,k}}{30}\right)\right) & \text{if picocell.} \end{cases} \quad (5.8)$$

The expressions are obtained using data fitting collected from field tests [179].

The shadow fading $L_{SF,c,k}$ between UE k and cell c in HetNet for any BS technology is modelled as a normal distribution for simplicity. The distribution means and standard deviations differ between LoS/NLoS conditions and BS technologies, as suggested in [175], [178] and listed in Table 5.1. The shadow fading is also LoS probability-weighted. Rayleigh fading is considered as multipath fading and varies between RBs. The overall per RB per TTI channel loss $L_{c,k}(n, t)$ is thus:

$$L_{c,k}(n, t) \text{ [dB]} = \left(L_{PL,c,k}^{LoS} \text{ [dB]} + L_{SF,c,k}^{LoS} \text{ [dB]}\right) \times prob_{c,k}^{LoS} + \left(L_{PL,c,k}^{NLoS} \text{ [dB]} + L_{SF,c,k}^{NLoS} \text{ [dB]}\right) \times (1 - prob_{c,k}^{LoS}) + L_{MPF,c,k}(n, t) \text{ [dB]}. \quad (5.9)$$

5.2.3 UE throughput and RAN Area Throughput

Using Shannon's formula, the per TTI UE throughput is:

$$\tilde{S}_{UE,k}(t) = \frac{12 \times 14 \times \sum_{n=1}^{N_{RB}} \log_2 \left(1 + I_{c,k}(n, t) \times \gamma_{c,k}(n, t) \right)}{\delta_t} \quad (5.10)$$

where 12 is the sub-carrier number included in the frequency domain of a RB, 14 is the symbol number included in the time domain of a RB, $I_{c,k}(n, t)$ is the RB allocation indicator which equals 1 if the RB is allocated to UE k in TTI t and 0 otherwise, δ_t is the 1 ms time spread of a RB, and:

$$\gamma_{c,k}(n, t) = \frac{P_{rx,c,k}(n, t)}{\sum_{c' \in \mathcal{C} \setminus \{c\}} P_{rx,c',k}(n, t) + \sigma_n^2}. \quad (5.11)$$

is the SINR on RB n in TTI t . In Eq. (5.11), \mathcal{C} is the total cell set in HetNet including macrocells and small cells, $c' \in \mathcal{C} \setminus \{c\}$ is an arbitrary cell c' from the set \mathcal{C} but $c' \neq c$, $\sum_{c' \in \mathcal{C} \setminus \{c\}} P_{rx,c',k}(n, t)$ is the total inter-cell and inter-layer interference experienced by UE k , and σ_n^2 is the total channel noise including both thermal noise and UE noise figure.

For the total observation time period T , the UE average throughput S_{UE} and RAN average throughput S_{HetNet} are:

$$S_{UE,k} = \frac{1}{T} \sum_{t=1}^T \tilde{S}_{UE,k}(t) \quad (5.12)$$

and

$$S_{HetNet} = \sum_{k=1}^K S_{UE,k} \quad (5.13)$$

respectively.

As previously stated, the HetNet area is the total macrocell area:

$$A_{HetNet} = A_c^{MBS} \times N_C^{MBS} \quad (5.14)$$

where

$$A_c^{MBS} = \frac{3\sqrt{3} \times (R^{MBS})^2}{8} \quad (5.15)$$

is the hexagonal area of a macrocell with radius R^{MBS} in units of kilometre. Eq. (5.13) and (5.14) can then be used for HetNet DVG calculation to evaluate the capacity performance.

5.2.4 Heterogeneous RAN Power Consumption

Including different BS technologies, the total HetNet power consumption is:

$$P_{HetNet} = \sum_{b=1}^{N_B^{MBS}} P_b^{MBS} + \sum_{b=1}^{N_B^{SBS}} P_b^{SBS} \quad (5.16)$$

where

$$P_b^{MBS} = \frac{n_c \times \hat{P}_{tx,c}}{\eta_{CL}} \left[\left(\frac{3.4121}{EER} + 1 \right) \frac{\sqrt{\alpha_c \times OBO}}{\eta_{PS} \times \hat{\eta}_{PA}} - \frac{3.4121}{EER} \alpha_c \right] + \left(\frac{3.4121}{EER} + 1 \right) \frac{n_a \times n_c}{\eta_{PS}} \times \frac{B}{\hat{B}} (\hat{P}_{BB} + \hat{P}_{TRX}) + P_{BH} \quad (5.17)$$

and

$$P_b^{SBS} = \frac{n_c \times \hat{P}_{tx,c} \times \sqrt{\alpha_c \times OBO}}{\eta_{CL} \times \eta_{PS} \times \hat{\eta}_{PA}} + \frac{n_a \times n_c}{\eta_{PS}} \times \frac{B}{\hat{B}} (\hat{P}_{BB} + \hat{P}_{TRX}) + P_{BH} \quad (5.18)$$

are the BS site power consumption for MBSs and SBSs, respectively. The parameter meanings and values can be found in Chapter 3. Eq. (5.16) and (5.14) can then be used for HetNet ECG calculation to evaluate energy consumption.

5.2.5 Heterogeneous RAN Simulation Flowchart

Fig. 5.3 shows the MATLAB-based flowchart of heterogeneous RAN DL traffic simulation. Having set the systematic parameters, the uniform MSBs are firstly distributed. This is fixed for all the independent Monte Carlo runs. Within each Monte Carlo run, cluster origins are distributed first, followed by UEs in the cluster, and the small cells are then distributed to cover these clusters. After UE-cell association which only considers the large-scale fading parameters to reduce the computation overhead, each cell schedules the resource to serve the associated UEs and RAN throughput is accumulated. Compared with the homogeneous case in Chapter 4, the HetNet case has different UE distributions and the extra step of distributing small cells, shown as the shaded process blocks in the figure.

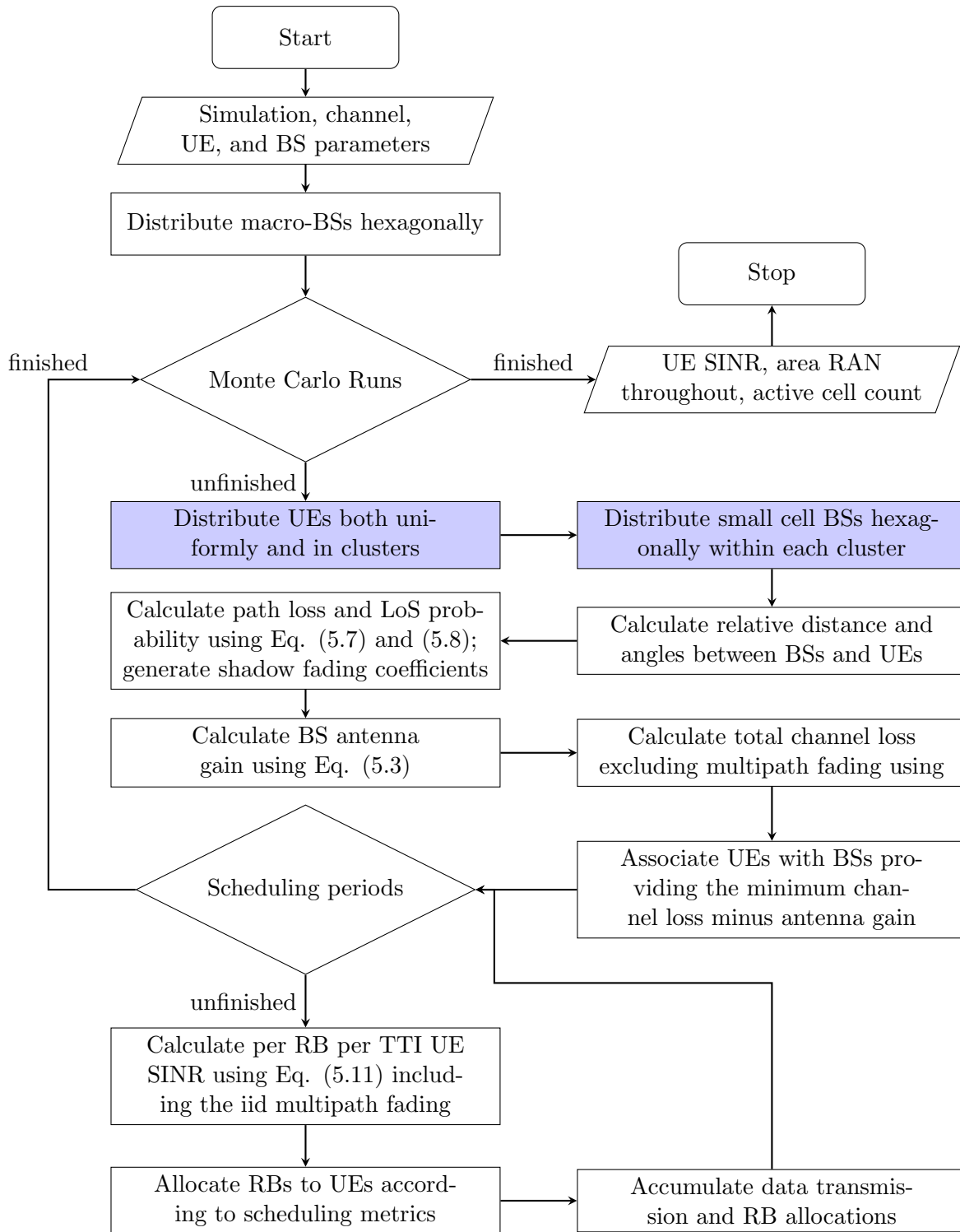


Figure 5.3: MATLAB based heterogeneous RAN simulator flowchart

5.3 Heterogeneous RAN Cell Peak Transmission Power Approach

This chapter evaluates the energy efficiency performance of the ultra-dense HetNet. The HetNet has two layers: the macrocell and the picocell layers. Both layers will be densified for potential capacity enhancement and energy efficiency improvement.

Table 5.1 lists the key parameters for HetNet densification simulation in both layers [175], [178]. All the macro-BSs have three cells, each with a single antenna; the pico-BSs have a single cell with a single antenna. The BSs use a 2 GHz frequency to carry data and share a 20 MHz bandwidth that provides 100 RBs per TTI. Moreover, the macrocell has a high peak transmission power level of 46.02 dBm, while it is only 21.14 dBm for picocells. The considered macro-BS ISD range is from 500 m down to 300 m, equivalent to 13.86 to 38.49 macrocells per square kilometre. In contrast, the pico-BS in clusters have ISDs ranging from 80 m down to 5 m, equivalent to 1 to 217 picocells per cluster. Each cluster has a radius of 40 m [10]. The small cell density depends on the RAN area and the in-cluster picocell ISD, so it changes with both the macro-BS ISD and the in-cluster pico-BS ISD. The occupied bandwidth B is assumed to equal the peak bandwidth \hat{B} . Also, for an active BS with at least one UE associated, the normalised load activity factor α_c is unity, while α_c is 10% for empty cells with no UE associations. In addition, there are in total 300 active and outdoor UEs per square kilometre in the RAN, each equipped with an isotropic antenna. Out of the total UE count, there are always 400 UEs in clusters, while the rest are uniformly distributed in the whole HetNet area. This fixed clustered UE number is chosen based on the RAN area-dependent total UE number and guarantees that the non-clustered UE number is larger than zero. In addition, the cluster UE number is fixed to model the relatively stable traffic in crowded shopping malls and alike during the busy daytime. This should be independent of macrocell or picocell layer densification. The total UE and non-clustered UE numbers are calculated using the HetNet area and the UE density. Round Robin (RR) is the scheduler for macrocells and picocells unless stated otherwise.

With the reduction in BS ISD brought by the increasing RAN densification level, UEs are closer to their serving cells and strengthen the signal power. However, the interference experienced by each UE is also increased as the UEs are also closer to the BSs in the interfering cells. Therefore, reducing the peak transmission power with the ISD while preserving the cell edge sensitivity could mitigate the increasing interference without degrading the UE throughput. The cell edge

Parameter Name	Macro-BS	Pico-BS
Antenna Count Per Cell (n_a)	1	
UE Density per km ²	300	
UE count in clusters	400	
Cluster count / Cluster radius [m]	5/40	
Carrier Frequency [GHz]	2	
Bandwidth [MHz]	20	
RB Count Per TTI (N_{RB})	100	
Shadow Fading Mean (μ^{LoS} / μ^{NLoS}) [dB]	0/0	
Noise Variance (σ_n^2) per RB [dBm]	-117.38	
Proportional Fair Observation Time Window (t_w) [ms]	50	
Cell Count Per Site (n_c)	3	1
BS/UE Height (h_{BS} / h_{UE})	15/1.5	3/1.5
BS ISD [m]	300-500	5-80
Peak Transmission Power Per Cell ($\hat{P}_{tx,c}$) [dBm]	46.02	21.14
Maximum Antenna Gain ($G_{BS,max}^{SC}$) [dBi]	14	0
Vertical/Horizontal HPBW ($\theta_{3dB} / \phi_{3dB}$) [degree]	32/70	360/360
Antenna Front-to-Back Attenuation (A_m) [dB]	20	-
Antenna Sidelobe Attenuation (SLA_v) [dB]	25	-
Pathloss Dimensionless Constants ($\beta^{LoS} / \beta^{NLoS}$) [dB]	30.8/2.9	41.1/32.9
Pathloss Exponents ($\zeta^{LoS} / \zeta^{NLoS}$)	24.2/42.8	20.9/37.5
Shadow Fading Standard Deviation ($\sigma^{LoS} / \sigma^{NLoS}$) [dB]	8/8	10/10

Table 5.1: HetNet densification simulation parameters

Macro-ISD [m]	500	450	400	350	300
$\hat{P}_{tx,c}$ [dBm]	46.02	43.95	41.61	38.92	35.78
Pico-ISD [m]	80	50	25	10	5
$\hat{P}_{tx,c}$ [dBm]	21.14	14.17	9.23	6.51	5.95

Table 5.2: Reduced cell peak transmission power against densification

sensitivity is interpreted as the received power level at the cell edge in this work. Therefore, with RAN densification, the peak transmission power $\hat{P}_{tx,c}$ could either be fixed or reduced with the decreasing ISDs on a specific reference. These are called the fixed $\hat{P}_{tx,c}$ and varied $\hat{P}_{tx,c}$ approaches, respectively. For HetNet, BSs in different layers could have different $\hat{P}_{tx,c}$ approaches. Table 5.2 shows the reduced $\hat{P}_{tx,c}$ for both macrocells, with the 500 m ISD case as reference, and picocells, with the 80 m ISD case as reference.

In HetNet, the macrocells use high $\hat{P}_{tx,c}$ to cover large areas. On the other hand, the small cells use low $\hat{P}_{tx,c}$ to cover small areas with high traffic intensities. Offloading traffic from macrocells to picocells is expected to improve capacity for two-fold reasons. Firstly, the offloading reduces the number of UEs per macrocell so that each remaining macro-UE (MUE) could have more resources to improve the individual throughput. Secondly, the offloaded UEs are served by the dense picocells with fewer competitors per cell, so they also have more resources allocated to improve their throughput. UEs served by picocells are called the pico-UEs (PUEs). However, the big transmission power difference between the two BS technologies, as given in Table 5.1, might prevent UEs from associating with picocells even though UEs are geographically closer to picocells.

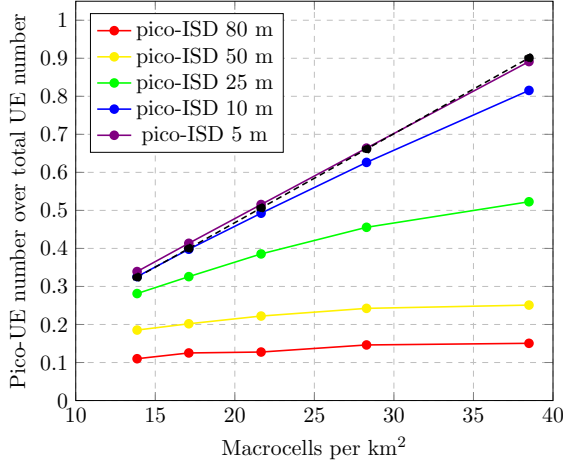
Fig. 5.4 shows the normalized number of PUEs over the total UE in the HetNet with the macrocell density as the variable, comparing different pico-ISDs and $\hat{P}_{tx,c}$ approaches for each HetNet layer. Given the fixed clustered UE number, the number of non-clustered UEs changes with the total UE number, which depends on the HetNet area for the fixed 300 UEs/km² density. The ratio between the clustered UE number and the total UE number is shown in each sub-figure as an increasing dashed black line. This is the reference line to evaluate the traffic offloading performance. Specifically:

1. Fixing $\hat{P}_{tx,c}$ in both HetNet layers enables the traffic offloading, especially for smaller picocell ISDs. This is reflected by the increasing normalised PUE percentage shown in Fig. 5.4a, and

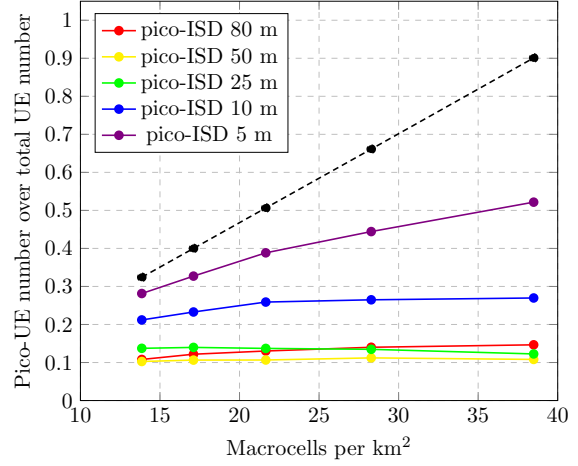
the increasing manner increases with pico-layer densification. Though the $\hat{P}_{tx,c}$ difference is fixed all the time, reducing the distance between clustered UEs and pico-BSs helps with the offloading and thus improves the RAN capacity. When the in-cluster pico-ISD is 5 m, almost all the clustered UEs are PUEs for all macrocell densities.

2. When macrocells fix their high $\hat{P}_{tx,c}$ while picocells reduce their low $\hat{P}_{tx,c}$ with the increasing densification level, Fig. 5.4b shows the compromised offloading results. This $\hat{P}_{tx,c}$ combination increases the transmission power difference, making it difficult for UEs to associate with picocells. For in-cluster pico-ISD larger than 10 m, densification has a negligible impact on the UE association. Only 10% of UEs are PUEs even though over 30% UEs are geographically within the picocell coverage. Further densification in picocell brings clustered UEs closer to picocells and strengthens the signal power, compensating the $\hat{P}_{tx,c}$ difference to some extent and enabling more traffic offloading. Nevertheless, only 55.56% of the clustered UEs are PUEs when the in-cluster pico-ISD is 5 m and macro-ISD is 300m (38.49 macrocells per square kilometre).
3. Fig. 5.4c has varied and fixed $\hat{P}_{tx,c}$ for macrocells and picocells, respectively. This $\hat{P}_{tx,c}$ combination results in the smallest transmission power difference and the most successful traffic offloading. When the in-cluster pico-ISD is not greater than 10 m, the PUE number is slightly higher than the clustered UE number for all the macrocell densities.
4. Fig. 5.4d shows the case where all cells adopt the varied $\hat{P}_{tx,c}$ approach. According to Table 5.2, the $\hat{P}_{tx,c}$ difference is greater than in Fig. 5.4c but lower than in Fig. 5.4a. So the offloading performance is in-between. When the in-cluster pico-ISD is 5 m, the clustered UE number is higher than the PUE number.

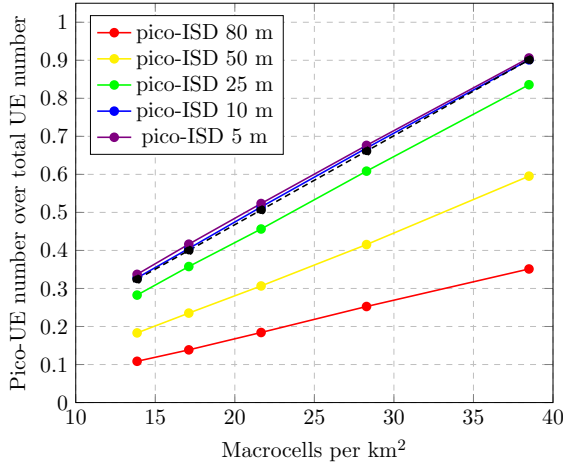
In summary, to benefit from the traffic offloading, the macrocells and picocells should adopt the varied and fixed $\hat{P}_{tx,c}$ approaches, respectively. Additionally, as shown by the simulation results in the previous chapter, reducing the macrocell $\hat{P}_{tx,c}$ against the increasing densification level does not degrade the capacity but rather improves the energy efficiency due to energy consumption reduction; and the $\hat{P}_{tx,c}$ approaches has negligible impact on the performance of picocell densification.



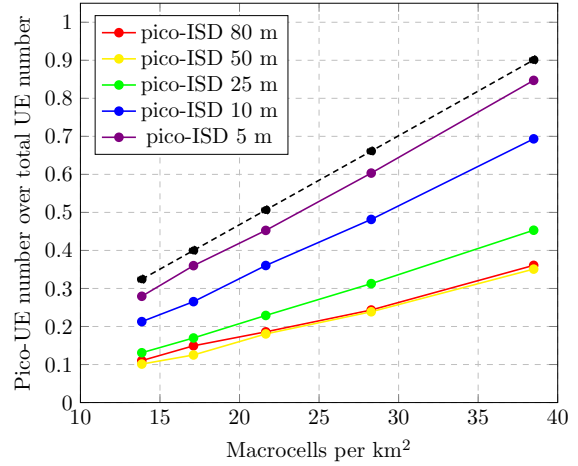
(a) Fixed $\hat{P}_{tx,c}$ for macro-layer, fixed $\hat{P}_{tx,c}$ for pico-layer



(b) Fixed $\hat{P}_{tx,c}$ for macro-layer, varied $\hat{P}_{tx,c}$ for pico-layer



(c) Varied $\hat{P}_{tx,c}$ for macro-layer, fixed $\hat{P}_{tx,c}$ for pico-layer



(d) Varied $\hat{P}_{tx,c}$ for macro-layer, varied $\hat{P}_{tx,c}$ for pico-layer

Figure 5.4: Pico-UE count over total UE count against the HetNet densification, with macro-layer and pico-layer using (a) fixed and fixed $\hat{P}_{tx,c}$ approach, (b) fixed and varied $\hat{P}_{tx,c}$ approaches, (c) varied and fixed $\hat{P}_{tx,c}$ approaches, and (4) varied and varied $\hat{P}_{tx,c}$ approach, respectively

5.4 Densification in Macrocell Layer of Heterogeneous RAN

Macrocell densification is a conventional approach to improve the RAN capacity [17]. The energy efficiency of the macrocell layer densification is thus first analysed using the evaluation framework from Chapter 3. Specifically, the macro-BS ISD will reduce from 500 m to 300 m, equivalent to increasing the macrocell density from 13.86 to 38.49 macrocells per square kilometre. The figures of merit DVG, ECG, and EEG are applied to compare the capacity, energy consumption, and energy efficiency performance of the densified HetNet with the reference homogeneous macro-RAN with 500 m ISD, uniform 300 UEs/km², and RR scheduler. Choosing the same reference RAN as the homogeneous case makes comparing the two RAN infrastructures straightforward. Note that the peak transmission power $\hat{P}_{tx,c}$ of macrocells reduces with the densification, and the PA output back-off *OBO* increases accordingly for a fixed PA saturation power level. In this section, macrocells and picocells adopt the varied and fixed $\hat{P}_{tx,c}$ approaches, respectively. All the active cells have unity α_c , while empty cells have 10% α_c without any sleep modes or 0% α_c if sleep mode is on. The scheduler is RR.

5.4.1 Macrocell Densification without Sleep Mode

Fig. 5.5 plots the HetNet Data Volume Gain against the increasing macrocell density, comparing different in-cluster pico-ISDs. The DVG results for the homogeneous macro-RAN densification using the varied $\hat{P}_{tx,c}$ approach are also included in the figure for capacity performance comparison. The key observations are:

1. When pico-ISD is 80 m in the cluster, there is only one picocell to cover each UE cluster. The RAN DVG first improves quickly, but the increasing rate slows down to the growing macrocell density. The turning point is 28.28 macrocells per square kilometre (macro-ISD of 350 m). The comparatively rapid capacity improvement is due to the signal strengthening experienced by MUEs, which occupy the majority of UEs. In contrast, PUEs suffer from increased interference from macrocells despite the reduction in macrocell $\hat{P}_{tx,c}$. This compromised PUE throughput gradually degraded the RAN capacity improvement. Compared with the homogeneous macro-RAN with the same macrocell density, HetNet has slightly degraded DVG due to extra interference experienced by MUEs from PBSs and interference experienced

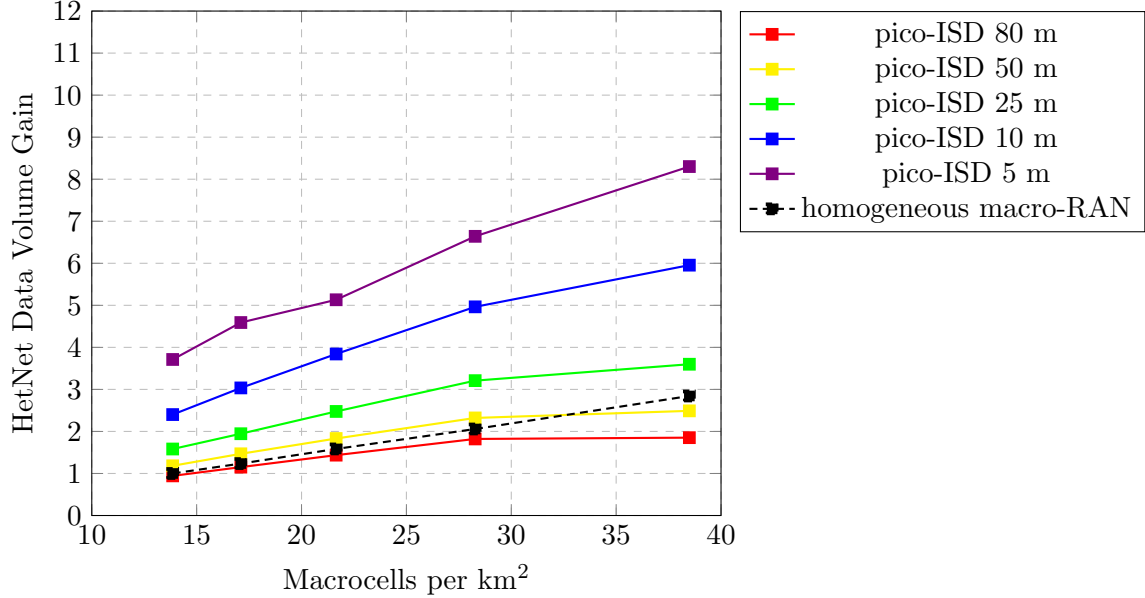


Figure 5.5: HetNet Data Volume Gain against macrocell density, comparing different picocell ISDs

by PUEs from MBSs.

2. For in-cluster pico-ISDs smaller than 80 m, the HetNet DVG behaves similarly but with improved absolute values due to traffic offloading (shown in Fig. 5.4c), UE signal strengthening (reduced ISD), and interference limitation (reduced $\hat{P}_{tx,c}$ difference). Compared with the homogeneous macro-RAN with the same macrocell density, the HetNet DVG is almost always higher, mainly due to traffic offloading.

In summary, HetNet capacity improves with the increasing macrocell density and outperforms the homogeneous macro-RAN counterpart. The major reason is traffic offloading.

Fig. 5.6 plots the HetNet Energy Consumption Gain against the increasing macrocell density, comparing different pico-ISDs within each cluster. The ECG results for the homogeneous macro-RAN densification using the reduced $\hat{P}_{tx,c}$ approach are included in the figure for energy consumption comparison. The figure shows that densification of picocells or macrocells increases RAN energy consumption. This is because of the increasing number of non-zero energy-consuming BSs in the RAN. Therefore, the ECG reduces against the increasing macrocell density and further with the reducing picocell ISD. Furthermore, HetNet almost always consumes more energy than the homogeneous macro-RAN counterpart with the same macrocell density because of the extra energy consumed by the overlaid picocells. The only exception is when macrocell density is 38.49

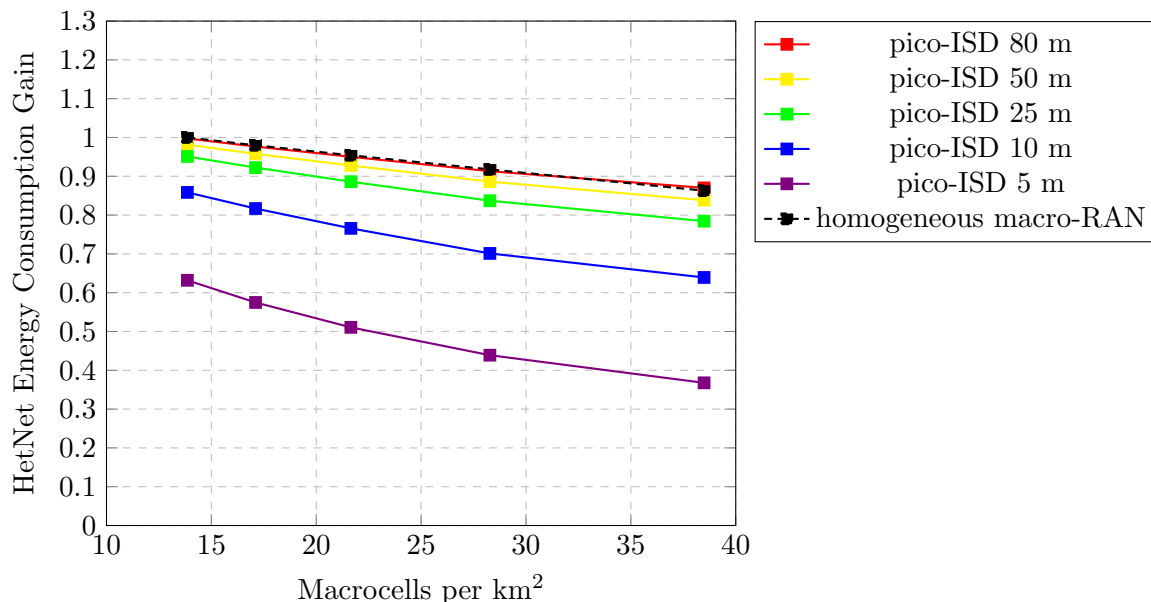


Figure 5.6: HetNet Energy Consumption Gain against macrocell density, comparing different picocell ISDs

macrocells per square kilometre (macro-ISR of 300 m) and pico-ISR is 80 m. The HetNet has a slightly higher ECG than the homogeneous macro-RAN counterpart due to fewer macrocells being active in the former when traffic is partly offloaded to low-powered picocells.

Fig. 5.7 shows the energy Efficiency Gain versus the macrocell density increase, with the pico-ISR as a parameter. The EEG results are the products of DVGs in Fig. 5.5 and ECGs in Fig. 5.6. The figure also includes the improving EEG of the homogeneous macro-RAN densification using the reduced $\hat{P}_{tx,c}$ approach as an energy efficiency performance reference. The figure shows that:

1. When pico-ISR is 80 m in the cluster, the RAN EEG first improves then degrades slightly with the increasing macrocell density. The energy efficiency improvement and degradation are dominated by improving capacity and reducing energy consumption, respectively. In addition, the homogeneous macro-RAN outperforms the HetNet with the same macrocell density due to higher capacity.
2. When the pico-ISR is reduced to 10 m in each cluster, the HetNet EEG behaves similarly but with higher absolute values due to signal strengthening and traffic offloading, despite the increasing energy consumption. Because of the traffic offloading, the HetNet gradually outperforms the homogeneous macro-RAN counterpart.

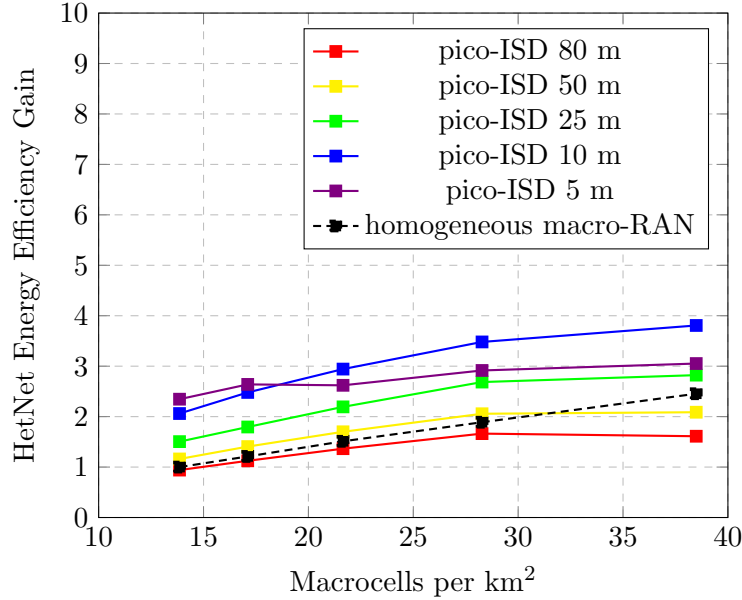


Figure 5.7: HetNet Energy Efficiency Gain against macrocell density, comparing different picocell ISDs

- When the in-cluster pico-ISD is further reduced to 5 m, the HetNet EEG improves in a diminishing manner against the increasing macrocell density. The reduction of the EEG improvement rate is dominated by energy consumption. However, compared with the in-cluster pico-ISD being a 10 m case, the HetNet EEG degrades. The improving capacity is insufficient to compensate for the increasing energy consumption.

In short, The HetNet energy efficiency improves with the increasing macrocell density. However, this energy efficiency improvement only comes from capacity enhancement because the energy consumption increases continuously.

5.4.2 Macrocell Densification with the Sleep Mode

The identified energy efficiency limiting factors of HetNet so far are the capacity-compromising interference and the significant energy consumption, especially at high picocell densification levels. For a fixed UE density, sufficiently dense HetNet would have empty cells with no UE association. This provides the opportunity for both interference limitation and energy consumption reduction. The popular solution is to put those empty cells into sleep mode, where empty cells consume low traffic independent overhead energy and do not transmit. The sleep mode could benefit both the

macrocell and picocell layers in the HetNet. Now the UEs are clustered, the chance of a macrocell being empty is higher than in the homogeneous macro-RAN scenario where UEs are uniformly distributed. For a macro-BS site with three macrocells, the sleep mode could be applied to the entire site or the individual cell, referred to as *Site Sleep Mode* and *Cell Sleep Mode*, respectively. Specifically, when *Site Sleep Mode* is on, the overhead energy is reduced only when all three cells are empty. In contrast, *Cell Sleep Mode* could reduce the overhead energy of an individual cell if it is empty. Note that *Site Sleep Mode* and *Cell Sleep Modes* turn off empty cell transmission and are differentiated by the overhead energy consumption. When the site/cell is empty, it is turned off completely, including the backhaul, in this section.

Fig. 5.8 plots the HetNet Data Volume Gain against the increasing macrocell density, comparing different in-cluster pico-ISDs, where all the empty cells or sites in the HetNet are in the completely-off sleep mode. Compared with the case without the sleep mode, turning off the empty cell transmission reduces the interference and improves the RAN capacity. This is reflected by the higher DVG with any sleep mode, especially for shorter pico-ISDs. Shorter in-cluster pico-ISD means more picocells to offload the traffic, ending up with more empty cells available for sleep mode. Moreover, *Site Sleep Mode* and *Cell Sleep Mode* have the same interference limitation, so the DVGs overlap.

Fig. 5.9 shows the HetNet Energy Consumption Gain against the densification in the macrocell layer, comparing different pico-ISDs and sleep modes. The ECG without sleep mode is included for energy consumption performance reference. *Site Sleep Mode* turns off the macro-BS site or pico-BS site completely if they are empty. This saves energy compared to the case without the sleep mode. The energy-saving scale increases against the picocell ISD reduction, which results in more empty cells in the HetNet. On the other hand, *Cell Sleep Mode* turns off empty macrocells or picocells. This saves more energy than the *Site Sleep Mode* since the chance of having an empty macrocell is much higher than having an empty macrosite. Specifically, when macrocell density is 38.49 macrocells per square kilometre (macro-ISD of 300 m), the HetNet ECG with *Cell Sleep Mode* recovers from the decreasing tendency due to macrocells being turned off. In short, sleep mode would reduce the HetNet energy consumption, especially for high densification levels with many empty cells. In addition, the *Cell Sleep Mode* saves more energy than the *Site Sleep Mode* and recovers the ECG.

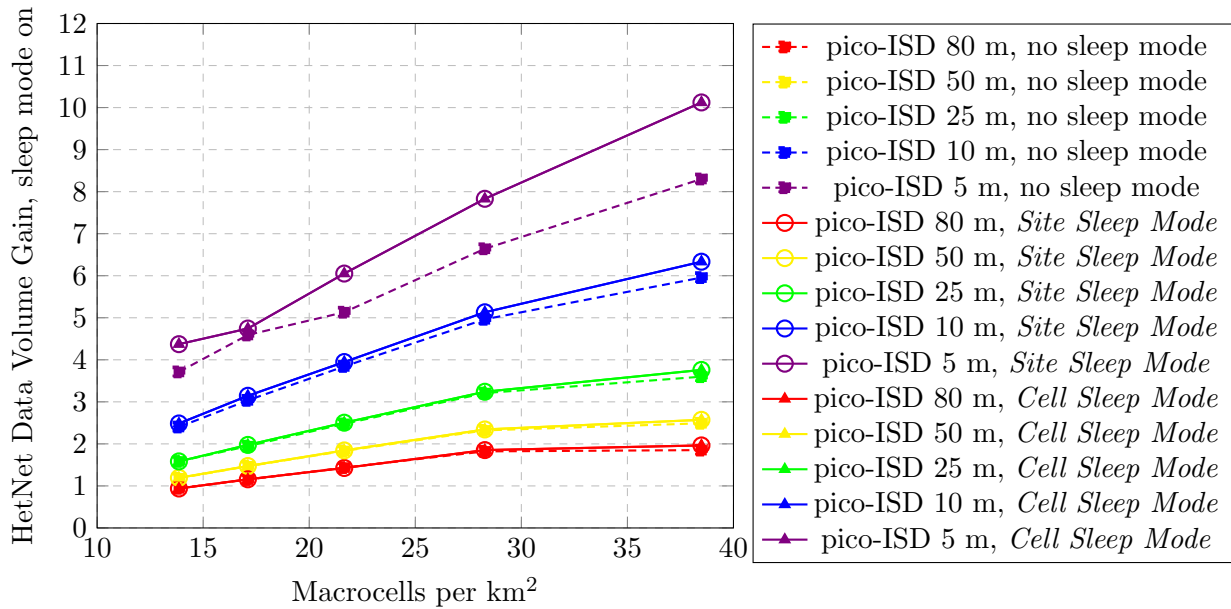


Figure 5.8: HetNet Data Volume Gain against macrocell density, comparing different picocell ISDs and sleep modes: *Site Sleep Mode* and *Cell Sleep Mode*

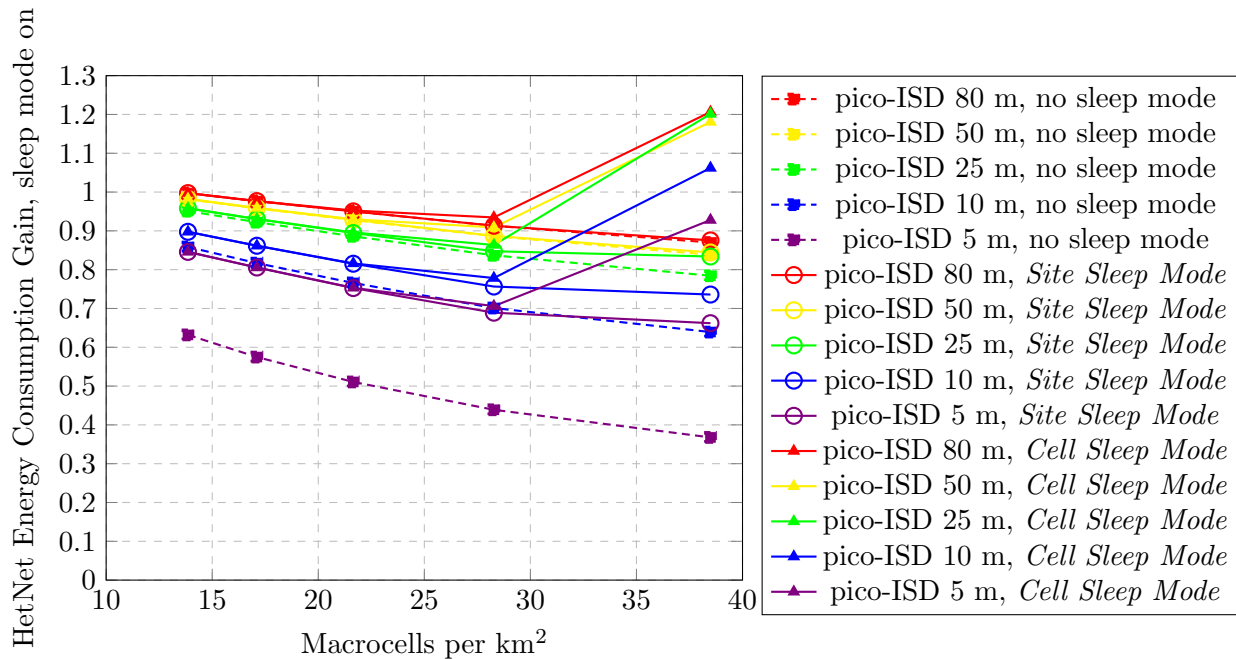


Figure 5.9: HetNet Energy Consumption Gain against macrocell density, comparing different picocell ISDs and sleep modes: *Site Sleep Mode* and *Cell Sleep Mode*

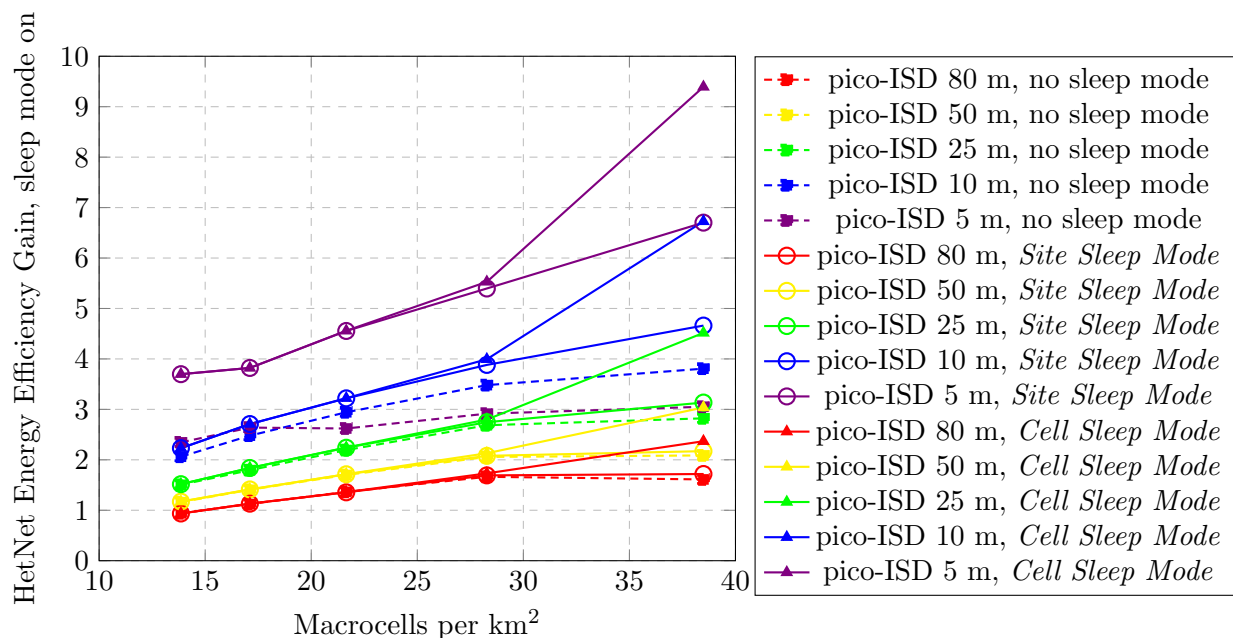


Figure 5.10: HetNet Energy Efficiency Gain against macrocell density, comparing different picocell ISDs and sleep modes: *Site Sleep Mode* and *Cell Sleep Mode*

Fig. 5.10 shows the product of the DVG results in Fig. 5.8 and the ECG results in Fig. 5.10 for the energy efficiency performance under the same conditions. The results show that, compared with the case without the sleep mode, turning *Site Sleep Mode* on improves HetNet EEG due to improved capacity and reduced energy consumption. Further energy efficiency improvement is achieved when switching to *Cell Sleep Mode*, caused by higher energy consumption reduction.

5.5 Densification in Picocell Layer of Heterogeneous RAN

Having analysed the densification in the macrocell layer of the HetNet, this section will turn attention to the densification in the picocell layer. Specifically, the ISD of the picocell would be reduced from 80 m down to 1 m within each UE cluster with a radius of 40 m. This is equivalent to 1 to 4921 picocells per cluster. Similarly, the figures of merit DVG, ECG, and EEG are applied to compare the capacity, energy consumption, and energy efficiency performance with the same reference macro-RAN with 500 m ISD and 300 UEs/km² density. The results of the homogeneous pico-RAN densification will also be included in the following analysis for performance comparison. In this section, macrocells and picocells reduce and fix $\hat{P}_{tx,c}$ against the increasing cell density. The

load activity factor α_c is unity for active cells, 10% for empty cells without sleep mode, and 0% for empty cells with sleep mode. The scheduler is RR.

5.5.1 Picocell Densification without Sleep Mode

Fig. 5.11 graphs the Data Volume Gain against the increasing picocell density, with the macrocell ISD as a parameter, without any sleep mode. The DVG for the homogeneous pico-RAN densification with fixed $\hat{P}_{tx,c}$ approach is also included in the figure for capacity performance comparison.

The main observations are:

1. The picocell density depends on the HetNet RAN area, which changes with the macro-ISD. Hence, the HetNet DVGs show slight picocell density shifts between different macro-ISDs.
2. When macro-ISD is 500 m, the HetNet DVG improves with the increasing picocell density. As picocell density increases, UEs are closer to the picocells, and the signal power is stronger. This enables more traffic offloading from macrocells to picocells. On the other hand, PUEs experience a similar level of interference from macrocells since the relative distance is unchanged. Therefore, PUEs have improved SINR and higher throughput. This leads to capacity and DVG improvement.
3. When macro-ISD reduces to 350 m, the HetNet DVG improves similarly with the increasing picocell density but with gradually bigger absolute values. This is mainly due to the traffic offloading.
4. When macro-ISD is 300 m, the HetNet DVG first increases but then decreases with the increasing picocell density. The capacity improvement is because of the traffic offloading and signal power strengthening. However, with the reduction in ISDs between PBSs and MBSs, the interference increase from the surrounding cells exceeds the signal power strengthening and degrades the SINR. This leads to capacity and DVG degradation. The performance turning point is 2130.46 picocells per square kilometre (pico-ISD of 3 m within the cluster) and macro-ISD of 300 m.
5. HetNet always has worse DVG than the homogeneous pico-RAN counterparts. The reasons are two-fold. First, there are usually many MUEs associated with the same macrocell, and

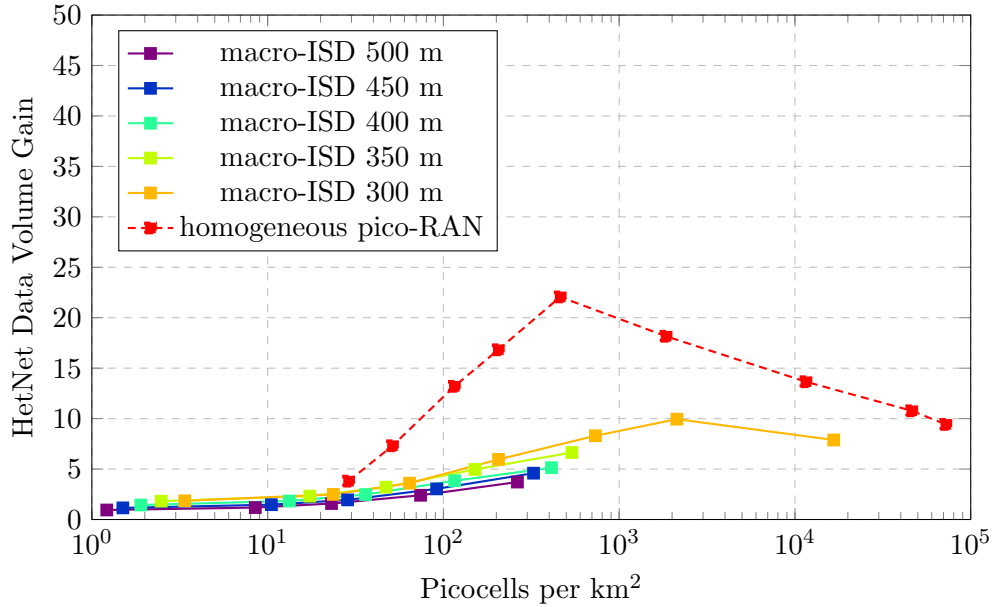


Figure 5.11: HetNet Data Volume Gain against picocell density, comparing different macrocell ISDs

each MUE has a limited RBs allocation. The resultant MUE throughput is low. On the other hand, PUEs have comparatively more RB allocations but suffer from high interference from macrocells. This compromises the PUE SINR and the PUE throughput. Therefore, HetNet achieves lower capacity and DVG than the homogeneous pico-RAN counterparts, in which all UEs are PUEs and free of macrocell interference. Note that HetNet has a higher performance turning point than the homogeneous pico-RAN. This is mainly due to picocells in HetNet being distributed in clusters with a minimum separation of 40 m (also the cluster radius). The interference level is lower than the case in the homogeneous pico-RAN with the same picocell density.

In summary, the boundless HetNet densification without the sleep mode would eventually degrade the capacity. This is true for homogeneous pico-RAN as well.

The Energy Consumption Gain of the densification in the picocell layer of the HetNet is illustrated in Fig. 5.12, with macro-ISD as a parameter. Without sleep mode, active and empty cells consume non-zero energy. Increasing the cell density in either HetNet layer always results in increased energy consumption. Therefore, HetNet ECGs decrease against the increasing picocell density and the reducing macro-ISD. Specifically, the macrocell energy consumption dominates the total energy consumption for picocell density between 1.22 and around 100 picocells per square

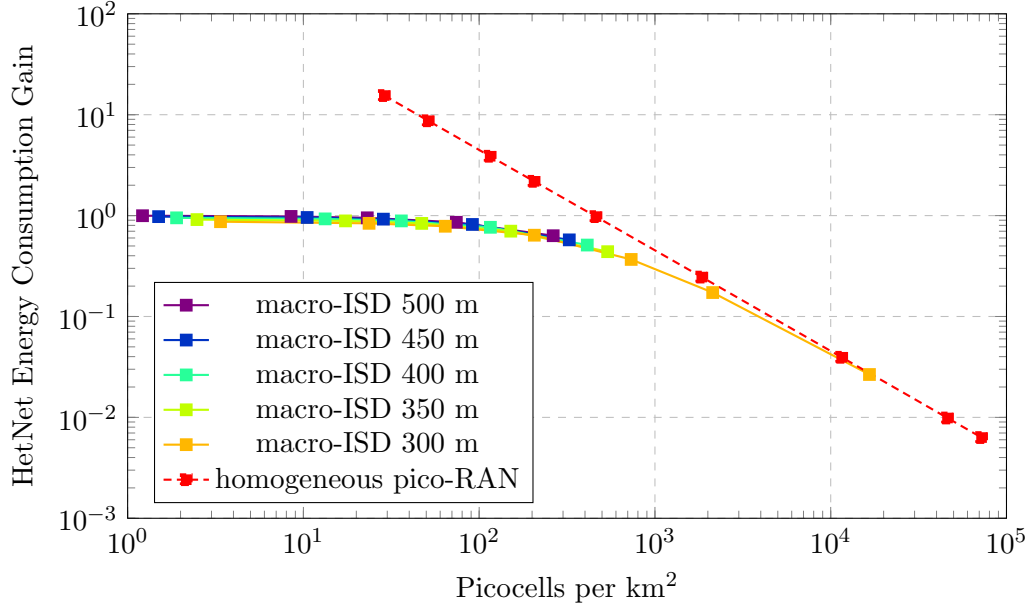


Figure 5.12: HetNet Energy Consumption Gain against picocell density, comparing different macro-cell ISDs

kilometre (pico-ISR between 80 m and 10 m within the cluster). Compared with the reference macro-RAN, the corresponding ECGs are close to unity with a negligible decrease despite the increasing number of picocells. However, further picocell densification changes the dominating role of energy consumption to picocells which has a large number. So the HetNet ECG starts to decrease with a more significant rate and scale. Eventually, the energy consumed by macrocells is negligible compared with the energy consumption by all the picocells; the ECG of HetNet finally overlaps with the homogeneous pico-RAN.

The combined effect of the first-increase-then-decrease capacity performance in Fig. 5.11 and the decreasing energy consumption performance in Fig. 5.12 is captured in Fig. 5.13 for the EEG evaluated HetNet energy efficiency performance. The key observations are:

1. For macro-ISR larger than 300 m, the HetNet energy efficiency performance is dominated by the capacity improvement, so EEG improves with the increasing picocell density.
2. However, when macro-ISR is 300 m, the HetNet EEG first improves due to the increasing DVG but then decreases with the reducing ECG against the growing picocell density. The performance turning point is 205.96 picocells per square kilometre (in-cluster pico-ISR of 10 m) and macro-ISR of 300 m. This is lower than the turning point for DVGs in Fig. 5.11 due

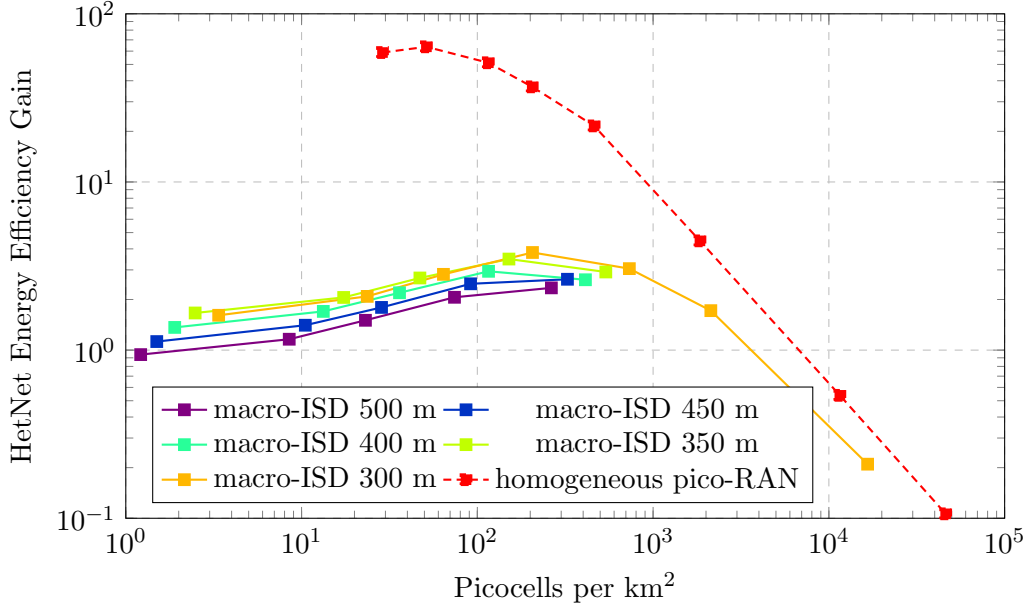


Figure 5.13: HetNet Energy Efficiency Gain against picocell density, comparing different macrocell ISDs

to the significant energy consumption. The energy efficiency degradation is first due to the energy consumption; then, the compromised capacity worsens the situation.

3. For picocell densities higher than 2130.46 picocells per square kilometre (in-cluster pico-ISD of 3 m), the EEG gap between HetNet and the homogeneous pico-RAN counterpart is caused by the capacity difference.

In summary, boundless densification of picocells in HetNet without the sleep mode degrades the energy efficiency because of the compromised capacity and continuously increasing energy consumption.

5.5.2 Picocell Densification with the Sleep Mode

Similarly, the capacity degradation and energy consumption increase caused by picocell densification can be potentially overcome by putting empty cells into sleep mode. Specifically, empty picocells are turned off completely in this sub-section unless stated otherwise; empty macrocells are turned off completely if the *Cell Sleep Mode* is enabled, or macro-BS sites are turned off completely if the *Site Sleep Mode* is on.

Fig. 5.14 illustrates the HetNet Data Volume Gain versus the increasing picocell density, with

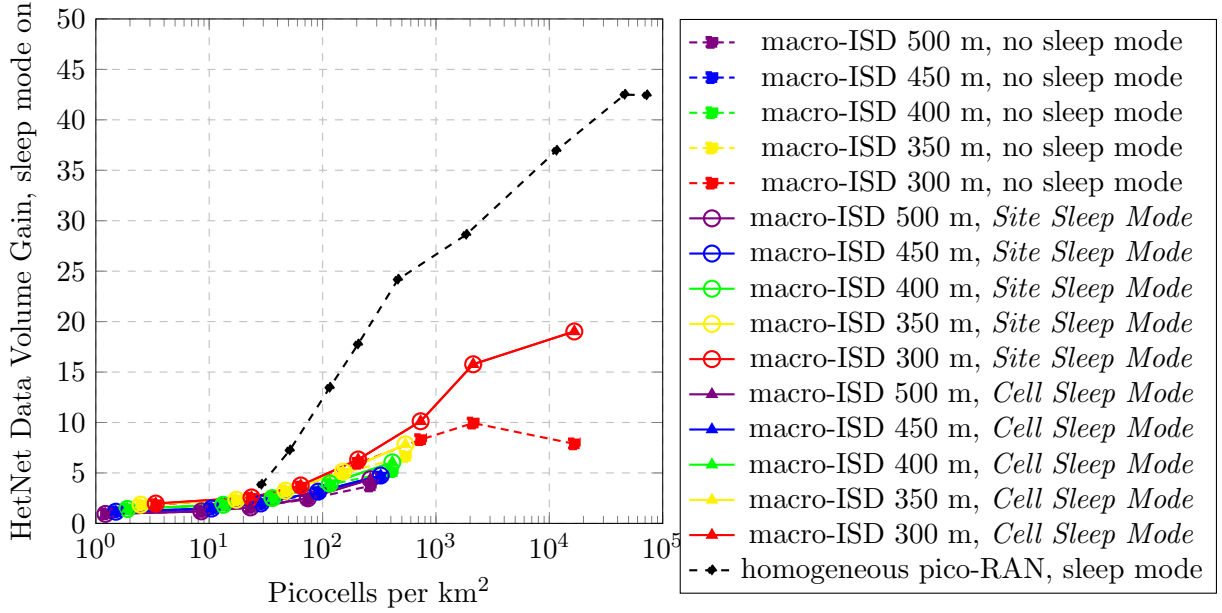


Figure 5.14: HetNet Data Volume Gain against picocell density, comparing different macrocell ISDs and sleep modes: *Site Sleep Mode* and *Cell Sleep Mode*

ma-ISD and sleep mode as variables. Sleep modes turn off the transmission from empty cells and limit the interference. Compared with the case without the sleep mode, this improves the UE SINR and increases the RAN capacity, especially at picocell densities higher than 2130.46 picocells per square kilometre (pico-ISD of 3 m within the cluster). Higher picocell density leads to more empty cells, given a fixed UE density. Therefore, with the sleep mode enabled, the HetNet DVG improves monotonically with the increasing picocell density. Moreover, *Site Sleep Mode* and *Cell Sleep Mode* limit the interference by the same level, so their DVGs overlap. The DVG gap between the HetNet and the homogeneous pico-RAN is caused similarly by the former's low MUE and PUE throughput.

Fig. 5.15 shows the HetNet energy consumption performance, evaluated by ECG, against the increasing picocell densities, comparing different macro-ISDs and sleep modes. The main observations are:

1. Without the sleep mode, HetNet ECG decreases with the increasing picocell density for all macro-ISDs since all the cells consume non-zero energy.
2. When the *Site Sleep Mode* is enabled, empty macrosites and picosites are turned off completely to save energy. This is more effective when picocell density is higher than 205.96 picocells per square kilometre (in-cluster pico-ISD of 10 m) and the number of empty cells increases.

3. When switching to the *Cell Sleep Mode*, empty cells are turned off completely to save energy. This reduces the total HetNet energy consumption further and improves the ECG further. This effect is most distinctive when macro-ISD is 300 m, where the HetNet ECG is above unity until reaching 205.96 picocells per square kilometre. ECG being higher than unity means the HetNet consumes less energy than the reference macro-RAN due to the shutting down of empty macrocells.
4. When picocell density is higher than 2130.46 picocells per square kilometre (pico-ISD of 3 m within the cluster), the HetNet is close to the one-UE-per-active-cell state. Increasing the picocell density further only adds slept cells into HetNet. The HetNet energy consumption increasing rate becomes negligible, and the ECG begins to saturate. This is true for both sleep modes, but the *Cell Sleep Mode* ends with lower energy consumption and thus higher ECG.
5. Compared with the homogeneous pico-RAN ECG result for any picocell density, HetNet consumes more energy and thus has lower ECG because some high-power macrocells are always active.

In summary, applying sleep mode reduces the energy consumption increase against the increasing picocell density. Highly densified HetNet has saturated energy consumption.

The HetNet energy efficiency performance is plotted in Fig. 5.16 against the increasing picocell density, with both macro-ISD and sleep modes as variables. It is shown in the figure that turning either sleep mode on improves the HetNet EEG continuously against the increasing picocell densities and macrocell densities. This energy efficiency improvement comes from the monotonically increasing capacity and constrained energy consumption. Moreover, the *Cell Sleep Mode* reduces the energy consumption more than the site mode; thus, the former has higher EEG than the latter, especially at higher cell densities. Furthermore, the traffic offloading enables the ultra-dense HetNet energy efficiency to behave towards the homogeneous pico-RAN. This EEG gap is because of the lower capacity and the higher energy consumption caused by the co-existing macrocells in HetNet.

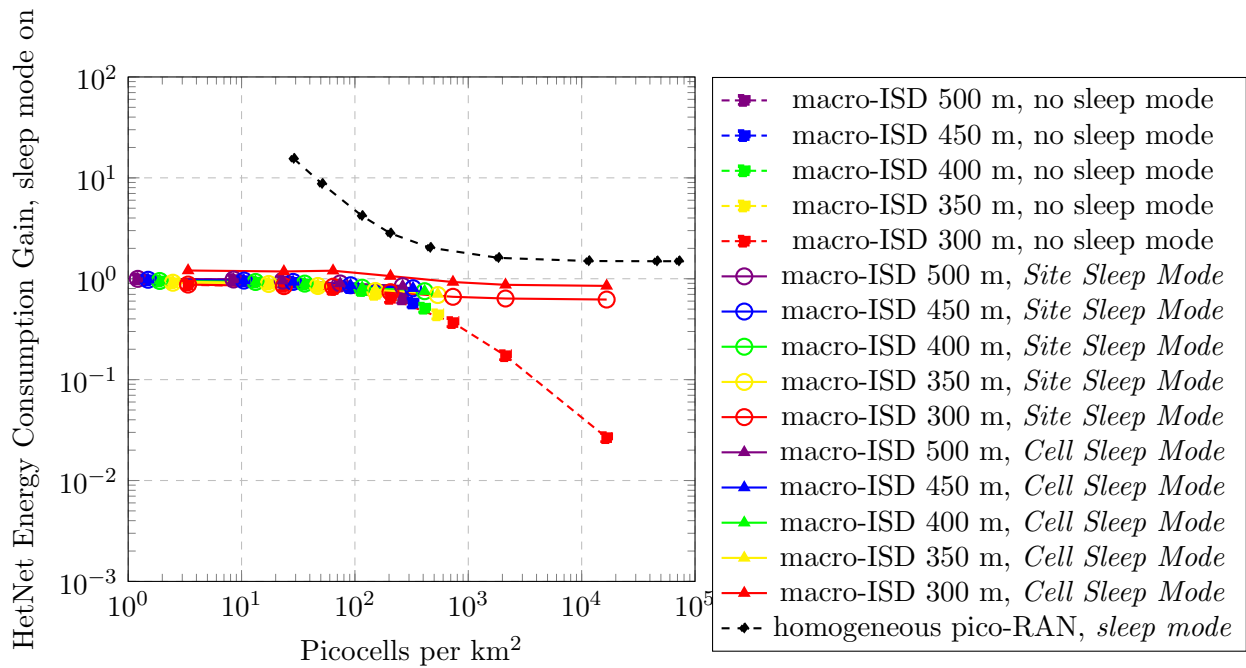


Figure 5.15: HetNet Energy Consumption Gain against picocell density, comparing different macrocell ISDs and sleep modes: *Site Sleep Mode* and *Cell Sleep Mode*

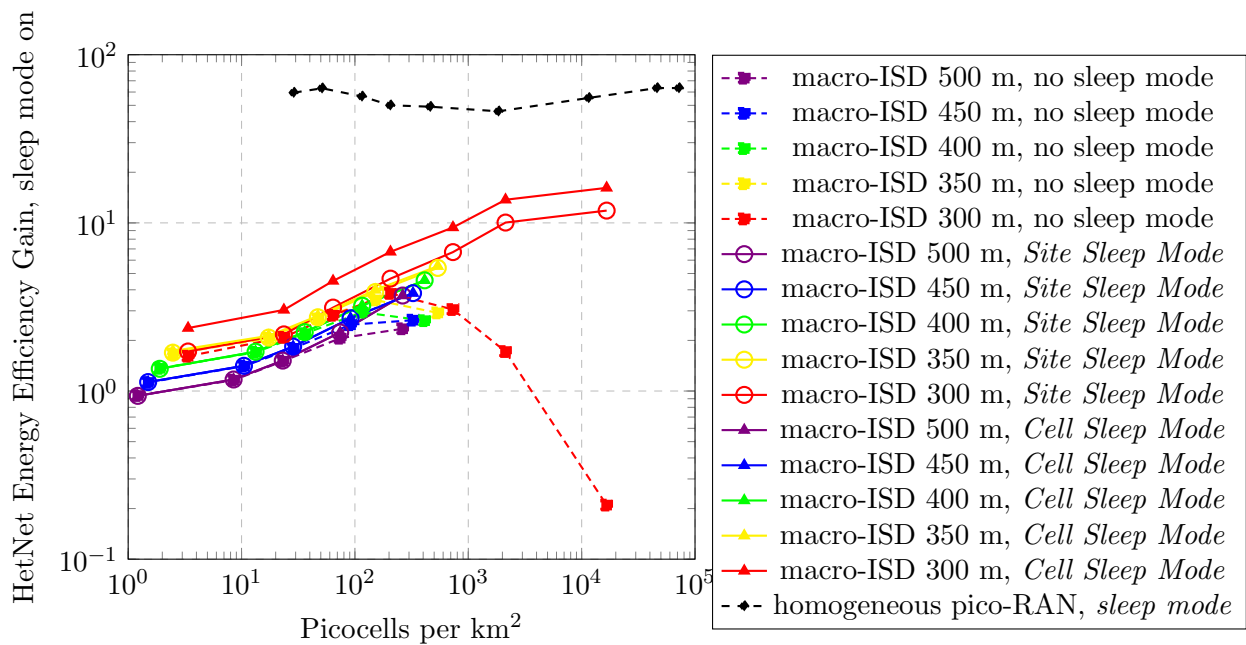


Figure 5.16: HetNet Energy Efficiency Gain against picocell density, comparing different macrocell ISDs and sleep modes: *Site Sleep Mode* and *Cell Sleep Mode*

5.5.3 Picocell Densification Sensitivities

For previous results, sleep modes turn off sites/cells completely to exploit the sleep mode to the extreme. In contrast, this sub-section investigates the HetNet densification sensitivity by gradually reducing the empty site/cell energy consumption to seek the impact on energy consumption and energy efficiency. Specifically, with the baseband and transceiver units staying off in empty sites/cells, the backhaul power consumption is gradually reduced from 10 W to 0 W. The concentration on backhaul is because of its power-consuming dominating role, using the current power model and parameters, in an active picocell, as shown in Chapter 3. Different backhaul power consumption represents different fibre power efficiencies. The DVG results are omitted in this sub-section, assuming that the reduction in backhaul power consumption does not affect the capacity performance. All the results in this sub-section are obtained for macro-ISD being 300 m.

Fig. 5.17 shows the HetNet Energy Consumption Gain, with *Site Sleep Mode* on, against the increasing picocell layer density, with the power consumption of backhaul, P_{BH} , as a variable. The ECG of the homogeneous pico-RAN with P_{BH} being 10 W and 0 W are also included in the figure as an energy consumption performance reference. The figure shows that the gradual reduction of P_{BH} in empty sites saves energy accordingly. However, the total HetNet energy consumption is highly P_{BH} sensitive such that only when empty sites are turned off completely and consume zero energy does the increase in energy consumption becomes negligible. Therefore, only when P_{BH} is 0 W does the ECG increases at a negligible rate against the increasing picocell density. In HetNet, ECG is bounded by the homogeneous pico-RAN ECG. The overlapping of highly densified HetNet and homogeneous pico-RAN ECGs for P_{BH} being 10 W is due to the negligible proportion of macrocell energy consumption. In contrast, the highly densified homogeneous pico-RAN outperforms HetNet when P_{BH} is 0 W because of the non-zero energy consumption of macrocells.

Fig. 5.18 shows the resultant HetNet Energy Efficiency Gain, which is the product of the DVG with macro-ISD 300 m in Fig. 5.14 and the ECGs using *Site Sleep Mode* in Fig. 5.17. The benefit of energy reduction improves energy efficiency accordingly. However, the energy consumption sensitivity shown in Fig. 5.17 is not observed here. For empty sites with P_{BH} higher than 0.1 W, the increasing energy consumption dominates the energy efficiency and the HetNet EEG decreases after reaching 2130.46 picocells per square kilometre (pico-ISD of 3 m within the cluster). In

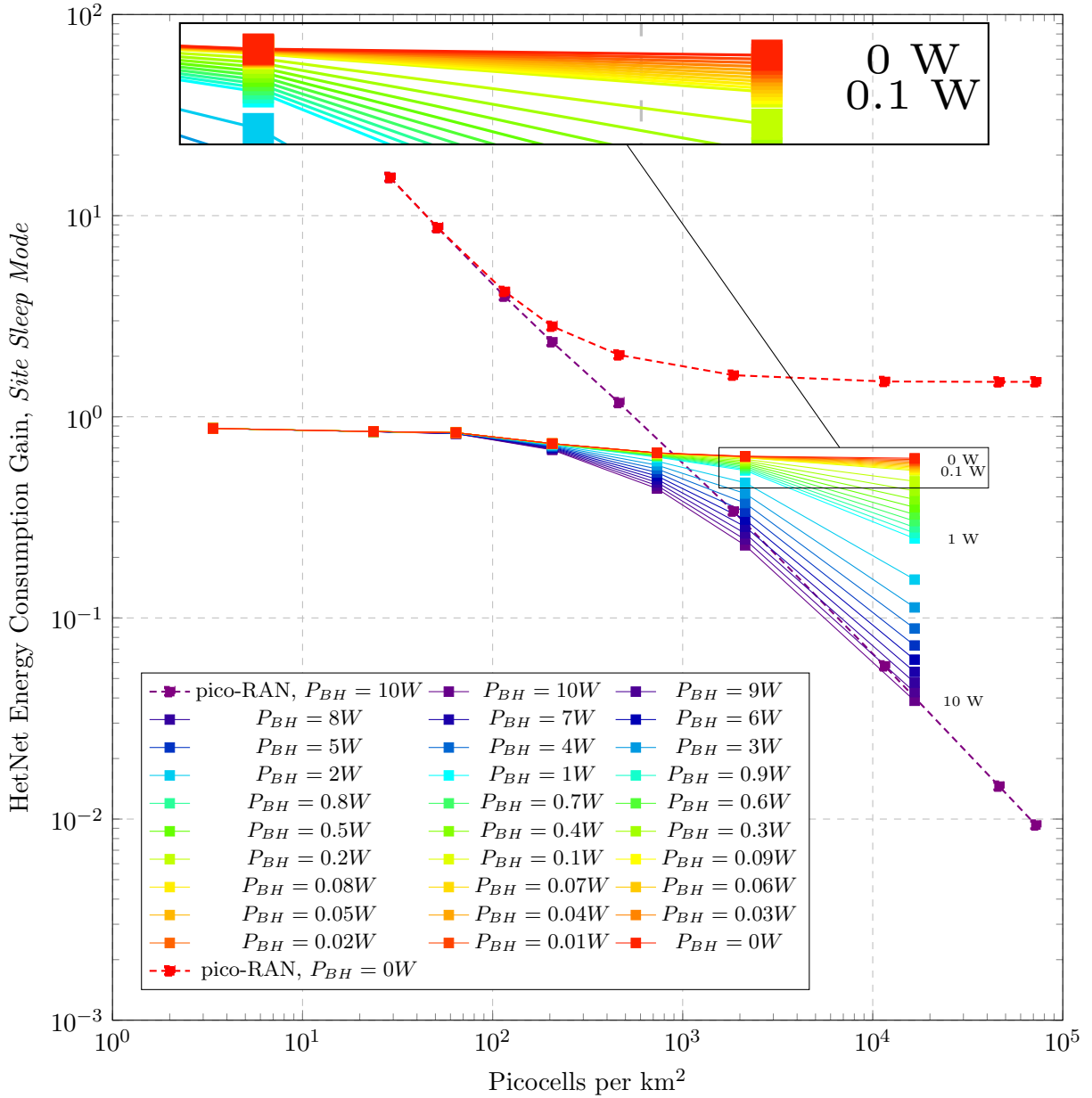


Figure 5.17: HetNet Energy Consumption Gain against picocell density, comparing different backhaul power consumption, P_{BH} , in empty picocells using *Site Sleep Mode*, macro-ISD 300 m

contrast, when P_{BH} in empty cells reduces below 0.1 W, the HetNet EEG improves monotonically with the increasing picocell density. This is because the improving capacity compensates for the small-scale increase in energy consumption. Lower P_{BH} consumed by empty sites results in lower RAN energy consumption and higher energy efficiency. The HetNet is always less energy efficient than the homogeneous pico-RAN with the same picocell density at the same empty cell P_{BH} level due to less capacity and more energy consumption from macrocells. Note that the maximum picocell density considered in HetNet is far less than the one in the homogeneous pico-RAN in Chapter 3 because of the clustered small cell distribution. The ECG behaviour of the homogeneous pico-RAN and HetNet is similar within the same picocell density range. Further picocell densification in HetNet might lead to similar energy consumption sensitivity as the homogeneous pico-RAN, where the energy efficiency improves monotonically only when empty cells are turned off completely. However, the minimum 1 m in-cluster picocell ISD considered for HetNet is already short. Further densification seems unnecessary.

Switching to *Cell Sleep Mode*, Fig. 5.19 shows similar but better HetNet ECGs than Fig. 5.17. Only when empty cells are completely turned off and consume zero energy does the HetNet ECG reduces with a negligible rate against the increasing picocell density. Nevertheless, the HetNet ECG is still bounded within the homogeneous pico-RAN ECG with P_{BH} being 10 W and 0W.

Similarly, Fig. 5.20 shows the impact of empty site P_{BH} on HetNet EEG against the increasing picocell density, which is similar but better than the HetNet EEG in Fig. 5.18 due to extra energy consumption reduction.

5.5.4 Picocell Densification with Schedulers

Previous results are obtained using the RR scheduler as a benchmark. As mentioned in the previous chapter, RR trades off RAN capacity for simple calculation. In contrast, PF trades off calculation complexity for RAN capacity by UE diversity exploitation. The UE diversity is the capability of choosing a certain UE among all the UEs, so it is proportional to the UE number in the cell. Moreover, since the PF performance depends on the UE count in each cell, small cells with a limited number of UE associations might benefit less than the macrocells. Therefore, in this subsection, different scheduling conditions are considered: all cells use RR (RR+RR), all cells use PF (PF+PF), and macrocells and picocells use PF and RR (PF+RR), respectively, to investigate the

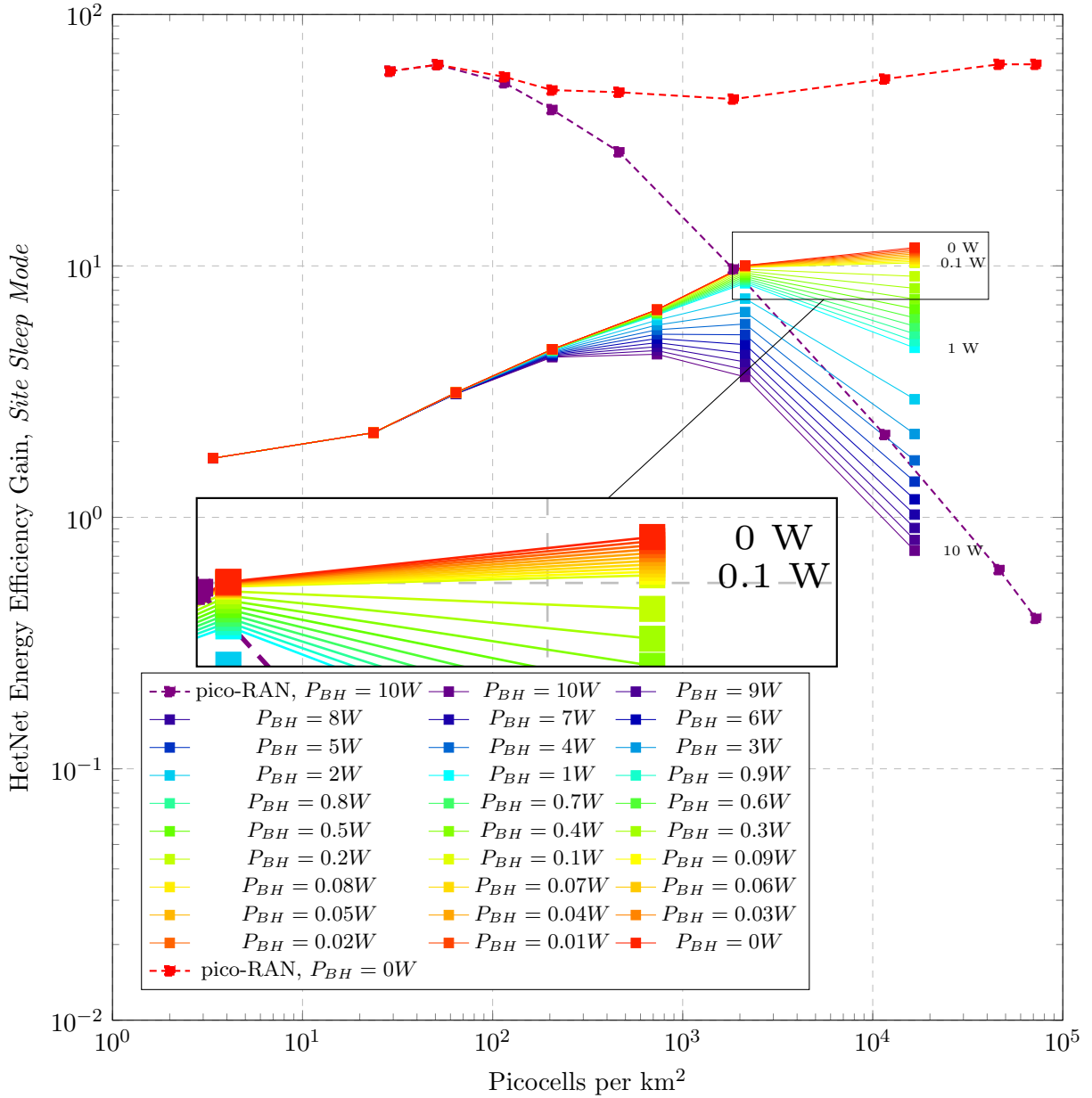


Figure 5.18: HetNet Energy Efficiency Gain against picocell density, comparing different backhaul power consumption, P_{BH} , in empty picocells using *Site Sleep Mode*, macro-ISD 300 m

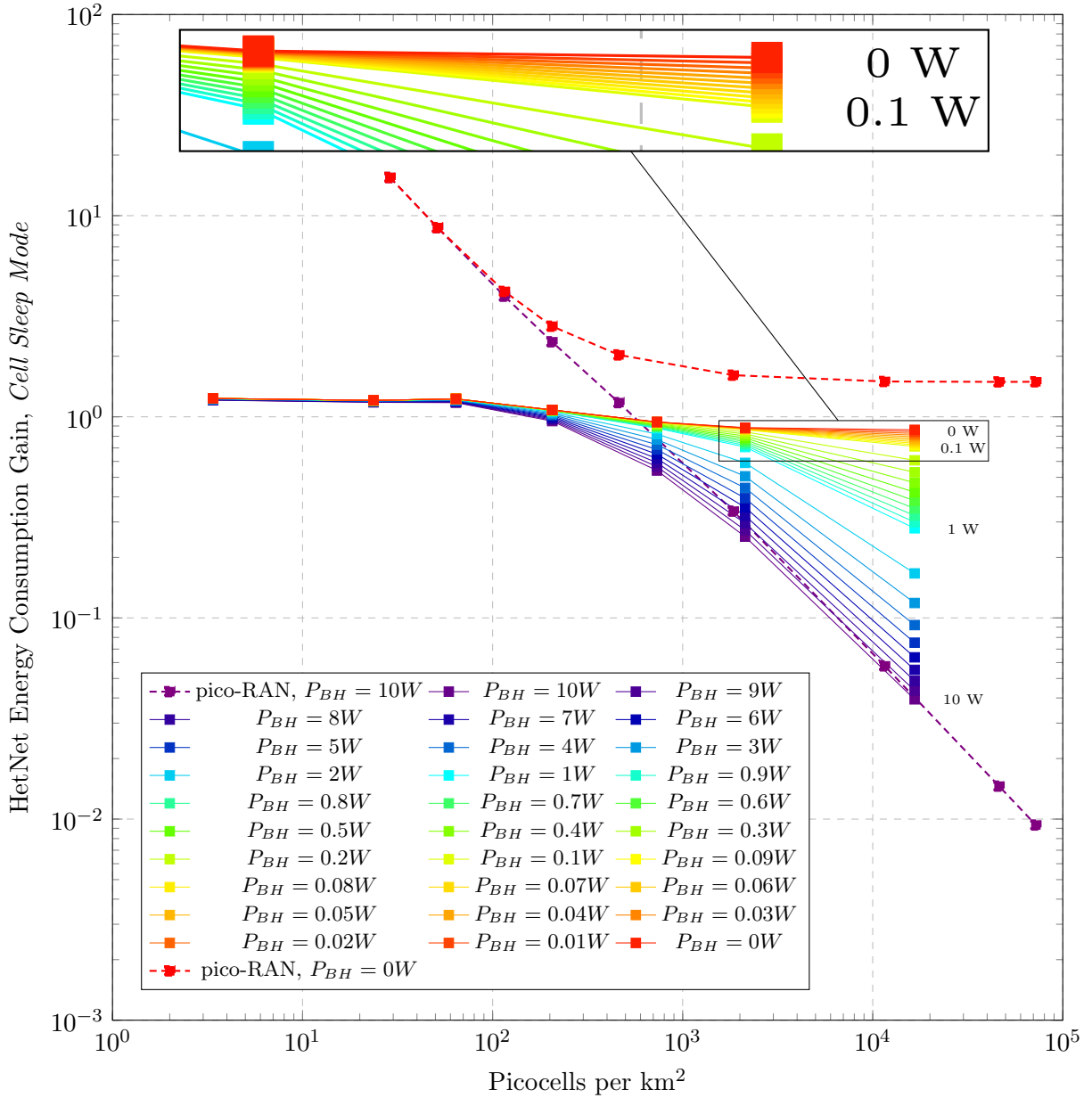


Figure 5.19: HetNet Energy Consumption Gain against picocell density, comparing different backhaul power consumption, P_{BH} , in empty picocells using *Cell Sleep Mode*, macro-ISD 300 m

impact on ultra-dense HetNet energy efficiency. MSINR is not considered here because it biases UE throughput significantly and compromises fairness. The *Site Sleep Mode* and *Cell Sleep Mode* are enabled with P_{BH} being 0 W in empty sites/cells. Macro-ISD is 300 m.

Fig. 5.21 shows the HetNet Data Volume Gain against picocell densities, comparing different sleep modes, *Site Sleep Mode* and *Cell Sleep Mode*, and schedulers. The key observations are:

1. Compared with the case where all cells use RR to schedule resources (RR+RR), the adoption of PF for all cells (PF+PF) improves the capacity via UE diversity exploitation at the cost of extra calculations using Eq. (4.19) to (4.20). However, the number of UEs per cell reduces with the increasing picocell density, and so does the capacity improvement using PF over RR.
2. When macrocells use PF to exploit UE diversity, and picocells use RR for simple computation; the HetNet DVG is in-between cases RR+RR and PF+PF. The number of UEs per macrocell is high for picocell densities below ten picocells per square kilometre, so PF+RR scheduling performs closer to PF+PF. When picocell density is below 1000 picocells per square kilometre, part of MUEs are offloaded to picocells, which reduces the MUE diversity and degrades the PF scheduling gain. Meanwhile, PUEs per picocell increase, leading to lower throughput when scheduled by RR. Overall, PF+RR perform towards RR+RR.
3. When picocell density is 16614.86 picocells per square kilometre (in-cluster pico-ISD of 1 m), there is one UE per active cell, so the DVGs of any scheduling choice converge.
4. *Site Sleep Mode* and *Cell Sleep Mode* turn transmission off in empty cells and limit the interference by the same scale. Therefore, they have the same impact on the HetNet capacity. The HetNet DVG profiles overlap and improve with the increasing picocell density.

Therefore, for ultra-dense HetNet, the RR scheduler is preferred for its simplicity without any performance degradation.

Fig. 5.22 shows the HetNet Energy Consumption Gain against the increasing picocell density, with the schedulers and sleep modes as variables. The scheduler change does not affect UE association, so the active cells in the HetNet are the same regardless of schedulers. Therefore, schedulers do not impact HetNet energy consumption, so ECGs for the same sleep mode, *Site Sleep Mode* or *Cell Sleep Mode*, overlap.

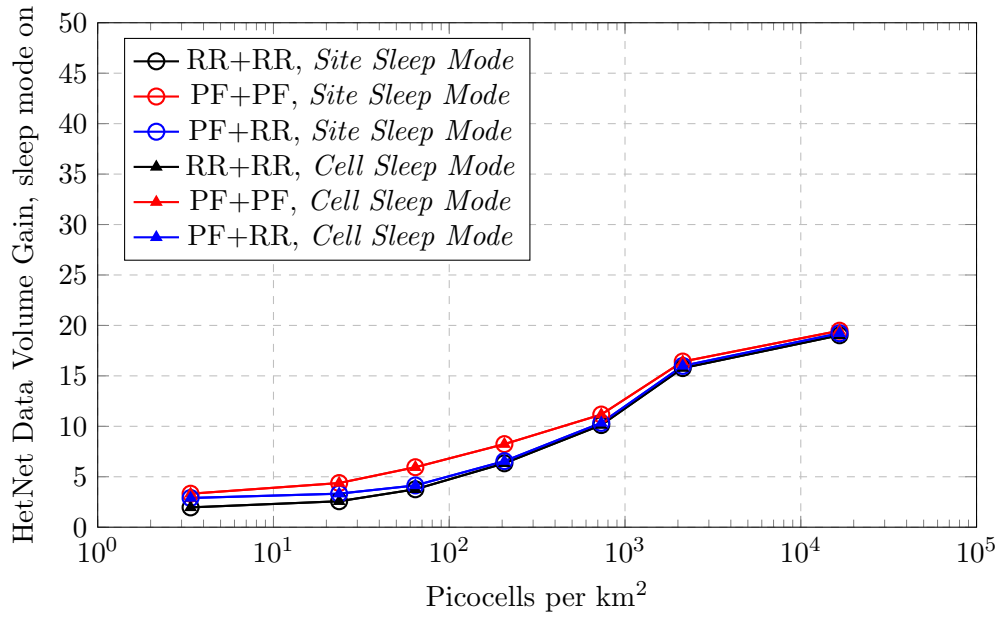


Figure 5.21: HetNet Data Volume Gain against picocell density, comparing different schedulers and sleep modes: *Site Sleep Mode* and *Cell Sleep Mode*, macro-ISD 300 m

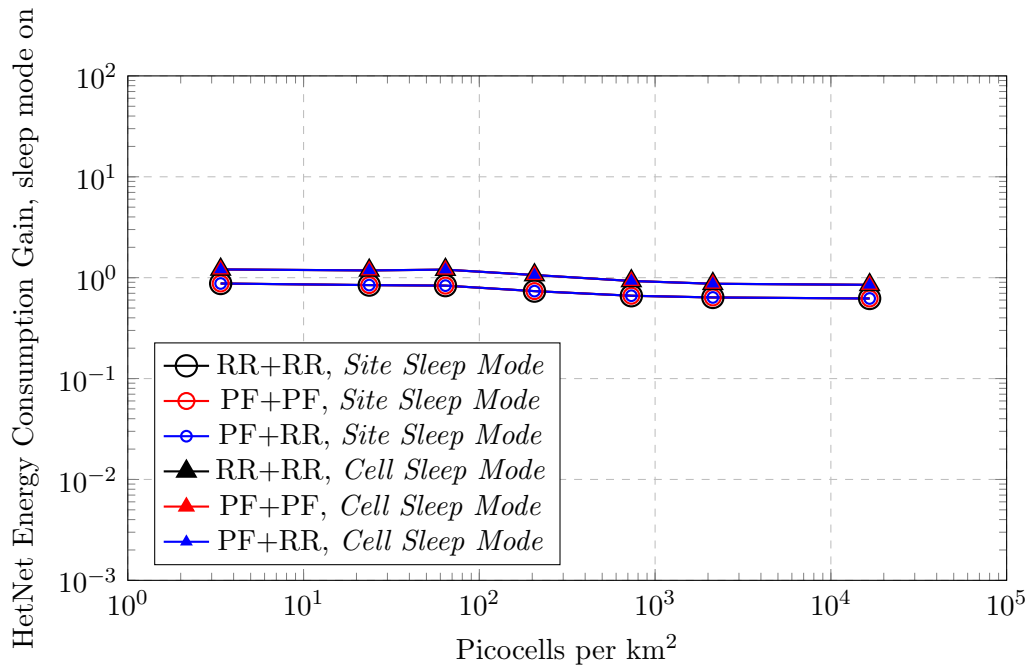


Figure 5.22: HetNet Energy Consumption Gain against picocell density, comparing different schedulers and sleep modes: *Site Sleep Mode* and *Cell Sleep Mode*, macro-ISD 300 m

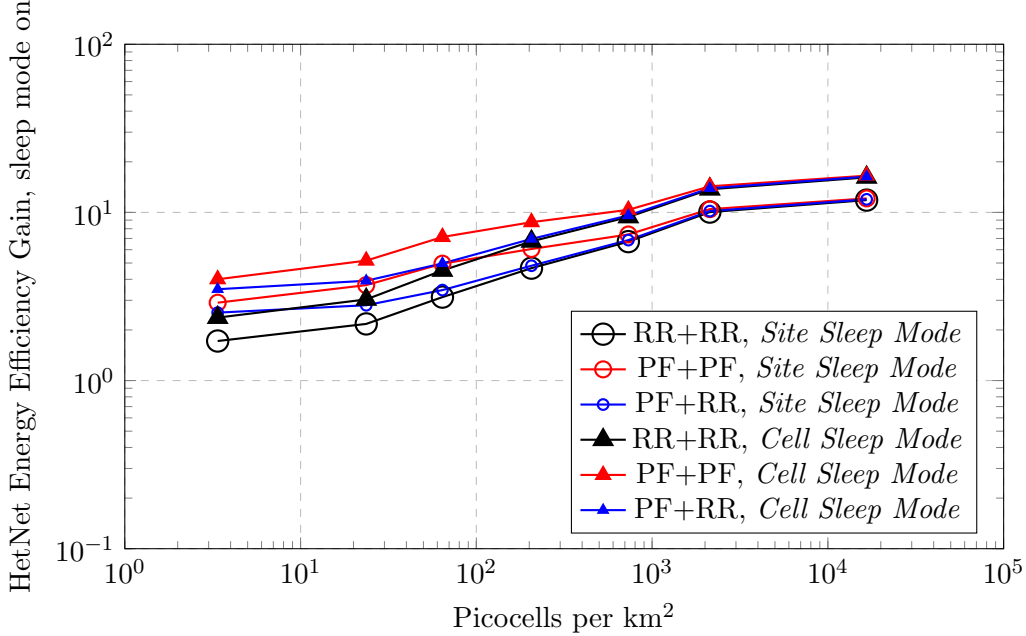


Figure 5.23: HetNet Energy Efficiency Gain against picocell density, comparing different schedulers and sleep modes: *Site Sleep Mode* and *Cell Sleep Mode*, ma-ISD 300 m

Fig. 5.23 plots the HetNet Energy Efficiency Gain against the picocell densities, comparing different schedulers and sleep modes. The EEG results are the corresponding product of DVGs in Fig. 5.21 and ECGs in Fig. 5.22. When the *Site Sleep Mode* is enabled, the always-less-than-unity ECG reduces the DVG difference between different schedulers when transferring to EEG. In contrast, when switching to *Cell Sleep Mode*, the first-larger-than-unity-then-less-than-unity ECG magnifies and then reduces the DVG difference between different schedulers when calculating the EEG. However, regardless of sleep mode types, PF always has the highest EEGs because of the highest DVGs; until the picocell is densified sufficiently, there is only one UE per active cell. Then the EEGs for different schedulers convergences.

Another performance indicator regarding scheduler performance is fairness, which is measured using Jain's fairness index for cell c as:

$$J_c = \frac{\left(\sum_{k \in \mathcal{K}'} S_{UE,k}\right)^2}{N_K \times \sum_{k \in \mathcal{K}'} S_{UE,k}^2} \quad (5.19)$$

where the set \mathcal{K}' contains all the N_K UEs associated with cell c . This is the UE throughput fairness. The RB allocation fairness introduced in Chapter 4 is omitted here as RR and PF behave similarly.

The more difference in the UE throughput in cell c , the lower the fairness. The maximum fairness is unity when all the elements have the same value, while the minimum fairness is $1/N_K$ where one element is unity and the rest are zero. The average fairness across all active cells is thus:

$$J = \frac{1}{N_C^{active}} \sum_{c=1}^{N_C^{active}} J_c \quad (5.20)$$

where N_C^{active} is the number of active cells in the HetNet.

Fig. 5.24 shows the HetNet average cell fairness, which is the UE throughput fairness, against the picocell density with scheduler as a variable. Since different sleep modes do not impact the scheduler performance, the UE throughput obtained using *Site Sleep Mode* is used to generate the fairness index. Based on the characteristics of RR, UEs in the same cell but with different channel conditions have the same share of RB allocations, so the achieved throughput varies a lot. This leads to the lowest fairness index in the figure when all the UEs are scheduled by RR. In contrast, PF allocates RBs partially based on the UE conditions, reducing the difference between the achieved UE throughput. The fairness of PF+PF thus outperforms RR+RR regarding fairness. The PF+RR approach has compromised fairness compared with the PF+PF approach because picocells use RR, increasing the UE throughput difference. Regardless of schedulers, the fairness improves with the increasing picocell density. This is due to the decreasing number of UEs per active cell that reduces the UE throughput difference, which also leads to the fairness convergence towards unity. The fairness analysis indicates that for ultra-dense HetNet, RR is preferred for its simplicity without fairness degradation.

5.6 Summary

This chapter has analysed the energy efficiency of heterogeneous network densification in both macrocell and picocell layers. The HetNet energy efficiency is evaluated using the evaluation framework introduced in Chapter 3, where the Data Volume Gain, Energy Consumption Gain, and Energy Efficiency Gain evaluate the HetNet capacity, energy consumption, and energy efficiency based on the corresponding performance of a pre-selected homogeneous macro-RAN.

The peak transmission power scheme for macrocell and picocell layers was first investigated

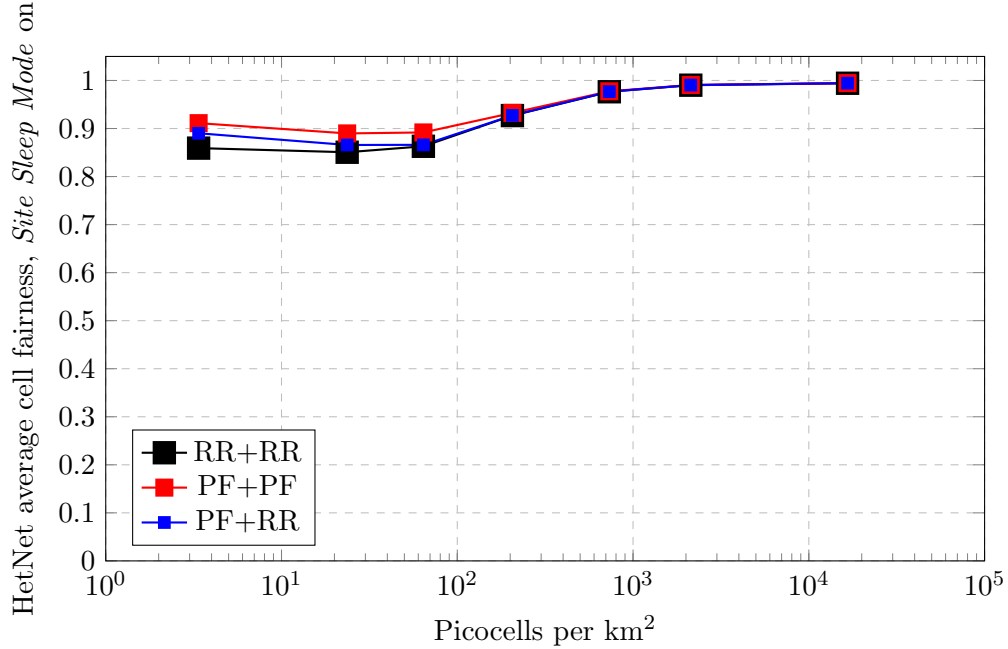


Figure 5.24: HetNet average cell fairness, or UE throughput fairness, against picocell density, comparing different schedulers, macro-ISD 300 m, *Site Sleep Mode* on

to find the best combination that maximises the traffic offloading from macrocells to picocells. The traffic offloading could benefit the HetNet capacity for both macrocell UEs and picocell UEs. The chosen peak transmission approaches are varied and fixed $\hat{P}_{tx,c}$ for macrocells and picocells, respectively, to reduce the transmission power difference.

The simulation results of the macrocell layer densification show that HetNet densification is more energy efficient than the homogeneous macro-RAN densification with the same macrocell density, which could be enhanced further by adopting sleep mode and turning off empty cells or sites completely. This energy efficiency improvement comes from enhanced capacity and constrained energy consumption.

In contrast, the simulation results of the picocell layer densification show that the capacity of HetNet first increases with the densification level and then decreases due to severe interference, which could be overcome by adopting sleep mode and turning off empty sites/cells completely. However, the HetNet capacity is always lower than the homogeneous pico-RAN with the same picocell density, with or without the sleep mode. This is due to the co-existence of macrocells within which MUEs have fewer resources, achieving lower throughput. Meanwhile, PUEs in picocells receive interference from macrocells that compromise the PUEs' throughput. Additionally, the

HetNet consumes more energy than the homogeneous pico-RAN at low picocell densities because of the high-powered macrocells. Further, picocell densification switches the dominating factor of the HetNet energy consumption to picocells, and eventually, HetNet consumes a similar amount of energy with the homogeneous pico-RAN. Adopting the sleep mode reduces energy consumption. However, it is still higher than the homogeneous pico-RAN counterpart for the extra energy consumption by all the active macrocells. Using the current power model, the energy consumption of the backhaul in HetNet is identified as the critical limiting factor of total energy consumption. As a result, the HetNet densification in the picocell layer is the most energy efficient when all the empty sites/cells are turned off completely. The HetNet energy efficiency is less than but approaching the energy efficiency of the homogeneous pico-RAN counterpart, as the former has lower capacity and higher energy consumption.

Finally, the above statements hold for different schedulers. For ultra-dense HetNet, the benchmark RR is preferred for its simplicity without compromising capacity or fairness.

In summary, without the sleep mode, the densification of HetNet, especially in the picocell layer, should be limited. Otherwise, both the capacity and energy efficiency would be compromised. Furthermore, highly densified HetNet with most UEs associated with picocells behaves towards the homogeneous small cell RAN. Therefore, with the sleep mode, the HetNet densification is also expected to be limited to a higher level where the capacity and energy consumption are saturated. However, the performance saturation could be prevented by adopting techniques that could improve capacity and reduce energy consumption. In the next chapter, the signal transmission band would migrate from the sub-6 GHz to millimetre wave for wider bandwidth to enhance capacity. Additionally, the integrated access and backhaul would be adopted so that not all small cells in the highly-dense distribution have to be equipped with wired backhaul, which reduces the implementation and maintenance cost.

Chapter 6

The Energy Efficiency of Dense Homogeneous RANs with Millimetre Wave and Integrated Access and Backhaul

6.1 Introduction

The combined effect of the increasing number of mobile devices and higher data rate requests for applications like online gaming and video watching has urged the communication network to improve capacity continuously and quickly [188]. Shannon's capacity equation $C = B \times \log_2(1 + \gamma)$, where C is the channel capacity, B is the bandwidth, and γ is the achieved SINR, shows that the capacity would improve with the channel bandwidth and the SINR. In addition to having the spatial reuse as the major cause for the capacity improvement of the densified small cell RAN, BS densification also brings UEs closer to their serving BSs and improves UE SINR in the noise limited region that improves capacity [189]. However, the capacity could only improve to some extent if the signal is transmitted using the conventional sub-6 GHz frequency band with limited bandwidth. Therefore, researchers and network designers are turning attention to the under-exploited frequency band above 6 GHz, also known as the mmWave band, whose bandwidth could be much higher for

further capacity boost.

The study on mmWave is already well developed in the literature [188]–[190]. The wide channel bandwidth that comes with mmWave is proved to improve the RAN capacity and energy efficiency [190]. Though the path loss decreases quickly with mmWave due to the high frequency, the application to dense small cell RANs is still effective [71]. Additionally, because of the short wavelength, implementing antenna arrays containing a large number of antennas of small dimensions becomes feasible [142]. This gives rise to the high directivity of a narrow antenna beam that could improve the RAN capacity [142]. Furthermore, the wide bandwidth makes the IAB technology feasible, where the UE traffic and backhaul traffic share the same resource. The application of IAB equips some BSs with wireless backhaul links, reducing the backhaul implementation and maintenance cost [71].

However, small cell RAN densification using mmWave still increases energy consumption, even worse when many antennas are included. Sleep mode is adopted to mitigate this problem where empty cells will be turned off.

This chapter analyses the energy efficiency of the small cell RAN densification using both mmWave and IAB techniques. The evaluation metrics include the three ratio-based figures of merit introduced in Chapter 3: the Data Volume Gain for capacity evaluation, the Energy Consumption Gain for energy consumption evaluation, and the Energy Efficiency Gain for energy efficiency evaluation. The homogeneous infrastructure is considered in this chapter as a fundamental starting point for the densification limit on the 5G RAN energy efficiency. The node association criteria, the time resource partitioning between access and backhaul links, the backhaul rate constraint approaches on node UEs, and sleep mode are investigated alongside the picocell densification. Access links are used for UE traffic between BSs and UEs, while backhaul links are used for backhaul traffic between BSs and the core network. The simulation results show that evolving to the mmWave band improves the RAN capacity, with or without the IAB. However, the energy consumption is significant using the current power model assuming fully digital signal processing. Sleep mode can overcome this issue and recover the energy efficiency when UE density is 300 UEs/km², but fail to preserve the energy efficiency when UE density is 900 UEs/km², which activates more small cells. Nevertheless, the pico-RAN on mmWave and IAB is less energy efficient than the pico-RAN on the LTE sub-6 GHz band within the considered picocell density.

The rest of the chapter is structured as follows. Section 6.2 provides the system model of mmWave and IAB, with extra details on node association, resource partitioning between access and backhaul links, and dynamic backhaul rate constraint calculation. The modified power model is also included to accommodate the wide bandwidth and large antenna number that comes with the mmWave. Section 6.3 presents the simulation results of pico-RAN densification with mmWave, in terms of with and without the IAB, node association criteria, time resource partitioning methods, backhaul rate constraint approaches, and sleep mode. Finally, Section 6.4 draws the conclusions.

6.2 System Model

This section introduces the system model of the homogeneous RAN with mmWave and IAB. Specifically, the mathematical expressions for UE received power, channel loss, UE SINR, and UE throughput are presented. After illustrating the simulation flowchart, extra detail will be introduced regarding the extension of the LTE-based MATLAB simulator to include the 5G mmWave and IAB techniques. Then the backhaul SINR and rate constraints on node UEs are presented, along with the constrained UE and RAN throughput. The modified power model to cope with mmWave is also included at the end.

6.2.1 Homogeneous RAN Layout

This chapter considers the downlink access and backhaul traffic with IAB. The investigated homogeneous RAN evolves from the 4G LTE technology covered in Chapters 4 and 5 into the 5G and beyond, including mmWave band, large antenna array, and IAB. The new UE rate cap is increased to 400 Mbit/s [191] due to technological advancement. Additionally, Time Division Multiplexing (TDM), where the resource between UEs and backhaul transmissions are divided in the time domain, and Spatial Division Multiplexing (SDM), via BS site sectorization, are considered here [192], [193]. There are N_B identical small cell BSs regularly distributed in the RAN area in a hexagonal manner. The small cell BS set is denoted as $\mathcal{B} = \{1, 2, \dots, b, \dots, N_B\}$. Each small cell BS includes three small cells that are denoted as the set $\mathcal{C} = \{1, 2, \dots, c, \dots, N_C\}$. Each small cell is equipped with a rectangular antenna array, and the radiation pattern will be discussed later. Among all the N_B BSs, N_D are pre-selected as donor sites with fibre backhaul links from the core network. The

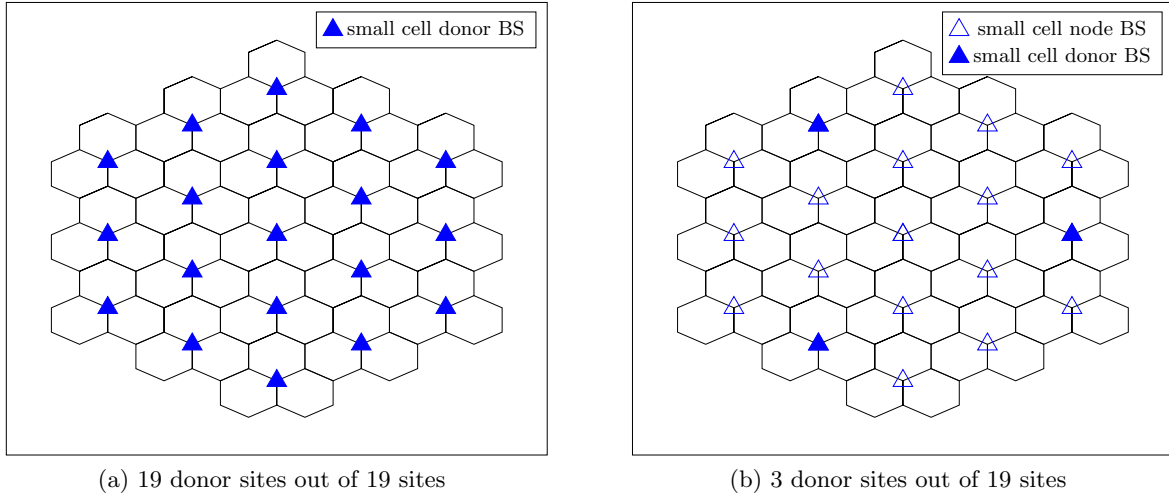


Figure 6.1: Example of a Homogeneous small cell RAN layout with 19 BS sites and 57 cells, 19 or 3 donor sites out of the total 19 donor sites

remaining $N_N = N_B - N_D$ BSs are node sites that receive wireless backhaul from donors and other nodes when multiple backhaul connection hops are allowed. Fig. 6.1 illustrates the small cell RAN layout examples where 19 and 3 out of 19 BS sites are pre-selected to be donor sites while the rest are nodes. When all the 19 small cell BSs are donors, IAB is disabled, and all the small cell sites have fibre backhaul links connecting with the core network directly. The edge effect is prevented using the wrap-around introduced in Chapter 4.

UEs have clustered distribution to model more closely to a realistic traffic scenario. The same as in Section 5.2, UEs are divided into two groups. UEs in the first group have uniform random x and y coordinates in the RAN area. In contrast, UEs in the second group are further divided evenly into several sub-groups, and UEs in each sub-group have uniform random angles and distances within a circular cluster area with reference to the cluster centre. The cluster centres have uniform random x and y coordinates within the RAN area, and the distances between each cluster centre pair are always above a minimum separation. The UE set is denoted as $\mathcal{K} = \{1, 2, \dots, k, \dots, K\}$. All UEs are assumed to be active and outdoor all the time, where each UE is equipped with an antenna array with fewer antenna element numbers than the BSs. The full buffer traffic model is assumed, so UEs always demand data from serving cells and the core network. UEs always choose the small cell from which they can receive the strongest signal.

6.2.2 UE Received Power and Channel Model

The signal received by an arbitrary UE k from the BS in a random small cell c experiences path loss (PL), shadow fading (SF), and multipath fading (MPF), which is enhanced by the BS antenna gain $G_{BS,c,k}$ in units of dBi and UE antenna gain $G_{UE,c,k}$ in units of dBi. Mathematically, the power in dBm received by UE k from the BS in small cell c on an arbitrary RB n in TTI $t = 1, \dots, T$ is:

$$P_{rx,c,k}(n, t) [\text{dBm}] = P_{tx,c,k}(n) [\text{dBm}] + G_{BS,c,k} [\text{dBi}] + G_{UE,c,k} [\text{dBi}] - L_{c,k}(n, t) [\text{dB}] \quad (6.1)$$

where $P_{tx,c,k}(n)$ is the per RB transmission power in dBm from the BS in small cell c , and $L_{c,k}(n, t)$ is the per RB per TTI channel loss. Power control is not considered in this chapter, so the transmission power for all the RBs are the same and is related to the total transmission power $P_{tx,c}$ from the BS in small cell c as:

$$P_{tx,c,k}(n) = \frac{P_{tx,c}}{N_{RB}} \quad (6.2)$$

where N_{RB} is the total number of RBs per TTI for the considered mmWave bandwidth.

As mentioned, small cells and UEs are equipped with rectangular panel antenna arrays, the schematic of which is shown in Fig. 6.2 [194]. In the figure, black squares represent antenna panels, each consisting of uniformly distributed antenna elements, represented by crosses. Antenna panels are separated by distances $d_{g,V}$ and $d_{g,H}$ in the vertical and horizontal directions, respectively. Each antenna panel has M and N cross-polarized antenna elements in the vertical and horizontal directions, respectively. This schematic helps explain the antenna arrays used for small cells and UEs.

The antenna array radiation patterns for small cells and UEs are shown in Fig. 6.3 and 6.4, respectively, as suggested in [194], [195]. Both patterns are generated using the MATLAB built-in object *phased.NRRectangularPanelArray* directly. This is available in MATLAB starting from version R2021a. The array schematics are shown at the bottom left of each figure. The small cell antenna array shown in Fig. 6.3 has two antenna panels in the vertical and horizontal directions, respectively, and each antenna panel has $M = 4$ and $N = 8$ cross-polarized antenna elements. This adds up to 128 antenna elements per small cell. In contrast, Fig. 6.4 shows the UE antenna array with a single antenna panel, consisting of $M = 2$ and $N = 4$ cross-polarized antenna elements. This

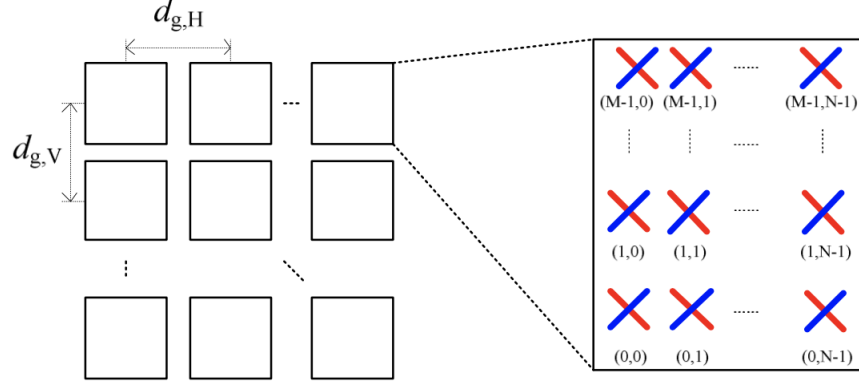


Figure 6.2: 3GPP rectangular panel antenna array schematic

adds up to 8 antenna elements per UE. For both small cells and UEs, antenna panels are separated by $d_{g,V} = 4 \times \lambda$ and $d_{g,H} = 2 \times \lambda$, and antenna elements are separated by $\lambda/2$ in both directions, where λ is the signal wavelength. Note that for BSs, the chosen separation values for antenna panels and elements cause overlapping antenna element positions, so only 96 antenna elements are visible in the schematic of Fig. 6.3 instead of 128. The mathematical antenna radiation pattern for individual antenna element for both small cells and UEs, as suggested in [194], [195], are:

$$G_V(\theta) [\text{dB}] = -\min \left[12 \left(\frac{\theta - 90^\circ}{\theta_{3dB}} \right)^2, SLA_v \right] \quad (6.3)$$

and

$$G_H(\phi) [\text{dB}] = -\min \left[12 \left(\frac{\phi}{\phi_{3dB}} \right)^2, A_m \right] \quad (6.4)$$

where G_V and G_H are the vertical and horizontal patterns of the antenna element, respectively; θ is the vertical angle ranging from 0 to 180 degree; ϕ is the horizontal angle ranging from -180 to 180 degree; θ_{3dB} and ϕ_{3dB} are the HPBWs in the vertical and horizontal directions, respectively, in units of degree; SLA_v is the absolute antenna sidelobe attenuation in dB; and A_m is the absolute front-to-back attenuation in dB. The antenna element is simulated using the built-in MATLAB object *phased.NRAntennaElement* directly, which is introduced in MATLAB R2021a version.

The per RB per TTI channel loss $L_{c,k}(n, t)$ includes PL, SF, and MPF, which are denoted as $L_{PL,c,k}$, $L_{SF,c,k}$, and $L_{MPF,c,k}(n, t)$, respectively. PL and SF depend on the locations of the UEs and BSs and change every independent Monte Carlo run. Specifically, as suggested in [194], the

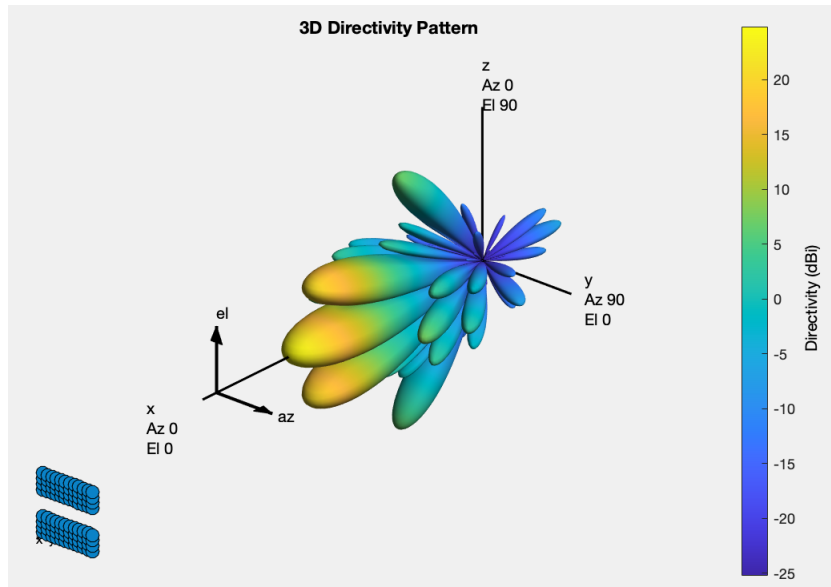


Figure 6.3: 3GPP small cell antenna array 3D radiation pattern, $G_{BS,c}$, maximum gain 32.08 dBi, boresight at (0,0) degrees, 128 antenna elements, cross-polarization, generated using MATLAB built-in objects and 3GPP suggested parameters

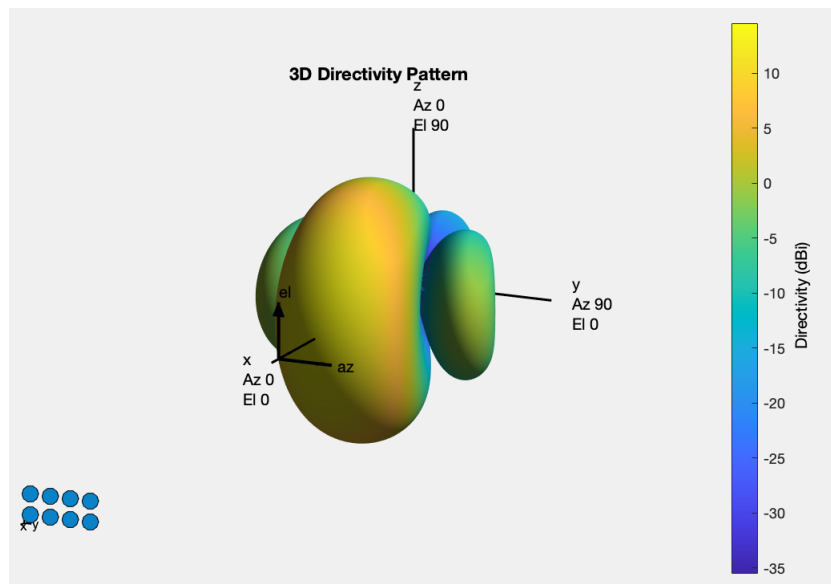


Figure 6.4: 3GPP UE antenna array 3D radiation pattern, $G_{UE,k}$, maximum gain 17.04 dBi, boresight at (0,0) degrees, 8 antenna elements, cross-polarization, generated using MATLAB built-in objects and 3GPP suggested parameters

PL along the LoS and NLoS paths are:

$$L_{PL,c,k}^{LoS} [\text{dB}] = \beta^{LoS} + \zeta^{LoS} \times \log_{10}(d_{3D,c,k}) \quad (6.5)$$

and

$$L_{PL,c,k}^{NLoS} [\text{dB}] = \max \left\{ L_{PL,c,k}^{LoS}, \beta^{NLoS} + \zeta^{NLoS} \times \log_{10}(d_{3D,c,k}) \right\}, \quad (6.6)$$

respectively, where β^{LoS} and β^{NLoS} are dimensionless constants for LoS and NLoS paths, respectively; ζ^{LoS} and ζ^{NLoS} are the path loss exponents for LoS and NLoS paths, respectively; and $d_{3D,c,k}$ is the 3D distance between UE k and BS in cell c with units of metre including the height difference. All the path loss related constants depend on BS and UE heights, the communication environment and the signal carrier frequency. The total path loss is weighted by the LoS probability, as suggested in [194], whose expression is:

$$Pr_{c,k}^{LoS} = \begin{cases} 1 & d_{2D,c,k} \leq 5 \text{ m} \\ \exp\left(-\frac{d_{2D,c,k}-5}{70.8}\right) & 5 \text{ m} < d_{2D,c,k} \leq 49 \text{ m} \\ \exp\left(-\frac{d_{2D,c,k}-49}{211.7}\right) \times 0.54 & d_{2D,c,k} > 49 \text{ m} \end{cases} \quad (6.7)$$

where $d_{2D,c,k}$ is the 2D distance between UE k and BS in small cell c with units of metre excluding the height difference.

The shadow fading $L_{SF,c,k}$ is modelled as a normal distribution for simplicity, the mean μ_{SF} and standard deviation σ_{SF} of which for LoS and NLoS paths are listed in Table 6.3 as suggested in [194]. This chapter also considers the correlation between locations using the shadow fading auto-correlation suggested in [194], with the normalised expression:

$$R_{cor} = \exp\left(-\frac{|d_{2D,k1,k2}|}{d_{cor}}\right) \quad (6.8)$$

where $|d_{2D,k1,k2}|$ is the absolute 2D distance between UEs $k1$ and $k2$ in units of metre, and d_{cor} is the correlation length with units of metre that is dependent on the communication environment. Similar to the path loss, the shadow fading capturing both the LoS and NLoS transmissions is also LoS probability weighted.

The per RB per TTI multipath fading in this chapter is still Rayleigh fading for simplicity. Though the application of Rayleigh fading on such a wide mmWave bandwidth is not accurate with maximum diversity between RBs, it provides a fundamental understanding and the general tendency investigation with simple calculation [68], [196]. Future studies would employ a more accurate multipath fading model that is less frequency selective.

The total channel loss experienced by the signal from the BS in small cell c to UE k per RB per TTI is thus:

$$L_{c,k}(n, t) \text{ [dB]} = \left(L_{PL,c,k}^{LoS} \text{ [dB]} + L_{SF,c,k}^{LoS} \times R_{cor}^{LoS} \text{ [dB]} \right) \times Pr_{c,k}^{LoS} + \left(L_{PL,c,k}^{NLoS} \text{ [dB]} + L_{SF,c,k}^{NLoS} \times R_{cor}^{NLoS} \text{ [dB]} \right) \times (1 - Pr_{c,k}^{LoS}) + L_{MPF,c,k}(n, t) \text{ [dB]}. \quad (6.9)$$

6.2.3 UE Throughput and RAN Area Throughput

Based on the received power by UE k from the BS in small cell c given by Eq. (6.1), the per RB per TTI SINR of the UE is:

$$\gamma_{c,k}(n, t) = \frac{P_{rx,c,k}(n, t)}{\sum_{c' \in \mathcal{C} \setminus \{c\}} P_{rx,c',k}(n, t) + \sigma_n^2}. \quad (6.10)$$

where c' is the index of the interfering cell of UE k , which belongs to the intersection of the total cell set \mathcal{C} and the set containing UE k 's serving cell c , and σ_n^2 is the noise variance including both a 13 dB UE noise figure [195] and the thermal noise [18], [32], [74]. Assuming universal frequency reuse, UEs experience inter-site and intra-site interference, the latter coming from the other two small cells belonging to the same BS site. This intra-site interference could be mitigated by positioning each cell antenna array appropriately.

Using the Shannon's capacity formula, when configured with a RB structure similar to LTE, the per TTI UE throughput is calculated as:

$$\tilde{S}_{UE,k}(t) = \frac{12 \times 14 \times \sum_{n=1}^{N_{RB}} \log_2 \left(1 + \gamma_{c_k,k}(n, t) \right)}{\delta_t} \quad (6.11)$$

where 12 is the sub-carrier number in RB n , 14 is the symbol number in RB n , and δ_t is the 1 ms

time spread of a single TTI. Under TDM, each UE is allocated with a certain number of TTIs and all the RBs included.

For a total period of T , the average UE throughput is:

$$S_{UE,k} = \frac{1}{T} \sum_{t=1}^T (I_{k,t} \times \tilde{S}_{UE,k}(t)) \quad (6.12)$$

where $I_{k,t}$ is the TTI allocation indicator which equals 1 if TTI t is allocated to UE k with all the RBs available included, and 0 otherwise.

6.2.4 Homogeneous RAN Simulation Flowchart Including Millimetre Wave and Integrated Access and Backhaul

Fig. 6.5 shows the MATLAB-based simulation flowchart of the homogeneous RAN using mmWave and IAB. Having set up the simulation parameters, BSs are distributed and fixed for all the independent Monte Carlo runs. In contrast, the cluster origins and UE positions within each cluster change every Monte Carlo run to generalise the results. The UE association process is shown in Fig. 6.6 and will be discussed later. If IAB is enabled, node association, resource partitioning between access and backhaul links, and backhaul rate constraint calculation are required. These are shaded in the flowchart and will be discussed in detail later. These three steps are not included in the sub-6 GHz case in Chapter 4. Finally, active cells with UE association will schedule the time resource to UEs and the resultant UE and RAN throughput can be calculated. The resource allocation process is also shaded in the flowchart because it has two differences from the sub-6 GHz case. First, UEs in this chapter are allocated with TTIs and all the RBs included, while the RBs in the same TTI can be assigned to different UEs in the sub-6 GHz case. Secondly, the total T TTIs are allocated to UEs in the sub-6 GHz case, while in this chapter, only a portion of T TTIs is allocated to UEs in some cells due to IAB.

The detailed UE association process is shown in Fig. 6.6. During the UE association phase, all small cells are assumed to transmit at the same peak transmission power, and the antenna arrays are beamformed to aim their main beam directly at the UE. Therefore, finding a small cell providing the strongest power is simplified to finding the small cell with the least channel loss using Eq. (6.5) to (6.9). Meanwhile, the UE association stage only considers the distance-dependent path loss and

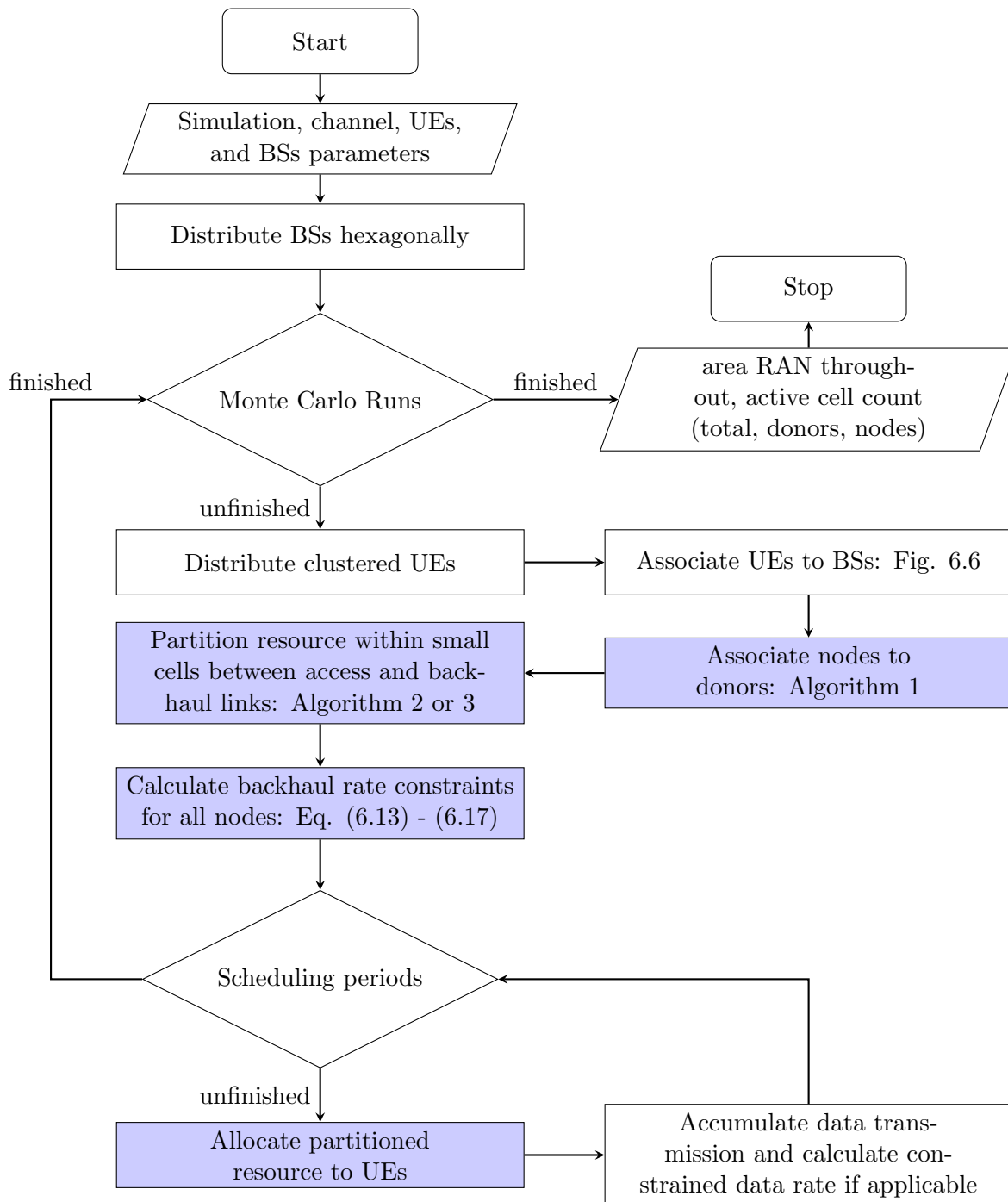


Figure 6.5: MATLAB-based simulation flowchart of homogeneous RAN using IAB

correlated shadow fading. This is a time-averaged channel loss without the multipath fading effect. This also reduces the calculation complexity because the UE association based on per TTI channel loss would generate significant overhead. Furthermore, before the association, all UEs are assumed to be isotropic for simplicity so that $G_{UE,c,k} = 0$ dBi. After association, on the other hand, all UEs would turn their main beam of antenna array facing directly at their serving cells. Small cells would aim their main beam at a specific UE in the corresponding time slots allocated to that UE. These change the relative angles between UEs and BSs in serving and interfering cells, requiring for re-calculation of antenna gains $G_{BS,c,k}$ and $G_{UE,c,k}$. In this chapter, the entire antenna pattern is assumed to rotate simultaneously for simplicity regarding beamforming. This assumption holds for UEs and BSs. Future work would employ codebooks for beamforming to improve the evaluation accuracy.

6.2.5 Node Association

The donor-node association process is presented using Algorithm 1, derived from [197]. The meanings for input and output parameters are:

nodeCellSet, *nodeSiteSet* : sets consisting of all the node cells and sites, respectively.

donorCellSet, *donorSiteSet* : sets consisting of all the donor cells and sites, respectively.

UEinSite : set consisting of the number of UEs associated with each BS site, which is the summation of the number of UEs associated with all the cells in the same BS site.

servDonorSite : set consisting of wireless backhaul serving sites for node sites. Specifically, $servDonorSite(b_1) = b_2$ means site b_2 transmits wireless backhaul traffic to site b_1 . Using multi-hop node association (like the wireless backhaul transmission from donor site A to node site C to node site D in Fig. 6.7), b_2 is either a parent node site (like node site C in Fig. 6.7) or a donor site (like donor site A in Fig. 6.7). If $b_1 \notin servDonorSite$, b_1 does not transmit wireless backhaul so it is a child node site (like node sites B and D in Fig. 6.7). $servDonorSite(b_1) = 0$ if b_1 is a donor site, or an empty node site if sleep mode is enabled.

servDonorCell : set consisting of wireless backhaul serving cells for relevant node cells. Specifically, $servDonorCell(c_1) = c_2$ means cell c_2 transmits wireless backhaul traffic to cell c_1 .

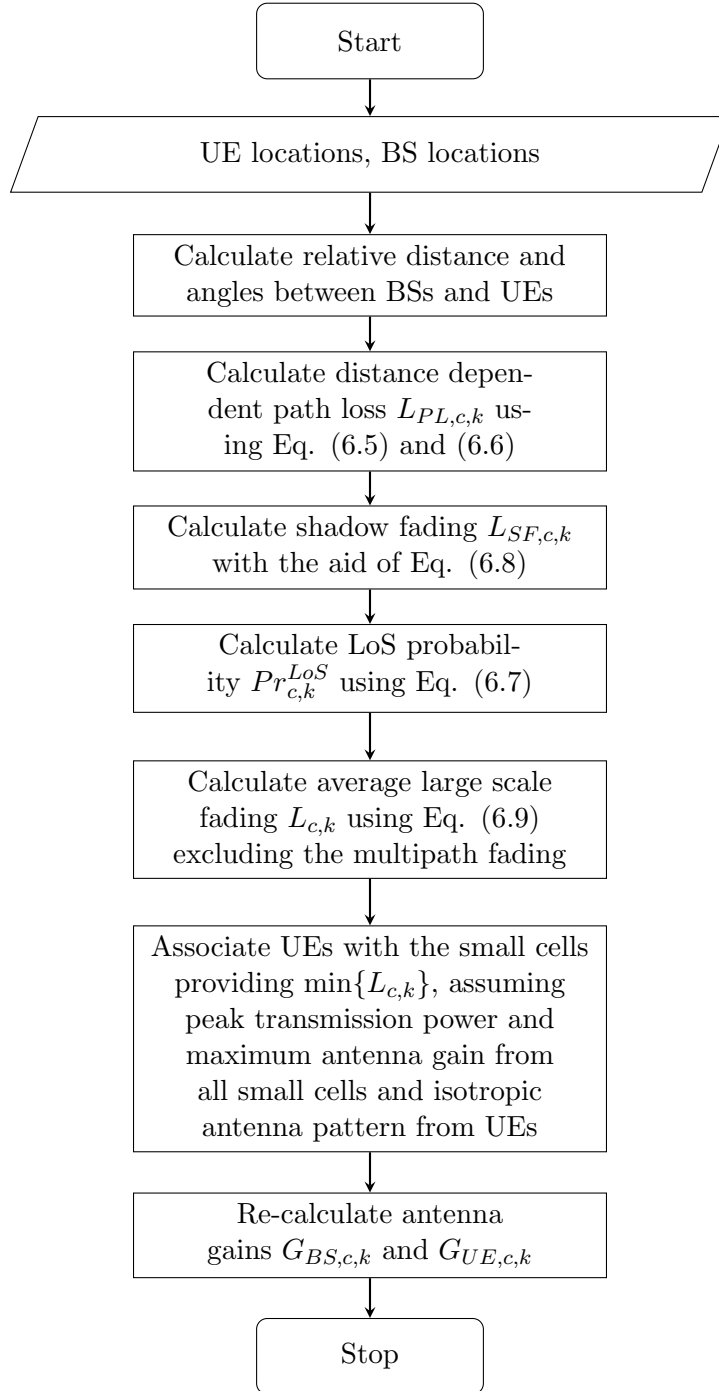


Figure 6.6: Flowchart of UE association

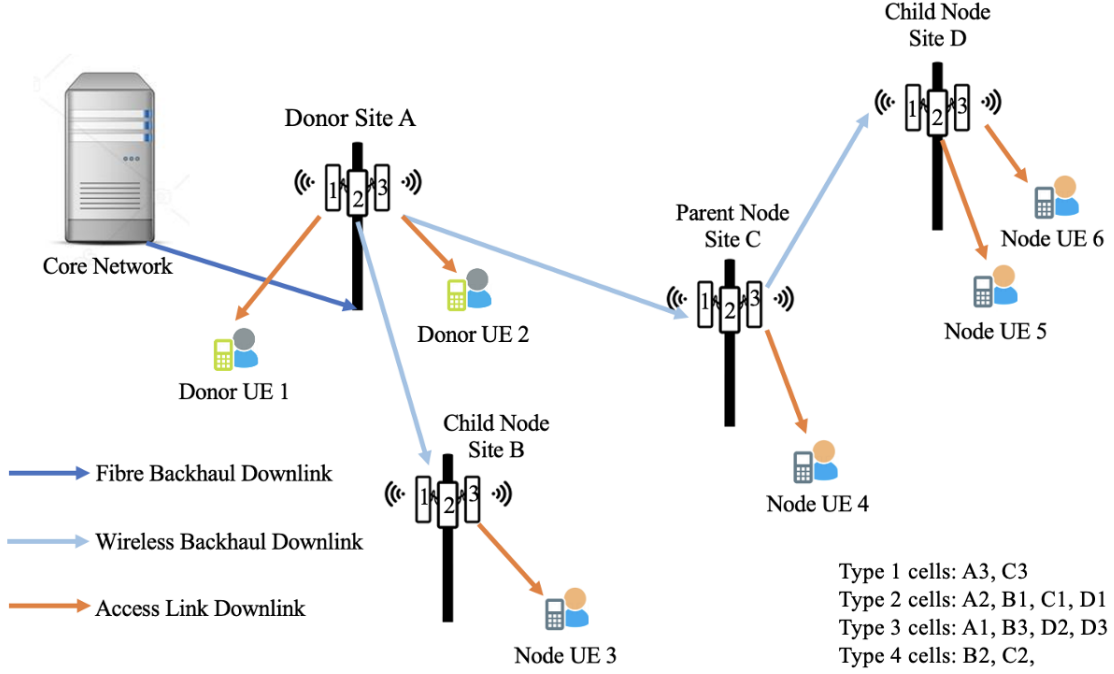


Figure 6.7: Example of donor-node association in IAB

Considering multi-hop node association, c_2 can either be a node cell in the parent node site, parent node cell for short, or a donor cell. If $c_1 \notin \text{servDonorCell}$, c_1 does not transmit wireless backhaul so it is a node cell in child node site, child node cell for short. $\text{servDonorCell}(c_1) = 0$ means c_1 does not receive wireless backhaul traffic, and either c_1 is a donor cell or other cells in the same node site as c_1 are responsible for wireless backhaul communication.

ueCount : set consisting of the number of UEs associated with all the sites directly and indirectly.

For example, UE 4 in Fig. 6.7 is associated with site C directly. In contrast, UEs 5 and 6 are associated with site C indirectly since UEs 5 and 6's serving site D receives wireless backhaul from site C. Therefore, $\text{ueCount}(C) = 3$. Similarly, UEs 1 and 2 associate with site A directly, while UEs 3 to 6 associate with site A indirectly. $\text{ueCount}(A) = 6$.

Sites A and B in Fig. 6.7 form a complete donor-node backhaul chain, and so do sites A, C, and D. The donor site A is referred to as the primary donor of both donor-node backhaul chains in the algorithm. The multi-hop approach extends the coverage range of the donor sites using parent node sites as relays along the donor-node backhaul chain [172]. When associating node cells for the wireless backhaul connection, this work considers four different association criteria:

1. **Power criteria:** unassociated node cells intending to associate with the donor or parent node cells with the strongest power. All the unassociated node cells are assumed to have isotropic antennas and would turn their main antenna beams toward the wireless backhaul servers after association [197].
2. **Angle criteria:** unassociated node cells should not associate with donor or parent node cells which have already served children node cells in the same direction. No permission for same angle association prevents severe interference on the backhaul downlink.
3. **Hop criteria:** unassociated node cells intending to associate with the donor or parent node cells with a limited number of relaying node cells in-between for the latter. The number of in-between relaying node cells plus one is the hop number. For example, in Fig. 6.7, the hop numbers for sites C and D are one and two, respectively. Limiting the hop count prevents the donor-node backhaul chain from being too long. Otherwise, the parent nodes closer to the primary donor might allocate most of the resources to backhaul and limit the access link performance. The hop count threshold per donor-node backhaul chain is denoted as HOP_{th} , which could be set to infinity if this criterion relaxes.
4. **Load criteria:** unassociated node cells intending to associate with the donor or parent node cell if the $ueCount$ of the potential association would not reach the maximum number. Otherwise, the imbalance of the UE associations among all the donor-node chains would congest some links while under-use the others [197]. The threshold of the UE count per donor-node chain is denoted as UE_{th} , which could be set to infinity if this criterion relaxes.

To check all the set criteria effectively, the nodes are associated one by one in Algorithm 1. Specifically, the algorithm finds a potential cell pair with the least channel loss (minus the antenna gain from donors or parent nodes), checks the criteria, and grants the association if all the criteria are met or refuses otherwise. In the case of association refusal, the algorithm sets the corresponding channel loss to infinity to avoid re-attempted association and finds the next potential pair. The thresholds for hop count and UE count should be selected carefully to prevent the scenario where all the possible associations are refused, and some nodes are left unassociated. Furthermore, the backhaul link is common to each BS site and is shared between all three cells. Therefore each

node BS site only needs to associate one out of three cells with a donor or a parent node cell; once associated, all the three node cells are moved from S_N to S_D .

Having associated all node BS sites for wireless backhaul connections, all the small cells in the RAN could be categorised based on the existence of backhaul and access link establishments. Table. 6.1 lists the four types of small cells, along with the indication of whether the time resource partitioning between access and backhaul links is required. Type 1 small cells have access and backhaul link establishments and thus need to partition the resources. Cell A3 in Fig. 6.7 is an example of a type 1 cell since it serves UE 2 in the access link and cell C1 in the backhaul link. Type 2 small cells do not serve UEs but relay backhaul traffic, so they do not need to partition the resource. However, the resource they allocate to backhaul traffic should be limited to prevent the possibility of their direct children nodes allocating all the resources to backhaul consequently and starving the associated UEs [198]. Cell A2 and C1 in Fig. 6.7 are examples of type 2 cells as A2 only transmit wireless backhaul to B1 without serving UEs, and C1 only receives wireless backhaul from A3 without serving UEs. In contrast, type 3 small cells only need to serve UEs so that all the resources would be allocated to UE traffic. An example is cell D2 in Fig. 6.7 that only serves UE 5 without backhaul communication. Finally, type 4 small cells have no traffic, so they just broadcast pilot transmissions all the time to detect the appearance of potential traffic, like cell B2 in Fig. 6.7.

Algorithm 2 presents the algorithm for resource partitioning using a fixed ratio η_1 of the total time resource T for all type 1 cells, donors or nodes. For type 2 cells with only backhaul traffic, $\eta_2 \times T$ resources are allocated to backhaul links so that children node cells with UE traffic could have non-zero resources reserved for UEs. Type 3 cells with only UE traffic could have all T for the access links. Type 4 cells are not considered as they broadcast pilots all the time. The output T_{ac} and T_{bh} save the TTI number allocated to access and backhaul links in each cell, respectively. In contrast, Algorithm 3 partitions the resource based on the load, which is $ueCount$ for all the sites. For donor sites, the total TTIs are divided between the access and backhaul links proportional to the ratio between the number of UEs associated directly and indirectly. In contrast, for node sites, the TTI partitioning depends on $ueCount$ of the bespoke node sites and the primary donor sites in the same donor-node backhaul chain. Having partitioned the resource in sites, each cell can partition accordingly based on its type. Both resource partitioning algorithms could easily extend from the time resource allocation to the time-frequency resource allocation. After the resource partitioning,

Algorithm 1: Node Association using Multi-Hop

Data: $nodeCellSet$, $nodeSiteSet$, $donorCellSet$, $donorCellSet$, $UEinSite$

Result: $servDonorSite$, $servDonorCell$, $ueCount$

```
 $n_{node} \leftarrow 0$  ; /* number of already associated node sites */
 $reCalculation \leftarrow 0$  ; /* indicator for channel loss re-calculation */
 $c'_0 \leftarrow []$  ; /* index of the node cell seeking for association */
 $S_N \leftarrow nodeCellSet$  ; /* set of unassociated node cells */
 $S_D \leftarrow donorCellSet$  ; /* set of donor cells and available parent node cells */
 $angSite\{1 : N_B\} \leftarrow []$  ; /* relative angle of nodes attached to each site */
 $hopCount(1 : N_B) \leftarrow 0$  ; /* hop count away from donor */
 $ueCount \leftarrow UEinSite$  ;
while  $n_{node} < N_N$  do
  if  $reCalculation = 0$  OR  $c'_0 \neq []$  then
    Calculate path loss  $L_{PL,c,c'}$  from cell  $c \in S_D$  to cell  $c' \in S_N$  using Eq. (6.5) and
    (6.6);
    Calculate 3 sets of correlated shadow  $L_{SF,c,c'}$  from cell  $c \in S_D$  to cell  $c' \in S_N$  and
    select the minimum value for each  $(c, c')$  pair;
    Calculate LoS probability  $Pr_{c,c'}^{LoS}$  from cell  $c \in S_D$  to cell  $c' \in S_N$  using Eq. (6.7);
    Calculate antenna gain  $G_{BS,c,c'}$  from cell  $c \in S_D$  based on relative angle  $A_{c,c'}$ ,
    assuming unassociated node cell  $c' \in S_N$  are equipped with isotropic antennas;
     $L_{c,c'} = (L_{PL,c,c'}^{LoS} + L_{SF,c,c'}^{LoS} \times R_{cor}^{LoS}) \times Pr_{c,c'}^{LoS} + (L_{PL,c,c'}^{NLoS} + L_{SF,c,c'}^{NLoS} \times R_{cor}^{NLoS}) \times (1 - Pr_{c,c'}^{LoS}) - G_{BS,c,c'}$ ;
    Find  $(c_0, c'_0) = \min \{L_{c,c'}\}$  ; /* least channel loss criteria */
    Find the BS sites  $b_0$  and  $b'_0$  containing cells  $c_0$  and  $c'_0$ , respectively;
     $check_a = A_{c_0,c'_0} \in angSite\{b_0\}$  ; /* angle criteria */
     $check_h = hopCount(b_0) + 1 \leq Hop_{th}$  ; /* hop count criteria */
    Find the primary donor site  $d_0$  that is the beginning of this donor-node backhaul chain;
     $check_u = ueCount(d_0) + UEinSite(b'_0) \leq UE_{th}$  ; /* UE count criteria */
    if  $check_a$  AND  $check_h$  AND  $check_u$  then
       $servDonorCell(c'_0) = c_0$  ; /* associated cell pair */
       $servDonorSite(b'_0) = b_0$  ; /* associated BS site pair */
       $angSite\{b_0\} = [angSite\{b_0\}, A_{c_0,c'_0}]$ ;
       $hopCount(b'_0) = hopCount(b_0) + 1$ ;
       $ueCount(d_0) = ueCount(d_0) + UEinSite(b'_0)$ ;
       $ueCount(b_0) = ueCount(b_0) + UEinSite(b'_0)$ ;
      Move the three cells belonging to BS site  $b'_0$  from  $S_N$  to  $S_D$ ;
       $c'_0 = []$ ;
       $n_{node} = n_{node} + 1$ ;
    else
      Set  $L_{c_0,c'_0}$  to infinity;
       $reCalculation = 1$ ;
    end
  end
end
```

Description	Provide/receive backhaul	Serve UEs	Partition of resource
Cell type 1	Yes	Yes	Yes
Cell type 2	Yes	No	No
Cell type 3	No	Yes	No
Cell type 4	No	No	No

Table 6.1: Small cell types with integrated access and bakchaul

UEs associated with the same cell share the dedicated access resource evenly according to the Round Robin scheduler.

Algorithm 2: Fixed Ratio Resource Partitioning

Data: T, η_1, η_2
Result: T_{ac}, T_{bh}
Categorize small cells into type 1 to 4;
for $i = 1 : N_C$ **do**
 if i *is type 1* **then**
 $T_{ac}(i) = \eta_1 \times T$;
 $T_{ac}(i) = T - T_{bh}(i)$;
 else if i *is type 2* **then**
 $T_{bh}(i) = \eta_2 \times T$;
 $T_{ac}(i) = T - T_{bh}(i)$;
 else if i *is type 3* **then**
 $T_{ac}(i) = T$;
 $T_{bh}(i) = 0$;
end

6.2.6 Backhaul Rate Constraint

As the required data from UEs is acquired from the core network through backhaul links, the node UE throughput achieved in the access link should be limited by the throughput in the backhaul link, which depends on the backhaul link channel conditions [199]. This is referred to as the dynamic backhaul rate constraint in this work. The backhaul rate constraint, $S_{BH,c}$, of an arbitrary node cell c is calculated by:

$$S_{BH,c} = \frac{12 \times 14 \times N_{RB} \times \log_2 \left(1 + \gamma_{BH,c',c} \right)}{\delta_t}, \quad (6.13)$$

Algorithm 3: Load Based Resource Partitioning

Data: $UEinSite, ueCount, T, \eta_2$

Result: T_{ac}, T_{bh}

Categorize small cells into type 1 to 4;

for $i = 1 : N_B$ **do**

if i is donor **then**

$AC(i) = T \times \frac{UEinSite(i)}{ueCount(i)};$

$BH(i) = T - AC(i);$

else

 Find the primary donor site d_i of the donor-node chain containing i ;

$BH(i) = T \times \frac{ueCount(i)}{ueCount(d_i)};$

$AC(i) = T - BH(i);$

end

end

for $j = 1 : N_C$ **do**

if j is type 1 **then**

 Find the site j belongs to as i_0 ;

$T_{acj} = AC(i_0);$

$T_{bh}(j) = BH(i_0);$

else if i is type 2 **then**

$T_{bh}(j) = \eta_2 \times T;$

$T_{ac}(j) = T - T_{bh}(j);$

else if i is type 3 **then**

$T_{ac}(j) = T;$

$T_{bh}(j) = 0;$

end

when configured with a RB structure similar to LTE, and $\gamma_{BH,c',c}$ is the time-averaged backhaul SINR experienced by the node cell c from its backhaul serving cell c' across all RBs in a single TTI excluding the multipath fading. The mathematical expression for the time-averaged SINR is:

$$\gamma_{BH,c',c} = \frac{P_{rx,c',c}}{\sum_{c'' \in \mathcal{C} \setminus \{c'\}} P_{rx,c'',c} + \sigma_n^2}. \quad (6.14)$$

where

$$P_{rx,c',c} [\text{dBm}] = P_{tx,c',c} [\text{dBm}] + G_{BS,c',c} [\text{dBi}] + G_{BS,c,c'} [\text{dBi}] - L_{c',c} [\text{dB}] \quad (6.15)$$

is the average received power in dBm from cell c' to node cell c and

$$\begin{aligned} L_{c',c} [\text{dB}] = & \left(L_{PL,c',c}^{LoS} [\text{dB}] + L_{SF,c',c}^{LoS} [\text{dB}] \times R_{cor}^{LoS} \right) \times Pr_{c',c}^{LoS} \\ & + \left(L_{PL,c',c}^{NLoS} [\text{dB}] + L_{SF,c',c}^{NLoS} [\text{dB}] \times R_{cor}^{NLoS} \right) \times \left(1 - Pr_{c',c}^{LoS} \right) \end{aligned} \quad (6.16)$$

is the time-averaged channel loss in the backhaul links excluding the multipath fading. The exclusion of multipath fading also copes with the highly focused antenna beam, which leads to a less frequency selective fading effect. This is similar to the channel loss in the access links, except for the generation of shadow fading coefficients [195]. Specifically, three independent sets of $L_{SF,c',c}^{LoS}$ and $L_{SF,c',c}^{NLoS}$ are generated and the minimum coefficient for each $c' - c$ pair is selected as the final coefficient [195]. Note that the main antenna beams of node cell c and its backhaul serving cell c_d are assumed to be aligned perfectly with each other, so maximum antenna gains are expected from both cells. Similarly, $L_{SF,c',c}^{LoS}$ and $L_{SF,c',c}^{NLoS}$ are obtained by selecting minimum values out of three independent normal distributions. Meanwhile, the relative angles between c and the interfering cells c'' would be adjusted accordingly to calculate $G_{BS,c'',c}$ and $G_{BS,c,c''}$. Type 3 node cells, whose T_{bh} equals 0 all the time, have infinite rate constraint on UEs. Assume c_1, c_2 , and c_3 are the three node cells belonging to the same node BS site b_0 . Then:

$$S_{BH,b_0} = \min\{S_{BH,c_1}, S_{BH,c_2}, S_{BH,c_3}\} \quad (6.17)$$

which should then be assigned back to cells c_1, c_2 , and c_3 , as they share the same backhaul link. Note that donors with fibre backhaul links are assumed to have infinite capacity so no backhaul

rate constraints on donor UEs. Constrained by the backhaul capacity $S_{BH,c}$ and the overall rate cap S_{cap} , the average UE k throughput becomes:

$$S_{UE,k} = \min \left\{ S_{BH,c}, S_{cap}, \frac{1}{T} \sum_{t=1}^T (I_{k,t} \times \tilde{S}_{UE,k}(t)) \right\} \quad (6.18)$$

The average RAN throughput is calculated as:

$$S_{RAN} = \sum_{k=1}^K S_{UE,k}. \quad (6.19)$$

In addition, the RAN area is calculated as:

$$A_{RAN} = \frac{3\sqrt{3} \times R^2}{8} \times N_C = \frac{3\sqrt{3} \times (ISD/1.5)^2}{8} \times N_C \quad (6.20)$$

assuming hexagonal small cell coverage area and the edge effect are prevented using wrap around algorithm. In Eq. (6.20), R is the small cell radius in units of kilometre and ISD is the inter small cell BS site distance that is 1.5 times the cell radius. Both Eq. (6.19) and (6.20) can be used for DVG calculation for capacity evaluation for a chosen reference.

6.2.7 Millimetre Wave Site Level Base Station Power Model

Using the same power model for the small cell BS site given in Eq. (3.24), the power consumption of a donor site on mmWave is:

$$P_b^{digital} = \frac{n_c \times \hat{P}_{tx,c} \times \sqrt{\alpha_c \times OBO}}{\eta_{CL} \times \eta_{PS} \times \hat{\eta}_{PA}} + \frac{n_a \times n_c}{\eta_{PS}} \times \frac{B}{\hat{B}} \times (\hat{P}_{BB}^{digital} + \hat{P}_{TRX}^{digital}) + P_{BH} \quad (6.21)$$

where the subscript *digital* refers to the fully digital architecture employed at the mmWave BSs where each antenna element has its own dedicated RF chain for signal processing [68], the same as the sub-6 GHz scenario. Table 6.2 lists all the parameters used for Eq. (6.21) and the total site power consumption of an active picocell ($\alpha_c = 1$), assuming the available bandwidth is fully occupied ($B = \hat{B}$). The transmission power per cell has increased from 0.13 W for the LTE sub-6 GHz case to 2 W for the mmWave for coverage improvement [195]. Each cell is equipped with a rectangular antenna array containing 128 antenna element that is beamformed to generate a

Parameter Name	Parameter Value
n_c	3
n_a	128 [195]
$\hat{P}_{tx,c}$ [W]	2 [195]
OBO [dB]	10 [200]
η_{CL} (%)	100
η_{PS} (%)	92 [146]
$\hat{\eta}_{PA}$ (%)	93
B [MHz]	400 [195]
$\hat{P}_{BB}^{digital}$ [W]	3.66 [147]
$\hat{P}_{TRX}^{digital}$ [W]	0.45 [200]
P_{BH} [W]	1 [146], [201]
$P_b^{digital}$ [W]	1737.82
$P_{b,RH}^{digital}$ [W]	22.18
$P_{b,OH}^{digital}$ [W]	1715.64

Table 6.2: Power parameters for pico-BS site

maximum 32.08 dBi gain in the boresight direction. The channel bandwidth has increased from 20 MHz for the LTE sub-6 GHz case to 400 MHz. The per antenna per cell power consumption of the baseband, $\hat{P}_{BB}^{digital}$, and the transceiver, $\hat{P}_{TRX}^{digital}$, should scale accordingly to cope with the wide channel bandwidth [146]. In addition, the power consumption of the mmWave BS backhaul could be reduced to 1 W [146] for donors, or 0 W for nodes if IAB is enabled. Substituting all the parameters into Eq. (6.21) gives the power consumption of an active mmWave donor site of 1737.82 W. This provides an optimistic estimation for a fully digital radio architecture. Note that the traffic independent overhead power consumption (regarding baseband, transceiver, and backhaul) dominates the total power consumption. Different from the LTE cases, the 1 W backhaul power consumption is negligible compared with the overhead power consumption or the total site power consumption.

The site power consumption could be reduced by employing a hybrid signal processing architecture where the total antennas could be divided into sub-groups. An RF chain is required only by each antenna sub-group [68]. The number of RF chains N_{RF} is usually much smaller than the number of antennas. This would reduce the site power consumption considerably. This would be considered future work.

Assuming $B = \hat{B}$, the overall mmWave and IAB-enabled RAN power consumption without

sleep mode is:

$$\begin{aligned}
P_{RAN,0}^{digital} &= \sum_{c=1}^{N_C} \left\{ \frac{\hat{P}_{tx,c} \times \sqrt{\alpha_c \times OBO}}{\eta_{CL} \times \eta_{PS} \times \hat{\eta}_{PA}} \right\} + \frac{n_a \times n_c}{\eta_{PS}} \times (\hat{P}_{BB}^{digital} + \hat{P}_{TRX}^{digital}) \times N_B + P_{BH} \times N_D \\
&= P_1 + P_2 + P_3
\end{aligned} \tag{6.22}$$

where P_1 is the total radio-head power consumption of N_C picocells, P_2 is the total baseband and transceiver units power consumption of N_B pico-BS sites, and P_3 is the total wired backhaul power consumption of N_D donors. The summation of P_2 and P_3 is the overhead power consumption. If IAB is not enabled, P_3 will change into $P_{BH} \times N_B$ for all the BS sites having fibre backhaul. If sleep mode is on but all the overhead units are left on, the RAN power consumption $P_{RAN,1}^{digital}$ is the same as $P_{RAN,0}^{digital}$ in Eq. (6.22) except the empty cells have α_c as zero instead of 0.1. In contrast, if the *Site Sleep Mode* is on, the RAN power consumption becomes:

$$\begin{aligned}
P_{RAN,2}^{digital} &= \sum_{c=1}^{N_C} \left\{ \frac{\hat{P}_{tx,c} \times \sqrt{\alpha_c \times OBO}}{\eta_{CL} \times \eta_{PS} \times \hat{\eta}_{PA}} \right\} + \frac{n_a \times n_c}{\eta_{PS}} \times (\hat{P}_{BB}^{digital} + \hat{P}_{TRX}^{digital}) \times N_{B,active} + P_{BH} \times N_D \\
&= P_1 + P_4 + P_3
\end{aligned} \tag{6.23}$$

where $N_{B,active}$ is the number of active BS sites in the RAN, within which at least one cell is active. In other words, the *Site Sleep Mode* shut down the pico-BS site completely when all the picocells in the site are empty. Otherwise only the pilot transmission is turned off in the empty cells. The energy consumption reduction using the *Site Sleep Mode* lies in P_4 . When the *Cell Sleep Mode* is on, the RAN power consumption is:

$$\begin{aligned}
P_{RAN,3}^{digital} &= \sum_{c=1}^{N_C} \left\{ \frac{\hat{P}_{tx,c} \times \sqrt{\alpha_c \times OBO}}{\eta_{CL} \times \eta_{PS} \times \hat{\eta}_{PA}} \right\} + \frac{n_a}{\eta_{PS}} \times \sum_{c=1}^{N_{C,active}} (\hat{P}_{BB}^{digital} + \hat{P}_{TRX}^{digital}) + P_{BH} \times N_D \\
&= P_1 + P_5 + P_3
\end{aligned} \tag{6.24}$$

where $N_{C,active}$ is the number of active small cells in the RAN. In contrast to the *Site Sleep Mode*, *Cell Sleep Mode* turns the empty cells off completely. The difference between P_2 and P_5 reflects the energy saving using the *Cell Sleep Mode*. Node sites do not consume backhaul energy and the

wired backhaul at donors are always on for the traffic transmission between the core network.

Having obtained all the models needed for the small cell RAN densification on mmWave with IAB, the following section will present the simulation results and analysis.

6.3 Small Cell RAN Densification using Millimetre Wave and Integrated Access and Backhaul

This section presents the simulation parameters and results for densifying the homogeneous small cell RAN on mmWave using IAB, with and without the sleep mode. Using the three figures of merit included in the evaluation framework, the reference RAN case selected for performance comparison is the 200 m ISD homogeneous picocell RAN on the sub-6 GHz frequency band, or LTE pico-RAN for short; each BS has an isotropic antenna. This reference choice enables direct performance comparison between LTE and mmWave RANs. 900 UEs/km² are uniformly distributed in the reference RAN. The area throughout for Data Volume Gain calculation is obtained from simulation, the area power consumption for Energy Consumption Gain calculation is calculated using Eq. (6.21) and the number of active and empty cells in RAN, and the Energy Efficiency Gain is calculated as the product of DVG and ECG.

The key simulation parameters are listed in Table 6.3 [194], [195]. Out of the 19 pico-BSs, three are donors if IAB is on. The tri-sectorised pico-BSs have ISD ranging from 200 m down to 50 m, equivalent to 86.60 to 1385.64 picocells per square kilometre. Each picocell has a rectangular antenna array with 128 antenna elements. The carrier frequency is now 28 GHz with a 400 MHz channel bandwidth, providing 2000 RBs per TTI. During the access link time slots, active picocells with UE association have unity normalised load activity α_c . Meanwhile, empty cells without sleep mode have 10% normalised load activity α_c , while turning sleep mode on reduces the normalised load activity α_c to zero. Similarly, during the backhaul link time slots, donor and parent node cells have $\alpha_c = 1$. During the same period, picocells not providing nor receiving wireless backhaul signal have $\alpha_c = 10\%$ without the sleep mode or 0 otherwise. Clustered UEs are equipped with rectangular antenna arrays with eight antenna elements each. The overall UE density, accounting for both uniformly and clustered distributed UEs, is 900 UEs/km². RR scheduling is adopted during the resource allocation process where UEs associated with the same picocell share the total

TTIs evenly. All the 2000 RBs are allocated to a specific UE if it is granted access to that TTI. Moreover, when partitioning the time resources between access and backhaul links, the fixed ratio method (based on η_1) carried out the division evenly to ensure the UEs have a certain amount of resource allocation and reasonable backhaul rate constraints. In addition, the half upper bound (η_2) on the maximum amount of resources a type 2 picocell could allocate to the backhaul link is chosen for the same reasons. In this section, the peak transmission power for all active picocells is kept fixed at 33 dBm (2 W) regardless of BS ISDs. The hop criteria threshold for node association is three if enabled. The UE criteria threshold for node association is half the total UE count. Given the donor count, the UE criteria threshold is not set as one-third of the total UE count because of the clustered UE distribution. Otherwise, some nodes would be stuck in the infinite loops and never be granted backhaul association.

6.3.1 The Impact of Enabling Integrated Access and Backhaul

This sub-section compares the energy efficiency of small cell RAN densification on mmWave, with or without IAB. When IAB is off, all pico-BSs are assumed to have wired fibre backhaul links connecting to the core network. All the wired backhaul links are assumed to have infinite capacity and thus have no rate constraints on UEs. However, the cost of backhaul link implementation and maintenance would be high. When IAB is included, the pre-selected donor sites have wired fibre backhaul links, while the node sites have wireless backhaul links that rely on donors to communicate with the core network. This would reduce the cost of backhaul implementation and maintenance. In this sub-section, node association depends on all the four criteria if IAB is enabled; resource partitioning is load based to cope with the changing traffic distributions in each Monte Carlo simulation run, and node UEs have dynamic backhaul rate constraints.

Fig. 6.8 illustrates the Data Volume Gain of pico-RAN on mmWave, with and without IAB, against the increasing picocell densities. Despite the difference in absolute values, the figure shows that pico-RAN DVG and capacity improve with the growing picocell density, with or without the IAB. In addition, moving from the reference LTE sub-6 GHz frequency band to the mmWave band improves the DVG and capacity for all the picocell densities, reflected by the always-higher-than-unity DVG. This is because of the broadened bandwidth and the highly directional antenna array with significant gain. Without the IAB, this capacity improvement is over 50-fold and increases

Parameter Name	Parameter Value
Site Count (N_B) / Cell Count (N_C) / Donor Site Count N_D	19/57/3
Cell Count Per Site (n_c)	3
Antenna Count Per Cell (n_a)	128
Antenna Count Per UE	8
BS/UE Height (h_{BS} / h_{UE}) [m]	10/1.5
UE Density per square kilometre	900
UE Distribution	Clustered
BS ISD [m]	200-50
Carrier Frequency [GHz]	28
DL Bandwidth [MHz]	400
RB Count Per TTI (N_{RB})	2000
Peak Transmission Power Per Cell ($\hat{P}_{tx,c}$) [dBm]	33
Maximum BS Antenna Gain ($G_{BS,max}^{MA}$) [dBi]	32.08
Maximum UE Antenna Gain ($G_{BS,max}^{MA}$) [dBi]	17.04
Vertical/Horizontal Antenna Element HPBW (θ_{3dB} / ϕ_{3dB}) [degree]	65/65
Antenna Element Front-to-Back Attenuation (A_m) [dB]	30
Antenna Element Sidelobe Attenuation (SLA_v) [dB]	30
Pathloss Dimensionless Constants (β^{LoS} / β^{NLoS}) [dB]	61.34/53.33
Pathloss Exponents (ζ^{LoS} / ζ^{NLoS})	17.3/38.3
Shadow Fading Mean (μ_{SF}^{LoS} / μ_{SF}^{NLoS}) [dB]	0/0
Shadow Fading Standard Deviation (σ_{SF}^{LoS} / σ_{SF}^{NLoS}) [dB]	3/8.03
Shadow Fading correlation length (d_{cor}^{LoS} / d_{cor}^{NLoS}) [m]	10/6
Noise Variance per RB (σ_n^2) [dBm]	-108.31
Hop Criteria Threshold (HOP_{th})	3
UE Criteria Threshold (UE_{th})	half total UE count
Fixed Resource Percentage for Access Link (η_1)	50%
Maximum Resource Percentage for BH link in Type 2 Cells (η_2)	50%

Table 6.3: Small cell RAN densification simulation parameters using millimetre wave and integrated access and backhaul

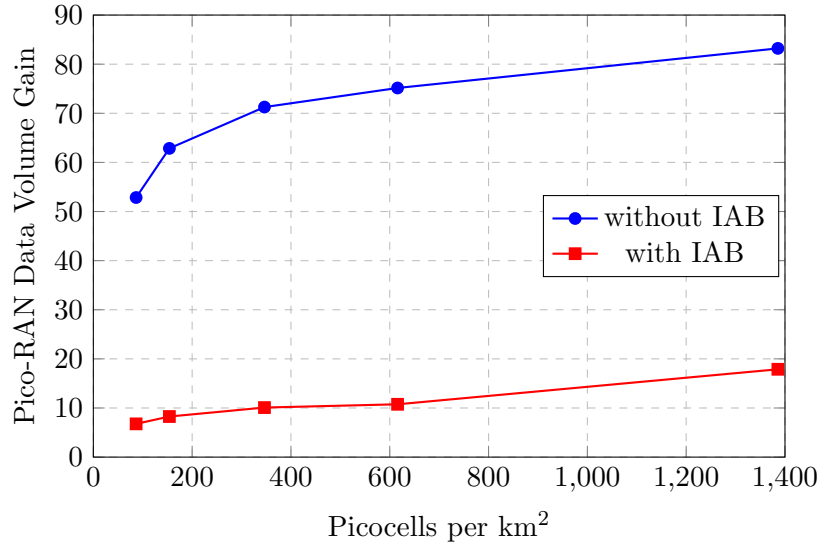


Figure 6.8: Pico-RAN Data Volume Gain on mmWave against picocell density, with or without IAB

with the picocell densities. However, the improvement is compromised by dividing the resources between UEs and backhaul traffic when IAB is enabled. The capacity improvement of mmWave and IAB is less than 20-fold for all the picocell densities. This indicates a trade-off between the RAN implementation and maintenance cost and the RAN capacity.

Fig. 6.9 illustrates the Energy Consumption Gain of pico-RAN densification, with and without IAB. The figure shows that adding more picocells always consumes more energy, decreasing the ECG against the increasing picocell density. This holds for mmWave and IAB techniques. Furthermore, an individual pico-BS site consumes extra energy to accommodate the mmWave with high bandwidth and large antenna numbers. Therefore, pico-RAN on mmWave always consumes more energy than the LTE pico-RAN for any picocell density. Thus the ECG is always lower than unity. The total mmWave pico-RAN energy consumption has negligible dependence on the number of wired fibre backhaul links. Therefore, the RAN ECG profiles with and without IAB almost overlap.

Fig. 6.10 illustrates the Energy Efficiency Gain of pico-RAN densification on the mmWave band, with and without the IAB. The EEG results in Fig. 6.10 is the product of the corresponding DVGs in Fig. 6.8 and ECGs in Fig. 6.9. The figure shows that the RAN EEG or energy efficiency decreases against the increasing picocell density, with or without IAB. This is dominated by the decreased

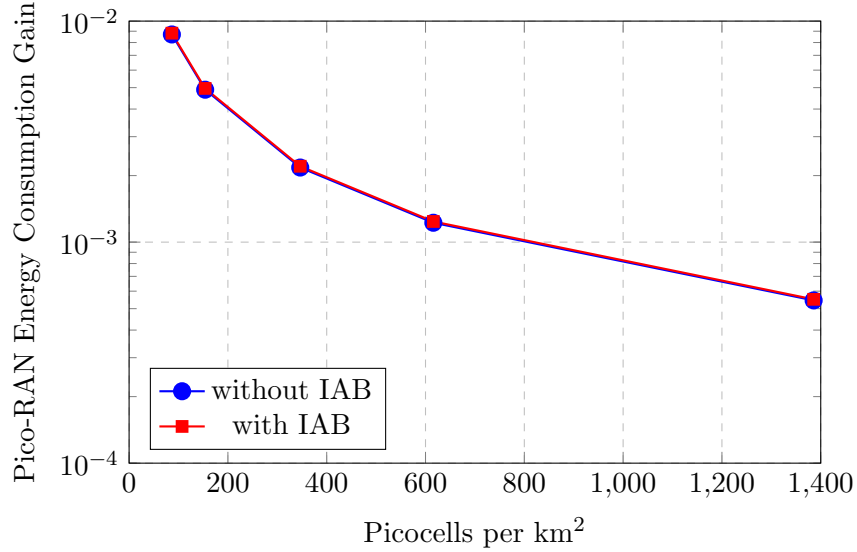


Figure 6.9: Pico-RAN Energy Consumption Gain on mmWave against picocell density, with or without IAB

ECG or the increased energy consumption, despite the improving DVG or capacity. Compared with the reference case, due to the significant energy consumption, the pico-RANs on mmWave become less energy efficient at all the picocell densities, with and without the IAB. Because of the capacity compromise caused by the reduced resources for UEs, pico-RAN on mmWave is more energy efficient without the IAB.

6.3.2 The Impact of Node Association Criteria

This sub-section focuses on the node wireless backhaul association and investigates the impact of different association criteria on the RAN energy efficiency. As mentioned, the node association criteria include the received signal power, the relative angle, the hop number, and the load conditions. The power criterion enables the node cell always to choose the donor or parent node cell with the strongest signal strength. The angle criterion prevents the node cell from choosing the donor or parent node cell that already provides wireless backhaul traffic in the same direction. These two criteria are default and always enabled. The hop number criterion limits the number of hops a node cell can use to get a wireless backhaul connection to a donor cell along the donor-node backhaul chain. The load criterion limits the number of UEs associated with all the donor-node backhaul chains starting with the same donor. These two criteria are optional and can be relaxed

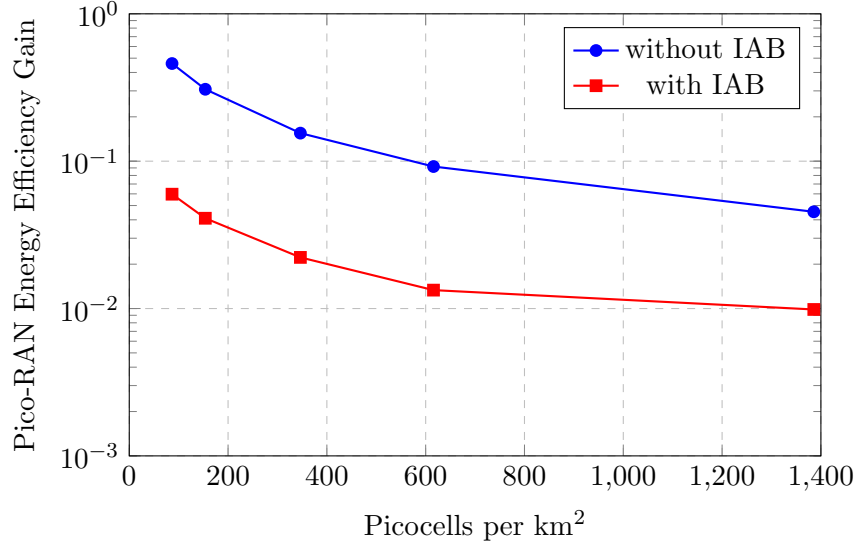


Figure 6.10: Pico-RAN Energy Efficiency Gain on mmWave against picocell density, with or without IAB

by setting the corresponding threshold to infinity. In this sub-section, IAB is enabled, UE density is 900 UEs/km², resource partitioning is load-based, and node UEs have dynamic backhaul rate constraints.

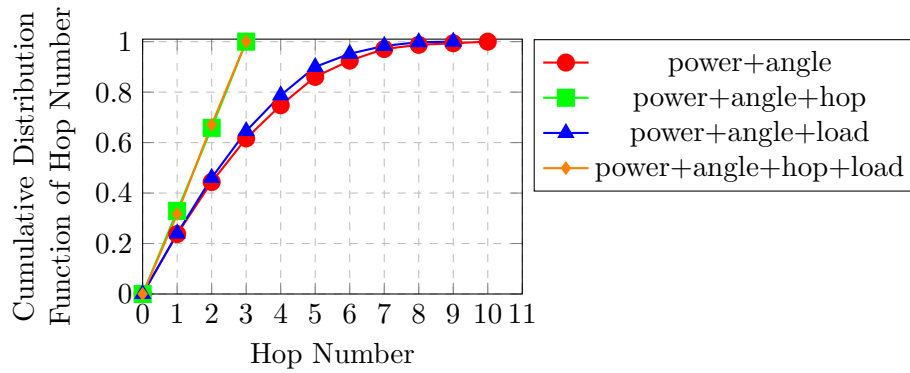
Fig. 6.11 illustrates the CDF of the hop count of each node, comparing different node association criteria combinations and pico-BS ISDs. The difference between pico-BS ISDs for any node association criteria combination is negligible. So the analysis will focus on Fig. 6.11a without loss of generality. When the hop and load criteria are relaxed, the hop number of all node sites varies significantly between 1 and 10. The long donor-node backhaul chain might degrade the UE throughput when parent node sites allocate most of their resources to backhaul links. The activation of the load criterion reduces the hop number variation slightly. Adding more node sites in the donor-node backhaul chain is likely to increase the load number. On the contrary, limiting the load number could restrict the hop count. Moreover, the non-infinite hop criterion limits the maximum hop number to three. This prevents the donor-node chain from being too long, but might cause more children node sites to associate with the same donor or parent sites. This might still compromise the UE throughput in donor and parent sites. Moreover, the non-infinite hop criterion also prevents some node sites from associating with the donor or parent sites with the strongest signal. This might degrade the backhaul SINR and decrease the backhaul rate constraints. These

CDFs of hop counts in Fig. 6.11 help analyse the capacity performance presented in Fig. 6.13.

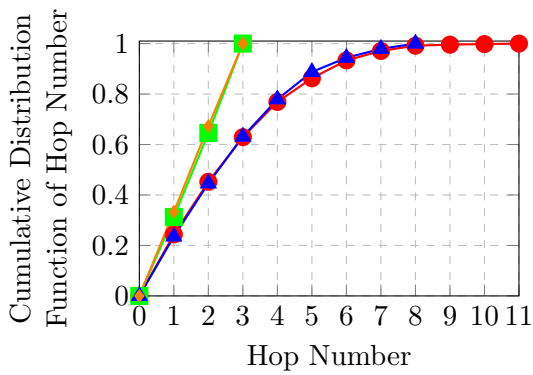
Fig. 6.12 plots the CDF of the normalised UE number attached to a donor site directly or indirectly, comparing different node association criteria combinations and pico-BS ISDs. The normalised UE number is calculated as the ratio between the actual *ueCount* of each donor site over the total UE number. The difference in the normalised UE number CDF between BS ISDs is negligible; thus, the following analysis will focus on Fig. 6.12a without loss of generality. The normalised UE number varies significantly when only the default power and angle criteria are enabled. Similarly, when the hop criterion is activated, the variance in the normalised UE number reduces slightly, shown as the lower five percentile and 95 percentile compared with the case where only default criteria are enabled. In contrast, activating the non-infinite load criterion further reduces the normalised UE variance and balances the load attached to donor sites directly and indirectly. When the load-based resource partitioning method is adopted, this load balancing also helps with resource allocation balancing, which might improve the UE throughput. Similarly, These CDFs of normalised UE count in Fig. 6.12 help analyse the capacity performance.

Fig. 6.13 plots the pico-RAN Data Volume Gain with mmWave and IAB against the increasing picocell density. Different combinations of node association criteria are compared in this figure. All DVG profiles or RAN capacity improves with the growing picocell density because of the signal power strengthening. At picocell densities up to 615.84 picocells per km² (ISD of 75 m), the DVGs with different criteria combinations have negligible differences. When the picocell density is 1385.64 picocells per square kilometre (50 m ISD), there are small-scale variations in the achieved RAN DVGs. Specifically, when only the default criteria are active, the DVG is 23.15. When the additional load criterion is enabled, the DVG improves slightly to 23.98 due to the load balancing between donor sites. When the default and hop criteria are enabled, the DVG degrades to 19.36. This is caused by preventing the node sites from associating with donor and parent node sites offering the strongest signal power on the backhaul links. This is the most difficult when all four criteria are enabled. The DVG degrades further to 17.88. Overall, the impact of node association criteria on capacity is negligible for the considered picocell densities.

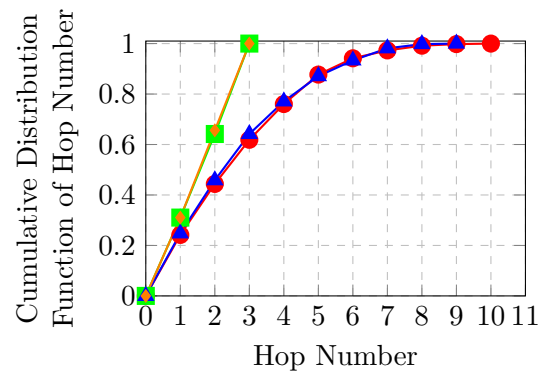
Fig. 6.14 plots the RAN Energy Consumption Gain of the pico-RAN on mmWave with IAB enabled, comparing the different node association criteria enabled. The RAN energy consumption depends on the UE association results, which only affects node association when sleep mode is



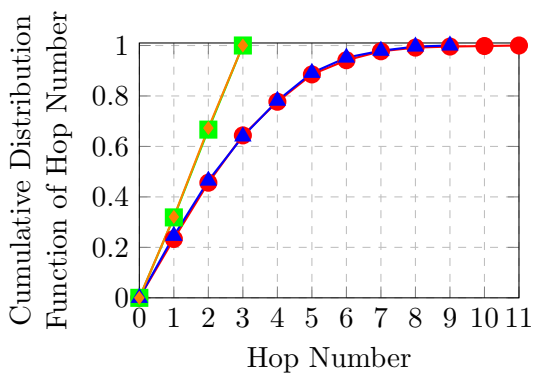
(a) ISD 200 m



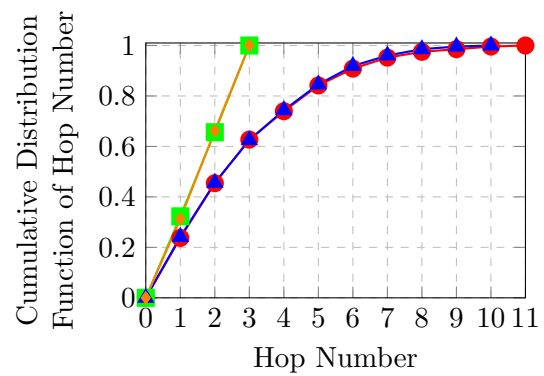
(b) ISD 150 m



(c) ISD 100 m

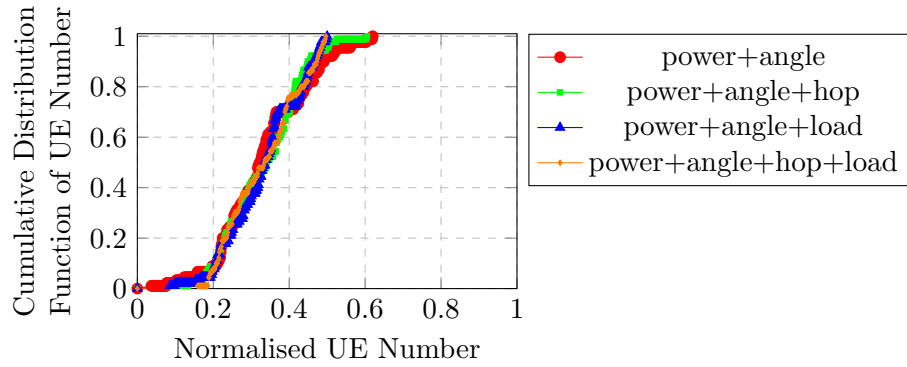


(d) ISD 75 m

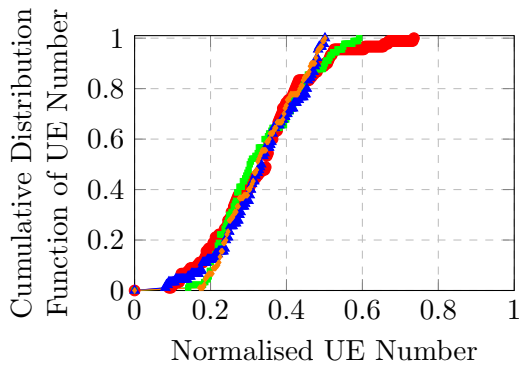


(e) ISD 50 m

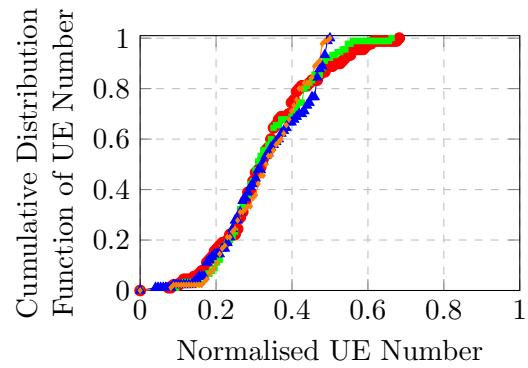
Figure 6.11: Cumulative Distribution Function of Hop number, comparing different node association criteria combinations and pico-BS ISDs



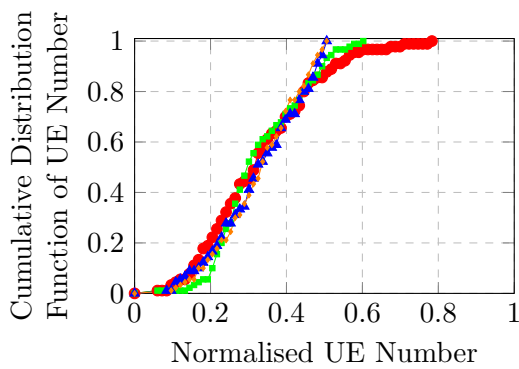
(a) ISD 200 m



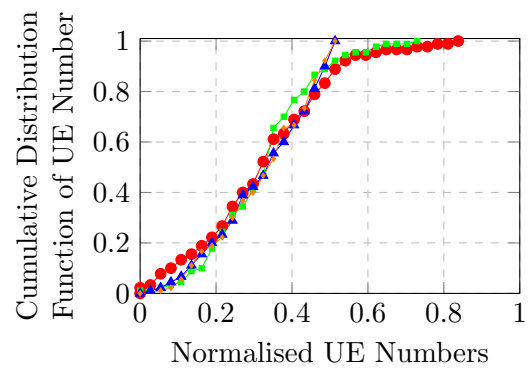
(b) ISD 150 m



(c) ISD 100 m



(d) ISD 75 m



(e) ISD 50 m

Figure 6.12: Cumulative Distribution Function of Normalised UE number associated with all the donor-node chain starting with the same donor, comparing different node association criteria combinations and pico-BS ISDs

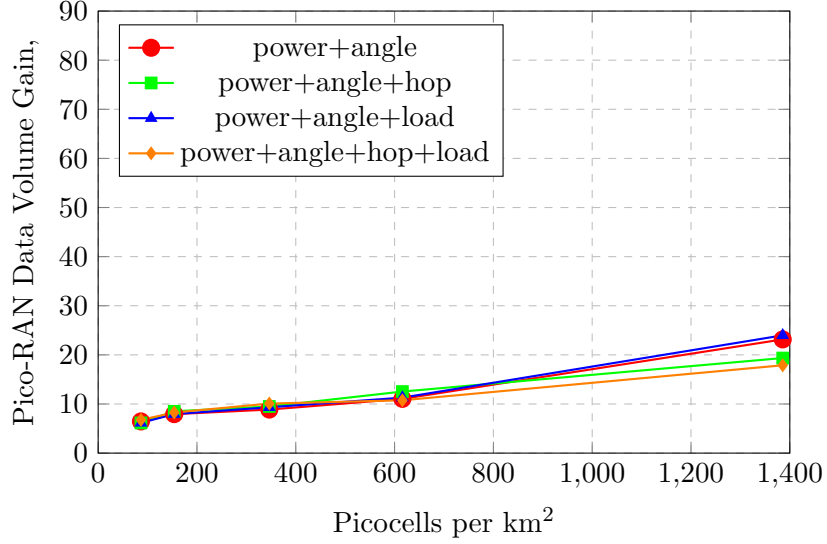


Figure 6.13: Pico-RAN Data Volume Gain on mmWave and IAB enabled against picocell density, with different node association criteria

considered. Therefore, the ECG profiles overlap and decrease against the increasing picocell density without any sleep mode.

Fig. 6.15 shows the RAN EEG, which is the product of the DVG results in Fig. 6.13 and ECG results in Fig. 6.14, against the increasing picocell density, comparing different node association criteria combinations. The figure shows that the overlapping ECG profiles with small values diminish the slight variations in DVG profiles. When the picocell density is 1385.64 picocells per square kilometre (50 m ISD), the EEG is 0.0128 only if the default criteria are enabled. When the power, angle, and load criteria are enabled, the EEG is improved to 0.0132. When the power, angle, and hop criteria are enabled, the EEG is 0.0107. When all the four criteria are enabled, EEG becomes 0.0099. Overall, the impact of node association criteria on energy efficiency is negligible for considered picocell densities.

6.3.3 Resource Partitioning Methods

This sub-section evaluates the impact of resource partitioning methods on the RAN capacity, energy consumption, and energy efficiency. Specifically, the fixed ratio and load-based methods are compared. In the fixed ratio method, cells partition the total time slots between access and backhaul links according to a constant ratio η_1 using Algorithm 2. η_1 is set to 50% for resource alloca-

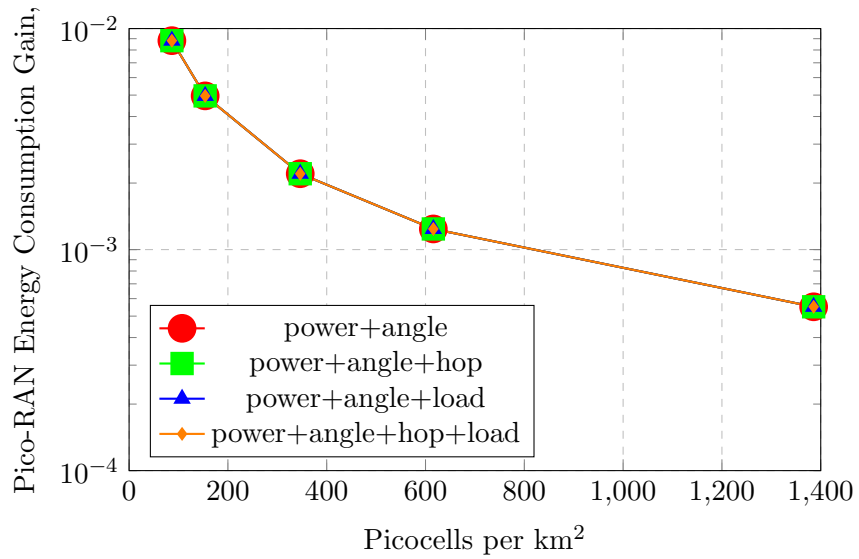


Figure 6.14: Pico-RAN Energy Consumption Gain on mmWave and IAB enabled against picocell density, with different node association criteria

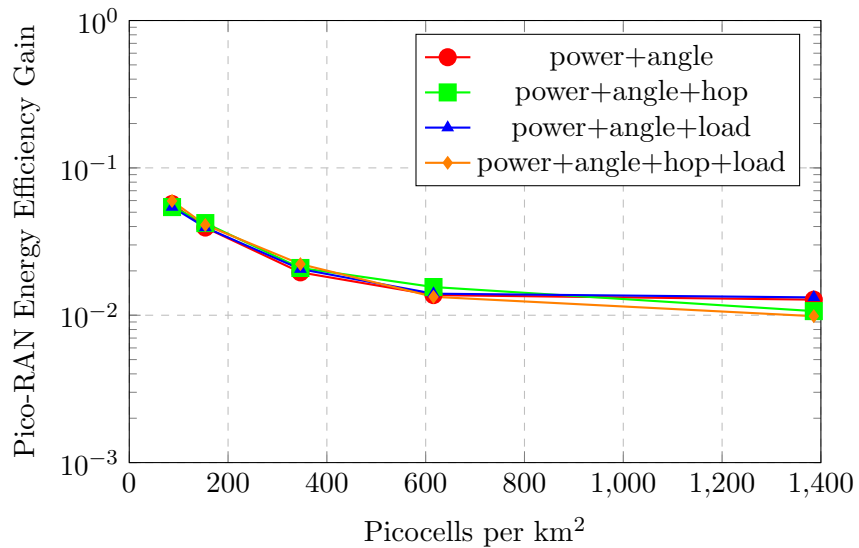


Figure 6.15: Pico-RAN Energy Efficiency Gain on mmWave and IAB enabled against picocell density, with different node association criteria

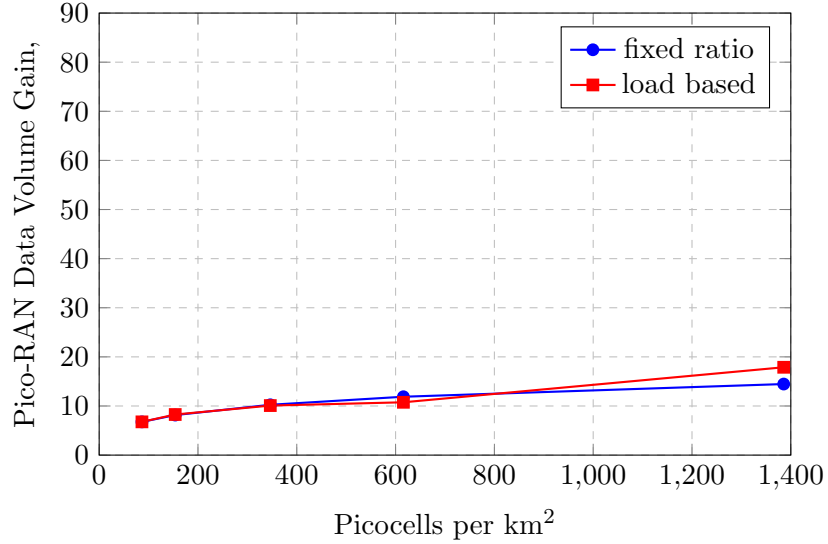


Figure 6.16: Pico-RAN Data Volume Gain on mmWave and IAB enabled, against picocell density, comparing fixed and load based resource partitioning methods

tion balancing. In contrast, the load-based resource partitioning depends on the load distribution shown in Algorithm 3. All four criteria are enabled, and the dynamic backhaul rate constraints are employed.

Fig. 6.16 plots the RAN Data Volume of mmWave pico-BS sites with IAB enabled against the increasing picocell density, comparing different resource partitioning methods. Different resource partitioning methods have similar RAN DVG and capacity performance within the considered picocell density range. When the picocell density is 1385.64 picocells per km² (ISD of 50 m), the load-based method has a slightly higher DVG at 17.88 compared with the 14.47 DVG achieved by the fixed ratio method. For high picocell density, the number of UE in the RAN is small for a fixed UE density and cell count. This causes the number of UEs associated with each active cell being smaller than the total number of UEs attached to the donor-node backhaul chains. According to Algorithm 3, node UEs will have more TTIs allocated to achieve higher throughput than the fixed ratio case.

Fig. 6.17 shows the Energy Consumption Gain of the mmWave small cell RAN with IAB enabled, comparing different time resource partitioning methods. Similarly, the resource partitioning does not change the UE association and thus does not change the number of active and empty cells in the RAN. The ECG profiles overlap.

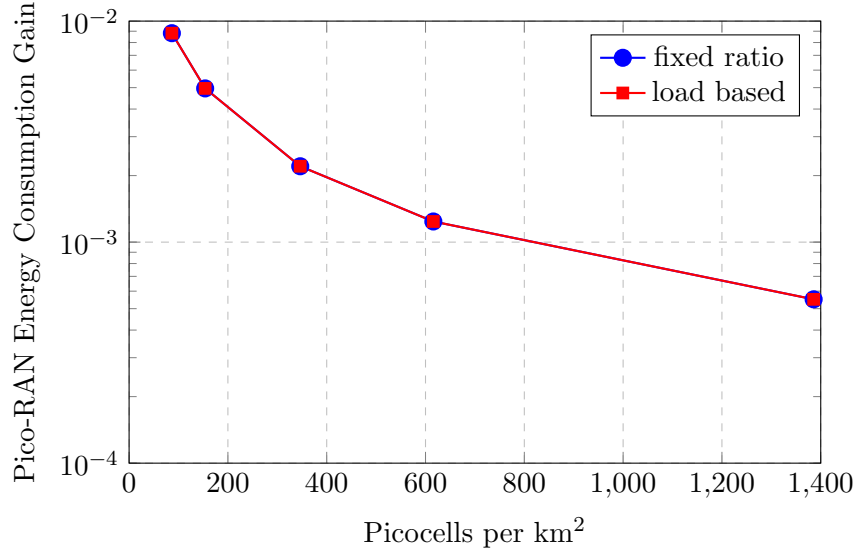


Figure 6.17: Pico-RAN Energy Consumption Gain on mmWave and IAB enabled, against picocell density, comparing fixed and load based resource partitioning methods

Fig. 6.18 illustrates the Energy Efficiency Gain of the small cell RAN with mmWave and IAB techniques, comparing different resource allocation methods. Given $EEG = DVG \times ECG$, the similar increasing DVG profiles in Fig. 6.16 and the overlapping decreasing ECG profiles in Fig. 6.17 result in the almost overlapping decreasing EEG profiles against the increasing picocell density. This indicates that the small ECG dominates EEG, and the resource partitioning methods have negligible impact on energy efficiency within the considered picocell density.

6.3.4 Node Backhaul Rate Constraints

This sub-section will analyse the impact of node backhaul rate constraints S_{BH} on the RAN capacity, energy consumption, and energy efficiency. The fibre backhaul links for donor sites are assumed to have infinite backhaul capacity, so there are no backhaul rate constraints on donor UEs. Different backhaul rate constraints are considered for node UEs. Specifically, the dynamic S_{BH} approach refers to the case where each node site has a different rate constraint on UEs, dependent on the backhaul channel conditions. The assumption is all the wireless backhaul links have the same limited link capacity. In contrast, the fixed S_{BH} approach refers to the case where all the node sites have the same limited constant rate constraint, independent of backhaul channel conditions. This is based on the assumption that node sites closer to donor sites have proportionally higher but

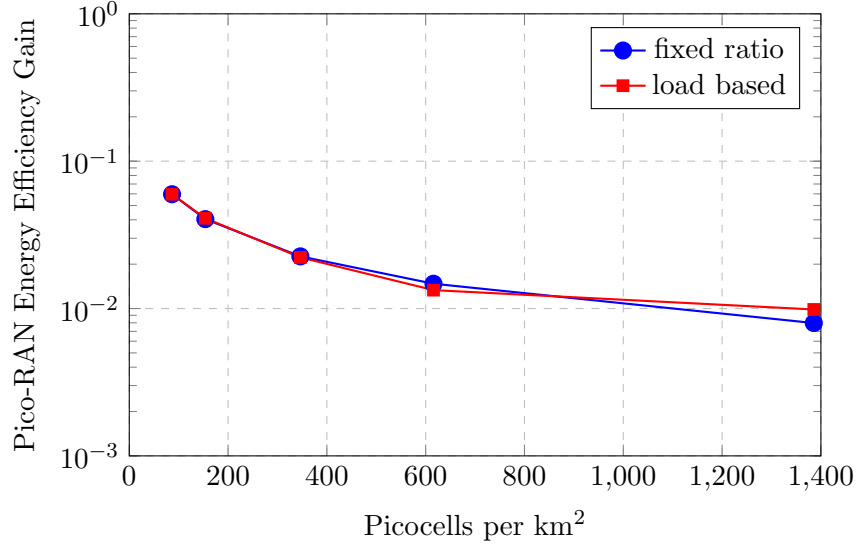


Figure 6.18: Pico-RAN Energy Efficiency Gain on mmWave and IAB enabled, against picocell density, comparing fixed and load based resource partitioning methods

still limited capacity. In this chapter, the constant S_{BH}^{fix} is set to half the maximum rate cap at 200 Mbit/s. Finally, the no S_{BH} approach refers to the case where all the wireless backhaul links have infinite link capacity like the fibre links. This would provide an upper bound on the capacity performance with IAB. All the four node association criteria are enabled in this sub-section, and the resource partitioning between access and backhaul links is load-based.

Fig. 6.19 plots the RAN Data Volume Gain against the increasing picocell density, comparing different backhaul rate constraints S_{BH} on node UEs. The main observations are:

1. When no S_{BH} approach is enabled, RAN DVG improves significantly with the increasing picocell density, approaching the case where IAB is not enabled. The slight capacity compromise lies in the limited TTIs allocated to UEs. However, this expects the wireless backhaul links to have the same capacity as the fibre ones, which is unrealistic using current techniques due to the large-scale fading. However, this approach sets the upper bound for capacity performance.
2. When the dynamic S_{BH} approach is used, node sites have the same limited backhaul link capacity. This constrains the node UE throughput compared with the no S_{BH} approach. Therefore, the RAN DVG is lower.
3. When the fixed S_{BH} approach is enabled, the achieved RAN DVG is similar to the dynamic S_{BH} approach. When the picocell density is 1385.64 picocells per km² (ISD of 50 m),

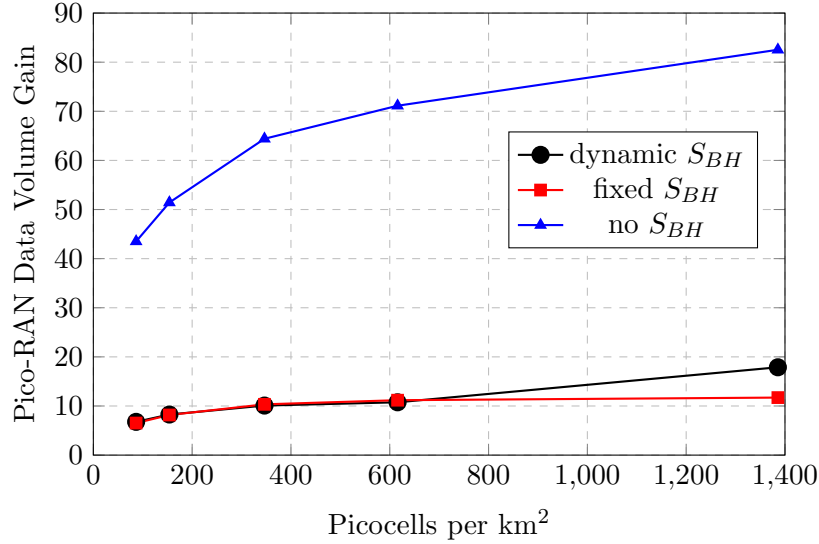


Figure 6.19: Pico-RAN Data Volume Gain on mmWave and IAB enabled against picocell density, comparing different backhaul rate constraints on node UEs: dynamic S_{BH} sets constraints based on backhaul channel conditions, fixed S_{BH} sets fixed constraints, and no S_{BH} does not set constraint

the backhaul SINR improves due to backhaul signal strengthening. Thus the backhaul rate constraints improve accordingly if dynamic S_{BH} is chosen, leading to node UE throughput increase and thus RAN capacity increase. In contrast, fixing S_{BH} would degrade the capacity.

Fig. 6.20 shows the RAN Energy Consumption Gain with mmWave and IAB, comparing different backhaul rate constraints on node UEs. Changing the backhaul rate constraints does not change the number of active and empty cells. The total RAN energy consumption and ECG does not change. Therefore in the figure, the ECG profiles for different node backhaul rate constraint approaches overlap and decrease with the increasing picocell density.

Fig. 6.21 plots the small cell RAN Energy Efficiency Gain with mmWave and IAB enabled, comparing different backhaul rate constraints S_{BH} on node UEs under the same conditions as Fig. 6.19 and 6.20. Given the same energy consumption, higher capacity leads to higher energy efficiency. The no S_{BH} approach achieves higher energy efficiency than the dynamic S_{BH} approach. The dynamic S_{BH} approach achieves similar energy efficiency performance to the fixed 200 Mbit/s S_{BH} approach except for a slight improvement at the picocell density of 1385.64 picocells per square kilometre due to capacity improvement.

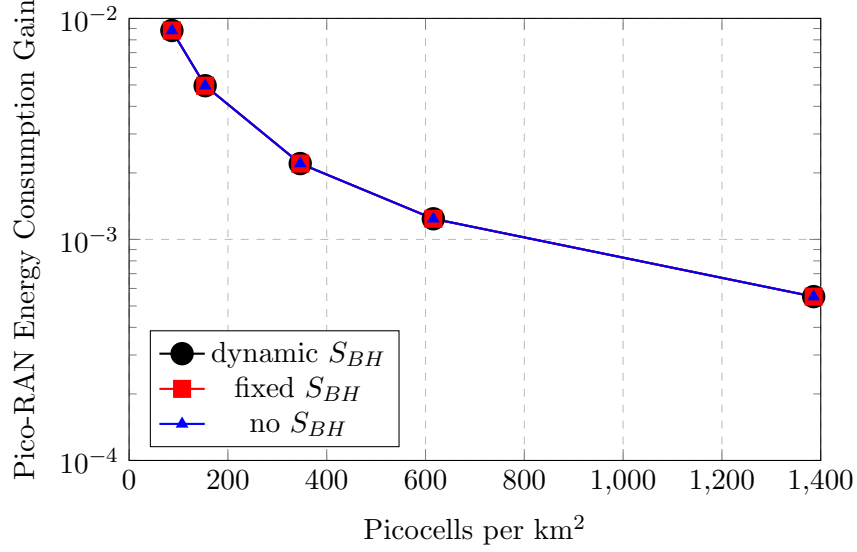


Figure 6.20: Pico-RAN Energy Consumption Gain on mmWave and IAB enabled against picocell density, comparing different backhaul rate constraints on node UEs: dynamic S_{BH} sets constraints based on bakchaul channel conditions, fixed S_{BH} sets fixed constraints, and no S_{BH} does not set constraint

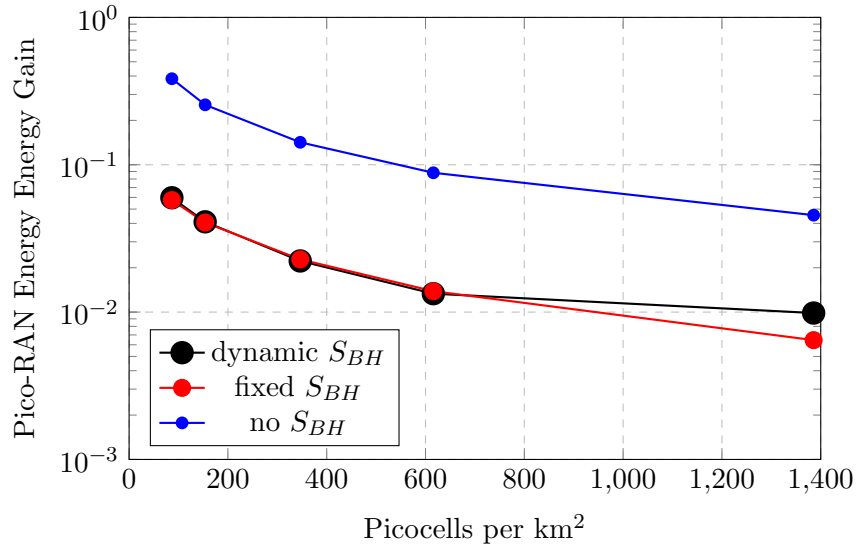


Figure 6.21: Pico-RAN Energy Efficiency Gain on mmWave and IAB enabled against picocell density, comparing different backhaul rate constraints on node UEs: dynamic S_{BH} sets constraints based on bakchaul channel conditions, fixed S_{BH} sets fixed constraints, and no S_{BH} does not set constraint

6.3.5 Sleep Modes

There are empty cells without UE association in densified RANs with limited UE density. Always keeping these empty cells active increases interference to UEs on the DL and consumes unnecessary energy. Therefore, putting these empty cells into low-power sleep mode would mitigate these two problems. In access time slots, the reduction in interference improves the UE SINR and thus the UE throughput. In the backhaul time slots, the reduction in interference improves the backhaul SINR and therefore the backhaul rate constraints, which eventually improve the UE throughput.

In this sub-section, the impact of sleep mode on pico-RAN densification is analysed. Without the sleep mode, empty cells have pilot power transmission at 10% of peak transmission power and all the overhead units on. The RAN power consumption is $P_{RAN,0}^{digital}$. There are three sleep mode depths considered: *Sleep1*, *Sleep2*, and *Sleep3*. *Sleep1* turns off the pilot transmission in empty cells in access time slots and non-transmitting cells in backhaul time slots but leaves all the overhead units on. The RAN power consumption is given by $P_{RAN,1}^{digital}$. *Sleep2*, or the *Site Sleep Mode*, turns off the pilot transmission in cells in the same way and turns all the overhead units off only if all the three cells in the pico-BS site are empty. The corresponding RAN power consumption is $P_{RAN,2}^{digital}$. In contrast, *Sleep3*, or the *Cell Sleep Mode*, turns off the pilot transmission similarly and turns all the overhead units off in empty cells. The RAN power consumption is $P_{RAN,3}^{digital}$. In addition, IAB is enabled all the time in this sub-section. The node wireless backhaul association is granted only if all four criteria are met. Resource partitioning is load-based, and node UEs have their throughput constrained by the dynamic backhaul rate.

Fig. 6.22 shows the pico-RAN Data Volume Gain with mmWave and IAB against the increasing picocell density, with and without the sleep mode. The key observations are:

1. All the sleep modes turn off the pilot transmission and limit the interference by the same scale. Different overhead power consumption does not change the capacity performance, so the DVGs between different sleep modes overlap.
2. In Fig. 6.22a, turning sleep mode on and turning pilot transmission off significantly improves the RAN DVG and capacity. This is because of the interference limitation in both the access and backhaul time slots. There are only a few empty picocells for low picocell densities. So the improvement in UE throughput caused by increasing the UE SINR is limited. In

contrast, many cells do not provide wireless backhaul to other cells in the backhaul time slots. Turning the transmission from these cells off reduces interference and raises the rate constraint. This improves the final UE throughput based on Eq. (6.18). The impact of the backhaul rate constraint on UE and RAN throughput will be discussed in more detail in the next sub-section. As picocell density increases further, the number of empty cells increases, so the interference is limited in access time slots. The same benefit of improved backhaul rate constraint still exists. Therefore, the UE throughput continues to improve compared with the case without the sleep mode, leading to improved area RAN throughput and DVG. When picocell density is 86.60 picocells per km^2 (ISD of 200 m), turning any sleep mode on increases the RAN DVG from 6.77 to 16.99. In contrast, when picocell density is 1385.64 picocells per km^2 (ISD of 50 m), turning any sleep mode on increases the RAN DVG from 17.88 to 45.62.

3. When the UE density is reduced to 300UEs/ km^2 , Fig. 6.22b shows similar capacity performance comparisons without and with the sleep mode. For the same RAN area, lower UE density means less UE in the RAN to activate fewer small cells. Less data volume will be transmitted; thus, less throughput will be achieved. Therefore, DVGs in Fig. 6.22b is always lower than the counterparts in Fig. 6.22a. In addition, less active small cell in the RAN leads to compromised backhaul link SINR caused by the increased separation between the wireless backhaul transmitting and receiving cells (empty node cells are not considered for node association when sleep mode is enabled). This leads to lower rate constraints on node UEs, limiting the capacity improvement brought by the sleep mode. Therefore, the DVG gap is small in Fig. 6.22b compared with Fig. 6.22a.

In summary, sleep mode improves the mmWave small cell RAN with IAB, and the improvement increases with the UE density.

Fig. 6.23 shows the RAN Energy Consumption Gain with mmWave and IAB, comparing sleep mode depths and UE densities. The key observations are:

1. As listed in Table 6.2, the site power consumption on mmWave is heavily overhead-dominated. As a result, RANs with different active cell numbers caused by different UE densities consume a similar amount of energy with negligible difference without the sleep mode (*Sleep0*), when

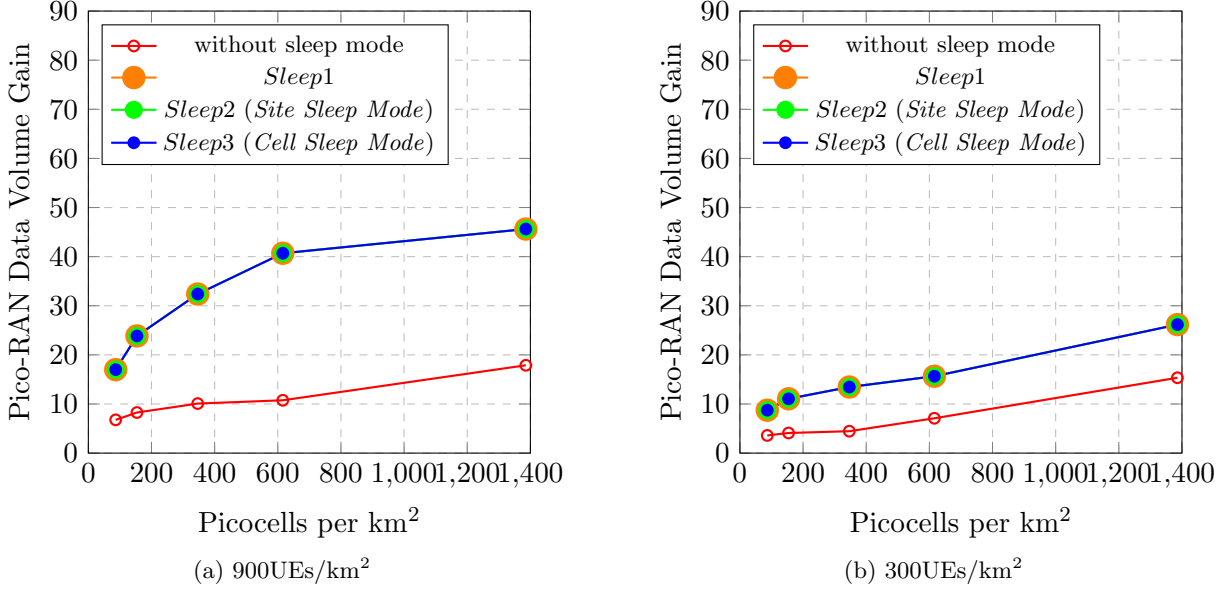


Figure 6.22: Pico-RAN Data Volume Gain on mmWave and IAB enabled against picocell density, with or without sleep mode, *Sleep1* only turns off pilot transmission in empty cells, *Sleep2 (Site Sleep Mode)* also turns empty sites off completely, *Sleep3 (Cell Sleep Mode)* turns empty cells off completely, UE densities of (a) 900UEs/km² (b) 300UEs/km²

comparing Fig. 6.23a with Fig. 6.23b. The same reason also causes the negligible energy reduction using *Sleep1* compared with *Sleep0*, shown by the overlapping ECG profiles in Fig. 6.23a and Fig. 6.23b.

2. *Site Sleep Mode*, or *Sleep2*, turns the radio-head and overhead of an empty pico-BS site off, saving considerable energy when the picocell density is higher than 615.84 picocells per km² (ISD 75 m) and 346.41 picocells per km² (ISD 100 m) for UE densities of 900 UEs/km² and 300 UEs/km², respectively. Lower UE density activates fewer small cells and leaves more empty cells. Thus *Site Sleep Mode* takes effect quicker than the higher UE density case. In addition, more empty cells increase the probability of having empty sites, reducing the total energy consumption. This results in ECG in 6.23b being higher than the counterpart in Fig. 6.23b when *Sleep2* is on.
3. *Cell Sleep Mode*, or *Sleep3*, further reduces the RAN total energy consumption by turning all the empty cells off, including both radio-head and overhead. This improves the RAN ECGs, especially when the picocell density is higher than 346.41 picocells per km² (ISD of 100 m) and 153.96 picocells per km² (ISD 100 m) for UE densities of 900 UEs/km² and 300

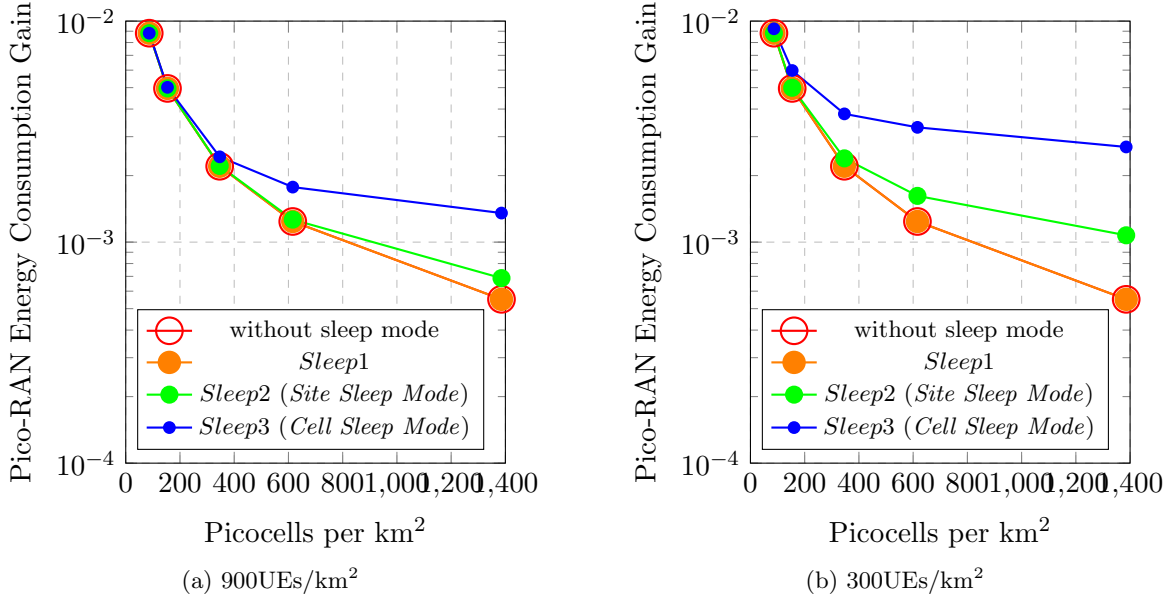


Figure 6.23: Pico-RAN Energy Consumption Gain on mmWave and IAB enabled against picocell density, with or without sleep mode, *Sleep1* only turns off pilot transmission in empty cells, *Sleep2* (*Site Sleep Mode*) also turns empty sites off completely, *Sleep3* (*Cell Sleep Mode*) turns empty cells off completely, UE densities of (a) 900UEs/ km^2 (b) 300UEs/ km^2

UEs/ km^2 , respectively. The turning points are lower than the *Sleep2* case.

Nevertheless, the overall RAN energy consumption still increases in a diminishing manner against the increasing picocell density, and the ECG decreases accordingly. With or without the sleep mode, the densified pico-RAN on mmWave with IAB enabled always consumes more energy than the reference LTE pico-RAN.

Fig. 6.24 shows the RAN Energy Efficiency Gain that is the product of the DVG results in Fig. 6.22, and the ECG results in Fig. 6.23. The key findings are:

1. When UE density is 900 UEs/ km^2 , Fig. 6.24a shows that the RAN EEG or energy efficiency degrades with the increasing picocell density, without or with the sleep mode. When *Sleep1* is enabled, the RAN EEG improves significantly compared with the case without the sleep mode for all picocell densities. The capacity enhancement causes this energy efficiency improvement as the energy consumption stays the same. When *Sleep2* (*Site Sleep Mode*) is enabled, the RAN EEG improves slightly compared with *Sleep1* when picocell density is larger than 615.84 picocells per km^2 (ISD of 75 m). This energy efficiency improvement is purely caused by energy consumption reduction as the capacity is the same. When *Sleep3* (*Cell Sleep Mode*)

is enabled, the RAN EEG improves further compared with *Sleep2 (Site Sleep Mode)* when picocell density is larger than 346.41 picocells per km² (ISD of 100 m). Similarly, this energy efficiency improvement is purely caused by energy consumption reduction but to a greater extent.

2. Fig. 6.24b shows the RAN EEG when UE density is 300 UEs/km². Without the sleep mode, the RAN EEG is lower than the counterpart in Fig. 6.24a because of the lower capacity. When *Sleep1* is enabled, the RAN EEG improves due to capacity improvement, but the decreasing tendency does not change. Compared with the EEG counterpart in Fig. 6.24a, the lower EEG in Fig. 6.24b is dominated by the lower capacity. When *Sleep2 (Site Sleep Mode)* is enabled, the reduced energy consumption recovers the energy efficiency after reaching 615.84 picocells per km² (ISD of 75 m). This is not observed in Fig. 6.24a because of the higher energy consumption that the capacity improvement cannot compensate for. Further energy efficiency improvement is shown when *Sleep3 (Cell Sleep Mode)* reduces more energy consumption. The energy efficiency recovers when the picocell density is 346.41 picocells per km² (ISD of 75 m).

Nevertheless, the densified pico-RAN on mmWave with IAB enabled within the considered picocell density range is always less energy efficient than the reference LTE pico-RAN. This is because of the significant energy consumption using the current power model and holds for both UE densities.

6.4 Summary

Measured by the three figures of merit included in the energy efficiency evaluation framework, the capacity (evaluated by the Data Volume Gain), energy consumption (evaluated by the Energy Consumption Gain), and energy efficiency (evaluated by the Energy Efficiency Gain) performance of the homogeneous pico-RAN densification is analysed in this chapter. Specifically, the signal carrier frequency has moved from the conventional LTE sub-6 GHz band to the mmWave band. The mmWave band can provide wide channel bandwidth for capacity improvement. The limited coverage caused by high path loss fading can be overcome by the BS peak transmission power increase and application into dense small cell infrastructure. In addition, the short wavelength of the mmWave signal makes the large-scale antenna array feasible, which could generate a narrow

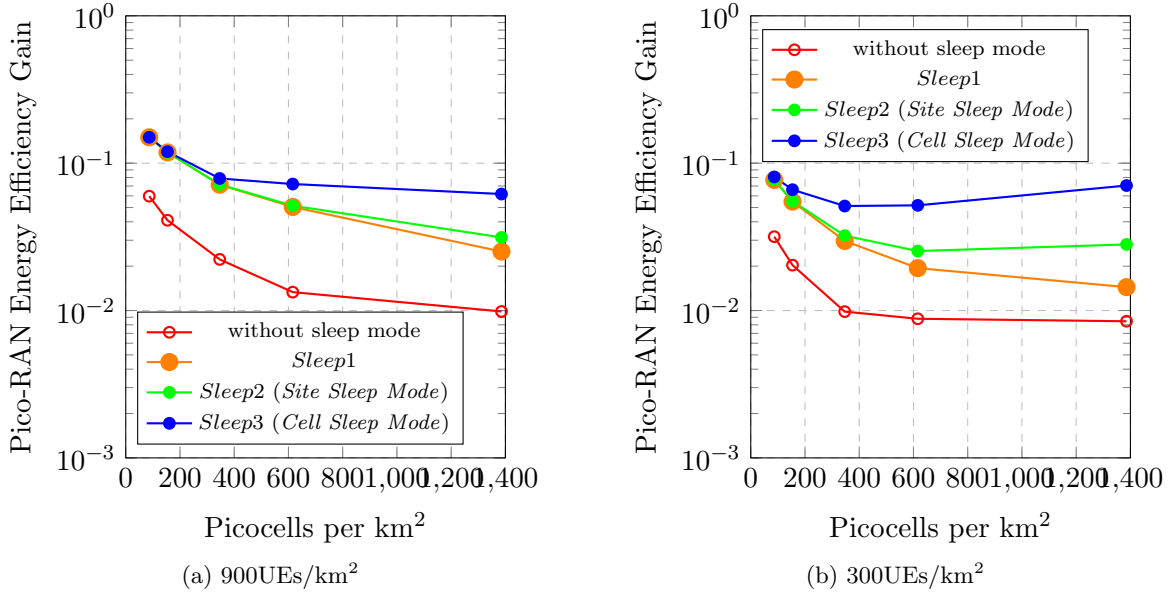


Figure 6.24: Pico-RAN Energy Efficiency Gain on mmWave and IAB enabled against picocell density, with or without sleep mode, *Sleep1* only turns off pilot transmission in empty cells, *Sleep2* (*Site Sleep Mode*) also turns empty sites off completely, *Sleep3* (*Cell Sleep Mode*) turns empty cells off completely, UE densities of (a) 900UEs/ km^2 (b) 300UEs/ km^2

antenna beam with high gain using beamforming. Another technique enabled by the mmWave band is IAB, which trades off the capacity for implementation and maintenance cost, especially for densified small cell RANs. This work considers three donor sites out of 19 sites when IAB is enabled. To compare the performance and calculate the figures of merit, the reference RAN chosen is the homogeneous pico-RAN with 200 m ISD on LTE sub-6 GHz frequency band, 900 UEs/ km^2 distributed uniformly in the RAN unless stated otherwise, and RR as the resource scheduler.

The capacity, energy consumption, and energy efficiency of the pico-RAN on mmWave are first evaluated against the increasing picocell density, with and without the IAB. The simulation results show that moving to mmWave without IAB improves the capacity significantly at the cost of increasing the energy consumption. This leads to energy efficiency degradation against the RAN densification compared with the reference LTE pico-RAN. When IAB is also enabled to reduce the backhaul implementation and maintenance cost, the capacity is compromised because the backhaul traffic occupies part of the resources. This indicates the trade-off between the implementation and maintenance cost and the RAN capacity.

Next, different node association criteria are compared for the densified pico-RAN with mmWave

and IAB, concentrating on the node backhaul link association. The simulation results show that limiting the number of UEs attached to the donor-node backhaul chains slightly improves the capacity, thus enhancing the energy efficiency. In contrast, limiting the number of hops for node sites degrades the capacity and energy consumption slightly. However, the overall impact of node association criteria on RAN capacity and energy efficiency is limited for the considered picocell densities. The energy consumption is not affected by the node association criteria.

The resource partitioning methods, either with fixed ratio or based on load, are compared for the densified pico-RAN on mmWave and IAB. The simulation results show that the load-based method outperforms the fixed ratio method at high picocell densities regarding capacity and energy efficiency. The resource partitioning methods do not affect the RAN energy consumption. Overall, the impact of the resource partitioning methods on RAN capacity and energy efficiency is also limited within the picocell density range.

Then the impact of the backhaul rate constraint on node UEs is investigated for the densified pico-RAN with mmWave and IAB regarding the capacity, energy consumption, and energy efficiency. The simulation results show that no rate constraint on node UEs would achieve similar energy efficiency performance to the case where IAB is not enabled. However, this requires the wireless backhaul links to perform similarly to the fibre links, which is unrealistic using current hardware technologies. The dynamic backhaul rate constraint is more realistic but leads to compromised capacity and energy efficiency without changing the energy consumption.

To reduce the energy consumption and limit the interference, the capacity, energy consumption, and energy efficiency of pico-RAN with mmWave and IAB are analysed against the increasing picocell density in terms of sleep mode at the end. The simulation results show that sleep mode can improve capacity and reduce energy consumption, enhancing energy efficiency. However, using the current power model, the energy reduced by turning all the empty cells completely off is insufficient to recover the degrading energy efficiency at high UE density at 900 UEs/km². In contrast, for medium UE density at 300 UEs/km², sleep mode manages to recover the energy efficiency. Nevertheless, within the considered picocell densities, the dense small cell RAN with mmWave and IAB is less energy efficient than the LTE counterpart using the current power model.

In summary, the mmWave improves the pico-RAN capacity but consumes significantly more energy. The sleep mode can only solve this energy issue when UE density is not high for the

considered picocell density range. Using the current power model, the pico-RAN on mmWave with IAB is less energy efficient than the LTE pico-RAN. For future works, the densification level could increase further to seek the limitation regarding the RAN capacity, energy consumption, and energy efficiency. In addition, more traffic intensities could be considered for the energy efficiency sensitivity study.

Chapter 7

Conclusions and Future Works

7.1 Conclusions

Small cell densification has been a promising technique to improve RAN capacity and energy efficiency. In addition, the limited channel bandwidth of the LTE sub-6 GHz frequency band constrains the capacity improvement, which could be mitigated when evolving to the mmWave frequency band with wide channel bandwidth. Applying the beamformed antenna array enhances the capacity more with the highly focused main beam. However, adding more always-on small cells increases energy consumption, compromising energy efficiency. To tackle this issue, sleep mode is applied to limit the interference from empty cells and reduce energy consumption by turning unnecessary hardware in empty cells off. Sleep mode is more effective for dense small cell infrastructures where the number of empty cells without UE associations is high. Moreover, the evolution to mmWave with wide channel bandwidth enables the advanced technique IAB, which allows access and backhaul links to share the same resource. IAB reduces the high cost of implementing and maintaining fibre backhaul, especially for ultra-dense small cell infrastructures. This research analysed the energy efficiency limitation of the ultra-dense small cell RANs to provide RAN design insights. Specifically, the analysis is done through a comprehensive energy efficiency evaluation framework, which provides a complete energy efficiency assessment regarding capacity, energy consumption, and energy efficiency.

The comprehensive energy efficiency evaluation framework is first presented in Chapter 3 to provide a complete energy efficiency assessment. Three radio-based figures of merit are included

in the framework: Data Volume Gain, Energy Consumption Gain, and Energy Efficiency Gain. These are used to compare the capacity, energy consumption, and energy efficiency performance of the test RAN to a reference RAN, respectively, and directly show performance improvement or degradation. Using this evaluation framework, the energy efficiency assessment is complete. A power model enhanced from the Green Radio Project is also included to quantify the BS site power consumption.

The energy efficiency of ultra-dense homogeneous LTE small cell RANs is analysed in Chapter 4 to seek the small cell densification limitation in terms of capacity, energy consumption, and energy efficiency. Small cell BSs are distributed uniformly to provide an optimistic performance because of the naturally bounded interference. The MATLAB-based simulation results show that small cell densification could only improve the RAN capacity to some extent. A high densification level, where the ISD between BSs is of the scale of several metres, leads to severe interference that compromises the RAN capacity. Meanwhile, adding more BSs with non-zero energy consumption continuously increases energy consumption. Dominated by the energy consumption increase, energy efficiency degrades with the RAN densification level. To save energy and limit interference, empty cells can be put into low-power sleep mode. Comparing the different transmission and power consumption levels of empty small cells, the results show that the ultra-dense small cell RAN is energy efficient only if all the empty cells are turned off completely, including the backhaul. This conclusion is tested and holds for UE density and scheduler variations. Furthermore, Round Robin is an effective resource scheduler for the ultra-dense small cell RAN for its simplicity without performance degradation. This is because there is only one UE in each active cell in ultra-dense small cell RAN, and schedulers like PF cannot exploit any UE diversity to improve capacity and energy efficiency.

The energy efficiency of ultra-dense small cells in LTE HetNets is analysed in Chapter 5 to explore the small cell densification limitation regarding capacity, energy consumption, and energy efficiency when co-existing with conventional macrocells. Macro-BSs are uniformly distributed for optimised performance, while small cell BSs are clustered to target the traffic hotspots. In addition, UEs are also clustered and distributed to model more closely to real-life traffic. The MATLAB-based simulation shows that macrocell densification improves the RAN capacity and energy efficiency while consuming more energy for a specific picocell density. Enabling sleep mode reduces the interference to enhance capacity and energy consumption to increase energy efficiency

further. In contrast, small cells are distributed in an ultra-dense manner for a particular density of macrocell. The simulation results show that picocell densification first improves and then degrades the RAN capacity, dominated by the signal strengthening and interference increase, respectively. However, the total RAN energy consumption increases continuously with the increasing picocell density, eventually compromising energy efficiency. When sleep mode is on, interference is limited, and energy consumption is reduced. The RAN energy efficiency increases monotonically with the increasing picocell density because of improving capacity and saturated energy consumption. These conclusions hold for different schedulers. Similarly, when HetNet is highly densified, the simple Round Robin scheduler is effective without performance degradation.

The energy efficiency of dense homogeneous small cell 5G RAN on mmWave is investigated in Chapter 6. IAB is also enabled because of the wide channel bandwidth to reduce the implementation and maintenance costs. Small cell BSs on mmWave also benefit from a large scale of antennas that can be beamformed to provide highly concentrated antenna gain. The MATLAB-based simulation results show that RAN capacity improves significantly without IAB compared with the reference LTE pico-RAN. However, the energy efficiency is compromised due to the increasing energy consumption caused by the wide channel bandwidth and large antenna number using the current power model. When IAB is enabled, UEs associated with the wireless-backhauled small cells have throughput constrained by the backhaul link conditions, compromising the overall capacity and energy efficiency performance compared with the case without IAB. Different backhaul rate constraints, time slots partitioning methods between UE and backhaul traffic, and small cell associations for wireless backhaul connection are evaluated to find the limited impact on RAN capacity and energy efficiency. The application of sleep mode reduces energy consumption and improves energy efficiency. Under the current power model, the RAN energy efficiency is highly energy consumption sensitive. Specifically, the energy efficiency against the increasing picocell density recovers from the decreasing tendency when UE density is 300 UEs/km², but fails to do so for the 900 UEs/km² UE density which activates more picocells to increase energy consumption.

This research studies the energy efficiency of ultra-dense small cell RANs with different advanced techniques using a rigorous evaluation framework. Specifically, the evaluation framework includes three ratio-based figures of merit to provide separate capacity, energy consumption, and energy efficiency performance analysis for a complete energy efficiency assessment. This gives RAN

designers a clear picture of potential performance trade-offs for an energy efficient ultra-dense small cell RAN. Moreover, the comprehensive studies of empty small cell transmission power and energy consumption levels show the necessity of turning BSs off when not in use to limit interference, save energy and improve energy efficiency. However, the current RAN policy does not support the complete BS turning-off due to the potential appearance of coverage holes on both downlinks and uplinks, and the difficulty to re-activate the BS regarding the transmission delay, re-synchronization and so on. Therefore, the standardisation of a complete BS shut down policy is urgently in demand. Additionally, advanced techniques like artificial intelligence (AI) are required for RAN management and sleep mode enabling. Moreover, based on the performance comparisons between LTE and 5G mmWave and IAB techniques, energy consumption is the limiting factor for energy efficiency. Therefore, the designs of 5G RAN and beyond should prioritise energy consumption constraining. This issue will become more severe for the sixth generation (6G) sub-THz techniques, which compact more antenna elements to trade energy consumption and energy efficiency for capacity improvement. This also requires a more comprehensive power model capable of accommodating different RAN architectures and advanced techniques with appropriate power consumption parameters, both of which are currently lacking.

7.2 Future Works

Future works include:

1. Different power consumption predictions. A more comprehensive power model is required to accommodate advanced techniques such as mmWave, and be adaptive to various hardware architectures (such as hybrid or fully digital signal processors) and BS infrastructures. Additionally, the constant power consumption assumed for the backhaul links lacks accuracy, especially when applied to the donor sites with the IAB technique enabled. For future work, factors like traffic aggregation in the RAN in relation to the backhaul link capacity should be considered. Moreover, appropriate parameters are in demand for the comprehensive power model to accurately predict the RAN energy consumption based on different scenarios.
2. Different BS modelling in the heterogeneous infrastructure. The uniform BS distribution where BSs have a fixed ISD limits the inter-cell interference and provides optimistic capacity

performance. In contrast, PPP BS distribution where BSs have varied ISDs and inter-cell interference provides pessimistic capacity performance. The PPP model might lead to a case where BSs have identical locations, incurring significant interference. Instead, the PPP model with minimum BS separation, or a uniform BS model with individual ISD bias, can be used to model more closely to the real-life infrastructure. Under the tractable PPP modelling, a mathematical analysis of UE SINR and RAN capacity could be carried out.

3. Inclusion of UE mobility and traffic model prediction. Specifically, mobile UEs would change the traffic distribution, requiring BSs to react accordingly. For example, BSs could use power control to limit interference and improve capacity. In addition, with the aid of traffic model prediction, BSs can predict the traffic and turn off and on when UEs are expected to leave or enter the coverage area. Advanced 6G techniques like machine learning and AI can be applied to predict the traffic model and manage RANs accordingly.
4. Further investigation of the mmWave technique. The current research stage has adopted a fully digital signal processing architecture for the mmWave BSs, which has optimal capacity performance but the energy consumption is also significant. Instead, digital processing and beamforming can change to analogue or hybrid where both digital and analogue architectures are employed. This would save considerable energy with the cost of limited capacity degradation, making the mmWave technique an energy efficient and green solution. In addition, the beamforming of the antenna array at BSs can be further developed to include the usage of codebooks.
5. Further investigation of the IAB technique. The current research state has a limited densification level, which could be extended further to seek capacity, energy consumption, and energy efficiency behaviour. In addition, different numbers of donors with fibre backhaul links can be investigated to explore the trade-off between cost and capacity performance.
6. Cuboid space volume expansion for the 3D ultra-dense small cell RANs. The current cuboid space in Chapter 4 has a width and length of 100 m and a height of 30 m. A larger 3D RAN could include more heterogeneous data types, BS types, and usage scenarios. For example, the 3D RAN could cover airborne and satellite traffic in addition to terrestrial traffic. The

performance of 3D ultra-dense infrastructure can be investigated regarding capacity (using VSE), energy consumption, and energy efficiency.

7. Application of further evolvement from 5G mmWave to 6G sub-THz techniques to the ultra-dense small cell RANs. Sub-THz techniques could provide wider bandwidth and a more focused antenna beam from a larger number of antenna elements than the mmWave technique for capacity enhancement. However, the energy consumption of such antenna arrays can be more significant, and the energy efficiency might be compromised. To tackle this issue, RAN and BS architectures should be smartly managed by machine learning and AI.

Bibliography

- [1] V. Jungnickel, K. Manolakis, W. Zirwas, B. Panzner, V. Braun, M. Lossow, M. Sternad, R. Apelfröjd, and T. Svensson, “The role of small cells, coordinated multipoint, and massive MIMO in 5G,” *IEEE Communications Magazine*, vol. 52, no. 5, pp. 44–51, 2014.
- [2] A. Osseiran, F. Boccardi, V. Braun, K. Kusume, P. Marsch, M. Maternia, O. Queseth, M. Schellmann, H. Schotten, H. Taoka, H. Tullberg, M. A. Uusitalo, B. Timus, and M. Fallgren, “Scenarios for 5G mobile and wireless communications: The vision of the METIS project,” *IEEE Communications Magazine*, vol. 52, no. 5, pp. 26–35, 2014.
- [3] F. Al-Turjman, E. Ever, and H. Zahmatkesh, “Small cells in the forthcoming 5G/IoT: Traffic modelling and deployment overview,” *IEEE Communications Surveys & Tutorials*, vol. 21, no. 1, pp. 28–65, 2019.
- [4] Cisco Visual Networking Index (VNI). (2017). “Global mobile data traffic forecast 2016–2021,” [Online]. Available: <http://www.cisco.com>.
- [5] E. Björnson, E. G. Larsson, and M. Debbah, “Massive MIMO for maximal spectral efficiency: How many users and pilots should be allocated?” *IEEE Transactions on Wireless Communications*, vol. 15, no. 2, pp. 1293–1308, 2016.
- [6] O. Teyeb, A. Muhammad, G. Mildh, E. Dahlman, F. Barac, and B. Makki, “Integrated access backhauled networks,” in *2019 IEEE 90th Vehicular Technology Conference (VTC2019-Fall)*, 2019, pp. 1–5.
- [7] Q. Zhang, W. Ma, Z. Feng, and Z. Han, “Backhaul-capacity-aware interference mitigation framework in 6G cellular internet of things,” *IEEE Internet of Things Journal*, vol. 8, no. 12, pp. 10 071–10 084, 2021.

- [8] ITU. (Jul. 2015). “IMT traffic estimates for the years 2020 to 2030.” International Telecommunication Union, Geneva, Switzerland, [Online]. Available: <https://www.itu.int/pub/R-REP-M.2370-2015>.
- [9] A. El Amine, J.-P. Chaiban, H. A. H. Hassan, P. Dini, L. Nuaymi, and R. Achkar, “Energy optimization with multi-sleeping control in 5G heterogeneous networks using reinforcement learning,” *IEEE Transactions on Network and Service Management*, pp. 1–1, 2022.
- [10] D. López-Pérez, M. Ding, H. Claussen, and A. H. Jafari, “Towards 1 Gbps/UE in cellular systems: Understanding ultra-dense small cell deployments,” *IEEE Communications Surveys & Tutorials*, vol. 17, no. 4, pp. 2078–2101, 2015.
- [11] 3GPP, “TR 36.808: Evolved universal terrestrial radio access (E-UTRA); carrier aggregation; base station (BS) radio transmission and reception,” 3rd Generation Partnership Project, Tech. Rep., 2013, Sophia Antipolis, France.
- [12] 3GPP, “TR 36.889: Feasibility study on licensed-assisted access to unlicensed spectrum,” 3rd Generation Partnership Project, Tech. Rep., 2014, Sophia Antipolis, France.
- [13] T. L. Marzetta, “Noncooperative cellular wireless with unlimited numbers of base station antennas,” *IEEE Transactions on Wireless Communications*, vol. 9, no. 11, pp. 3590–3600, 2010.
- [14] V. M. Nguyen and M. Kountouris, “Performance limits of network densification,” *IEEE Journal on Selected Areas in Communications*, vol. 35, no. 6, pp. 1294–1308, 2017.
- [15] *Arraycomm & william webb*, Ofcom, London, 2007.
- [16] J. Hoydis, M. Kobayashi, and M. Debbah, “Green small-cell networks,” *IEEE Vehicular Technology Magazine*, vol. 6, no. 1, pp. 37–43, 2011.
- [17] S. F. Yunas, T. Isotalo, J. Niemelä, and M. Valkama, “Impact of macrocellular network densification on the capacity, energy and cost efficiency in dense urban environment,” *International Journal of Wireless and Mobile Networks (IJWMN)*, vol. 5, pp. 99–118, Oct. 2013.

- [18] H. Fu and T. O'Farrell, "An energy efficiency evaluation framework for radio access networks," in *2018 International Conference on Information and Communication Technology Convergence (ICTC)*, 2018, pp. 577–580.
- [19] J. G. Andrews, "Seven ways that HetNets are a cellular paradigm shift," *IEEE Communications Magazine*, vol. 51, no. 3, pp. 136–144, 2013.
- [20] N. Bhushan, J. Li, D. Malladi, R. Gilmore, D. Brenner, A. Damnjanovic, R. T. Sukhavasi, C. Patel, and S. Geirhofer, "Network densification: The dominant theme for wireless evolution into 5G," *IEEE Communications Magazine*, vol. 52, no. 2, 2014.
- [21] M. Kamel, W. Hamouda, and A. Youssef, "Ultra-dense networks: A survey," *IEEE Communications Surveys & Tutorials*, vol. 18, no. 4, pp. 2522–2545, 2016.
- [22] J. G. Andrews, S. Buzzi, W. Choi, S. V. Hanly, A. Lozano, A. C. K. Soong, and J. C. Zhang, "What will 5G be?" *IEEE Journal on Selected Areas in Communications*, vol. 32, no. 6, pp. 1065–1082, 2014.
- [23] H. Claussen, D. López-Pérez, L. Ho, R. Razavi, and S. Kucera, "Small cells—the future of cellular networks," in *Small Cell Networks: Deployment, Management, and Optimization*. 2018, pp. 1–21.
- [24] C. Ma, M. Ding, D. López-Pérez, Z. Lin, J. Li, and G. Mao, "Performance analysis of the idle mode capability in a dense heterogeneous cellular network," *IEEE Transactions on Communications*, vol. 66, no. 9, pp. 3959–3973, 2018.
- [25] J. Wu, Y. Zhang, M. Zukerman, and E. K.-N. Yung, "Energy-efficient base-stations sleep-mode techniques in green cellular networks: A survey," *IEEE Communications Surveys & Tutorials*, vol. 17, no. 2, pp. 803–826, 2015.
- [26] E. Chavarria-Reyes, I. F. Akyildiz, and E. Fadel, "Energy consumption analysis and minimization in multi-layer heterogeneous wireless systems," *IEEE Transactions on Mobile Computing*, vol. 14, no. 12, pp. 2474–2487, 2015.
- [27] J. He, P. Loskot, T. O'Farrell, V. Friderikos, S. Armour, and J. Thompson, "Energy efficient architectures and techniques for green radio access networks," in *2010 5th International ICST Conference on Communications and Networking in China*, 2010, pp. 1–6.

- [28] O. Alamu, A. Gbenga-Ilori, M. Adelabu, A. Imoize, and O. Ladipo, “Energy efficiency techniques in ultra-dense wireless heterogeneous networks: An overview and outlook,” *Engineering Science and Technology, an International Journal*, vol. 23, no. 6, pp. 1308–1326, 2020.
- [29] W. Guo and T. O’Farrell, “Capacity-energy-cost tradeoff in small cell networks,” in *2012 IEEE 75th Vehicular Technology Conference (VTC Spring)*, 2012, pp. 1–5.
- [30] X. Cheng, Y. Hu, and L. Varga, “5G network deployment and the associated energy consumption in the uk: A complex systems’ exploration,” *Technological Forecasting and Social Change*, vol. 180, 2022.
- [31] L. Belkhir and A. Elmeligi, “Assessing ICT global emissions footprint: Trends to 2040 & recommendations,” *Journal of Cleaner Production*, vol. 177, pp. 448–463, 2018.
- [32] H. Fu and T. O’Farrell, “The spectral and energy efficiency of ultra-dense IoT networks,” in *2022 IEEE 8th International Conference on Network Softwarization (NetSoft)*, 2022, pp. 55–60.
- [33] B. Li, “Effective energy utilization through economic development for sustainable management in smart cities,” *Energy Reports*, vol. 8, pp. 4975–4987, 2022.
- [34] A. C. Şerban and M. D. Lytras, “Artificial intelligence for smart renewable energy sector in europe—smart energy infrastructures for next generation smart cities,” *IEEE Access*, vol. 8, pp. 77 364–77 377, 2020.
- [35] R. Carli, M. Dotoli, and R. Pellegrino, “A hierarchical decision-making strategy for the energy management of smart cities,” *IEEE Transactions on Automation Science and Engineering*, vol. 14, no. 2, pp. 505–523, 2017.
- [36] M. Rim and C. G. Kang, “Cache partitioning and caching strategies for device-to-device caching systems,” *IEEE Access*, vol. 9, pp. 8192–8211, 2021.
- [37] A. M. Ibrahim, A. A. Zewail, and A. Yener, “Device-to-device coded-caching with distinct cache sizes,” *IEEE Transactions on Communications*, vol. 68, no. 5, pp. 2748–2762, 2020.

- [38] Z. Hasan, H. Boostanimehr, and V. K. Bhargava, “Green cellular networks: A survey, some research issues and challenges,” *IEEE Communications Surveys & Tutorials*, vol. 13, no. 4, pp. 524–540, 2011.
- [39] J. T. Louhi, “Energy efficiency of modern cellular base stations,” in *INTELEC 07 - 29th International Telecommunications Energy Conference*, 2007, pp. 475–476.
- [40] S. Buzzi, C.-L. I, T. E. Klein, H. V. Poor, C. Yang, and A. Zappone, “A survey of energy-efficient techniques for 5G networks and challenges ahead,” *IEEE Journal on Selected Areas in Communications*, vol. 34, no. 4, pp. 697–709, 2016.
- [41] C. Ma, M. Ding, H. Chen, Z. Lin, G. Mao, and D. López-Pérez, “On the performance of multi-tier heterogeneous cellular networks with idle mode capability,” in *2018 IEEE Wireless Communications and Networking Conference (WCNC)*, 2018, pp. 1–6.
- [42] M. Ding, D. López-Pérez, G. Mao, and Z. Lin, “Performance impact of idle mode capability on dense small cell networks,” *IEEE Transactions on Vehicular Technology*, vol. 66, no. 11, pp. 10 446–10 460, 2017.
- [43] M. Ding, D. López-Pérez, Y. Chen, G. Mao, Z. Lin, and A. Y. Zomaya, “Ultra-dense networks: A holistic analysis of multi-piece path loss, antenna heights, finite users and bs idle modes,” *IEEE Transactions on Mobile Computing*, vol. 20, no. 4, pp. 1702–1713, 2021.
- [44] 3GPP, “ETSI ES 203 228: Environmental engineering (EE); assessment of mobile network energy efficiency,” 3rd Generation Partnership Project, Tech. Rep., Jan. 2015, V1.0.0.
- [45] T. Chen, H. Kim, and Y. Yang, “Energy efficiency metrics for green wireless communications,” in *2010 International Conference on Wireless Communications & Signal Processing (WCSP)*, 2010, pp. 1–6.
- [46] L. Yang, H. Zhang, M. Li, J. Guo, and H. Ji, “Mobile edge computing empowered energy efficient task offloading in 5G,” *IEEE Transactions on Vehicular Technology*, vol. 67, no. 7, pp. 6398–6409, 2018.
- [47] E. Björnson, M. Kountouris, and M. Debbah, “Massive MIMO and small cells: Improving energy efficiency by optimal soft-cell coordination,” in *ICT 2013*, 2013, pp. 1–5.

- [48] A. Aligrudic and M. Pejanovic-Djurisic, “Energy efficiency metrics for heterogeneous wireless cellular networks,” in *2014 Wireless Telecommunications Symposium*, 2014, pp. 1–4.
- [49] Y. Li, P. Fan, A. Leukhin, and L. Liu, “On the spectral and energy efficiency of full-duplex small-cell wireless systems with massive MIMO,” *IEEE Transactions on Vehicular Technology*, vol. 66, no. 3, pp. 2339–2353, 2017.
- [50] G. Miao, N. Himayat, G. Y. Li, and S. Talwar, “Distributed interference-aware energy-efficient power optimization,” *IEEE Transactions on Wireless Communications*, vol. 10, no. 4, pp. 1323–1333, 2011.
- [51] A. Yadav, O. A. Dobre, and H. V. Poor, “Is self-interference in full-duplex communications a foe or a friend?” *IEEE Signal Processing Letters*, vol. 25, no. 7, pp. 951–955, 2018.
- [52] L. Zhao, G. Zhao, and T. O’Farrell, “Efficiency metrics for wireless communications,” in *2013 IEEE 24th Annual International Symposium on Personal, Indoor, and Mobile Radio Communications (PIMRC)*, 2013, pp. 2825–2829.
- [53] L.-C. Wang and S.-H. Cheng, “Data-driven resource management for ultra-dense small cells: An affinity propagation clustering approach,” *IEEE Transactions on Network Science and Engineering*, vol. 6, no. 3, pp. 267–279, 2019.
- [54] W. Zhu, P. Xu, H. Jiang, and Y. He, “A resource allocation and cell association algorithm for energy efficiency in HetNets,” *International Journal of Communication Systems*, vol. 32, no. 16, 2019. [Online]. Available: <https://onlinelibrary.wiley.com/doi/abs/10.1002/dac.4123>.
- [55] Y. Wei, F. R. Yu, M. Song, and Z. Han, “User scheduling and resource allocation in HetNets with hybrid energy supply: An actor-critic reinforcement learning approach,” *IEEE Transactions on Wireless Communications*, vol. 17, no. 1, pp. 680–692, 2018.
- [56] T. Liu, J. Tong, Q. Guo, J. Xi, Y. Yu, and Z. Xiao, “Energy efficiency of massive MIMO systems with low-resolution ADCs and successive interference cancellation,” *IEEE Transactions on Wireless Communications*, vol. 18, no. 8, pp. 3987–4002, 2019.

- [57] R. Yin, Y. Zhang, F. Dong, A. Wang, and C. Yuen, “Energy efficiency optimization in LTE-U based small cell networks,” *IEEE Transactions on Vehicular Technology*, vol. 68, no. 2, pp. 1963–1967, 2019.
- [58] L. D. Nguyen, H. D. Tuan, T. Q. Duong, O. A. Dobre, and H. V. Poor, “Downlink beamforming for energy-efficient heterogeneous networks with massive MIMO and small cells,” *IEEE Transactions on Wireless Communications*, vol. 17, no. 5, pp. 3386–3400, 2018.
- [59] J. Tang, A. Shojaeifard, D. K. C. So, K.-K. Wong, and N. Zhao, “Energy efficiency optimization for CoMP-SWIPT heterogeneous networks,” *IEEE Transactions on Communications*, vol. 66, no. 12, pp. 6368–6383, 2018.
- [60] S. A. R. Naqvi, H. Pervaiz, S. A. Hassan, L. Musavian, Q. Ni, M. A. Imran, X. Ge, and R. Tafazolli, “Energy-aware radio resource management in D2D-enabled multi-tier HetNets,” *IEEE Access*, vol. 6, pp. 16 610–16 622, 2018.
- [61] J. Ye, X. Ge, G. Mao, and Y. Zhong, “5G ultradense networks with nonuniform distributed users,” *IEEE Transactions on Vehicular Technology*, vol. 67, no. 3, pp. 2660–2670, 2018.
- [62] C. Turyagyenda, T. O’Farrell, and W. Guo, “Long term evolution downlink packet scheduling using a novel proportional-fair-energy policy,” in *2012 IEEE 75th Vehicular Technology Conference (VTC Spring)*, 2012, pp. 1–6.
- [63] H. Zhang, Y. Nie, J. Cheng, V. C. M. Leung, and A. Nallanathan, “Sensing time optimization and power control for energy efficient cognitive small cell with imperfect hybrid spectrum sensing,” *IEEE Transactions on Wireless Communications*, vol. 16, no. 2, pp. 730–743, 2017.
- [64] E. Turgut and M. C. Gursoy, “Coverage in heterogeneous downlink millimeter wave cellular networks,” *IEEE Transactions on Communications*, vol. 65, no. 10, pp. 4463–4477, 2017.
- [65] I. Alqerm and B. Shihada, “Sophisticated online learning scheme for green resource allocation in 5G heterogeneous cloud radio access networks,” *IEEE Transactions on Mobile Computing*, vol. 17, no. 10, pp. 2423–2437, 2018.
- [66] B. Yang, Z. Yu, J. Lan, R. Zhang, J. Zhou, and W. Hong, “Digital beamforming-based massive MIMO transceiver for 5G millimeter-wave communications,” *IEEE Transactions on Microwave Theory and Techniques*, vol. 66, no. 7, pp. 3403–3418, 2018.

- [67] W. Hong, Z. H. Jiang, C. Yu, D. Hou, H. Wang, C. Guo, Y. Hu, L. Kuai, Y. Yu, Z. Jiang, Z. Chen, J. Chen, Z. Yu, J. Zhai, N. Zhang, L. Tian, F. Wu, G. Yang, Z.-C. Hao, and J. Y. Zhou, "The role of millimeter-wave technologies in 5G/6G wireless communications," *IEEE Journal of Microwaves*, vol. 1, no. 1, pp. 101–122, 2021.
- [68] J. G. Andrews, T. Bai, M. N. Kulkarni, A. Alkhateeb, A. K. Gupta, and R. W. Heath, "Modeling and analyzing millimeter wave cellular systems," *IEEE Transactions on Communications*, vol. 65, no. 1, pp. 403–430, 2017.
- [69] B. Yang, Z. Yu, Y. Dong, J. Zhou, and W. Hong, "Compact tapered slot antenna array for 5G millimeter-wave massive MIMO systems," *IEEE Transactions on Antennas and Propagation*, vol. 65, no. 12, pp. 6721–6727, 2017.
- [70] C. Saha, M. Afshang, and H. S. Dhillon, "Bandwidth partitioning and downlink analysis in millimeter wave integrated access and backhaul for 5G," *IEEE Transactions on Wireless Communications*, vol. 17, no. 12, pp. 8195–8210, 2018.
- [71] D. Yuan, H.-Y. Lin, J. Widmer, and M. Hollick, "Optimal joint routing and scheduling in millimeter-wave cellular networks," in *IEEE INFOCOM 2018 - IEEE Conference on Computer Communications*, 2018, pp. 1205–1213.
- [72] H. Willebrand and B. Ghuman, "Fiber optics without fiber," *IEEE Spectrum*, vol. 38, no. 8, pp. 40–45, 2001.
- [73] G. Kwon and H. Park, "Joint user association and beamforming design for millimeter wave UDN with wireless backhaul," *IEEE Journal on Selected Areas in Communications*, vol. 37, no. 12, pp. 2653–2668, 2019.
- [74] A. Arbi, T. O'Farrell, F.-C. Zheng, and S. Fletcher, "Toward green evolution of cellular networks by high order sectorisation and small cell densification," in *Interference Mitigation and Energy Management in 5G Heterogeneous Cellular Networks*, Jan. 2017.
- [75] L. Zhao, G. Zhao, and T. O'Farrell, "Efficiency metrics for wireless communications," in *2013 IEEE 24th Annual International Symposium on Personal, Indoor, and Mobile Radio Communications (PIMRC)*, 2013, pp. 2825–2829.

- [76] Y. Niu, C. Gao, Y. Li, L. Su, D. Jin, Y. Zhu, and D. O. Wu, "Energy-efficient scheduling for mmwave backhauling of small cells in heterogeneous cellular networks," *IEEE Transactions on Vehicular Technology*, vol. 66, no. 3, pp. 2674–2687, 2017.
- [77] X. Xu, C. Yuan, W. Chen, X. Tao, and Y. Sun, "Adaptive cell zooming and sleeping for green heterogeneous ultradense networks," *IEEE Transactions on Vehicular Technology*, vol. 67, no. 2, pp. 1612–1621, 2018.
- [78] A. Mesodiakaki, F. Adelantado, L. Alonso, M. Di Renzo, and C. Verikoukis, "Energy- and spectrum-efficient user association in millimeter-wave backhaul small-cell networks," *IEEE Transactions on Vehicular Technology*, vol. 66, no. 2, pp. 1810–1821, 2017.
- [79] Y. Niu, Y. Liu, Y. Li, X. Chen, Z. Zhong, and Z. Han, "Device-to-device communications enabled energy efficient multicast scheduling in mmwave small cells," *IEEE Transactions on Communications*, vol. 66, no. 3, pp. 1093–1109, 2018.
- [80] Z. Tan, H. Qu, J. Zhao, G. Ren, and W. Wang, "Self-sustainable dense cellular M2M system with hybrid energy harvesting and high sensitivity rectenna," *IEEE Access*, vol. 7, pp. 19 447–19 460, 2019.
- [81] N. N. Moghadam, G. Fodor, M. Bengtsson, and D. J. Love, "On the energy efficiency of MIMO hybrid beamforming for millimeter-wave systems with nonlinear power amplifiers," *IEEE Transactions on Wireless Communications*, vol. 17, no. 11, pp. 7208–7221, 2018.
- [82] I. AlQerm and B. Shihada, "Energy-efficient power allocation in multitier 5G networks using enhanced online learning," *IEEE Transactions on Vehicular Technology*, vol. 66, no. 12, pp. 11 086–11 097, 2017.
- [83] Y. Jiang, Y. Zou, H. Guo, T. A. Tsiftsis, M. R. Bhatnagar, R. C. de Lamare, and Y.-D. Yao, "Joint power and bandwidth allocation for energy-efficient heterogeneous cellular networks," *IEEE Transactions on Communications*, vol. 67, no. 9, pp. 6168–6178, 2019.
- [84] T. M. Nguyen, A. Yadav, W. Ajib, and C. Assi, "Centralized and distributed energy efficiency designs in wireless backhaul hetnets," *IEEE Transactions on Wireless Communications*, vol. 16, no. 7, pp. 4711–4726, 2017.

- [85] L. Venturino and S. Buzzi, “Energy-aware and rate-aware heuristic beamforming in downlink MIMO OFDMA networks with base-station coordination,” *IEEE Transactions on Vehicular Technology*, vol. 64, no. 7, pp. 2897–2910, 2015.
- [86] L. Venturino, A. Zappone, C. Risi, and S. Buzzi, “Energy-efficient scheduling and power allocation in downlink OFDMA networks with base station coordination,” *IEEE Transactions on Wireless Communications*, vol. 14, no. 1, pp. 1–14, 2015.
- [87] E. Initiative. (2010). “Network and telecom equipment - energy and performance assessment test procedures and measurement methodology.” Tech Rep Draft 3.0.1, Deutsche Telekom AG, Germany, [Online]. Available: http://www.ecrinitiative.org/pdfs/ECR%5C_3%5C_0%5C_1.pdf.
- [88] H. Hamdoun, P. Loskot, T. O’Farrell, and J. He, “Survey and applications of standardized energy metrics to mobile networks,” *annals of telecommunications - annales des télécommunications*, vol. 67, pp. 113–123, Apr. 2012.
- [89] B. Badic, T. O’Farrell, P. Loskot, and J. He, “Energy efficient radio access architectures for green radio: Large versus small cell size deployment,” in *2009 IEEE 70th Vehicular Technology Conference Fall*, 2009, pp. 1–5.
- [90] D. Muirhead, M. A. Imran, and K. Arshad, “Insights and approaches for low-complexity 5G small-cell base-station design for indoor dense networks,” *IEEE Access*, vol. 3, pp. 1562–1572, 2015.
- [91] F. Fang, J. Cheng, and Z. Ding, “Joint energy efficient subchannel and power optimization for a downlink NOMA heterogeneous network,” *IEEE Transactions on Vehicular Technology*, vol. 68, no. 2, pp. 1351–1364, 2019.
- [92] X. Song, L. Dong, J. Wang, L. Qin, and X. Han, “Energy efficient power allocation for downlink NOMA heterogeneous networks with imperfect CSI,” *IEEE Access*, vol. 7, pp. 39 329–39 340, 2019.
- [93] F. Fang, J. Cheng, Z. Ding, and H. V. Poor, “Energy efficient resource optimization for a downlink NOMA heterogeneous small-cell network,” in *2018 IEEE 10th Sensor Array and Multichannel Signal Processing Workshop (SAM)*, 2018, pp. 51–55.

- [94] Z. Yan, S. Chen, Y. Ou, and H. Liu, “Energy efficiency analysis of cache-enabled two-tier HetNets under different spectrum deployment strategies,” *IEEE Access*, vol. 5, pp. 6791–6800, 2017.
- [95] L. D. Nguyen, T. Q. Duong, H. Q. Ngo, and K. Tourki, “Energy efficiency in cell-free massive MIMO with zero-forcing precoding design,” *IEEE Communications Letters*, vol. 21, no. 8, pp. 1871–1874, 2017.
- [96] Z. Chang, Z. Han, and T. Ristaniemi, “Energy efficient optimization for wireless virtualized small cell networks with large-scale multiple antenna,” *IEEE Transactions on Communications*, vol. 65, no. 4, pp. 1696–1707, 2017.
- [97] M. Miozzo, L. Giupponi, M. Rossi, and P. Dini, “Switch-on/off policies for energy harvesting small cells through distributed Q-learning,” in *2017 IEEE Wireless Communications and Networking Conference Workshops (WCNCW)*, 2017, pp. 1–6.
- [98] H. Zhang, N. Liu, K. Long, J. Cheng, V. C. M. Leung, and L. Hanzo, “Energy efficient subchannel and power allocation for software-defined heterogeneous VLC and RF networks,” *IEEE Journal on Selected Areas in Communications*, vol. 36, no. 3, pp. 658–670, 2018.
- [99] C. Xiong, L. Lu, and G. Y. Li, “Energy-efficient spectrum access in cognitive radios,” *IEEE Journal on Selected Areas in Communications*, vol. 32, no. 3, pp. 550–562, 2014.
- [100] C. Shen, C. Tekin, and M. van der Schaar, “A non-stochastic learning approach to energy efficient mobility management,” *IEEE Journal on Selected Areas in Communications*, vol. 34, no. 12, pp. 3854–3868, 2016.
- [101] S. Samarakoon, M. Bennis, W. Saad, M. Debbah, and M. Latva-aho, “Ultra dense small cell networks: Turning density into energy efficiency,” *IEEE Journal on Selected Areas in Communications*, vol. 34, no. 5, pp. 1267–1280, 2016.
- [102] M. Chen, Y. Hao, M. Qiu, J. Song, D. Wu, and I. Humar, “Mobility-aware caching and computation offloading in 5G ultra-dense cellular networks,” *Sensors*, vol. 16, no. 7, p. 974, 2016.

- [103] J. Oueis, E. C. Strinati, and S. Barbarossa, “The fog balancing: Load distribution for small cell cloud computing,” in *2015 IEEE 81st Vehicular Technology Conference (VTC Spring)*, 2015, pp. 1–6.
- [104] Z. Becvar, M. Vondra, P. Mach, J. Plachy, and D. Gesbert, “Performance of mobile networks with UAVs: Can flying base stations substitute ultra-dense small cells?” In *European Wireless 2017; 23th European Wireless Conference*, 2017, pp. 1–7.
- [105] Z. Zhou, M. Dong, K. Ota, and Z. Chang, “Energy-efficient context-aware matching for resource allocation in ultra-dense small cells,” *IEEE Access*, vol. 3, pp. 1849–1860, 2015.
- [106] J. Zhang, J. Feng, C. Liu, X. Hong, X. Zhang, and W. Wang, “Mobility enhancement and performance evaluation for 5G ultra dense networks,” in *2015 IEEE Wireless Communications and Networking Conference (WCNC)*, 2015, pp. 1793–1798.
- [107] W. Guo and T. O’Farrell, “Relay deployment in cellular networks: Planning and optimization,” *IEEE Journal on Selected Areas in Communications*, vol. 31, no. 8, pp. 1597–1606, 2013.
- [108] W. Guo, S. Wang, Y. Wu, J. Rigelsford, X. Chu, and T. O’Farrell, “Spectral- and energy-efficient antenna tilting in a HetNet using reinforcement learning,” in *2013 IEEE Wireless Communications and Networking Conference (WCNC)*, 2013, pp. 767–772.
- [109] A. Arbi and T. O’Farrell, “Energy efficiency in 5G access networks: Small cell densification and high order sectorisation,” in *2015 IEEE International Conference on Communication Workshop (ICCW)*, 2015, pp. 2806–2811.
- [110] S. Wang, W. Guo, and T. O’Farrell, “Optimising femtocell placement in an interference limited network: Theory and simulation,” in *2012 IEEE Vehicular Technology Conference (VTC Fall)*, 2012, pp. 1–6.
- [111] L. Xu, Y. Mao, S. Leng, G. Qiao, and Q. Zhao, “Energy-efficient resource allocation strategy in ultra dense small-cell networks: A stackelberg game approach,” in *2017 IEEE International Conference on Communications (ICC)*, 2017, pp. 1–6.

- [112] B. Yang, G. Mao, X. Ge, M. Ding, and X. Yang, “On the energy-efficient deployment for ultra-dense heterogeneous networks with NLoS and LoS transmissions,” *IEEE Transactions on Green Communications and Networking*, vol. 2, no. 2, pp. 369–384, 2018.
- [113] C. Yang, J. Li, Q. Ni, A. Anpalagan, and M. Guizani, “Interference-aware energy efficiency maximization in 5G ultra-dense networks,” *IEEE Transactions on Communications*, vol. 65, no. 2, pp. 728–739, 2017.
- [114] C. Yang, J. Li, and M. Guizani, “Cooperation for spectral and energy efficiency in ultra-dense small cell networks,” *IEEE Wireless Communications*, vol. 23, no. 1, pp. 64–71, 2016.
- [115] T. Zhang, J. Zhao, L. An, and D. Liu, “Energy efficiency of base station deployment in ultra dense HetNets: A stochastic geometry analysis,” *IEEE Wireless Communications Letters*, vol. 5, no. 2, pp. 184–187, 2016.
- [116] N. Saxena, A. Roy, and H. Kim, “Traffic-aware cloud RAN: A key for green 5G networks,” *IEEE Journal on Selected Areas in Communications*, vol. 34, no. 4, pp. 1010–1021, 2016.
- [117] A. Ghazanfari, H. Tabassum, and E. Hossain, “Ambient RF energy harvesting in ultra-dense small cell networks: Performance and trade-offs,” *IEEE Wireless Communications*, vol. 23, no. 2, pp. 38–45, 2016.
- [118] W. Guo and T. O’Farrell, “Dynamic cell expansion with self-organizing cooperation,” *IEEE Journal on Selected Areas in Communications*, vol. 31, no. 5, pp. 851–860, 2013.
- [119] W. Guo and T. O’Farrell, “Green cellular network: Deployment solutions, sensitivity and tradeoffs,” in *2011 Wireless Advanced*, 2011, pp. 42–47.
- [120] T. Zhou, N. Jiang, Z. Liu, and C. Li, “Joint cell activation and selection for green communications in ultra-dense heterogeneous networks,” *IEEE Access*, vol. 6, pp. 1894–1904, 2018.
- [121] X. Huang, S. Tang, Q. Zheng, D. Zhang, and Q. Chen, “Dynamic femtocell gNB on/off strategies and seamless dual connectivity in 5G heterogeneous cellular networks,” *IEEE Access*, vol. 6, pp. 21 359–21 368, 2018.

- [122] S. Samarakoon, M. Bennis, W. Saad, and M. Latva-aho, "Opportunistic sleep mode strategies in wireless small cell networks," in *2014 IEEE International Conference on Communications (ICC)*, 2014, pp. 2707–2712.
- [123] G. Yu, Q. Chen, and R. Yin, "Dual-threshold sleep mode control scheme for small cells," *IET Communications*, vol. 8, no. 11, pp. 2008–2016, Jul. 2014.
- [124] R. Tao, W. Liu, X. Chu, and J. Zhang, "An energy saving small cell sleeping mechanism with cell range expansion in heterogeneous networks," *IEEE Transactions on Wireless Communications*, vol. 18, no. 5, pp. 2451–2463, 2019.
- [125] A. Ebrahim and E. Alsusa, "Interference and resource management through sleep mode selection in heterogeneous networks," *IEEE Transactions on Communications*, vol. 65, no. 1, pp. 257–269, 2017.
- [126] I. Ashraf, F. Boccardi, and L. Ho, "SLEEP mode techniques for small cell deployments," *IEEE Communications Magazine*, vol. 49, no. 8, pp. 72–79, 2011.
- [127] A. N. Uwaechia and N. M. Mahyuddin, "A comprehensive survey on millimeter wave communications for fifth-generation wireless networks: Feasibility and challenges," *IEEE Access*, vol. 8, pp. 62 367–62 414, 2020.
- [128] S. A. Busari, K. M. S. Huq, S. Mumtaz, L. Dai, and J. Rodriguez, "Millimeter-wave massive MIMO communication for future wireless systems: A survey," *IEEE Communications Surveys & Tutorials*, vol. 20, no. 2, pp. 836–869, 2018.
- [129] E. Turgut and M. C. Gursoy, "Coverage in heterogeneous downlink millimeter wave cellular networks," *IEEE Transactions on Communications*, vol. 65, no. 10, pp. 4463–4477, 2017.
- [130] S. Khalid, R. Mehmood, W. bin Abbas, F. Khalid, and M. Naeem, "Energy efficiency maximization of massive MIMO systems using RF chain selection and hybrid precoding," *Telecommunication Systems*, vol. 80, pp. 251–261, 2022.
- [131] H. Zhang, S. Huang, C. Jiang, K. Long, V. C. M. Leung, and H. V. Poor, "Energy efficient user association and power allocation in millimeter-wave-based ultra dense networks with energy harvesting base stations," *IEEE Journal on Selected Areas in Communications*, vol. 35, no. 9, pp. 1936–1947, 2017.

- [132] C. Han, T. Harrold, S. Armour, I. Krikidis, S. Videv, P. M. Grant, H. Haas, J. S. Thompson, I. Ku, C.-X. Wang, T. A. Le, M. R. Nakhai, J. Zhang, and L. Hanzo, “Green radio: Radio techniques to enable energy-efficient wireless networks,” *IEEE Communications Magazine*, vol. 49, no. 6, pp. 46–54, 2011.
- [133] M. Gruber, O. Blume, D. Ferling, D. Zeller, M. A. Imran, and E. C. Strinati, “EARTH — energy aware radio and network technologies,” in *2009 IEEE 20th International Symposium on Personal, Indoor and Mobile Radio Communications*, 2009, pp. 1–5.
- [134] O. Blume, D. Zeller, and U. Barth, “Approaches to energy efficient wireless access networks,” in *2010 4th International Symposium on Communications, Control and Signal Processing (ISCCSP)*, 2010, pp. 1–5.
- [135] J. Thompson and C. Khirallah, “Overview of green radio research outcomes,” in *2012 1st IEEE International Conference on Communications in China Workshops (ICCC)*, 2012, pp. 69–73.
- [136] G. Auer, O. Blume, and V. Giannini, “Energy efficiency analysis of the reference systems, areas of improvements and target breakdown,” EARTH Project, INFISO-ICT-247733 EARTH, Deliverable D2.3, Dec. 2010, pp. 1–68.
- [137] L. N. Ribeiro, S. Schwarz, M. Rupp, and A. L. F. de Almeida, “Energy efficiency of mmWave massive MIMO precoding with low-resolution DACs,” *IEEE Journal of Selected Topics in Signal Processing*, vol. 12, no. 2, pp. 298–312, 2018.
- [138] X. Ge, Y. Sun, H. Gharavi, and J. Thompson, “Joint optimization of computation and communication power in multi-user massive MIMO systems,” *IEEE Transactions on Wireless Communications*, vol. 17, no. 6, pp. 4051–4063, 2018.
- [139] G. Wang, A. Bytyn, D. Khajavi, Y. Wang, R. Negra, and G. Ascheid, “Power efficiency of millimeter wave transmission systems with large number of antennas,” in *2016 IEEE 84th Vehicular Technology Conference (VTC-Fall)*, 2016, pp. 1–6.
- [140] S. Mondal, L. R. Carley, and J. Paramesh, “Dual-band, two-layer millimeter-wave transceiver for hybrid MIMO systems,” *IEEE Journal of Solid-State Circuits*, vol. 57, no. 2, pp. 339–355, 2022.

- [141] X. Yu, J.-C. Shen, J. Zhang, and K. B. Letaief, “Alternating minimization algorithms for hybrid precoding in millimeter wave MIMO systems,” *IEEE Journal of Selected Topics in Signal Processing*, vol. 10, no. 3, pp. 485–500, 2016.
- [142] W. Shahjehan, A. Ullah, S. W. Shah, I. Khan, N. S. Sani, and K.-I. Kim, “A sparse optimization approach for beyond 5G mmWave massive MIMO networks,” *Computers, Materials & Continua*, vol. 72, no. 2, pp. 2797–2810, 2022.
- [143] A. Salh, L. Audah, Q. Abdullah, Ö. Aydoğdu, M. A. Alhartomi, S. H. Alsamhi, F. A. Almalki, and N. S. M. Shah, “Low computational complexity for optimizing energy efficiency in mm-wave hybrid precoding system for 5G,” *IEEE Access*, vol. 10, pp. 4714–4727, 2022.
- [144] A. Israr, Q. Yang, and A. Israr, “Power consumption analysis of access network in 5G mobile communication infrastructures — an analytical quantification model,” *Pervasive and Mobile Computing*, vol. 80, no. 101544, 2022.
- [145] E. Björnson, L. Sanguinetti, J. Hoydis, and M. Debbah, “Optimal design of energy-efficient multi-user mimo systems: Is massive MIMO the answer?” *IEEE Transactions on Wireless Communications*, vol. 14, no. 6, pp. 3059–3075, 2015.
- [146] B. Debaillie, C. Desset, and F. Louagie, “A flexible and future-proof power model for cellular base stations,” in *2015 IEEE 81st Vehicular Technology Conference (VTC Spring)*, 2015, pp. 1–7.
- [147] X. Ge, J. Yang, H. Gharavi, and Y. Sun, “Energy efficiency challenges of 5G small cell networks,” *IEEE Communications Magazine*, vol. 55, no. 5, pp. 184–191, 2017.
- [148] M. N. Islam, N. Abedini, G. Hampel, S. Subramanian, and J. Li, “Investigation of performance in integrated access and backhaul networks,” in *IEEE INFOCOM 2018 - IEEE Conference on Computer Communications Workshops (INFOCOM WKSHPS)*, 2018, pp. 597–602.
- [149] T. Bai and R. W. Heath, “Coverage and rate analysis for millimeter-wave cellular networks,” *IEEE Transactions on Wireless Communications*, vol. 14, no. 2, pp. 1100–1114, 2015.

- [150] C. Saha and H. S. Dhillon, "Millimeter wave integrated access and backhaul in 5G: Performance analysis and design insights," *IEEE Journal on Selected Areas in Communications*, vol. 37, no. 12, pp. 2669–2684, 2019.
- [151] T. Tian, Y. Dou, G. Ren, L. Gu, J. Chen, Y. Cui, T. Takada, M. Iwabuchi, J. Tsuboi, and Y. Kishiyama, "Field trial on millimeter wave integrated access and backhaul," in *2019 IEEE 89th Vehicular Technology Conference (VTC2019-Spring)*, 2019, pp. 1–5.
- [152] X. Ge, S. Tu, G. Mao, V. K. N. Lau, and L. Pan, "Cost efficiency optimization of 5G wireless backhaul networks," *IEEE Transactions on Mobile Computing*, vol. 18, no. 12, pp. 2796–2810, 2019.
- [153] W. Lei, Y. Ye, and M. Xiao, "Deep reinforcement learning-based spectrum allocation in integrated access and backhaul networks," *IEEE Transactions on Cognitive Communications and Networking*, vol. 6, no. 3, pp. 970–979, 2020.
- [154] R. Gupta and S. Kalyanasundaram, "Resource allocation for self-backhauled networks with half-duplex small cells," in *2017 IEEE International Conference on Communications Workshops (ICC Workshops)*, 2017, pp. 198–204.
- [155] J. Y. Lai, W.-H. Wu, and Y. T. Su, "Resource allocation and node placement in multi-hop heterogeneous integrated-access-and-backhaul networks," *IEEE Access*, vol. 8, pp. 122 937–122 958, 2020.
- [156] W. Pu, X. Li, J. Yuan, and X. Yang, "Resource allocation for millimeter wave self-backhaul network using markov approximation," *IEEE Access*, vol. 7, pp. 61 283–61 295, 2019.
- [157] A. Hlukowa and V. Venkatasubramanian, "Dynamic in-band self-backhauling for 5G systems with inter-cell resource coordination," *International Journal of Wireless Information Networks*, vol. 26, pp. 319–330, 2019.
- [158] S. Zhang, X. Xu, M. Sun, X. Tao, and C. Liu, "Joint spectrum and power allocation in 5G integrated access and backhaul networks at mmWave band," in *2020 IEEE 31st Annual International Symposium on Personal, Indoor and Mobile Radio Communications*, 2020, pp. 1–7.

- [159] B. Zhang, F. Devoti, and I. Filippini, “RL-based resource allocation in mmWave 5G IAB networks,” in *2020 Mediterranean Communication and Computer Networking Conference (MedComNet)*, 2020, pp. 1–8.
- [160] M. Lashgari, B. Maham, and H. Kebriaei, “Energy-efficient self-backhauling in heterogeneous wireless networks: A game-theoretic approach,” *Physical Communication*, vol. 29, pp. 296–306, 2018.
- [161] D. Yu, Y. Liu, and H. Zhang, “Energy-efficient beamforming design for user-centric full-duplex wireless backhaul networks,” in *2021 IEEE Global Communications Conference (GLOBECOM)*, 2021, pp. 1–6.
- [162] S. Rajoria, A. Trivedi, and W. Godfrey, “Energy efficiency optimization for massive MIMO backhaul networks with imperfect CSI and full duplex small cells,” *Wireless Personal Communications*, vol. 119, pp. 691–712, 2021.
- [163] W. Hao, M. Zeng, Z. Chu, S. Yang, and G. Sun, “Energy-efficient resource allocation for mmWave massive MIMO HetNets with wireless backhaul,” *IEEE Access*, vol. 6, pp. 2457–2471, 2018.
- [164] Z. Gao, L. Dai, D. Mi, Z. Wang, M. A. Imran, and M. Z. Shakir, “Mmwave massive-MIMO-based wireless backhaul for the 5G ultra-dense network,” *IEEE Wireless Communications*, vol. 22, no. 5, pp. 13–21, 2015.
- [165] A. Giannopoulos, S. Spantideas, N. Kapsalis, P. Karkazis, and P. Trakadas, “Deep reinforcement learning for energy-efficient multi-channel transmissions in 5G cognitive HetNets: Centralized, decentralized and transfer learning based solutions,” *IEEE Access*, vol. 9, pp. 129 358–129 374, 2021.
- [166] Y. Zhang, Y. Xu, Y. Sun, Q. Wu, and K. Yao, “Energy efficiency of small cell networks: Metrics, methods and market,” *IEEE Access*, vol. 5, pp. 5965–5971, 2017.
- [167] T. O’Farrell and S. Fletcher, “Green communication concepts, energy metrics and throughput efficiency for wireless systems,” in *Green Communications: Principles, Concepts and Practice*, K. Samdanis, P. Rost, A. Maeder, M. Meo, and C. Verikoukis, Eds., John Wileys & Sons. Ltd, 2015, pp. 19–42.

- [168] D. Persson, T. Eriksson, and E. G. Larsson, “Amplifier-aware multiple-input multiple-output power allocation,” *IEEE Communications Letters*, vol. 17, no. 6, pp. 1112–1115, 2013.
- [169] Y. Roth, J.-B. Doré, L. Ros, and V. Berg, “The physical layer of low power wide area networks: Strategies, information theory’s limit and existing solutions,” 2018.
- [170] C. Desset, B. Debaillie, V. Giannini, A. Fehske, G. Auer, H. Holtkamp, W. Wajda, D. Sabella, F. Richter, M. J. Gonzalez, H. Klessig, I. Gódor, M. Olsson, M. A. Imran, A. Ambrosy, and O. Blume, “Flexible power modeling of LTE base stations,” in *2012 IEEE Wireless Communications and Networking Conference (WCNC)*, 2012, pp. 2858–2862.
- [171] D. Liu, L. Wang, Y. Chen, M. Elkashlan, K.-K. Wong, R. Schober, and L. Hanzo, “User association in 5G networks: A survey and an outlook,” *IEEE Communications Surveys & Tutorials*, vol. 18, no. 2, pp. 1018–1044, 2016.
- [172] H. Claussen, D. López-Pérez, L. Ho, R. Razavi, and S. Kucera, “Backhaul for small cells,” in *Small Cell Networks: Deployment, Management, and Optimization*. 2018, pp. 419–441.
- [173] C.-H. Liu and L.-C. Wang, “Optimal cell load and throughput in green small cell networks with generalized cell association,” *IEEE Journal on Selected Areas in Communications*, vol. 34, no. 5, pp. 1058–1072, 2016.
- [174] H. Holma and A. Toskala, “LTE standardization,” in *LTE for UMTS: Evolution to LTE-Advanced*. 2011, pp. 13–21.
- [175] 3GPP, “TR 36.828: 3rd generation partnership project; technical specification group radio access network; evolved universal terrestrial radio access (E-UTRA); further enhancements to LTE time division duplex (TDD) for downlink-uplink (DL-UL) interference management and traffic adaptation (release 11),” 3rd Generation Partnership Project, Tech. Rep., Jun. 2012, V11.0.0.
- [176] C. Meraki, *Meraki dual-band sector antenna*, MA-ANT-27 datasheet.
- [177] Pasternack, *698-960/1710-2700 MHz 3/4 dBi omni directional DAS antenna*, PE51OM1020 datasheet, 2020.

- [178] 3GPP, “TR 36.814: 3rd generation partnership project; technical specification group radio access network; evolved universal terrestrial radio access (E-UTRA); further advancements for E-UTRA physical layer aspects (release 9),” 3rd Generation Partnership Project, Tech. Rep., Mar. 2017, V9.2.0.
- [179] K. Haneda, J. Zhang, L. Tan, G. Liu, Y. Zheng, H. Asplund, J. Li, Y. Wang, D. Steer, C. Li, T. Balercia, S. Lee, Y. Kim, A. Ghosh, T. Thomas, T. Nakamura, Y. Kakishima, T. Imai, H. Papadopoulos, T. S. Rappaport, G. R. MacCartney, M. K. Samimi, S. Sun, O. Koymen, S. Hur, J. Park, C. Zhang, E. Mellios, A. F. Molisch, S. S. Ghassamzadeh, and A. Ghosh, “5G 3GPP-like channel models for outdoor urban microcellular and macrocellular environments,” in *2016 IEEE 83rd Vehicular Technology Conference (VTC Spring)*, 2016, pp. 1–7.
- [180] E. Sisinni, A. Saifullah, S. Han, U. Jennehag, and M. Gidlund, “Industrial internet of things: Challenges, opportunities, and directions,” *IEEE Transactions on Industrial Informatics*, vol. 14, no. 11, pp. 4724–4734, 2018.
- [181] J. Liu, C.-H. R. Lin, Y.-C. Hu, and P. K. Donta, “Joint beamforming, power allocation, and splitting control for SWIPT-enabled IoT networks with deep reinforcement learning and game theory,” *Sensors*, vol. 22, no. 6, 2022. [Online]. Available: <https://www.mdpi.com/1424-8220/22/6/2328>.
- [182] H. Shokri-Ghadikolaei, C. Fischione, P. Popovski, and M. Zorzi, “Design aspects of short-range millimeter-wave networks: A MAC layer perspective,” *IEEE Network*, vol. 30, no. 3, pp. 88–96, 2016.
- [183] K. Wong and T. O’Farrell, “Coverage of 802.11g WLANs in the presence of bluetooth interference,” in *14th IEEE Proceedings on Personal, Indoor and Mobile Radio Communications, 2003. PIMRC 2003.*, vol. 3, 2003, pp. 2027–2031.
- [184] CORDIS. (2021). “Beyond 5G: 3D network modelling for THz-based ultra-fast small cells.” 5G-ACE, Horizon 2020, [Online]. Available: <https://cordis.europa.eu/project/id/839573/reporting/de>.

- [185] I. Yaqoob, E. Ahmed, I. A. T. Hashem, A. I. A. Ahmed, A. Gani, M. Imran, and M. Guizani, "Internet of things architecture: Recent advances, taxonomy, requirements, and open challenges," *IEEE Wireless Communications*, vol. 24, no. 3, pp. 10–16, 2017.
- [186] M. Agiwal, A. Roy, and N. Saxena, "Next generation 5G wireless networks: A comprehensive survey," *IEEE Communications Surveys & Tutorials*, vol. 18, no. 3, pp. 1617–1655, 2016.
- [187] D. López-Pérez, X. Chu, and Í. Guvenc, "On the expanded region of picocells in heterogeneous networks," *IEEE Journal of Selected Topics in Signal Processing*, vol. 6, no. 3, pp. 281–294, 2012.
- [188] C. Madapatha, B. Makki, C. Fang, O. Teyeb, E. Dahlman, M.-S. Alouini, and T. Svensson, "On integrated access and backhaul networks: Current status and potentials," *IEEE Open Journal of the Communications Society*, vol. 1, pp. 1374–1389, 2020.
- [189] A. Alammouri, M. Gupta, F. Baccelli, and J. G. Andrews, "Escaping the densification plateau in cellular networks through mmwave beamforming," *IEEE Wireless Communications Letters*, vol. 9, no. 11, pp. 1874–1878, 2020.
- [190] C. Singh and P. C. Kishoreraja, "An energy efficient resource allocation and transmit antenna selection scheme in mm-wave using massive multiple-input multiple-output technology," *International Journal of Communication Systems*, vol. 35, no. 6, 2022.
- [191] J. Rogerson and S. Kavanagh. (May 2022). "How fast is 5G?" 5G Comparison Site, [Online]. Available: <https://5g.co.uk/guides/how-fast-is-5g/>.
- [192] 3GPP, "R1-1812199: System performance evaluation in multi-hop IAB network," 3rd Generation Partnership Project, Tech. Rep., Nov. 2018, 3GPP TSG RAN WG1 Meeting #95 agenda item 7.2.3.2.
- [193] 3GPP, "R1-1812487: Evaluation methodology and results on NR IAB," 3rd Generation Partnership Project, Tech. Rep., Nov. 2018, 3GPP TSG RAN WG1 Meeting #95 agenda item 7.2.3.2.
- [194] 3GPP, "TR 38.901: 5G; study on channel model for frequencies from 0.5 to 100 GHz (release 14)," Tech. Rep., May 2017, V14.0.0.

- [195] 3GPP, “TR 38.874: 3rd generation partnership project; technical specification group radio access network; NR; study on integrated access and backhaul (release 16),” Tech. Rep., Dec. 2018, V16.0.0.
- [196] A. K. Gupta, J. G. Andrews, and R. W. Heath, “On the feasibility of sharing spectrum licenses in mmWave cellular systems,” *IEEE Transactions on Communications*, vol. 64, no. 9, pp. 3981–3995, 2016.
- [197] 3GPP, “R1-1805924: IAB system evaluation methodology and preliminary results,” Tech. Rep., May 2018, 3GPP TSG RAN WG1 Meeting #93 agenda item 7.7.2.
- [198] M. Polese, M. Giordani, A. Roy, S. Goyal, D. Castor, and M. Zorzi, “End-to-end simulation of integrated access and backhaul at mmWaves,” in *2018 IEEE 23rd International Workshop on Computer Aided Modeling and Design of Communication Links and Networks (CAMAD)*, 2018, pp. 1–7.
- [199] S. Singh, M. N. Kulkarni, A. Ghosh, and J. G. Andrews, “Tractable model for rate in self-backhauled millimeter wave cellular networks,” *IEEE Journal on Selected Areas in Communications*, vol. 33, no. 10, pp. 2196–2211, 2015.
- [200] TMYTEK, *BBoard 28 GHz*, BB-BOARD-BP-28 datasheet, V 0.2.0, Jun. 2021.
- [201] P. Vetter, T. Ayhan, K. Kanonakis, B. Lannoo, K. Lee, L. Lefevre, C. Monney, F. Saliou, and X. Yin, “Towards energy efficient wireline networks, an update from GreenTouch,” in *2013 18th OptoElectronics and Communications Conference held jointly with 2013 International Conference on Photonics in Switching (OECC/PS)*, 2013, pp. 1–2.